4-2016

# Development of an Integrated Reformer and Fuel Cell System for Portable Power Applications

Michael G. Waller
mgw7167@rit.edu

# DEVELOPMENT OF AN INTEGRATED REFORMER AND FUEL CELL SYSTEM FOR PORTABLE POWER APPLICATIONS

by

MICHAEL G. WALLER

A DISSERTATION

Submitted in partial fulfillment of the requirements
for the degree of Doctor of Philosophy
in
Sustainability

Department of Sustainability

Golisano Institute for Sustainability
Rochester Institute of Technology

April 2016

Author: _____
Sustainability Program

Certified by: _____
Dr. Thomas A. Trabold
Associate Professor and Department Head, Sustainability Program

Certified by: _____
Dr. Nabil Nasr
Assistant Provost and Director, Golisano Institute for Sustainability and CIMS

# NOTICE OF COPYRIGHT

**DEVELOPMENT OF AN INTEGRATED REFORMER AND FUEL CELL SYSTEM FOR PORTABLE POWER APPLICATIONS**

by

Michael G. Waller

Submitted by Michael G. Waller in partial fulfillment of the requirements for the degree of Doctor of Philosophy in Sustainability and accepted on behalf of the Rochester Institute of Technology dissertation committee.

We, the undersigned members of the Faculty of the Rochester Institute of Technology, certify that we have advised and/or supervised the candidate on the work described in this dissertation. We further certify that we have reviewed the dissertation manuscript and approve it in partial fulfillment of the requirements of the degree Doctor of Philosophy in Sustainability.

**Approved by:**

Dr. Christopher L. Lewis _____
(External Examiner and Chair) Date

Dr. Thomas A. Trabold _____
(Dissertation Advisor)

Dr. Nenad Nenadic _____

Dr. Clark G. Hochgraf _____

SUSTAINABILITY PROGRAM
ROCHESTER INSTITUTE OF TECHNOLOGY
April 2016

**ABSTRACT**

Golisano Institute for Sustainability
Rochester Institute of Technology

Degree: Doctor of Philosophy Program: Sustainability

Name of Candidate: Michael Waller

Title: Development of an integrated reformer fuel cell system for portable applications

In order for fuel cells to play a large part in a global sustainable energy infrastructure, fuel cell-based systems need to be built to meet the demands of a wide range of applications in all aspects of society. To date, the majority of fuel cell research has been focused on developing systems to power applications such as passenger vehicles, commercial buildings, and small handheld devices. These applications typically require power outputs that are either greater than 100 kW or less than 20 W, and a gap remains in developing viable fuel cell systems for applications requiring electric power between 100 W and 100 kW. Some of these applications include unmanned aerial vehicles (UAVs), residential power generators, equipment pumps, camping and recreational devices, lawn and garden equipment, and auxiliary power units. Key requirements for these applications include a power system that is portable, has a quick startup time, and can be easily refueled. The focus of this dissertation is to identify and address the engineering gaps encountered when developing a viable fuel cell system capable of meeting the requirements for these "medium"-sized power applications. Ultimately, an integrated reformer fuel cell system is proposed; this system utilizes a propane catalytic partial oxidation rector coupled with a HT-PEM fuel cell. Using this structure, the optimal operating conditions for propane catalytic partial oxidation were investigated. Additionally, the performance of a HT-

PEM fuel cell under various conditions while operating directly on propane fuel reformate was assessed. After investigation into the weight, power, run time, and durability requirements of military UAVs, a reformer fuel cell system is proposed that produces a net power of 250 W with a total mass 2.23 kg, and is capable of a 200-hour lifetime. This proposed design offers significant advantages over current UAV propulsion technologies in that it is both quiet and capable of long flight durations, unlike battery and internal combustion engine technology presently used that suffer from either low specific energy or high noise level. The proposed system also has advantages over other fuel cell systems in that it is fueled with commonly available propane, where other mobile fuel cells require high purity $H_2$ that is difficult to obtain. In addition to assessing the technical feasibility of such a system, the potential environmental benefits relative to incumbent technology are described.

## ACKNOWLEDGMENTS

The work completed in this dissertation could not have been achieved without significant time, support, and guidance from many others. First and foremost, I would not have been able to accomplish all of the work discussed in this dissertation without the support, edits, and extreme patience from my wife Emily. She consistently encouraged and pushed me forward throughout this whole process, spending many hours editing my work and learning much more about fuel cells than I think she ever thought she would. I do not believe it would have been possible for me to complete this work without her, and I am extremely blessed to have her as my wife.

Additionally, without the guidance and help from Tom Trabold and Mark Walluk, who both went above and beyond what I would have expected from University faculty and staff engineers, I could not have learned as much as I have, or even come close to accomplishing what is described throughout this dissertation. They both set the bar extremely high for how to best advise their graduate students as a faculty advisor, and how to guide and coach students successfully as a staff engineer. The majority of fond memories I have from this whole process were times working with both Tom and Mark, and I hope there will be many more. I could not have been more fortunate to work with both of them, and am extremely grateful for all of their support and guidance.

I also want to thank Mike Bradley for all of his help and guidance in the lab, where much of my work took place. Without his help and advice, much of the data and assessments could not have been completed. I have learned quite a lot of hands-on experience from him, and am very grateful for the time I had working with him.

I am also deeply appreciative of those who supported and encouraged me when I needed help or was simply discouraged and did not feel like continuing on. My mother, Vicki Waller, and my

in-laws John and Susan Foley, consistently encouraged and provided practical advice to me. Without their thoughts, prepared meals, and kind words, this whole PhD journey would have been much more difficult.

My time at RIT was made enjoyable in large part to the many friendships and groups that I was able to connect with. I am very grateful for both Schuyler Matteson and Steve Barber who were always available for help and support when I needed it, as well as the many hours playing corn hole or other games at the student office. Additionally, the many friends and lasting relationships I made through Cru at RIT and the Caleb Tutoring Ministry greatly enriched my experience, and I am very blessed to have been part of those ministries.

Finally, I wish to dedicate this work my children, Caleb and Elise. You both bring so much joy and happiness to my life, and I am so fortunate and proud to be your Dad. Although right now it does not seem that you understand at all how fuel cells work (in spite of my attempts to teach you), I hope this work completed here will help me to be a good example in how we can serve and make a positive impact on other in our community. I love you both very much, and am enjoying every moment watching you grow up.

Thank you all again, for all of your support.

Michael G. Waller
Rochester Institute of Technology
April 2016

# Table of Contents

# List of Tables

# List of Figures

# Abbreviations and Symbols

| | |
|---|---|
| AFC | alkaline fuel cell |
| ATR | autothermal reforming |
| cPOx | catalytic partial oxidation |
| DMFC | direct methanol fuel cell |
| $F$ | Faradays constant (C/mol) |
| $\Delta\bar{G}_f$ | Gibbs free energy (kJ/mol) |
| HOR | hydrogen oxidation reaction |
| HT-PEM | high temperature proton exchange membrane |
| $i$ | current density (A/cm$^2$) |
| $i_o$ | exchange current Density (mA/cm$^2$) |
| IPCC | Integovernmental Panel on Climate Change |
| LHV | lower heating value (MJ/kg) |
| LT-PEM | low temperature proton exchange membrane |
| $\lambda_a$ | anode stoichiometric ratio |
| $\lambda_c$ | cathode stoichiometric ratio |
| MEA | membrane electrode assembly |
| MCFC | molten carbonate fuel cell |
| OCV | open circuit voltage |
| $O_2$/C | oxygen-to-carbon ratio |
| $\theta_{CO}$ | fractional catalyst CO surface coverage (between 0 and 1) |
| $P$ | pressure (kPa, MPa, bar) |

| | |
|---|---|
| $P_i$ | partial pressure of gas species *i*, (MPa or bar) |
| $P^0$ | standard pressure of 0.1 MPa or 1 bar |
| PA | phosphoric acid |
| PAFC | phosphoric acid fuel cell |
| PBI | polybenzimidazole |
| PCI | Precision Combustion Incorporated |
| PEM | proton exchange membrane |
| $R$ | universal gas constant (J/(K-mol)) |
| S/C | steam-to-carbon ratio |
| SCT | short contact time |
| SMR | steam methane reforming |
| SOFC | solid oxide fuel cell |
| SR | steam reforming |
| $T$ | temperature (K) |
| UAV | unmanned aerial vehicle |
| WGS | water gas shift |

# 1 Introduction

The $CO_2$ concentration in the atmosphere is nearing its tipping point of 450 ppm, the critical level established by the Intergovernmental Panel on Climate Change (IPCC) [1]. At this tipping point, there is a 50% chance of stabilizing the average global temperature rise below $2^oC$. Above a $2^oC$ temperature rise, models predict that severe and potentially irreversible climate change may occur, leading to direct impacts such as sea level rise and a higher frequency of extreme weather events [2]. Data describing the $CO_2$ concentration over the past 420,000 years reveals that the maximum atmospheric $CO_2$ concentration has never peaked above 300 ppm until the past several decades, indicating anthropogenic causes [3]. Without ambitious policies put in place, baseline worldwide climate scenarios project atmospheric $CO_2$ concentrations could reach 685 ppm by 2050 [4]. In order to reach the goal of keeping the global $CO_2$ concentration below 450 ppm, energy generation technology used in all sectors of the economy must to be converted to sustainable architectures that balance economic, environmental and social considerations.

Sustainability can be defined as developments that meet the current needs of society without compromising the ability of future generations to meet their needs. Creating a truly sustainable solution is a complex challenge, as a much wider array of stakeholders must be engaged than has been the case in conventional technology development. When considering energy generating technologies, the current fossil fuel-based system is clearly unsustainable. Under the present paradigm that predominantly relies on fossil fuels, the energy needs of those today are being met but at the cost of sacrificing the quality of life of future generations. Not only will fossil fuel resources eventually be depleted, but also the long-term environmental impact of combusting the remaining resources will be catastrophic. While the physical effects of pollution are already

beginning to be felt, it is the current generation's children and grand-children that will either suffer or reap the benefits of today's choices in energy technologies. It is therefore imperative that we develop and implement energy generating technologies in all sectors of the economy that are capable of meeting the current energy demands, while also drastically reducing harmful emissions. It is hoped that the work discussed in this dissertation will contribute to the development and implementation of renewable energy technologies.

The most obvious approach to developing a sustainable energy infrastructure is to increasingly implement technologies that generate electricity from renewable sources. Due to the practical limitations of renewable energy technologies, there is not a one-size-fits-all approach, and a long-term solution will likely consist of a mix of primary fuel sources including solar, wind, hydro, and geothermal energy. While each individual technology deployment may have a small but positive environmental impact, the contribution of the technologies implemented together can result in drastic reductions of energy use and emissions.

Primary renewable energy sources unfortunately come with some drawbacks, chief of which is that they do not always generate energy when it is needed, and the location of resources does not always match demand. Therefore, excess renewable generation capacity coupled with some sort of energy storage and transfer technology is required for renewables to work at a large scale. Fuel cells are a technology that can be used to fill the gaps in demand that renewables such as solar and wind cannot provide. Fuel cells are electrochemical devices that generate electricity through combining hydrogen with oxygen in air to make electricity, heat, and water. They are capable of having a long operating range, high power-to-weight ratio, and have, because of their higher efficiency operation, the potential to produce far fewer emissions than internal combustion engines (ICEs) that generate similar levels of power. Excess renewable energy can

be used to generate hydrogen gas that can then be stored and converted to electricity using a fuel cell when needed.

For fuel cells to play a large part in the global sustainable energy infrastructure, systems need to be built to meet the demands of a wide range of power outputs for applications found in all sectors of the economy. To date, the majority of fuel cell system research has been focused on developing solutions for applications such as passenger vehicles [5], large stationary power [6], and small hand-held devices [7]. These applications typically require power outputs that are either greater than 50 kW or less than 20 W, and there remains a gap in developing fuel cell systems that produce power levels within that range. Some example devices requiring this "medium" level of power include unmanned aerial vehicles (UAV), residential power generators, equipment pumps, camping and recreational devices, lawn and garden equipment, and auxiliary power units. Typical power requirements for these types of devices tend to lie between 0.5 and 5 kW. Many of the applications that use medium levels of power also require a power plant that is portable, has a quick start-up time, and can be easily refueled. In meeting these requirements, one of the biggest advantages fuel cells have over comparable ICEs and battery systems is the potential for a higher specific energy, or the energy per unit mass, which is very important for mobile applications.

Ironically, the fact that fuel cells are powered from hydrogen gas is simultaneously both their greatest strength and weakness. While hydrogen is the most abundant element in the universe, diatomic hydrogen, the primary fuel used in fuel cells, does not exist naturally and must therefore be generated from some other source. $H_2$ generation can result from a renewable pathway such as water electrolysis powered by solar or wind, but it is presently generated in vast quantities through the cracking of hydrocarbon fuels into primarily $CO_2$ and $H_2$ via a process

called steam reforming (SR). While SR obviously generates carbon emissions, it is presently the cheapest method of $H_2$ production, and thus should be seen as an incremental process towards developing a fully sustainable pathway where $H_2$ is generated from renewable primary sources. The work in this dissertation is yet another incremental step towards a fully sustainable fuel cell pathway, but focuses on the devising solutions to the engineering gaps required for a practical commercial system.

The focus of this dissertation therefore is to investigate the engineering gaps encountered when developing a viable fuel cell system that is capable of meeting the requirements of applications that use medium levels of power (250 W to 5 kW). These types of applications require a power plant that has a short start-up time, is portable (has a high power-to-weight ratio), and can be easily refueled. To fully comprehend a practical solution, this effort is centered on developing a prototype system that will be used to inform the development of a first generation commercially viable device. It is believed that the process of developing a practical fuel cell based system is the most effective way of determining the challenges and difficulties associated with actually implementing such a technology. Ultimately, it is hoped that this work will contribute as an incremental step towards a fully sustainable energy infrastructure.

# 2 Fuel Cell Fundamentals

Before the design and construction of a fuel cell system can occur, a thorough understanding of the different fuel cell types and their advantages/disadvantages is required. In this chapter, the different fuel cell options will be evaluated and the primary reasons why a high temperature PEM fuel was selected for this program will be discussed. Additionally, the fundamental thermochemistry that governs fuel cell operations will be described.

A basic level of understanding on the chemistry and design for most types of fuel cells is fairly straightforward. A single fuel cell, as shown in Figure 1, consists of two chambers separated by a medium that only allows positive ions to transport across it, referred to as an electrolyte. In this arrangement, hydrogen ($H_2$) gas enters the left chamber called the anode, while oxygen ($O_2$) gas enters the right chamber called the cathode. With the aid of a catalyst dispersed on electrodes applied to either side of the electrolyte, the $H_2$-$O_2$ redox reaction drives the $H_2$ and $O_2$ molecules to split into their atomic constituents. The electrolyte only allows the positive $H^+$ ions to transport through, forcing the electrons around an external circuit generating electrical work. Two hydrogen ($H^+$) ions then recombine in the cathode chamber with $O^{2-}$ ions to form $H_2O$.

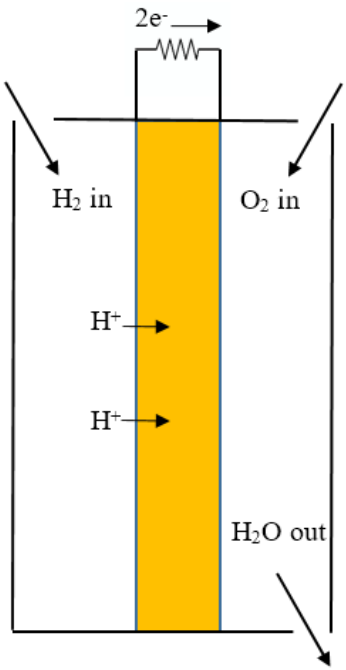


Figure 1: Schematic of the operations of a single fuel cell when operating on $H_2$ and $O_2$.

A single fuel cell is a high current/low voltage device where the maximum theoretical voltage of the $H_2$-$O_2$ redox reaction at room temperature is approximately 1.2 V. The current

generated by a fuel cell directly correlates to the area of the MEA where current outputs are conventionally discussed in units of $A/cm^2$. To obtain the total current of a single cell, or stack connected in series, one simply multiples the area of a single cell by the operating current density. To obtain high voltages for large power applications, many cells are connected in series to form a fuel cell stack. The amount of cells stacked together is dependent upon the final power output required. For a vehicle application, the newly released Toyota Mirai comes with a 370 cell stack that produces approximately 114 kW at maximum power [8]. For larger power applications that might require > 1 MW of power, such as large commercial buildings, multiple stacks can be put together in series and/or parallel for even higher power outputs.

There are several fuel cell types that are typically differentiated by their electrolyte and/or temperature of operation. The most widely studied type, and the focus of this dissertation, is the proton exchange membrane (PEM) fuel cell. Conventional (i.e., low temperature) PEM fuel cells operate at around $80^oC$, whereas the type studied in this research operates between 160 and $200^oC$ and is therefore referred to as a high temperature PEM fuel cells (HT-PEMFC). The heart of the HT-PEMFC is called the membrane electrode assembly (MEA), which consists of a membrane sandwiched between anode and cathode electrodes. It is desirable for the membrane to be made of a material with a high proton conductivity while simultaneously capable of withstanding the harsh environment within the fuel cell. For a HT-PEMFC, phosphoric acid doped polybenzimidazole (PBI) is the membrane of choice [9].

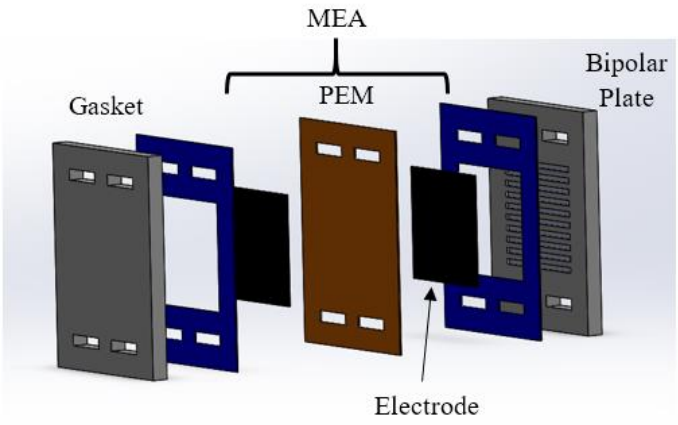


Figure 2: Exploded view of a single fuel cell

The electrodes on either side of the proton-conducting membrane are typically made of carbon-based material such as carbon cloth or paper, imbibed with fine particles of some kind of catalyst. Catalysts work by providing an alternate reaction pathway to the reaction product that has a substantially lower activation energy requirement than if there was no catalyst. In a fuel cell that runs on pure $H_2$ (anode) and $O_2$ (cathode), the catalyst increases the $H_2$-$O_2$ redox reaction rate significantly. Platinum (Pt)-based catalysts are traditionally the most effective catalysts in the hydrogen-oxidation reaction however, other catalysts including palladium, copper and nickel-based ones are also used in fuel cell applications.

## 2.1 Types of Fuel Cells

Creating a viable fuel cell system that is safe, easy to refuel, low weight, durable, and cost effective remains an elusive target for those in the industry. These design challenges come down to two fundamental technical problems: slow reaction kinetics that lead to low power densities, and hydrogen that is not a readily available as a fuel. Slow reactions kinetics are typically dealt with by increasing the operating temperature of the fuel cell, increasing the operating pressure, or through use of sophisticated catalysts. The challenge with the increased temperature strategy is

finding inexpensive materials that can effectively operate in high temperature environments. Increasing the operating pressure of the fuel cell also poses problems, as the performance gain may not outweigh the energy required to pressurize the fuel and/or air. The challenge associated with using sophisticated catalysts is also finding low cost materials that work effectively.

When addressing the issue of low availability of hydrogen, there are generally two approaches. The first is to simply assume that pure hydrogen will eventually become available, whereas the second is to develop some kind of system that will allow fuel cells to run on a hydrogen-rich fuel stream. This is primarily done through use of a fuel reforming devices that converts a hydrocarbon fuel (e.g., propane, methane, gasoline, etc.) into a hydrogen-rich gas stream supplied to the anode side of the fuel cell. Attempts to manage these fundamental challenges has led to the development of several types of fuel cells that operate on the same basic principles, but have unique advantages and disadvantages. The state of fuel cell technology now includes seven classes of fuel cell types that are most often differentiated by their electrolyte, as shown below.

Table 1: Fuel cell classifications

| **Fuel Cell Type** | **Electrolyte** | **Temperature of Operation** |
|---|---|---|
| Proton exchange membrane (PEMFC) | Polymeric Membrane | 80$^{o}$C |
| High temperature PEM (HT-PEMFC) | Polymeric Membrane | 160-200$^{o}$C |
| Solid Oxide Fuel Cell (SOFC) | YSZ | 800-1100$^{o}$C |
| Alkaline Fuel Cell (AFC) | KOH | ~100$^{o}$C |
| Phosphoric Acid Fuel Cell (PAFC) | $H_3PO_4$ | ~200$^{o}$C |
| Molten Carbonate Fuel Cell (MCFC) | $Li_2CO_3K_2CO_3$ | 600-700$^{o}$C |
| Direct Methanol Fuel Cell (DMFC) | Polymeric Membrane | ~200$^{o}$C |

Development of the different fuel cell types can be traced back to the early 1800s when scientists like Anthony Carlisle, William Nicholson, and Humphrey Davey worked on what is now known as electrolysis using galvanic cells, particularly the Volta battery that was recently developed around that same time period [10], [11]. Building on these principles, William Grove created what is thought of as the first fuel cell by demonstrating that $H_2$ and $O_2$ could be recombined to form water while simultaneously producing a small current [12]. In the 1930s, Sir Francis Bacon worked on constructing the alkaline fuel cell (AFC) that was to be later used in the 1970s for the Apollo space program as a means to generate electricity and water.

Prior to the AFC being used on spacecraft, scientists at General Electric (GE) developed the first PEM fuel cell that was adopted by the National Aeronautics and Space Administration (NASA) for the Gemini program [10]. Today, PEM fuel cells are arguably the most popularized type of fuel cell, largely due to their use in automobiles. As described earlier, PEM fuel cells use a solid polymer as an electrolyte, with the state-of-the-art MEA composed of a Nafion membrane with carbon paper electrodes and a platinum catalyst [13]. PEM fuel cells operate at a relatively low temperature of (nominally) $80^oC$ and address the problem of slow reaction kinetics by utilizing sophisticated catalysts. Perfluorosulfonic acid (tradename Nafion) membranes are capable of high efficiencies at relatively low temperatures, but require very pure $H_2$ gas for operation, typically with carbon monoxide (CO) concentrations of less than 10 ppm. In this family of fuel cells exists the high temperature PEM (HT-PEM) fuel cells that began receiving greater attention in the late 1990s. These fuel cells operate very similarly to traditional Nafion based fuel cells, but at temperatures between 160-$200^oC$. This high temperature operation provides them much greater tolerance to typical fuel contaminates such as CO and $CO_2$, to the extent that it is possible to operate on hydrocarbon fuels by integrating a fairly simple fuel

reforming processes. The majority of this dissertation is focused on HT-PEM research, and is the main subject of the following chapters.

One way some researchers have tried to solve the hydrogen supply issue was to develop direct methanol fuel cells (DMFC) that are constructed and operate in the same manner as PEMFCs, but are fueled by liquid methanol. Although methanol is not a widely distributed fuel, it is nevertheless easier to store and transport than hydrogen gas because it can be stored in a liquid form. While this type of fuel cell unfortunately tends to have very low power outputs [14], it nevertheless seems to be useful for portable electronics [15].

Alkaline fuel cells (AFC) were the first widely used fuel cell in practical applications, namely the Apollo space program where they were used as a means to generate electricity and water on-board space craft [10]. AFCs use a potassium hydroxide (KOH) electrolyte, and are most often operated around or below 100$^{o}$C. When on-board the Orbiter spacecraft as part of the Apollo missions, though, they were run at temperatures up to 150$^{o}$C and at pressures of 200 psi [16]. Under these conditions, the AFCs used produced approximately 9 A/cm$^2$ at just above 0.7 V or 6.3 W/cm$^2$. To put that in perspective, state-of-the-art PEM fuel cells used today for automotive purposes may run around 0.75 W/cm$^2$ [17]. That's only twelve percent of the power output of the fuel cells on the Orbiter space-craft! To be fair, the Apollo space mission fuel cells were effectively not constrained financially, used both pure hydrogen and oxygen as fuel, and were operated under extremely high pressures that greatly enhanced their performance. While capable of high power densities and efficiencies, AFCs are relatively intolerant to impurities and thus require very pure hydrogen and oxygen along with complicated balance of plant equipment [18]. As a result, they are not economically viable for most practical applications.

Phosphoric acid fuel cells (PAFC) were the first type of fuel cell to achieve some degree of commercial success, with a number of large stationary systems installed in the USA, Europe, and Asia [18]. In fact, a 400 kWe system built by UTC Fuel Cells is presently being used as a combined heat and power unit to provide both electric power and heat primarily for the Golisano Institute for Sustainability (GIS) building on the RIT campus. Excess electricity and heat not used by the GIS building is sent to other surrounding buildings on campus. These types of fuel cells employ an inorganic phosphoric acid electrolyte that conducts protons like a PEM fuel cell, and operates around 220$^{o}$C. The PAFC is typically constructed to use natural gas as a fuel, and requires a large upfront fuel reforming system. Because of its higher temperature operation, it is much more tolerant of impurities in the inlet fuel gas streams than other lower operating temperature fuel cells. PAFCs are often run at or near atmospheric pressure so their power densities are much lower than other types of fuel cells, on the order of 0.35 W/cm$^2$ [19]. PAFCs typically achieve around 35-40% electrical conversion efficiencies and are viewed as one of the most reliable fuel cell types that are capable of operating at constant power for years with minimal maintenance.

Molten carbonate fuel cells (MCFC) are another type of fuel cell that have seen widespread adoption in the stationary sector. MCFCs use a mixture of alkali metal carbonates as its electrolyte and are operated at high temperatures of around 600-700$^{o}$C. Unlike many of the other kinds of fuel cells, MCFCs require $CO_2$ mixed with $O_2$ on the cathode side. The $CO_2$ and $O_2$ mix on the cathode to form $CO_3$ ions that transport through to the anode side of the cell. Hydrogen fuel that is fed into the anode, combines with the $CO_3$ ions to form $H_2O$ and $CO_2$ in the reactions described below. The specific cathode and anode reactions are

$$(Cathode) \quad O_2 + 2CO_2 + 4e^- \rightarrow 2{CO_3}^{2-}$$

$$(Anode) \quad 2H_2 + 2{CO_3}^{2-} \rightarrow 2H_2O + 2CO_2 + 4e^-$$

whereas the overall cell reaction is

$$H_2 + \frac{1}{2}O_2 + CO_2 \rightarrow H_2O + CO_2$$

Because of the high temperature operation of MCFCs, activation energies for the anode and cathode reactions are much lower such that they do not require noble metals for catalysis. Instead, cheaper catalysts like nickel are most often used [18]. Current MCFCs are capable of producing electric power at efficiencies around 50%.

A solid oxide fuel cell (SOFC) is the final type of common fuel cell technologies. Similar in operation to the MCFC, the SOFC uses an oxide ion-conducting material as its electrolyte, and operates typically between 800-1100$^{o}$C [20]. SOFCs primarily use yttria ($Y_2O_3$) stabilized zirconia ($ZrO_2$) as its electrolyte. However, new materials that enable lower temperature operation have recently been developed [21]. Because of the higher temperature operation, SOFC catalysts are often made of lower cost materials such as nickel, and are capable of internal fuel reforming. Thus, inlet fuel feeds are often a mixture of a hydrocarbon fuel and steam, eliminating the need for an external fuel reforming system. SOFCs are seen by many in the industry as the long-term fuel cell of choice, due very high electrical conversion efficiencies of about 60%, already achieved in commercially available systems [22].

## 2.2 Fuel Cell Selection

For the present research program, the chosen fuel cell technology had to meet the demands of mobile applications that use power levels between 0.5–5 kW, and required a design that particularly emphasized portable features. One of the primary criteria used for evaluating the

different fuel cell options was its commercial availability, as fuel cell system development as the focus of this work, not fundamental electrolyte science per se. Thus, it was preferable that both the MEAs and full stacks of the fuel cell type are commercially available, so the system design and characterization could be completed in a timely fashion. An additional criterion was the relative complexity of different fueling and refueling options that greatly impact both the design of the fuel cell system and its daily operation. The required startup time is also a crucial issue where systems that require substantially long startup times render them unusable for most mobile applications. Additionally, understanding the limits of contaminate tolerance of the different fuel cell options is a primary concern that effects both the design and durability of the overall system. Also, the operational performance of the fuel cell in terms of power density and overall efficiency directly impact the overall weight of the system and its run time. It is particularly important for mobile applications to have a high power to weight ratio while simultaneously being capable of operating at high efficiencies. Finally, durability of the fuel cell must be achievable in the mobile environment.

In order to further clarify the power density, energy density, and specific power requirements for low power mobile applications, a survey of existing equipment that uses current ICE or battery technology was completed. In addition to a literature review, informal surveys were conducted with experts in the field requesting information on how much power and run time is required given certain weight and volumetric restrictions for various applications. Many of these surveys were specifically centered on the power plant design requirements for unmanned aerial vehicles (UAVs), which is the focus of a case study discussed in Chapter 7. When reading literature discussing power and energy densities, careful attention must be paid to what components are included within the defined system boundaries. Particularly for fuel cell systems,

much of the published literature focuses on fuel cell stack power densities which is useful when comparing different stack designs of the same type of fuel cell, but not all that useful when comparing different technologies. When comparing different propulsion technologies that may be used for the same application, the power density of the entire power plant (i.e., the fuel cell stack and BoP equipment) is ultimately what matters.

When defining the capabilities of power plants for mobile applications, system integrators need to know how much power it can produce, its weight, its volume, and how long it will run given a certain amount of fuel. These practical requirements can be translated to technical metrics including its specific power (W/kg), power density (W/liter), the specific energy (Wh/kg) or the density (Wh/liter). If provided the power output in addition to these four metrics, one can calculate its weight, volume, and run-time. The target power and energy metrics for some example applications that fuel cells may be used to power are compared against typical battery and ICE technologies used in those applications Table 3.

The applications discussed are portable electronics powered with fuel cells, lawn mowers, and military fixed-wing UAVs. Data for the requirements of portable electronics were determined in [23] and data for lawn mowers were determined from [24]. The data used to calculate the UAV metrics was largely obtained through interviews with engineers and program managers within the U.S. military that have first-hand experience designing and operating UAVs. Due to confidentiality concerns, those sources cannot be listed.

Table 2: Target power and energy metrics of power plant systems used in selected applications compared to existing battery and ICE engine capabilities. Weight and volume calculations include the engine and BoP equipment only, and do not include the weight or volume associated with the fuel storage device, on-board fuel, or device frame. Battery information was determined from [25] and [26], while UAV ICE engine information was largely determined from [27] and interviews.

| Application | Specific Power (W/kg) | Power Density (W/liter) | Specific Energy (Wh/kg) | Energy Density (Wh/liter) | Example Power Output (W) |
|---|---|---|---|---|---|
| Portable Electronics | 50 | 100 | 500 | 1000 | 25 |
| Push Lawn Mower | 213 | 44 | 142 | 29 | 3200 |
| Minimum Military Mid-Sized UAV Fixed Wing | 105 | 30 | 1050 | 297 | 875 |
| Li-ion Batteries | 1000 | 2500 | 200 | 500 | 500 |
| Current Mid-Sized UAV ICE Engine [27] | 746 | 211 | 2237 | 632 | 3000 |

It is important to note that the values in Table 2 are only guidelines where specific metrics may differ depending on the environmental conditions, load profile, and the final system design. While these values are for the propulsion plant and BoP equipment only, including other aspects of a device into the system boundaries, such as the fuel and fuel storage tank weight, may result in substantially different values. Nevertheless, they provide good targets to work towards when developing new systems and comparing them to conventional technologies.

There are several interesting results from the metrics shown in Table 2. If used to power portable electronics, Li-ion batteries generate more than enough power, but fall short in energy content. However, for applications like lawn mowers, Li-ion batteries easily exceed all of the power and energy metrics for current technology. Other external factors such as cost, durability, and operational familiarity, are some potential reasons why Li-ion batteries are not widely used

to power lawn mowers. If used to power UAVs, Li-ion batteries meet almost all of power and energy metrics except for specific energy. Presently, some commercial UAVs are powered using batteries alone, but those devices are typically only capable of approximately one-hour flight times (although some military UAV operators stated they were able to stretch this to two hours) as compared to a desired flight time of at least eight hours. The relatively low specific energy of Li-ion batteries is their primary shortcoming and meeting this metric is one of the potential advantages of fuel cells.

Interestingly, ICE engines meet all of the power and energy metrics for portable electronics except for energy density. Additionally, ICE engines meet all of the power and energy metrics for push lawn mowers and mid-sized fixed-wing UAVs, and are presently the choice technology for those applications. Overall though, the power and energy metrics do not account for other desirable power plant requirements such as low noise, durability, maintenance requirements, and ease of use. ICE engines often fail in these area as they are very loud, require continual maintenance, and they are prone to break down which is catastrophic during flight. Interviews conducted revealed that ICE engines require regular maintenance every 50 hours, and need a complete replacement around 500 hours. In the field, this maintenance schedule requires significant time, expertise, and cost, making them unattractive. The failings of ICE engines in these areas is where fuel cell power plants can offer clear advantages.

Selecting a suitable fuel cell technology that is capable of meeting all of the power and energy requirements, has a short startup time, is commercially available, and can be easily refueled, is quite challenging as conventional fuel cell technologies that meet or exceed one requirement often falls short on others.

Table 3 lists the different fuel cell options and how they compare with respect to the aforementioned criteria. Several of the fuel cell options simply will not work (alkaline fuel cell, AFC; phosphoric acid fuel cell, PAFC; and molten carbonate fuel cell, MCFC) because commercial fuel cell stacks that produce power in the range 0.5-5 kW could not be identified. Other types of fuel cells, including the proton exchange membrane fuel cell (PEMFC), solid oxide fuel cell (SOFC), and direct methanol fuel cell (DMFC) are presently commercially available.

The DMFC attempts to overcome the hydrogen refueling challenge by operating on a methanol-water mixture that is internally reformed into $H_2$ to feed the fuel cell. Unfortunately, these methanol-water mixtures are not widely available, and thus obtaining fuel would be quite difficult for widespread adoption. Additionally, the power densities of most DMFC systems are reportedly very low [15], [28], and are only suitable for low power applications such as small hand-held electronic devices.

The SOFC is another type of fuel cell that is commercially available, has highly efficient performance, and is capable of operating directly on hydrocarbon fuels, thereby eliminating the hydrogen supply challenges. However, SOFCs often require system startup times on the order of several hours due to their high temperature operation, which is not practical for most mobile applications. Additionally, the electrolyte inside SOFCs is made of a very thin ceramic material that can easily fracture in the high stress environments encountered with many mobile applications.

Conventional PEM fuel cells seem to be a logical choice for this design as they have short startup times, and are capable of efficient performance. However, they are presently not a viable solution due to significant fuel supply challenges, including expensive on-board hydrogen

storage tanks, a lack of widespread hydrogen refueling infrastructure, and consumer unfamiliarity when using hydrogen as a primary fuel. One way to circumvent refueling issues is to develop an on-board reforming system that generates hydrogen from a hydrocarbon fuel. Unfortunately, since low temperature (LT)-PEM fuel cells require very pure hydrogen, this upfront reforming system becomes impractically complex for portable applications.

A high temperature PEM fuel cell, while similar in operation and construction to a LT-PEM fuel cell, is based on a different type of membrane that performs most efficiently at temperatures between 160-200$^{o}$C rather than 80$^{o}$C. Operating a PEM fuel cell at temperatures above 100$^{o}$C offers several technological advantages such as enhanced chemical kinetic rates, a simplified water management system, the ability to recover waste heat, and greater fuel tolerance [29]. This allows the fuel cell to operate on a lower quality reformed hydrogen while also retaining the capability of much shorter start up times than higher operating temperature fuel cells like the SOFC. Because fuel cell systems based on HT-PEM technology are capable of operating on impure hydrogen, this opens up the opportunity to design a practical power generation system that can run on many different fuel sources such as biodiesel, gasoline, propane, or natural gas. A practical fuel cell system based on a HT-PEM fuel cell can be envisioned that has a short start-up time, is portable, and can be easily refueled.

Table 3: Fuel cell selection criterion. An (X) indicates the fuel cell type meets or exceeds requirements.

| | Fuel Cell Type | | | | | | |
|---|---|---|---|---|---|---|---|
| **Criterion** | **HT-PEMFC** | **LT-PEMFC** | **SOFC** | **DMFC** | **AFC** | **PAFC** | **MCFC** |
| Commercially Available | X | X | X | X | | | |
| Ease of fueling | X | | X | | | X | X |
| Startup time | X | X | | X | X | | |
| Contaminant Tolerance | X | | X | X | | X | X |
| Performance | X | X | X | | X | X | X |
| Durability | X | X | | | X | X | X |

Of the seven different fuel cell options, the HT-PEM fuel cell is the only one that satisfies all desired criteria for a viable mobile fuel cell device. The system discussed in this dissertation is therefore centered on the characterization of the unique operating conditions and system level requirements of the HT-PEM fuel cell. Chapter 3 discusses in detail the fundamentals of HT-PEM fuel cells; but, before moving to that section, a thorough understanding of the basic chemistry and thermodynamics for fuel cells is necessary to understand the limits and benchmarks of a viable system design.

## 2.3 Fuel Cell Basic Chemistry and Thermodynamics

Power outputs of fuel cells can be easily calculated using the well-known formula, Power = Voltage x Current. The challenge is determining how to effectively incorporate all of the operational factors that impact the voltage and current outputs so that performance-limiting mechanisms can be suppressed. In fuel cell modeling, the voltage is primarily modeled as a

function of current density and is most often characterized using a polarization curve that graphs voltage on the y-axis and current density on the x-axis, as shown in Figure 3. Any physical or operational modifications are made with the end goal of moving the polarization curve up the y-axis. The optimal operating point does not necessarily occur under conditions that result in the highest power density or greatest efficiency, but rather a balance of power density, efficiency, durability, balance of plant design, and system size needs to be considered. In modeling the voltage of a fuel cell, the theoretical maximum voltage of the $H_2$-$O_2$ redox reaction is first determined, described as the Nernst voltage, and then the voltage losses resulting from physical design limitations, also known as irreversibilities, are subtracted. The rest of Section 2.3 discusses the mathematical models and their practical implications used to describe fuel cell operations.

### 2.3.1 Nernst Voltage

The Nernst Eq. is used to calculate the maximum voltage available for a fuel cell while indicating the effect of a large number of variables, including cell operating temperature and pressure [18]. The Nernst voltage can be understood when considering the general reaction:

$$jJ + kK \rightarrow mM \qquad \textit{(Eq. 1)}$$

Where *j* moles of *J* react with *k* moles of *K* to form *m* moles of *M*. Each reactant and product has an associated activity, $a_i = \frac{P_i}{P^0}$, where $P_i$ is the partial pressure of gas species $i$ and $P^0$ is the standard pressure 0.1 MPa or 1 bar. It can be shown then that the available energy of the chemical reaction, or Gibbs free energy is equal to:

$$\Delta \bar{G}_f = \Delta \bar{G}_f^0 - RTln\left(\frac{a_J^j a_K^k}{a_M^m}\right) \qquad \textit{(Eq. 2)}$$

where $R$ is the universal gas constant and $T$ is the temperature of the fuel cell. In the case of the hydrogen fuel cell reaction, this Equation becomes:

$$\Delta\bar{G}_f = \Delta\bar{G}_f^0 - RTln\left(\frac{a_{H_2}a_{O_2}^{0.5}}{a_{H_2O}}\right) \quad \textit{(Eq. 3)}$$

In order to obtain the reaction EMF, we divide by the number of electrons passed around the external circuit for each water molecule formed (-2), and Faradays constant, *F*, to obtain the Equation:

$$E = \frac{-\Delta\bar{G}_f^0}{2F} + \frac{RT}{2F}ln\left(\frac{a_{H_2}a_{O_2}^{0.5}}{a_{H_2O}}\right) \quad \textit{(Eq. 4)}$$

As a reminder, the Eq. for the activity of each gas species is, $a_i = \frac{P_i}{P^0}$. If all the pressures are given in **bar**, then $P^0$ is equal to 1 and *Eq. 4* can simplify to:

$$E(T,P) = E^0 + \frac{RT}{2F}ln\left(\frac{P_{H_2}P_{O_2}^{0.5}}{P_{H_2O}}\right) \quad \textit{(Eq. 5)}$$

Note the replacement of $E^0$ which is the EMF at standard pressure (1 bar), and is also a function of temperature. The final Nernst equation, shown in *Eq.5* can continue to be simplified when assuming certain operating conditions, but for our purposes here it is simplified enough. The reference Gibbs free energy values, $\Delta\bar{G}_f^0$, used throughout this work are provided below in Table 4.

Table 4: Gibbs free energy values for the fuel cell reaction $H_2 + \frac{1}{2}O_2 \rightarrow H_2O$ as a function of temperature [18]

| Temperature (K) | $\Delta\bar{G}_f^0$ (kJ/mol) |
|---|---|
| 298 | -237.2 |
| 353 | -228.2 |
| 373 | -225.2 |
| 473 | -220.4 |
| 673 | -210.3 |
| 873 | -199.6 |
| 1073 | -188.6 |

Notice that the Gibbs free energy values are negative, indicating that energy is released during the reaction. Take, for example, the values at 200$^o$C (473K); if all of the Gibbs free energy released were converted into electricity, then the voltage of a single cell should be approximately 1.14 volts regardless of how much current is being drawn. In practice, unfortunately, this is not always the case as irreversibilities resulting from material and physical designs reduce the operating voltage of the cell.

Calculating the Nernst voltage is the first step in modeling the electrochemical reactions within the fuel cell. What we can see from the Nernst Equation is that increases in operating pressure have a positive effect on the cell voltage; however, the effect from increasing the operating temperature is a little bit unclear. The second term of *Eq. 5* shows that an increase in performance should occur as the temperature increases. However, the first term that includes the Gibbs free energy decreases as a function of temperature. Except at very high and atypical pressures, an increased temperature has a net effect of lowering the Nernst voltage. Additionally, an increase in operating pressure has a much greater positive impact on the Nernst voltage than

any changes in operating temperature. However, the operating temperature does have a big impact in performance when considering the fuel cell irreversibilities. As we will see from the next few sections, an increase in cell temperature significantly increases the fuel cells' net power output.

### 2.3.2 Fuel Cell Irreversibilities

The Nernst voltage calculates the maximum voltage achievable assuming all of the Gibbs free energy is converted into electricity. In practice, there are several causes of fuel cell voltage losses that are described as overpotentials or irreversibilities. These irreversibilities can be visualized along three distinct regions of the polarization curve as seen in Figure 3.

The first primary source of voltage loss is due to activation losses [30]. Activation losses are caused by the "slowness" of reactions taking place on the electrodes. Some of the voltage generated is lost from driving the chemical reaction that causes the transfer of electrons onto or from the electrodes. These losses are primarily seen in the first part of the polarization curve.

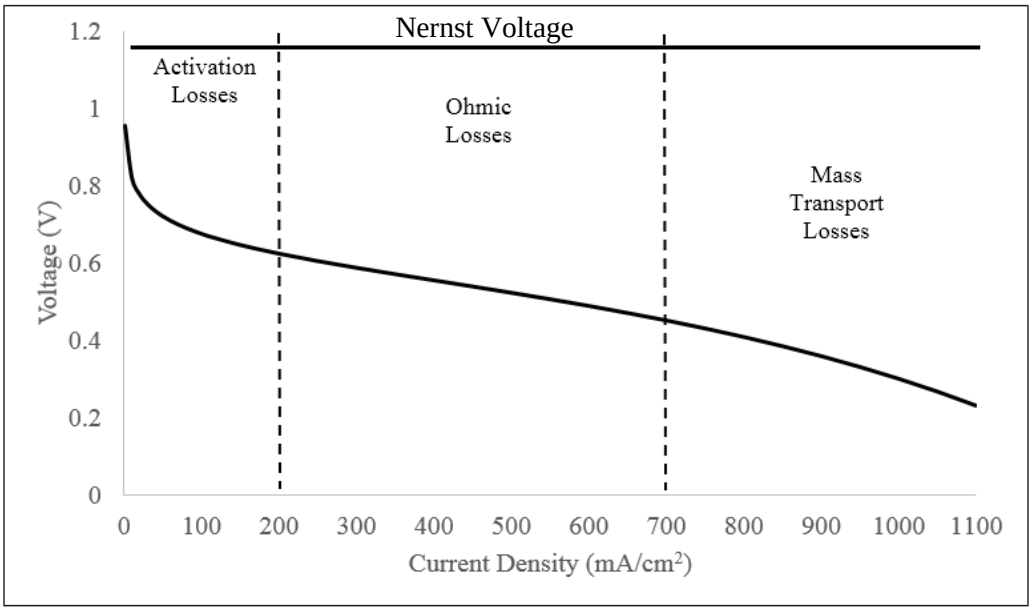


Figure 3: Regions of fuel cell irreversibilities

Activation losses can be modeled using the Tafel Eq. given as:

$$V_{act} = Aln\left(\frac{i}{i_o}\right) \qquad \textit{(Eq. 6)}$$

where $i$ is the current density and $i_o$ is referred to as the exchange current density. The exchange current density is the current that is being generated in both directions at the anode and cathode, even when a load is not being drawn. It is used to normalize the net current density at all voltage levels and can be determined from *Eq. 6.*

$A$ is a constant calculated using, $A = \frac{RT}{2\alpha F}$ where $\alpha$ is the charge transfer coefficient. The charge transfer coefficient is the proportion of the electrical energy applied that is used for changing the rate of an electrochemical reaction, and its value is between 0 and 1. At the anode, $\alpha_a$ is often assumed to be 0.5 and at the cathode it is typically $0.1 < \alpha_c < 0.5$. Using these values and assuming an operating temperature of 160$^o$C, $A_a$ can be calculated to be about 0.04 V while $A_c$ would lie in the range of 0.04 to 0.19 V.

In a fuel cell, the total activation losses are:

$$V_{act} = A_a ln\left(\frac{i}{i_{o_a}}\right) + A_c ln\left(\frac{i}{i_{o_c}}\right) \qquad \textit{(Eq. 7)}$$

This can still be expressed in the form of *Eq. 6* such that:

$$V_{act} = Aln\left(\frac{i}{b}\right) \qquad \textit{(Eq. 8)}$$

where:

$$A = A_a + A_c \text{ and } b = i_{o_a}^{\frac{A_a}{A}} + i_{o_c}^{\frac{A_c}{A}}$$

Again, using the values above for $A_a$ and $A_c$, one can calculate the constant $A$ to be between 0.08 V and 0.23 V for a fuel cell operating at 160$^o$C. Since the cathode exchange current density is

typically substantially smaller than the anode exchange current density, many researchers do not include the anode parts of the above Equations in their calculations, assuming they are negligible. Therefore, the activation losses are often modeled only using *Eq. 6* where the coefficients $\alpha$, $A$, and $i_o$ are often assumed equal to the cathode coefficients only.

As can be seen from *Eq. 6*, it is desirable to increase the exchange current density as much as possible in order to minimize the activation overpotential. This can be done by increasing the cell temperature, using more effective catalysts, increasing the roughness of the electrodes, increasing the reactant concentrations, or increasing the operating pressure of the fuel cell [18]. Each strategy comes with its own limitations, where most engineers take an all of the above approach in order to minimize the activation overpotential. It is important to note that temperature has a particularly strong effect on the exchange current density. For example, for low temperature PEM fuel cells, $i_o$ is around 0.1 mA/cm$^2$ and for high temperature fuel cells such as solid oxide fuel cells that operate around 800$^o$C, $i_o$ might be around 10 mA/cm$^2$. For HT-PEM fuel cells operating around 160$^o$C, one would expect the exchange current density to be within the range of 0.1 to 10 mA/cm$^2$ however, reported exchange current densities are sometimes much lower around 0.01 mA/cm$^2$ [29]. Catalyst design optimized for HT-PEM fuel cells could potentially increase the exchange current density to what one might expect based assuming it is overwhelmingly temperature dependent as is often the case for many researchers [31], [32].

The second main source of overpotential results from ohmic losses. This voltage loss is caused by the resistance of the fuel cell materials, including the electrolyte, electrodes, and various interfaces. The ohmic resistance losses are generally the simplest to understand and model, and can be written as:

$$V_{ohm} = ir \qquad \textit{(Eq. 9)}$$

where $r$ corresponds to the area specific resistance in $\Omega/cm^2$. As an example value, area specific ohmic $r$ values for a HT-PEMFC have been determined to be between 0.223 - 0.251 $\Omega/cm^2$ by the authors in [33]. Ohmic resistance may change over time depending on loss of membrane and electrode materials, as well as reorientation of molecules within the MEA due to normal operation involving temperature and pressure swings. Conventionally, fuel cells require a "break-in" procedure that will reduce these losses to some empirically determined minimal point, after which normal operation will most often result in greater ohmic losses.

The final primary irreversibility is described as the mass transport or concentration losses, which take effect towards the end of the polarization curve. The mass transport losses begin at the "knee" of the polarization curve, and result from the reduction of the primary reactant concentrations such that sufficient reactants cannot be adsorbed to the electrode surface quickly enough. If one can imagine that each Pt catalyst particle acts as a room with many doors for $H^+$ ions to move though, the limiting current density occurs when all of the doors are filled with ions and no more can get through. For low temperature fuel cells, these losses typically occur when large amounts of liquid water is being formed to the extent that it cannot be removed from the cell quickly enough for the $H_2$-$O_2$ redox reaction to take place. Modeling mass transport losses using an empirical relationship is one of the more common methods because it provides an excellent fit [34]. While there are many theoretical models, they tend to have extremely complex parameters that are not entirely useful when estimating the general effects of operational parameters, such as temperature, pressure, and inlet/outlet gas concentration levels. To understand those relationships, a simple model will suffice. The relationship that seems to best fit experimental data is:

$$V_{trans} = m\, exp(ni) \qquad \textit{(Eq. 10)}$$

where $m$ and $n$ are empirically determined coefficients. The mass transport losses are related to the rate at which the electrochemical reactions occur as well as the mechanical design of the system. Thus, reducing the mass transport losses can be addressed in the same manner as reducing the activation losses. The coefficients *m* and *n* are related to what is referred to as the limiting current density, that is, the current density where the voltage level begins to decrease rapidly.

Increasing the operating pressure of the fuel cell particularly has a large effect in reducing the mass transport overpotential. Intuitively, this makes sense because a high inlet pressure pushes the reactant products out of the cell more quickly, allowing for the incoming reactants to reach the active catalyst sites faster. Fuel crossover may also play a role in affecting the mass transport losses as more gases that cross from the cathode to the anode, or vice versa, will push the limiting current density further up the polarization curve. Fuel crossover typically results from high membrane permeability and physical deformities, such as pin holes, found in the MEA.

The overall voltage of a single fuel cell can be calculated by taking the Nernst voltage found in *Eq. 5* and subtracting the irreversibilities from Equations *Eq. 6 – Eq. 10,* as shown below in *Eq. 11*.

$$V_{cell} = E^0 + \frac{RT}{2F} ln\left(\frac{P_{H_2} P_{O_2}^{1/2}}{P_{H_2O}}\right) - \frac{RT}{2\alpha F} ln\left(\frac{i}{i_o}\right) - ir - m \exp(ni) \qquad \textit{(Eq. 11)}$$

This Equation fits experimental values very well, and can be used for modeling the expected performance when varying operational parameters such as pressure and temperature. In this

work, this is the primary model used to understand the impacts that different operating parameters have on HT-PEM fuel cell operation.

# 3 Fundamentals of the HT-PEM Fuel Cell

This chapter discusses in depth the existing literature of HT-PEM fuel cells, including their unique advantages and operational challenges. Specific attention is given to the pertinent research gaps found in literature.

## 3.1 Primary Advantages of the HT-PEM Fuel Cell and its Origins

As described earlier, one of the biggest challenges limiting widespread fuel cell adoption involves hydrogen fuel supply issues. Not only is it difficult to obtain hydrogen gas because it rarely exists in nature in its elemental state, hydrogen is also very difficult to store in useful amounts for a mobile system. For example, one liter of gasoline has approximately nine times the energy of one liter of hydrogen gas compressed to 10,000 psi, based on the lower heating value (LHV) [35]. Hydrogen fuel supply challenges can be dealt with by using hydrocarbons as a primary fuel source in fuel cells. The chief problem with operating fuel cells on hydrocarbons, though, is that most fuel reforming processes that generate hydrogen rich gas streams also generate significant amounts of carbon monoxide (CO) that is very difficult to remove and detrimental to many types of fuel cells. In particular, CO is very poisonous to LT-PEM fuel cells because it adsorbs strongly to the surface of Pt at low temperatures [36]. This CO adsorption occupies hydrogen oxidation reaction (HOR) sites, which reduces the activity of Pt in the anode, effectively disabling the fuel cell. Unless complex cleanup processes are used, as discussed in Chapter 4, hydrocarbon fuel reforming processes will generate reformate mixtures that contain too much CO. Unfortunately, these complex cleanup processes are generally only practical for

large stationary applications, as they are very heavy and difficult to operate under transient conditions.

The challenge of CO adsorption onto Pt can be addressed by increasing the operating temperature of the fuel cell, as CO adsorption onto Pt is not thermodynamically favored at high temperatures. However, increasing the operating temperature of a fuel cell requires appropriate materials, particularly a membrane electrolyte, that are capable of performing well at these higher temperatures. The most widely used electrolyte for LT-PEM fuel cells, Nafion, does not function effectively at temperatures above 100$^{o}$C due to the need for high levels of membrane humidification. Therefore, significant research has been conducted to develop PEM fuel cell materials capable of operating above 100$^{o}$C, which has ultimately led to the development of HT-PEM fuel cells.

Higher temperature operation provides additional advantages, including faster reaction kinetics and simpler heat and water management. As described in Chapter 2, an increase in operating temperature positively impacts the exchange current density that in turn decreases the activation and mass transport losses. Additionally, operating at temperatures between 160-200$^{o}$C ensures that product water exists in gaseous form rather than as a liquid in the LT-PEM fuel cell. This reduces the need for heavy and energy intensive balance of plant equipment such as humidifiers and high pressure air blowers required to push the exhaust liquid water out of the bipolar plate flow channels in a LT-PEM fuel cell stack. In a HT-PEM fuel cell, water management is greatly simplified since the transport of water in the membrane, electrodes, and diffusion layers is much easier, thus the bipolar plate designs are much simpler.

In a LT-PEM fuel cell, 40-50% of the energy generated is heat that needs to be removed to maintain an approximate operating temperature of 80$^{o}$C [9]. As the temperature gradient between

80°C and ambient temperature is not that large, specialized cooling equipment is necessary to adequately cool the fuel cell. Since the temperature gradient of a HT-PEM fuel cell is much larger, cooling is significantly more efficient. While not discussed in-depth in this dissertation, the high grade waste heat of a HT-PEM fuel cell may also be useful for cogeneration [37] and/or on-board fuel reforming [38].

The most common membrane material used for HT-PEM fuel cells is phosphoric acid doped polybenzimidazole (PBI), which is a high temperature resistant polymer that is well known for its use in industrial applications and as a garment material worn by firefighters. Patents for polybenzimidazole were awarded to Du Pont as early as 1955 [39]. At the time, it was invented as an improved polymer characterized by high stiffness, resistance to water and oxygen, and the ability to retain these properties at elevated temperatures. As the quest for higher temperature fuel cell materials continued, researchers began experimenting with processes that would increase the conductivity of the PBI material under anhydrous conditions by doping it with phosphoric acid (PA, $H_3PO_4$) [40]. Since then, PA/PBI materials for use in fuel cells have been extensively characterized.

Functional development of phosphoric acid doped PBI membranes were first described in 1995 by Wainwright et al. of Case Western Reserve University [40]. PBI exhibits many qualities that are useful for fuel cells, including excellent oxidative and thermal stability, and it is known as a good vapor barrier. However, the ionic conductivity of pure PBI is quite low, such that it is not suitable for use in fuel cells without further modification. The Case Western group determined that, when doped with phosphoric or sulfuric acid, the conductivity of the PBI material increases in direct proportion to the level of doping. In their work published in 1995, they measured the ionic conductivity and permeability of acid doped PBI revealing this material

as potentially a new type of PEM fuel cell. They additionally constructed a HT-PEM MEA using Pt/C electrodes with a Pt loading of 0.5 mg/cm$^2$, and measured a maximum power output of 0.25 W/cm$^2$ while operating at 150$^o$C and atmospheric pressure. Initial developments were focused on using this new type of MEA for direct methanol fuel cells (DMFCs). While the DMFC efforts are still being pursued, the advantages offered by the phosphoric acid doped PBI membrane also opened up the possibility for a fuel cell system to be designed that could be easily fueled with hydrocarbons such as propane or natural gas. To date, there are currently two types of membranes used for HT-PEMFCs that are commercially available: phosphoric acid-doped PBI [41] and TPS® based membranes [42].

## 3.2 State-of-the-art PA/PBI HT-PEM Performance

The focus of this section is to provide a general idea regarding the power outputs that HT-PEM fuel cells are capable of when operating under conditions similar to LT-PEM fuel cells, as well as conditions where HT-PEM fuel cells are uniquely capable. The performance of PA/PBI membranes for use in HT-PEM fuel cells has been extensively studied using pure $H_2/O_2$ or $H_2$/air as anode/cathode gas feeds, as well as a substantial number of investigations operating HT-PEM fuel cells on simulated reformate. The overwhelming majority of studies that have investigated HT-PEM fuel cell performance while operating on actual reformate only considered reformate compositions produced by methanol steam reforming (SR) [28], [42].

As compared to LT-PEM fuel cells used in automotive applications, HT-PEM fuel cells generally have lower performance when operating under similar conditions. The standard operating conditions in a state-of-the-art LT-PEM fuel cell system includes a cell temperature of 80$^o$C, cell pressure of 150 kPa, anode/cathode $H_2$/air stoichiometric ratios ($\lambda_a/\lambda_c$) of 1.5/2.0, and 100% humidification of inlet gas feeds. Under these operating conditions, a power density of

approximately 700 mW/cm$^2$ will be generated at a current density of 1.0 A/cm$^2$ [17]. Under similar, typical operating conditions for a HT-PEM fuel cell, including operating temperature of 160$^o$C, cell pressure of 150 kPa, no humidification, and stoichiometric ratios $\lambda_a/\lambda_c$ of 1.5/2.0, the power density at 1.0 A/cm$^2$ is about 540 mW/cm$^2$ (reported in Chapter 6 of this dissertation), which is a 23% lower than the LT-PEM performance. In spite of this lower power output, the inherent advantages of a HT-PEM fuel cell, including no need for a humidification system, the ability to operate at atmospheric pressure, and much greater tolerance to fuel impurities, make the HT-PEM fuel cell a compelling option, particularly for applications where operating on a hydrocarbon fuel would be extremely advantageous.

Polarization data from various published HT-PEM studies are shown in Figure 4 was used to describe the evolution of HT-PEM PA/PBI fuel cell performance. Early performance of PA/PBI fuel cells was quite low, where in 1995 researchers Wainright et al. achieved a maximum power density of 250 mW/cm$^2$ at 0.7A/cm$^2$ with a pure $H_2/O_2$ system while operating at 150$^o$C, 101 kPa, and with no humidification. Later, in 2003, while similarly using pure $H_2$ and $O_2$, researchers Li et al. achieved power densities of 300 mW/cm$^2$ at 0.7 A/cm$^2$ while operating at 150$^o$C and at atmospheric pressure [41]. Although developed and trademarked earlier, by the year 2006, the Celtec MEA design series solidified itself as the standard HT-PEM based on a PA/PBI membrane [29], [43], [44]. Today, production rights of the Celtec series MEAs are owned by BASF. Directly from BASF, the performance of the Celtec P1000 and P1100W are compared in [45] while operating on $H_2$/air and using simulated reformate. At 160$^o$C, 101 kPa, and using $H_2$/air with $\lambda_a/\lambda_c$ of 1.2/2.0, the state-of-the-art P1100W series has a power density of 400 mW/cm$^2$ at 0.7 A/cm$^2$. This equates to a 60% increase in power over the initial MEA

performance developed by Wainright et al., even while operating with air at the cathode rather than pure $O_2$, and presumably at lower stoichiometries.

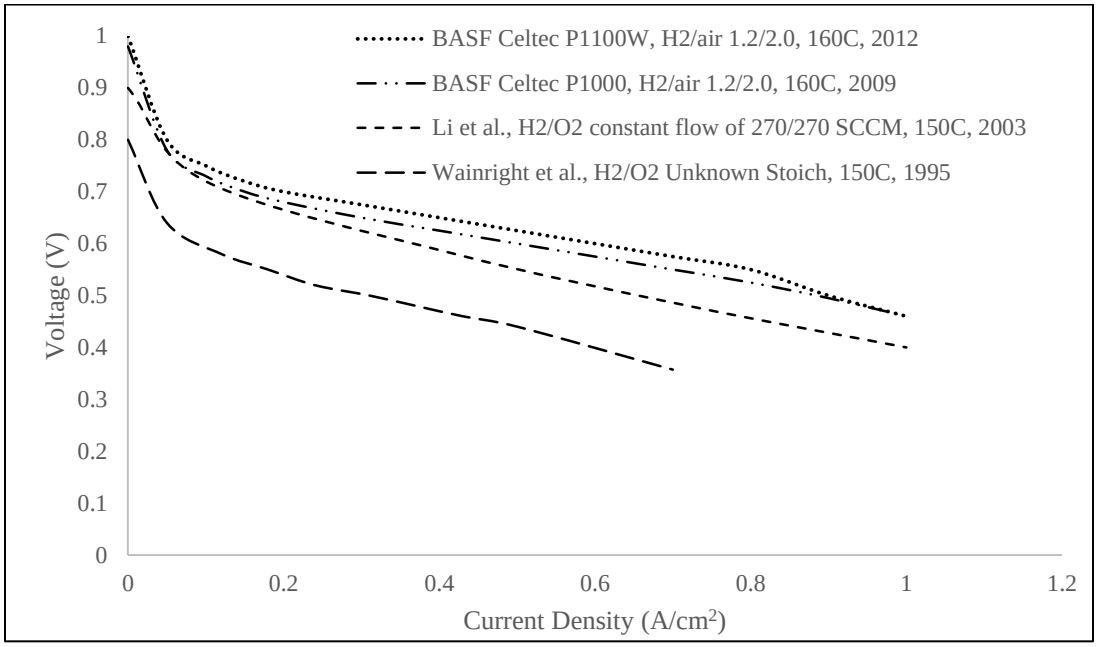


Figure 4: Evolution of PA/PBI Performance of selected publications. Each curve is labeled with the research organization or author, the anode and cathode fuel feeds and flow rates, the operating temperature, and the publication year for the data source. The sources for each polarization curve from the top down are as follows: [40], [41], [45], and [46].

It is important to note that presently, BASF no longer manufactures and sells their Celtec series MEAs, but rather licenses the formulation and manufacturing process to other corporations. Advent Technologies [47] is one such company where Celtec P1100W MEAs are manufactured, and is the current source for all of the MEAs used for the single cell experiments conducted in this dissertation. Danish Power Systems [48] is another manufacturer of commercial PA/PBI MEAs; however, the performance of these cells reported on their website is not quite as high as their Celtec counterparts when operating under the same conditions.

Performance of HT-PEM fuel cells while operating on simulated and actual reformates have also been investigated. Li et al. studies the effect of anode feed mixtures containing gas feed combinations of $H_2/CO/CO_2$, $H_2/N_2$, and $H_2/CO$ [41]. Although this study was completed in the early days of the PA/PBI MEA development, several important findings resulted that led to very important system design implications. One test showed the results of a PA/PBI MEA operated at 200$^oC$ with a gas mixture of 84% $H_2$ and 16% CO. The high concentration of CO investigated for this test is significant because the overwhelming majority of studies only consider CO concentrations up to 5%. While the performance of the PA/PBI MEA under these operating conditions was the lowest reported in this publication, power densities around 300 mW/cm$^2$ were produced at 0.7 A/cm$^2$, indicating that the PA/PBI HT-PEM fuel cells can produce useful power levels even under high CO concentrations. The authors additionally investigated the effect of high concentrations of $N_2$ and $CO_2$ in the anode gas feed. While operating at 175$^oC$ with inlet gas concentrations of 75% $H_2$ with 25% $N_2$, or 75% $H_2$ with 25% $CO_2$, the power loss at 1.0 A/cm$^2$ equated to approximately 4%. This shows two important results: first that diluent gases (i.e., $N_2$ and $CO_2$) that are commonly produced in reforming processes do not substantially reduce the power output of a PA/PBI based fuel cell, even at relatively high concentrations, and second that the effect of $CO_2$ is essentially equivalent to the effect of $N_2$ while operating at high temperatures.

Many years ago, programs that were developing LT-PEM fuel cell systems that could run on a hydrocarbon fuel were abandoned because they required fuel processors that involved three or more stages to generate pure enough $H_2$, which is simply too impractical to operate on a mobile platform. The relatively high performance of the HT-PEM while operating with high concentrations of contaminates including CO, $N_2$, and $CO_2$ indicate that a fuel cell system built

using PA/PBI MEAs can be fueled with a single stage hydrocarbon fuel processor. As operating a single stage fuel processor is much simpler to control than three stages simultaneously, a practical fuel cell system that can be coupled with a simple on-board reformer can now be envisioned.

Several other researchers have helped to characterize the performance of HT-PEM fuel cells while operating on simulated or actual reformate. Mamlouk and Scott tested the effect of a 90% $H_2$, 10% CO gas mixture on a PBI based membrane electrode assembly (MEA) at 175$^oC$. They reported an over-potential of 62 mV at a current density of 600 A/cm$^2$, as compared to an over-potential of 24 mV when operating on pure hydrogen at the same current density [49]. They also tested the effect of CO concentrations up to 30%; however, current densities above 600 A/cm$^2$ were not achievable. Pan et al. integrated a two-cell HT-PEMFC stack with a methanol reformer using a SR process [38]. They successfully demonstrated the possibility of integrating a methanol steam reformer with a HT-PEMFC stack. Although they did not measure the reformer effluent concentration, they assumed the reformate CO concentration was $\leq$ 1% and the rest of the reformate was comprised of $H_2O$ and $CO_2$. The authors also measured the performance of the stack while operating on 75% $H_2$ and 25% $CO_2$ for comparison. In this scenario, $CO_2$ had little impact.

Wang et al. experimented with anode compositions containing various amounts of $H_2$, CO, $CO_2$, and $N_2$, but their focus was on developing a model that predicts CO tolerance, and little performance data was provided [50]. Andreasen et al. characterized the Celtec MEA using electrochemical impedance spectroscopy with anode gas feed concentrations up to 1% CO and 25% $CO_2$ [51]. Their results showed $CO_2$ had a strong negative impact on the cell's resistance at operating temperatures below 140$^oC$. At higher temperatures, it has minimal impact on reducing

the cell's resistance. BASF has published performance data of their Celtec MEAs while operating on an inlet anode feed containing 71% $H_2$, 2% CO, and 27% $CO_2$, a composition that might be generated from methanol SR [45]. At 180°C, 101 kPa, and with anode/cathode $\lambda_a/\lambda_c$ of 1.4/5.0, they achieved a power density of ~410 mW/cm$^2$ at 0.7 A/cm$^2$.

Other researchers have tested the performance of PA/PBI fuel cell stacks with good results. In [52], a 400 W liquid cooled HT-PEM stack constructed by Serenergy [53] (one of the few commercial suppliers of HT-PEM fuel cell stacks) was characterized while operating on $H_2$ and air. The stack was constructed of eight BASF Celtec-P 1100 W PA/PBI MEAs with an active area of 163.5 cm$^2$, and operated around 160°C, atmospheric pressure, and with anode/cathode $\lambda_a/\lambda_c$ of 1.26-1.48/2.42-3.03. The maximum power attained was approximately 350 mW/cm$^2$ at a current density of 0.6 A/cm$^2$.

In summary, the primary operating conditions that PA/PBI doped fuel cell systems have been operated under are 160°C, 101 kPa, $H_2$/air $\lambda_a/\lambda_c$ of 1.2-1.5/2.0, and 0% RH. Baseline polarization curves run at these operating conditions are presented in Figure 4. Selecting a current density of 0.7 A/cm$^2$ at these operating conditions, state-of-the-art HT-PEM fuel cells can be expected to generate around 400 mW/cm$^2$ and 570 mV, at an efficiency of 38% assuming $\lambda_a$ = 1.2 [45]. While these power output levels are not as high as other types of fuel cells, such as LT-PEM fuel cells using Nafion membranes, from a system level perspective, the power levels and efficiencies are high enough given the added operational advantages of a HT-PEM system, such as operating without inlet humidification and at atmospheric pressure.

## 3.3 PBI-Based Proton Exchange Membrane (PEM) Conductivity

The primary purpose of the PEM is twofold. The first is to serve as a rigid support material that can withstand the harsh fuel cell environment. The second is to either act as an adequate proton carrier on its own, or adequately support some other proton conducting medium. Typically, PEM materials that can survive the harsh fuel cell environment have low conductivities in their purified states, and are thus highly saturated with a proton carrier such as water for low temperature PEM fuel cells, or phosphoric acid in high temperature PEM fuel cells. In determining the best PEM material and proton carrier combinations, there are several important considerations. Firstly, if the membrane material itself is not a good conductor, it must be capable of absorbing an optimal amount of the proton conducting agent, where too much may weaken the membrane, but too little will result in poor conductivity. Secondly, the membrane material must retain the maximum amount of the proton carrier over a long period of time (about 1,000 hours for non-road mobile use). The loss of the conducting agent may result in lower conductivity, damage to the electrodes, and blockage of the flow field plate channels, all of which will lead to lower performance or catastrophic failure.

Phosphoric acid (PA) doped PBI membranes have shown promising performance as a fuel cell electrolyte material that can retain good conductivities in the harsh fuel cell environment. The dominant theory regarding the conductivity mechanism within the PA/PBI electrolyte, where its chemical formula is show in Figure 5 is that it follows a proton hopping method (Grotthus mechanism) [54]. In the PA/PBI electrolyte, this mechanism is strongly dependent on acid doping level (defined as the molar percent of the acid per repeat unit of the polymer), water content, and temperature. At lower doping levels, proton hopping has been suggested to occur between the N–H sites of the polymer and phosphate anion. At high doping levels, it is believed

that the presence of "free" acids provide additional proton transport sites because the phosphate anions are able to diffuse more rapidly [55]. Higher operating temperatures seem to greatly enhance proton transport; however, this must be balanced with durability concerns such as an increased PA evaporation rate at higher temperatures. The presence of water has also been suggested to enhance conductivity where ions such as $H_3O^+$ may serve as proton carriers [56]. In practice, though, water content does not have as strong of an effect on conductivity as acid content and high operating temperatures.

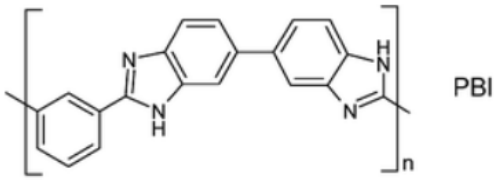


Figure 5: Chemical structure of the PBI material as described in [9]

The protonic conductivity of PBI material was first reported in 1977 and was found to be around 2 x $10^{-4}$ S/cm [57]. Except for more advanced concepts, PA/PBI material maintains conductivities in the region of $10^{-2}$ S/cm under anhydrous conditions [58]. The early PA/PBI materials developed by Wainright et al. achieved conductivities of approximately 0.025 S/cm or one fourth of what is typically achieved now [40]. At the time, this was likely a result of the high thickness of the membrane at 100 μm, as compared to Nafion membranes used at that time that were about 30 μm thick. Since then, conductivities of PA/PBI membranes have increased by an order of magnitude.

Ma et al. [59] (from the same research group at Case Western Reserve University) generated a complete set of conductivity data for the PA/PBI membranes as a function of temperature (60-200$^{o}$C), relative humidity (RH, 5-30%), and acid doping level (300-600 mol%). They showed

that the temperature dependence of conductivity, $\sigma$, can be accurately described using an Arrhenius Eq., $\sigma T = \sigma_o \exp(-Ea/RT)$ $[S/K\ cm]$. Activation energies $Ea$ and pre-exponential factors $\sigma_o$ were derived using this relationship and can be found in [59]. Ma et al. achieved a conductivity of 0.059 S/cm at 150$^o$C and an RH of 30%. It is also important to note that the membrane tested under these conditions had doping level of 630%, (defined as the molar percent of the acid per repeat unit of the polymer). Hasiotis et al. studied the conductivity dependence of PA PBI/polysulfone (SPSF) blends as a function of temperature, doping level, sulfonation degree of SPSF, RH, and blend composition. They achieved a conductivity level of around 1 S/cm at 500% doping level, 160$^o$C, and 80% RH [60]. They also reported that at extremely high PA doping levels of approximately 2300% for PBI-SPSF blends, conductivities of 7 S/cm were measured at 160$^o$C. While impressive conductivities, the blends suffer from low mechanical strength and were deemed not suitable for fuel cell use. Overall, Hasiotis et al. stated that doping levels >1000 mol % $H_3PO_4$ are not desirable for fuel cell applications.

Kim et al. worked on developing a cross-linked copolymeric membrane based on PBI and polybenzoxazine that increased the durability of the existing PA/PBI membranes [61]. In this work, they reported conductivities of 0.12 S/cm at 150$^o$C under anhydrous conditions. Verma and Scott developed a PA doped composite membrane that bonded heteropolyacids with PBI [62]. They achieved a conductivity of 0.177 S/cm under anhydrous conditions at 150$^o$C. The MEA that they assembled, however, did not exhibit good performance which the authors attributed to electrode polarization and/or hydrogen crossover to the cathode. More recently, researchers have tested doping sulfonate polybenzimidazoles (s-PBI) with PA in order to increase protonic conductivity with high success. Mader and Benicewicz developed PA/s-PBI membranes with conductivities above 0.3 S/cm [63]. Using this membrane, the researchers built

a MEA that when operated continuously at 160$^{o}$C showed minimal performance degradation for over 2500 hours.

It is clear from literature that the conductivity of PA/PBI membranes is much lower than fully humidified Nafion, which is about two to three times greater than that of PA/PBI membranes [31]. Nevertheless, because of its superior mechanical strength compared to Nafion, PA/PBI membranes can be made much thinner, such that its effective resistance to proton conduction is on the same order of magnitude as Nafion.

In order to increase conductivity, an effective strategy would be to increase the doping level, operating temperature, and atmospheric RH within the cell. Unfortunately, each of these strategies has limitations, and in some cases, adverse effects on other components or operations of the fuel cell. The doping level can only be increased to a point before the excess acid content begins to reduce the mechanical strength of the PBI membrane material [60]. The operating temperature can also be increased; however, because PA has a boiling point of approximately 213$^{o}$C [64], the vapor pressure of PA increases rapidly as 213$^{o}$C is approached, causing the PA in the membrane to evaporate quickly. Once evaporated, not only does the conductivity of the membrane decrease, but the evaporated PA may also contribute to the corrosion of carbon-based bipolar plates [65], reduce catalyst utilization [66], and ultimately increase the ohmic resistances within the cell. The RH of the inlet gases can also be increased, but most literature sources show that minimal cell performance is typically gleaned from high RH levels [60]. In fact, some studies show an overall performance decrease as the increase in membrane conductivity due to a high RH is offset by the cell voltage loss associated with the higher partial pressure of water causing lower reactant partial pressures [56]. On the other hand, other investigations indicate that small amounts of water in the anode is helpful, particularly if CO is in the anode gas feed [67].

From a system design perspective, a minor increase in performance does not warrant the additional complexities required for a humidification system.

## 3.4 CO Poisoning

Tolerance to carbon monoxide poisoning is one of the greatest advantages of the HT-PEM fuel cell. Oxidation of $H_2$ onto the anode Pt catalyst takes place in two steps: dissociative chemisorption and electrochemical oxidation [41]. In the anode, the H-H molecule adsorbs onto two Pt activation sites. Driven by the electrochemical oxidation of hydrogen, the two adsorbed hydrogen atoms are then absorbed through the electrolyte, resulting in two free platinum sites, two hydrogen ions, and two electrons. This two-step process occurs very quickly in the anode, corresponding to a very large exchange current density.

When the inlet hydrogen gas stream contains carbon monoxide, the CO competes with $H_2$ for the adsorption sites on the Pt catalyst, covering up surface area. Fortunately, CO desorption occurs via oxidation of the CO into $CO_2$ where the oxygen atom is supplied from the disassociation of the humidification water, or water generated from the HOR, so that CO is not a permanent effect. This desorption rate is limited by the formation of oxygen-containing adsorbate that is oxidized with CO to form $CO_2$. The CO poisoning creates a new limiting current density in the same way as the mass transport overpotential does. Therefore, CO poisoning manifests itself in the polarization curve by moving the mass transport limiting current density to a much lower value. Because of the relatively slower CO desorption reaction rate, fractional coverage of the Pt catalyst is what dictates the limiting current density.

The voltage losses from CO concentration can be modeled after determining the fractional coverage of the gases on the catalyst, i.e. $\theta_{H_2}$ and $\theta_{CO}$. In the phosphoric acid HT-PEM

environment, Pt catalyst activation sites are not simply covered by just $H_2$ and CO such that, $\theta_{H_2} + \theta_{CO} = 1$, but rather there are a number possible adsorbed species. Firstly, the disassociation of water generates $OH^-$ ions that may adsorb onto the Pt. Second, in PBI doped membranes, the acidic anion $H_2PO_4^-$ may adsorb onto Pt [61] and may result in up to 4% of surface coverage [41]. Finally, there is always some amount of surface area that is unblocked and available for the next adsorbate species. Therefore, the surface coverage of the adsorbed species should be:

$$\theta_{H_2} + \theta_{CO} + \theta_{H_2O} + \theta_{H_2PO_4} + \theta_{unblocked} = 1 \qquad \textit{(Eq. 12)}$$

Many researchers have suggested methods for determining the fractional coverage of CO on the catalyst surface area. Leading models suggest that at a specific voltage lever, the ratio of the current density produced by a fuel cell while running on $H_2$ and CO compared to operating on pure $H_2$, is proportional to $(1 - \theta_{CO})^2$ [68], or just simply $(1 - \theta_{CO})$ [69], [70]. Mathematically this is written as:

$$i_{H_2+CO}/i_{H_2} = (1 - \theta_{CO})^2, at\ a\ specified\ voltage \qquad \textit{(Eq. 13)}$$

$$i_{H_2+CO}/i_{H_2} = 1 - \theta_{CO}, at\ a\ specified\ voltage \qquad \textit{(Eq. 14)}$$

In Das et al. [70], the authors measured the performance of PBI MEAs from 140-180$^o$C and calculated the fractional Pt surface coverage of CO with anode inlet CO concentrations up to 5%using both *Eq. 13* and *Eq. 14*. At 0.5 V, their results indicated a near linear relationship with fractional surface CO coverage and temperature, where at 190$^o$C, $\theta_{CO}$ equals 8% when using *Eq. 13* and 13% when using *Eq. 14*.

Another model was developed in 1987 by Dhar et al., as they sought to understand the effect of CO poisoning on Pt in a PAFC [71]. They were specifically trying to model how the $\frac{[CO]}{[H_2]}$ concentration ratio impacts the fractional Pt CO coverage and voltage loss in a range of temperatures from 110-190$^o$C. After applying *Eq. 13* to their results, they showed that $\theta_{CO}$ is directly proportional to $\ln\left(\frac{[CO]}{[H_2]}\right)$, and takes the form of:

$$\theta_{CO} = a + b \ln\left(\frac{[CO]}{[H_2]}\right) \qquad \textit{(Eq. 15)}$$

where $a$ and $b$ are empirically determined constants at a given temperature. They showed that the relationship fits the Temkin isotherm for CO adsorption given as:

$$\theta_{CO} = \frac{-\Delta {G_o}^o}{r} + \frac{RT}{r} ln\, H + \frac{RT}{r} ln\, \left(\frac{[CO]}{[H_2]}\right) \qquad \textit{(Eq. 16)}$$

In the above Eq., $\Delta {G_o}^o$ is the standard free energy of adsorption, $r$ is the interaction parameter, and $H$ is the Henry's law constant for CO solubility in units of [atm/(mol/L)].

Dhar et al. also determined that the voltage loss as a function of CO concentration followed a linear relationship that took the form:

$$\theta_{CO} = ai + bi\, ln\, \left(\frac{[CO]}{[H_2]}\right) \qquad \textit{(Eq. 17)}$$

where $a$ and $b$ are empirically determined constants at a given temperature, and $i$ is the current density in mA/cm$^2$. For example, using *Eq. 17* at a [CO/$H_2$] ratio of 3.3%, a current density of 0.4 A/cm$^2$, and an operating temperature of 190$^o$C, a voltage loss of around 10 mV was observed. Based on their data, the generalized empirical model of voltage loss as a function of temperature ($T$), current density ($i$) and the $\frac{[CO]}{[H_2]}$ ratio was determined to be:

$$\Delta V_{pois} = 2.5\ x\ 10^{7} \exp(-0.0424\ T)\ i + 7.48\ x\ 10^{6} \exp(-0.0436\ T)\ i\ ln\ \left(\frac{[CO]}{[H_2]}\right)$$ *(Eq. 18)*

Dhar et al. [71] observed that *(Eq. 18* is only valid for positive values of CO poisoning that do not result in voltage losses greater than 30 mV, as a deviation of linearity in the values of poisoning losses occurred. However, linear deviations in voltage loss seem to only occur at relatively lower temperatures of 150$^{o}$C or less, so it might still be useful at higher temperatures even with high concentrations of CO beyond what was tested by Dhar et al. Because the authors did not measure the voltage loss at current densities beyond 0.4 A/cm$^2$, it is difficult to estimate at what current density deviations from linearity occur when operating at higher temperatures. A much more sophisticated model that estimated the impact of CO poisoning on PEM fuel cells was developed by Springer et al. [72] for low temperature PEM fuel cells, and adapted by Oh et al. [73] for HT-PEM fuel cells. Unfortunately, the model adapted by Oh et al. was not used to model CO concentrations greater than 0.5%, or at operating current densities above 0.3 A/cm$^2$.

Depending on the fuel reforming reaction and fuel type, the amount of CO present in the effluent gas stream of the reformer may exceed 20%; however, the majority of literature has reported performance results with CO concentrations only up to 5%. Korsgaard et al. [32] tested PA/PBI membranes with CO concentrations up to 5% while operating at 180$^{o}$C and 200$^{o}$C. Using this data, they developed an empirical model to estimate the anode overpotential due to CO poisoning. Das et al. [70] evaluated the performance of PA/PBI cells with CO concentrations up to 5% and at 180$^{o}$C. Their results revealed that the impact of CO poisoning is most strongly dependent upon temperature over any other parameter such as doping level, current density, and stoichiometric ratio. For example, when operating at a current density of 0.5 A/cm$^2$ and with a CO concentration of 5%, increasing the operating temperature from 165$^{o}$C to 180$^{o}$C resulted in a voltage increase from 375 mV to 500 mV. Li et al. [41] tested the performance of PA/PBI

membranes with some of the highest CO concentrations reported, up to 16% at 200$^{o}$C. Under these conditions and at a constant voltage of 0.5 V, the cell exhibited a power loss of approximately 30% relative to zero CO content.

To reduce the CO poisoning effect, the two primary operational strategies are to reduce the incoming CO concentration or to increase the operating temperature. Increasing the operating temperature increases both the adsorption rate of $H_2$ and the desorption rate of CO, moving the limiting current density further to the right on the polarization curve. When operating in the range of 160-200$^{o}$C, CO adsorption onto the anode catalyst is much less favored than at temperatures below 100$^{o}$C. By defining the CO tolerance as a voltage loss of less than 10 mV, Li et al. [41] determined that 3% CO in hydrogen can be tolerated at current densities up to 0.8 A/cm$^2$ at 200$^{o}$C, 0.1% CO can be tolerated at current densities up to 0.3 A/cm$^2$ at 125$^{o}$C, and 0.0025% of CO (25 ppm) can be tolerated at current densities up to 0.2 A/cm2 at 80$^{o}$C.

Another way to reduce the CO poisoning effect might be to simply increase the amount of Pt catalyst, or tailor the catalyst material to aid the CO desorption reaction rate, which has been the strategy of many researchers. For example, in a study published in 1967, Niedrach et al. determined that the addition of Ru, Rh, and Ir onto Pt could improve the CO tolerance [74]. Since then, other researchers have investigated many types of alloys that might prove effective without adding too much cost, such as Pt-Mo [75], Pt-WC [76], and PtRuNi [77]. It seems that in most of these studies, though, the quest for the most effective catalyst comes at such a high cost that it is not practically feasible for most applications.

## 3.5 Modeling

The mathematical models discussed Chapter 2 of this dissertation are the primary ways researchers estimate the performance of fuel cells. These models begin with calculating the theoretical potential of how a fuel cell should perform, then subtract off the various polarization losses including the activation, ohmic, mass transport, and contaminate poisoning losses. The full model presented initially above in *Eq. 11* is provided again as:

$$V_{cell} = E^0 + \frac{RT}{2F} ln\left(\frac{P_{H_2} P_{O_2}^{1/2}}{P_{H_2O}}\right) - \frac{RT}{2\alpha F} ln\left(\frac{i}{i_o}\right) - ir - m \exp(ni) \qquad \textit{(Eq. 11)}$$

Scott et al. [78] generated a steady-state isothermal model of a PBI-based PEM fuel cell that can be used to estimate the effect different electrode Pt/C ratios will have on performance. In their studies, a 40 wt.% Pt/C ratio gave the highest peak power density. Cheddie and Munroe [31] generated a one-dimensional mathematical model of a PBI-based PEM fuel cell. Their model indicated that the ohmic resistance value $r$ actually decreased at high current densities and was not constant, despite the fact that this is a common assumption made. This likely results from the high rate of production of water at high concentrations that leads to increased humidity within the membrane, and ultimately greater protonic conductivity. Additionally, their results show that the most dramatic performance improvements result from an increase in membrane conductivity, or an increase in catalyst effectiveness as it interfaces with the membrane. While these models are all similar to that presented in *Eq. 11*, they are only accurate with pure $H_2/O_2$ or an $H_2$/Air system. Since the primary advantage of using PA/PBI is that it can operate with inlet anode gases that may contain high concentrations of other gases such CO, $CO_2$, and $N_2$, these models are limited in their capabilities. Particularly with CO poisoning, the model shown in *Eq. 11* does not explicitly include the poisoning effect.

Several HT-PEM fuel cell researchers have developed full polarization models that attempt to account for the CO poisoning effect. Korsgaard et al. [79], for example, generated a semi-empirical model that accounts for the anode overpotential due to CO using the Pt surface coverage model that was developed for low temperature PEM fuel cells discussed in [72]. The anode overpotential due to CO coverage is expressed in the Korsgaard model using the hyperbolic sine function as:

$$\eta_a = \frac{RT_{cell}}{\alpha F}\ sinh^{-1}\left[\frac{i}{2\ k_{eh}\ \theta_{H_2}}\right] \qquad \textit{(Eq. 19)}$$

where $k_{eh}$ is the $H_2$ electrooxidation rate and $\theta_{H_2}$ is the surface coverage of $H_2$. The authors merged this model with one similar to that in *Eq. 11*. The level of detail describing how the authors determined the $H_2$ electrooxidation rate, and other pre-exponential factors used, is a bit sparse. It appears that they assume these factors are constant, where it would seem that $H_2$ electrooxidation rate is, in fact, a function of operating temperature and pressure. Nevertheless, the model fit well for most of their experimental data that considered CO concentrations up to 5%, operating temperature ranges from 160-200$^{o}$C, and at current densities up to 1 A/cm$^2$. It seemed to only deviate at high current densities when the mass transport losses began to take effect.

Another way of modeling the performance of a PA/PBI doped fuel cell might be to merge *Eq. 11* with the overpotential model developed by Dhar et al. [71], shown in its empirical form in *Eq. 18*. The complete merged model using these two Equations would be:

$$V_{cell} = E^0 + \frac{RT}{2F} ln\left(\frac{P_{H_2} P_{O_2}^{1/2}}{P_{H_2O}}\right) - \frac{RT}{2\alpha F} ln\left(\frac{i}{i_o}\right) - ir - m\exp(ni) - a\ exp(-b\ T)\ i\ ln\left(\frac{[CO]}{[H_2]}\right)$$

*(Eq. 20)*

where $a$, $b$, $m$, and $n$ are all empirically determined constants. At this point, it is important to note that the performance impact of other gas species such as $N_2$ and $CO_2$, which are commonly found in reformate mixtures, is typically seen as a voltage loss resulting from the reduction of partial pressures of the reactants $H_2$ and $O_2$. Hence, they are not explicitly included in the model.

## 3.6 Degradation Modes and Durability

A PEM fuel cell will exhibit a gradual decline in power output over its operational lifetime. Initially, the cumulative effect of this decline is small enough so as not to affect functionality; however, at a certain point in time, the decline in power output becomes so large that the fuel cell can no longer be used to power its particular application. At this point, the degradation is deemed unacceptable. In the fuel cell world, significant progress determining the causes of these degradation modes with subsequent mitigation strategies has been made, but the root causes of gradual performance decline are still not completely understood. There are many degradation mechanisms that are highly dependent on materials used as well as operational conditions. The choice of electrode material or operating temperature, for example, will have cascading effects for multiple degradation modes. This obviously makes modeling and a full understanding of the underlying science behind different degradation modes difficult, but such an understanding is necessary to adequately develop systems that meet practical design considerations. This section focuses on the primary degradations modes of particular concern for PA/PBI based HT-PEM fuel cells. Mitigation strategies for these degradation mechanisms are also described below unless discussed as part of another section as noted.

Although there are unique failure mechanisms for each fuel cell type, common degradation modes typically result from causes such as exposure to fuel and air contaminates, startup and shutdown procedures, and operating conditions like potential cycling, fuel starvation, and

temperature variation. These failure mechanisms most often manifest themselves as permanent physical changes of the MEA materials, altering its composition to a state that is unacceptable for normal operations.

Performance losses resulting from fuel and air contaminants can be permanent, irreversible, or temporary. Carbon monoxide is a common contaminant, as discussed in Section 3.4, that is both irreversible and temporary, as its harmful impact can be eliminated simply by removing it from the inlet fuel. Other common fuel impurities include ammonia, hydrogen sulfide, hydrogen cyanide, hydrocarbons, formaldehyde, and formic acid, where common air contaminates might be sulfur dioxide, nitrogen oxides, and particulate matter [80]. These impurities all cause performance problems in the same manner, through impeding or completely blocking reaction sites used for chemisorption, charge transfer, and/or protonic conduction.

Ammonia ($NH_3$), which may be generated at trace levels through hydrocarbon fuel reforming, leads to deleterious performance effects in fuel cells at levels as low as 13 ppb [81]. Short-term exposure has been shown to have reversible effects; however, long-term exposure leads to permanent degradation. Similarly, exposure to hydrogen sulfide $H_2S$ at concentrations as low as 10 ppb, commonly found at trace levels in hydrocarbon fuels, leads to negative effects in the anode after exposure [82]. $H_2S$ adsorbs onto Pt much like CO, but the electrochemical desorption of sulfur requires potentials unachievable in a continuously operating $H_2$/air fuel cell. Cathode contaminates like nitrogen oxides have been shown to cause significant performance loss from $NO_2$ concentrations as low as 10 ppm [83]. It is assumed by the researchers that the adsorption affinity of NOx onto Pt is weak, but strong enough to block a noticeable amount of available surface area required for the oxygen reduction reaction at the cathode. They also

observed that complete recovery occurred within a few hours when the cathode air feed was replaced with neat air.

Mitigation strategies to eliminate common fuel and air impurities such as hydrogen sulfide include requiring stringent fuel composition targets or some sort of pre-filtering. For developing a practical system that runs on propane commonly available hydrocarbon fuel, the latter option seems more feasible as changing fuel standards for an existing world product is prohibitively difficult. Thus, for the experiments in this dissertation (described in Chapters 4 – 6), sulfur reducing sorbents were purchased from an existing company called SulfaTrap [84]. These sorbents could be easily integrated into a mobile system using a cartridge like configuration with a well-defined schedule for replacement.

One of the primary degradation modes for fuel cells that use carbon-based electrodes is described as the "reverse-current" mechanism; a very thorough description has been provided by Reiser et al. [85]. This reverse-current mechanism causes oxidation of the carbon catalyst support that causes electrical isolation of the catalyst particles, resulting in a decrease of electrochemical performance. The mechanism is primarily an outcome of operating at high cell potentials, which can result from many different operating conditions. The corrosion reaction of carbon material with water is generalized as [85]:

$$C + 2H_2O \rightarrow CO_2 + 4H^+ + 4e^-, E^o = 0.207\,V \qquad \textit{(Eq. 21 )}$$

Cell voltage levels around 0.2 V were often experienced in the experiments of this dissertation during startup and shutdown of the test cell. This indicates that carbon corrosion is likely occurring; however, it may not be at a rate that significantly alters the performance of the cell, particularly during the short test durations conducted that were rarely beyond 200 hours.

Mathias et al. [86] show that the rate of carbon corrosion depends on material type, operating temperature, and cell potential, where higher cell potentials and operating temperatures exacerbate the corrosion rate. Because of the higher temperature operation of PA/PBI based fuel cells, this is particularly concerning and should be avoided in order to ensure high lifetime operation.

The root cause of the reverse-current mechanism begins before startup, or in some cases when running at very low anode stoichiometries, where both the anode and cathode catalysts are exposed to oxygen. With respect to the electrolyte potential, the oxygen from the air causes the anode and cathode catalyst potentials to both be about 1.23 V, the equilibrium potential of oxygen. Since both the anode and cathode are at the same potential, this results in an overall cell potential difference of 0 V. Once $H_2$ enters the anode chamber, the $H_2$ is oxidized, lowering the inlet portion of anode potential close to the equilibrium potential of hydrogen, around 0 V. During the time it takes for the anode potential to reduce to 0 V, though, the remaining oxygen towards the outlet of the anode chamber causes the membrane potential to reduce in order to maintain the interfacial potential difference between the anode catalyst and the membrane to be close to the equilibrium potential of oxygen, 1.23 V. Because the voltage of the membrane is lowered while the voltage at the cathode catalyst remains the same, the potential difference between the membrane and the cathode catalyst becomes much larger than 1.23 V where some studies show it reaches as high as 1.6 V [87]. This high cathode interfacial potential difference results in oxygen evolution, leading to carbon corrosion and ultimately damaging the cathode electrode structure. At this high of a potential, the carbon in the cathode electrode can be completely corroded within a few hours [85]. The protons generated during the carbon corrosion

process are consumed in the oxygen reduction reaction occurring in the anode, generating current in the reverse direction, hence the naming of this mechanism.

Other studies have shown that Pt catalyzes the oxidation of carbon where voltages as low as 0.9 V lead to carbon oxidation of the electrodes [88], [89]. One study has also shown that high operating temperatures exacerbate the effect of carbon oxidation [90]. One complete start/stop cycle at 160$^{o}$C results in four times the amount of carbon corrosion than the same start/stop cycle completed at 80$^{o}$C. One strategy that is implemented in existing phosphoric acid fuel cells to mitigate carbon corrosion is to use electrodes that are resistant to carbon oxidation. This is the primary reason why the choice for catalyst support material for PAFCs has been graphitized versions of carbon that exhibits lower carbon oxidation rates than typical carbon support materials used for low temperature PEM fuel cells, such as Vulcan carbon black [91]. Another strategy to minimize electrode corrosion is to limit the cell potentials to below 0.9 V. However, this is quite difficult during start/stop cycles since the open circuit voltage of the cell when no load is being drawn is typically greater than 1.0 V when operating at temperatures around 200$^{o}$C. Unless operating continuously, inevitably high cell potential excursions will occur during startup and shutdown. Mitigation strategies should therefore be focused on minimizing the amount of time that the cell is held at high potentials. These specific strategies are discussed below in Section 3.6.

Fuel starvation is another degradation mechanism that is often observed when operating full fuel cell stacks. When fuel cells are operated in a stack configuration, they are required to generate the same amount of current, but because of mechanical design issues, each individual cell may experience different flows of fuel, air, and coolant. Under fuel starvation conditions, the potential of the cells that have insufficient fuel to carry the current being pushed through by

adjacent cells will climb higher until oxidation of the carbon support structure occurs, resulting in the reverse-current mechanism discussed earlier [91]. It has also been suggested that localized fuel starvation within individual cells may also result, particularly due to flow channel blockage [85].

Pt dissolution or particle growth is another degradation mode that is common to all fuel cells that use Pt as its primary catalyst. Pt dissolution occurs when the Pt catalyst is somehow dislodged from the catalyst support and is either lost in the exhaust or migrates into the membrane. Pt particle growth or agglomeration results when Pt particles merge together to form larger particles. Both mechanisms result in a lower surface area available for reactants, ultimately reducing the overall performance of the fuel cell. Significant research has been conducted in this area, particularly for PAFCs, which operate under very similar conditions as HT-PEM fuel cells that use PA/PBI membranes. Honji et al. show that Pt dissolution and agglomeration is accelerated by the simultaneous presence of air and phosphoric acid at cell potentials above 0.8 V, and high temperatures around 200$^{o}$C [92]. This is a particular concern for HT-PEM PA/PBI-based fuel cells, because all of these conditions will exist simultaneously under normal operations. The authors, however, do stress that Pt dissolution and agglomeration is most strongly related with operating at high cell potentials rather than higher temperatures or in the PA environment. Although there is still debate on exactly what the mechanism is [91], one possible explanation is that Pt dissolution or agglomeration is not directly related to high potentials, but rather it results from carbon corrosion of the catalyst support at high potentials, that in turn generates free moving Pt particles that could either migrate into the membrane or be lost in the exhaust. The best mitigation strategy for this degradation mechanism is to limit the

amount of time the cell is operated at high potentials, a common theme for many degradation mechanisms.

Temperature swings or long-term operations at high temperatures are the final primary degradation modes that are particularly important for HT-PEM fuel cells that use PA/PBI membranes. The boiling point for PA at atmospheric pressure is approximately 213$^{o}$C [64], where the vapor pressure of PA increases exponentially as the temperature approaches 213$^{o}$C. As PA is the primary agent providing protonic conductivity through the membrane, it is essential that PA stays imbibed within the PBI membrane to ensure maximum performance for long durations. T. J. Schmidt, a research scientist from BASF, investigated the evaporation rate of PA in PA/PBI membranes as a function of temperature, with a reproduction of their results displayed below [90].

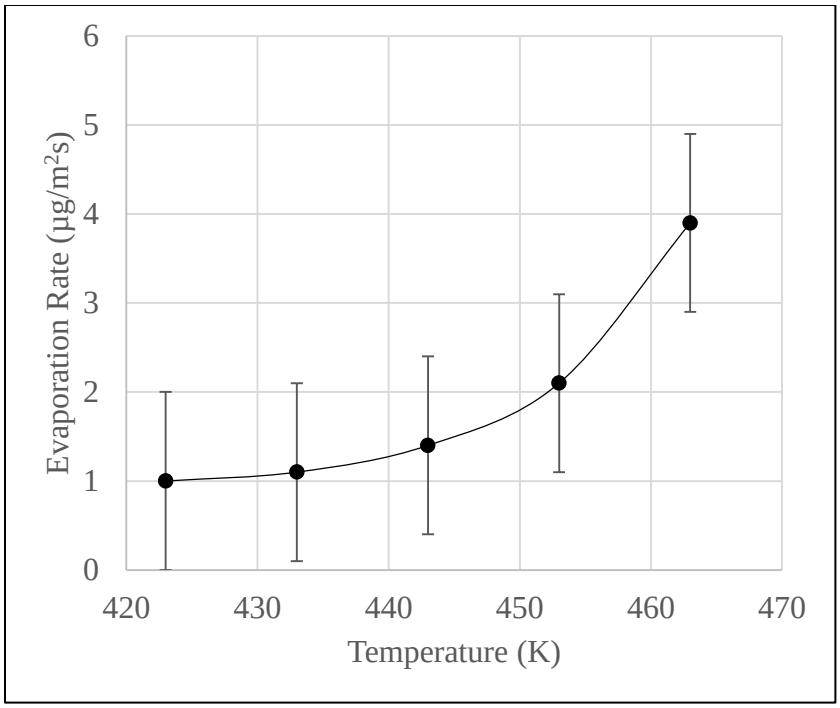


Figure 6: Phosphoric acid evaporation rates in Celtec® PA/PBI MEAs produced by BASF. Data taken from [90] under no load conditions, and is suggested to represent the maximum amount of evaporation that could be expected at different operating temperatures.

From Figure 6 it seems that the PA evaporation has somewhat of an exponential relationship with operating temperature, although a third order polynomial seems to fit the data quite well. Schmidt additionally studied the total evaporation of PA from a Celtec membrane when operating at a constant current density of 0.2 A/cm$^2$ for over 8,800 hours at 160$^o$C. An average acid evaporation rate was determined to be 0.5 µg/m$^2$s over this time period, significantly less than the values provided in Figure 6 which are suggested by Schmidt to represent the maximum amount of evaporation to be expected [90]. If it is assumed that the trend in Figure 6 can be extrapolated to higher temperatures, when operating at 200$^o$C (473K) the PA will evaporate at more than six times the rate as when operating at 160$^o$C (433K). This study also showed that the PA evaporation rate declines over time when holding the other operating conditions constant. Defining the end of life of the MEA where 10% of the initial acid in the membrane is

evaporated, they calculated an approximate lifetime of 50,000 hours. Schmidt additionally investigated the effect of start/stop cycling on HT-PEM MEAs and compared them to conventional LT-PEM MEAs. Their results indicated that the carbon corrosion rates caused by the high voltage excursions during the start/stop cycles were the same for both fuel cell types, a surprising result since it was expected that the HT-PEM would have higher carbon corrosion rates due to the high operating temperature of approximately 160$^{o}$C. This is thought to be a result of the difference in relative humidities where the LT-PEM was operated at 66% RH and the HT-PEM was operated under anhydrous conditions. The higher RH in the LT-PEM is known to increase the carbon oxidation reaction rate.

Another problem resulting from high PA evaporation rates is the impact of PA on other fuel cell components, particularly the bipolar plates. Due to the presence of phosphoric acid, a highly corrosive environment is created which can lead to an increased bipolar plate porosity [66]. This is then followed by an uptake of electrolyte into the void volume of the increasingly porous bipolar plates, ultimately resulting in MEA degradation and increased ohmic resistances of the cell. A similar effect was witnessed when developing PAFCs several decades ago, which ultimately led to the design of acid filled prous plates by UTC [93]. These graphite based plates work well for long-term durability concerns, but are not suitable for mobile applications due to their high gravimetric density. Metallic materials are more easily manufacturable, cheaper to produce can be made to be much thinner and lighter than graphite based plates. Hartnig et al. tested four different types of bipolar plates, two graphite composite materials, surface sealed graphite, and gold plated stainless steeel, in order to examine the durability of the different materials while operating with a PA/PBI MEA at 180$^{o}$C [66]. The gold plated stainless steel showed the lowest performance drop over a 1600 hour run time, where the authors attributed the

performace drop to reduced conductivity of the membrane and Pt agglomeration, rather than increased ohmic resistances in the bipolar plates. The material choices for bipolar plate materials for a PA/PBI based system are discussed in greater detail in Chapter 7.

Several papers have investigated the performance of HT-PEM fuel cells over extended periods of time. Generally, though, these investigations are conducted while operating the cell at a single current density using pure $H_2$ and air. The study descrbied earlier by Schmidt shows a 40 mV drop in potential over 7000 hours when operating at 0.2 $A/cm^2$, 160$^oC$ and atmospheric pressure, translating to a voltage decay rate of 5.7μV/hr [90]. The same study also considered the impact of a start/stop protocol over the same time period with a total of 270 start/stop cycles. While operating under the same conditions as above, the MEA operating with the start/stop protocol showed a 50 mV loss after 5000 hours (decay rate of 10 μV/hr) and reached a 100 mV loss at 7000 hours. Another study that operated under the same operating conditions for close to 6000 hours also reported an average voltage decay rate of 10 μV/hr [94]. During this test, the researchers increased the operating temperature to 180$^oC$ for 600 hours, then decreased the temperature back to 160$^oC$. During this temperature spike, the voltage decay rate increased substantially to 19 μV/hr.

One final degradation mechanism specific to HT-PEMFCs relates to the hyrgroscopic nature of PA/PBI membranes. Since PA/PBI membranes are extremely hygroscopic, if any oxygen and hydrogen were to enter the cell below temperatures of 100$^oC$ at the same time, they would react to form liquid water. This would cause the PA imbibed in the PBI membrane to move to the surface of the membrane, thereby reducing the overall protonic conductivity [95]. This problem would only occur during startup and shutdown procedures where the fuel cell temperature drops below 100$^oC$. Therefore, liquid water formation can be eliminated by developing proper startup

and shutdown sequences that avoid the presence of $H_2$ and $O_2$ within the cell at temperatures below 100$^{o}$C.

Overall, there are many issues which cause durability concerns for HT-PEM fuel cells. It should be noted that except for the issues relating to the PA environment or high temperature operations, the majority of the degradation mechanisms described are present for all fuel cell types, and can largely be mitigated through material choices and specific operational strategies. For a practical system, these strategies must be balanced with size, weight, cost, durability, and user operability requirements. To summarize, the primary degradation mechanisms result from high cell potentials and high temperature operations. Mitigation strategies for a HT-PEM fuel cell that will impact the majority of durability concerns discussed are to keep the cell potential below 0.8 V, which will avoid carbon corrosion and Pt dissolution, and minimize high temperature operation beyond 200$^{o}$C as much as possible to avoid PA evaporation loss. The latter is particularly challenging when operating the fuel cell on reformate containing high concentrations of CO, as the effect of CO poisoning is greatly decreased at higher temperatures. Other mitigation techniques such as operating at high pressures may reduce the PA evaporation rate to acceptable levels. Like all fuel cell types, PA/PBI have their unique degradation challenges; however, when operating under the proper conditions, the studies discussed in this section show that PA/PBI membranes are capable of operating for several thousands of hours. How these operational protocols and strategies are translated into a physical system design are discussed throughout the rest of this dissertation.

## 3.7 Startup and Shutdown Procedures

The startup/shutdown sequences for fuel cells are often the cause of significant cell degradation unless proper protocols are developed. There are several common startup/shutdown

procedures inherent for most fuel cell types in order to minimize occurrences of $H_2$/air fronts that lead to carbon corrosion of the electrodes as discussed in Section 3.5. As discussed by Reiser et al. [85], one strategy to mitigate this degradation mechanism might be to introduce a reducing gas into both the anode and cathode during shutdown, and then maintain this gas while sealing the inlet and outlet ports to the fuel cell. The procedure developed by UTC Fuel Cells (now known as UTC Power, with much less activity in the fuel cell business) has been shown to be quite effective, with almost zero performance loss after 2315 start/stop cycles [96]. The process for this procedure, labeled *Protocol A*, is as follows:

*Protocol A*

1) The primary load is disconnected and a much smaller dummy load is connected across the anode and cathode whereupon the cathode air is turned off.
2) After a short amount of time for the oxygen to be consumed in the cathode, the anode feed gas is then turned off.
3) Air is then fed into the anode until a $H_2$ concentration between 1-3% is reached in the anode.
4) Both the anode and cathode exhaust ports are sealed.
5) The cell voltage should be monitored to ensure the voltage stays below 0.2 V during storage where additional $H_2$ can be added when necessary to maintain a low voltage level.

After Step 4, the anode and cathode are primarily comprised of $N_2$, $H_2O$, and $H_2$. While this method has been shown to be highly effective, using a reducing gas in a mobile system may be difficult as it would need to be stored on-board in some manner, adding additional weight, complexity, and cost.

Instead of using a reducing gas, another strategy would be to use only an inert gas such as $N_2$ to completely fill the anode and cathode chambers during shutdown, thus removing any oxygen from the fuel cell. In order for this to be successful, both the inlet and outlet ports of the fuel cell need to be sealed after being filled with $N_2$. If the $N_2$ were maintained in both chambers during startup, then there would not be an $H_2$/air front in the anode chamber as $H_2$ is introduced. In this scenario, it would also be prudent to involve a dummy load to keep the cell potential low.

Several researchers have investigated different startup/shutdown sequences using HT-PEM fuel cells with varying results. Using a 5 cell stack constructed with PA/PBI Celtec P1100 MEAs, Kannann et al. tested the following protocol, identified here as *Protocol B* [97]:

*Protocol B*

1) Heat stack at a rate of 2.5 K/min under $N_2$ flow on the anode, and no flow on the cathode.
2) When the stack reaches 115$^{o}$C (~40 mins), $H_2$ flow is started on the anode followed by air flow on the cathode after 30 seconds.
3) The stack is operated at open circuit voltage (OCV) for 30 seconds, then current is ramped up to 0.25 A/cm$^2$, and is held until the stack reaches 165$^{o}$C.
4) The current is stepped down to 0.03 A/cm$^2$ and the stack is allowed to cool for 10 minutes then the air flow to the cathode is shut off.
5) After 60 seconds of zero air flow, the $H_2$ in the anode is switched to $N_2$ and then the stack is cooled to 80$^{o}$C. The sequence is then repeated.

Using this five-step process, the researchers were able to operate the stack for 4160 hours with 1562 start/stop cycles. This resulted in an average voltage loss of 133 µV/cycle. It is also important to note that the anode gas feed for the majority of the cycles was comprised of

$H_2/CO_2/CO$ mixture of 74.8/25/0.2 volume %. It does not seem that the fuel contaminants would acontribute to the performance loss. The other cycles had an anode gas feed of 80/20 $H_2/N_2$. For comparison, a continuously operated stack under similar conditions exhibited a voltage decay of 13.25 µV/hr. The voltage decay is likely caused by carbon corrsion, largely due to the length of time operated at OCV. The open circuit voltage recorded in this study never went beyond 0.93 V which is not very high.

Other researchers, including Yu et al., have conducted durability studies investigating the effect of start/stop cycles, load cycling, and thermal cycling in [98]. Their start/stop protocols began with heating the cell up to 120$^o$C with both $H_2$ and air flowing and keeping the cell at OCV. Once the cell reached 120$^o$C, a small load was turned on (0.01 A/cm$^2$) while the cell was heated up to 180$^o$C where the load was then increased to 0.2 A/cm$^2$, and operated for 3 hours. The cell was then run at OCV for 1 minute and then cooled to 55$^o$C before the next startup process. The cells used for these start/stop cycle tests were only operated for ~700 hours where the cell with the lowest degradation rate was 179.3 µV/cycle, 46 µV/cycle greater than the procedure discussed in [97]. Although not explicitely tested, the amount of time spent at the high potentials encountered during OCV operation could have led to the majority of the voltage decay. The researchers could have incorporated a dummy load into their procedure that kept the cell voltage low at around 0.2 V.

In the context of developing a practical mobile device based on a HT-PEM fuel cell, the hygroscopic nature of PA/PBI membranes presents unique challenges in devising effective startup and shutdown procedures. While the procedure developed by UTC seems very effective and does not require additional balance-of-plant equipment to function properly, it would introduce water into both the anode and cathode. Once the cell cools, any condensed water

would cause migration of the imbibed PA to the surface of the membrane and reduce the overall conductivity of the MEA.

One possible effective shutdown method that could be implemented for a mobile fuel cell system with minimal additional BoP equipment could be the following process, labeled as *Protocol C*:

1) For startup, heat the fuel cell up to operating temperature, then flow fuel to the anode first for several seconds.
2) Then flow air to the cathode while maintaining a dummy load that keeps the cell potential below 0.8 V.
3) Once the fuel cell reaches a steady state (~30 seconds), set the load to the desired current density and run the fuel cell for the desired time frame.
4) To begin shutdown, turn off the primary load and switch over to a small dummy load that maintains the cell potential below 0.8 V.
5) Turn off air flow to the cathode and maintain a dummy load until the cell voltage drops to below 0.2 V.
6) Open a port that allows the anode gas feed to fill both the anode and cathode, ensuring that the voltage of the cell remains below 0.2 V using a dummy load, and purge the cell for a period of time that allows for adequate removal of $H_2O$ and $O_2$ from the test cell.
7) Seal both the inlet and exhaust ports of the anode and cathode for the cell to remain in storage. Repeat steps 1-3 for the next operation.

Assuming minimal $H_2O$ is fed into the cell via the anode or cathode, *Protocol C* eliminates oxygen that leads to high voltage excursions like *Protocol A*, and reduces the chance for liquid water formation during storage like in *Protocol B*. One way to ensure minimal water input during

these protocols is to place a desiccant in line with the anode and cathode gas feeds before they enter the fuel cell.

Examination of the effects of *Protocol C* could not be found in published literature. Additionally, this type of procedure was never tested in this work, so further investigation is necessary to ascertain its effectiveness. For the studies conducted throughout this dissertation, very few start/stop cycles were completed for each MEA (no more than 20 for each tested cell). In order to eliminate oxygen and the possibility for liquid water formation within the test cell during shutdown, a procedure similar to that of *Protocol B* was followed where the anode and cathode were continuously purged with $N_2$ for several minutes, whereupon the exhaust and inlet ports were sealed to maintain an $N_2$ atmosphere within the cell. This also served to reduce the cell voltage levels to below 0.2 V. Every test that continued experimenting with a previously used MEA began with a baseline curve to compare with the former trial. This $N_2$ purging procedure proved to be very effective for the relatively few start/stop cycles completed, and other degradation mechanisms such as PA evaporation were the primary causes of performance loss for each tested cell.

# 4 Hydrogen Generation for PEM Fuel Cells

The most sustainable primary fuels to use in a fuel cell-based system include hydrogen generated from a renewable source or some type of carbon-neutral biofuel. However, as already discussed, using hydrogen is presently impractical for widespread adoption due to its unavailability. Similarly, biofuels suffer from the same drawback as renewable hydrogen in that there is insufficient infrastructure for widespread use. While it is expected that technology and infrastructure for renewable hydrogen and biofuels will continue to develop, a more practical

primary fuel for fuel cell applications in the interim is to use a hydrocarbon fuel. Of the fuels available, for the practicality of mobile applications, a fuel such as propane is preferred because it can be easily condensed to a liquid form for transport and storage. Additionally, ease of refueling, wide availability, public familiarity, and existing guidelines for safe operation make propane an attractive primary fuel for a fuel cell system. Specific to mobile fuel cell applications, use of the wide availability of 1 lb propane canisters, as shown in *Figure 7*, allows for a similar user experience to existing propane-fueled devices. Propane has a gravimetric energy density of 46.35 MJ/kg [35], equivalent to 5.85 kWh/lb. Assuming a system to be designed to produce 500 W and overall energy conversion efficiency of just 20%, a 1 lb propane canister could power this device for around 2.5 hours.


Figure 7: 1 lb propane canister widely available in the U.S.

Hydrogen gas does not exist naturally and must therefore be generated from some other source. The primary way to generate $H_2$ is through steam methane reforming (SMR); over 95% of the world's hydrogen gas is generated in this manner [99]. The other 5% of $H_2$ is primarily generated through the splitting of water in $H_2$ and $O_2$ using electrolysis. If the main source of electricity is generated from renewables such as wind or solar power, producing $H_2$ via

electrolysis can be a carbon neutral process. Whatever the generating method, hydrogen can then be stored for use in a fuel cell device.

For a practical mobile system, though, on-board hydrogen gas storage is very complex and suffers from low volumetric energy density, requiring large and heavy storage tanks for useful amounts. Even at pressures of 10,000 psi, which require very heavy and expensive storage tanks, the volumetric energy density of $H_2$ is approximately 4.7 MJ/L, almost 1/5 of the energy found in the same volume of propane, for example [100]. Therefore, utilizing a hydrocarbon fuel over a compressed or liquefied hydrogen storage system is advantageous due to lower cost, simple on-board storage mechanization, high energy density, and wide availability for refueling. For the system described in this dissertation, propane is the fuel of choice because of its universal availability, high energy density, and its ability to be more easily reformed than heavier hydrocarbons such as diesel or gasoline.

## 4.1 Primary Principles of Fuel Reforming

Fuel reforming is the general term used to describe the conversion of hydrocarbon fuels into other useful products such as syngas ($H_2$ + CO), ammonia, and methanol. For most fuel reforming reactions, the first stage or step involves breaking apart the hydrocarbon molecule into a gas mixture of primarily $H_2$ and CO using a catalytic reactor. When pure hydrogen is the desired product, additional stages to separate or purify the gases are typically integrated into the process.

There are two main types of fuel reforming defined as steam reforming (SR) and partial oxidation or catalytic partial oxidation (cPOx). In SR, fuel is mixed with steam over a catalytic bed while in cPOx, fuel is instead mixed with air. SR is an endothermic reaction whereas cPOx

is exothermic. Another common type of fuel reforming process is referred to as auto-thermal reforming (ATR), which combines SR with cPOx by mixing fuel with air and water. A subset of ATR that is often referred to in literature is called oxidative steam reforming (OSR), where the endothermic SR reaction is assisted by the addition of small amounts of oxygen to generate an exothermic reaction and offset some of the energy costs. Fuel reforming reactions typically operate at temperatures between 800$^{o}$C and 1000$^{o}$C, but sometimes exceed 1000$^{o}$C. Often, exotic materials such as Inconel are used for housing the catalyst in order to withstand the high temperatures.

## 4.2 Steam Reforming and Autothermal Reforming

Steam methane reforming (SMR) is by far the most widely used process to generate $H_2$ gas. The earliest recorded example of SMR was reported by Sabatier and Senderens in 1902 when they witnessed the formation of synthesis gas (CO + $H_2$) from mixing steam with methane [101]. SR is a strongly endothermic reaction where additional heat is consistently required to maintain the reaction. Because of the additional H atoms found in water, SMR has a greater potential to generate high $H_2$/CO ratios than cPOx.

Figure 8 is a block flow diagram of the primary steps involved with a hydrogen generation processing plant. Natural gas and steam are first fed to the steam reformer where the methane/steam mixture is catalytically converted to synthesis gas, or syngas, which is primarily composed of $H_2$, CO, and $CO_2$ [102]. The syngas is then sent to multiple water gas shift (WGS) reactors with the first called a high temperature shift (HTS) reactor and the second a low temperature shift (LTS) reactor. The WGS reactions convert the majority of the CO and steam into $CO_2$ and additional $H_2$. The final pressure swing adsorption (PSA) step separates the $H_2$

from total gas stream to an industrial gas purity level of 99.95%. Overall efficiencies for existing SMR plants range from 63% to 70% [103].

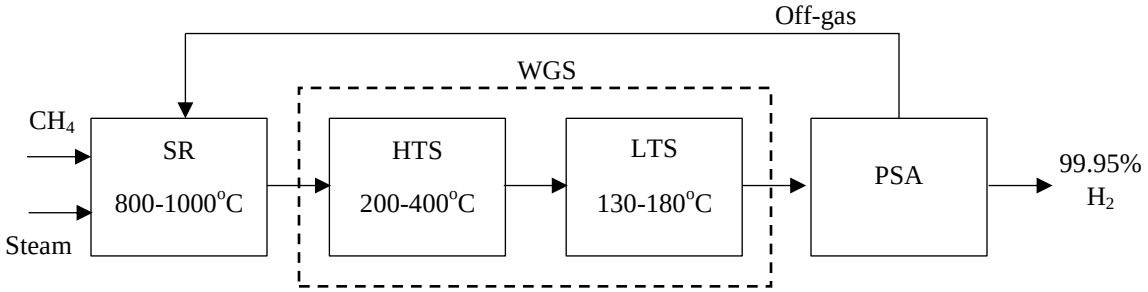


Figure 8: Simplified SMR hydrogen processor plant block flow diagram

Although SMR is the most widely used fuel reforming process for generating hydrogen gas, the number of stages and components, such as additional water tanks and management sub-systems, make the overall system too bulky and complex for a practical mobile fuel processor [104], [105]. A desirable mobile fuel processor would be highly efficient, durable, light-weight, simple to control, and have a short start-up time. A fuel reformer based on a cPOx reaction seems to best fit all of these requirements because only air and fuel are necessary, eliminating the need for a complex water management system essential to SR or ATR reformers.

## 4.3 Catalytic Partial Oxidation

cPOx is facilitated by mixing a hydrocarbon fuel with air over a catalyst bed at an elevated temperature. At optimal operating conditions, the oxygen reacts with the fuel to form primarily $H_2$, $N_2$, CO, and typically small amounts of $CO_2$ and $H_2O$ in the effluent. cPOx is an exothermic reaction, and its mechanisms have been investigated in many studies including [106], [107], [108]. Because propane is the fuel of choice in this research, the primary reaction for propane cPOx is:

$$C_3H_8 + 1.5O_2 \rightarrow 3CO + 4H_2 \quad (1)$$

where several other reactions may also occur including:

$$C_3H_8 + 5O_2 \rightarrow 3CO_2 + 4H_2O \ (2)$$

$$C_3H_8 + 3O_2 \rightarrow 3CO_2 + 4H_2 \ (3)$$

$$CO + H_2O \leftrightarrow CO_2 + H_2 \ (4)$$

$$C_3H_8 + H_2O \leftrightarrow 3CO + 5H_2 \ (5)$$

$$C_3H_8 + 3CO_2 \leftrightarrow 6CO + 4H_2 \ (6)$$

$$C_3H_8 + 2H_2O \leftrightarrow 3CO_2 + 6H_2 \ (7)$$

$$CO + H_2 \leftrightarrow C + H_2O \ (8)$$

$$C_3H_8 \leftrightarrow 3C + 4H_2 \ (9)$$

$$CO + 0.5O_2 \rightarrow CO_2 \ (10)$$

$$H_2 + 0.5O_2 \rightarrow H_2O \ (11)$$

While it is theoretically possible to completely catalyze reaction 1 only, the remaining reactions are observed to some degree in most systems.

Even though a cPOx reaction is much more attractive for mobile applications as compared to SR or ATR, the advantage of simpler design unfortunately comes with a loss of overall efficiency due to the nature of the exothermic reaction, as well as low $H_2$/CO ratios when compared to SR or ATR. These disadvantages can be nullified to some degree through finding use for the waste heat in other parts of the system.

To generate as much $H_2$ as possible using cPOx, reactors are typically operated at very high temperatures [108]. Unfortunately, operating at high temperatures causes excessive thermal stress on the reactor, which may lead to catalyst metal sintering. Additionally, high temperature operation requires the use of exotic and expensive materials for reactor bodies such as Inconel in

order achieve optimal performance. Therefore, there is a balance between performance and cost with practical designs.

## 4.4 Catalyst Design and Failure Mechanisms

The heart of the fuel reformer is the catalyst, where its primary role is to achieve equilibrium conversion. It must additionally ensure well-distributed flow within the reformer to avoid local hot spots that may lead to a shorter lifetime. The catalyst should also be mechanically stable as any structural defects or breakdowns may result in partial or total blockage of the reformer. Furthermore, the catalyst should be shaped in a way that maximizes surface area for efficient catalytic activity while minimizing the pressure drop across the reformer.

In order to fulfill all of these requirements, catalysts are typically constructed from a ceramic support imbibed with catalytic material such as Pt, Pd, Rh, Ni, etc. Example fuel reformers investigated at RIT are shown in Figure 9. Typically, fuel reformers are formed in a cylindrical shape with one or more gas flow channels [109] or take the form of a monolith structure which looks similar to a honeycomb [110].

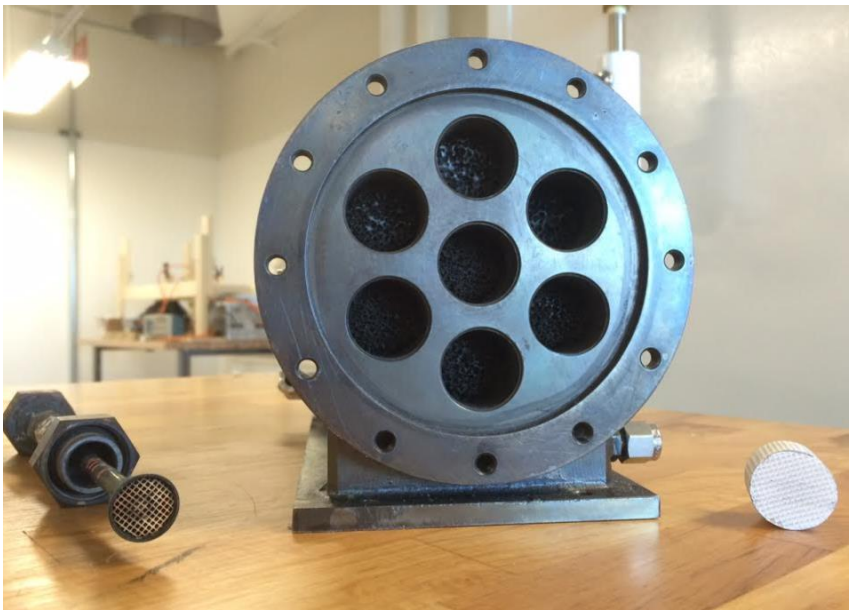

Figure 9: Left – Cylindrical fuel reformer using a monolith structure. Center – Multi-cylinder monolith-based fuel reformer developed for diesel reforming through a partnership with Delphi and RIT. Right – Microchannel ceramic support insert for constructing a catalytic fuel reformer.

Beyond the physical design of the catalyst structure and shape, efficient conversion and unwanted side reactions such as solid carbon formation (coking), can be controlled through several operating parameters. To achieve equilibrium conversion, maintaining specific air/fuel and steam/fuel ratios is essential, as operating marginally above or below certain ratio can considerably alter the effluent composition.

For all reaction types, primary catalyst degradation modes include metal sintering, coke deposition, and sulfur contamination [111], [112], [113]. Metal sintering of the catalyst occurs when the fuel reformer is operated at excessive temperatures. This may result from internal hot spots forming or a malfunction in the air/fuel ratio that causes an excessive spike in temperature. Solid carbon formation, or coking, results when carbon atoms from the fuel are not oxidized to form CO and/or $CO_2$. Coking typically occurs under fuel rich conditions and at low temperatures [114], and poses a significant threat to the catalyst's durability. Generated solid carbon may plug

the reactor, leading to hot spots and non-uniform fuel reforming, as well as reduce catalytic activity by permanently adhering to the catalyst, thereby reducing its overall active area. It has been shown that operating under fuel rich conditions in a cPOx system leads to coking for heavy hydrocarbons [115]. Specifically for propane cPOx, coking has been observed when operating at temperatures below 800$^{o}$C [114].

## 4.5 Micro-reforming Technologies

Simple fuel reforming can be understood using only a few governing Equations; however, the most efficient systems are a complex combination of mechanical design, heat transfer, and catalysis. While very efficient reformation processes have been developed at large scales, scaling down the reformer for small-scale applications creates significant challenges due to the requirement for quick startup and transient response, a small operating volume, and high efficiencies.

The Short Contact Time (SCT) reactor design is an approach that allows for high volumes of fluid flow such that the residence time of the gas mixture inside the catalyst bed is on the order of milliseconds [116]. These SCT reactors provide several advantages over traditional packed bed or monolith bed designs because of their high geometric surface area (GSA) per unit volume of the reactor, and their high specific surface area of the catalyst support/washcoat. Additionally, near theoretical equilibrium reactions for partial oxidation experiments have been observed using these reactor designs, which results in high selectivity of the desired product as well as high reformer efficiencies [117]. The fuel reforming phase of this program was focused on assessing the performance of a propane cPOx SCT Microlith® catalyst from Precision Combustion Inc. (PCI) under propane cPOx conditions, so that its compatibility with a HT-PEM fuel cell could be assessed. The results are described in Chapter 5.

# 5 Propane Catalytic Partial Oxidation

Of the various fuel reforming reactions, propane partial oxidation requires only fuel and air to operate, and therefore seems to be best suited for integration with a fuel cell device because of its simplicity. When designing a practical device, eliminating the need for complex water management systems that would be required in a SR or ATR system, greatly reduces the BoP equipment necessary for an integrated reformer fuel cell device. This reduces the overall weight and complexity of a final system design for a portable fuel cell device. In this section, the experimental results for testing a catalytic reactor provide by Precision Combustion Inc. (PCI) are reported.

## 5.1 Literature Review of Propane Fuel Reforming

While propane fuel reforming has not been as widely studied as natural gas fuel reforming, there exists a small amount of published literature, particularly for propane SR and ATR reactions. Modafferi et al. reported reforming of propane tests under SR and ATR conditions using a Ni-Ru/GDC (Ceria-gadolinia) catalyst (weight ratio, 5:5:90), prepared using the hydrothermal method [118]. For ATR tests, reactions were carried out in a temperature range between 600-800$^{o}$C, with a steam to carbon ratio (S/C) of 2.5, an oxygen to carbon ratio (O/C) of 0.5, and a space velocity of 1,000,000 hr$^{-1}$. Propane conversion ranged from 70% to 100% from 600 to 800$^{o}$C. At reaction temperatures higher than 700$^{o}$C, high propane conversion and syngas production were obtained. Maximum hydrogen and syngas yields of 59% and 79%, respectively, occurred at 800$^{o}$C. They also found that coke formation was indistinguishable across the temperature range tested. The results from this group's research suggests that oxygen plays a decisive role in promoting catalyst activity and stability during SR since the catalyst deactivates

at increasing rates as the temperature decreases. However, under ATR conditions, the catalyst exhibits good stability across all temperatures.

Corbo et al. focused on partial oxidation (POx) reforming of propane, as the reaction mechanization is simpler in part due to the need for only fuel and air as inputs to the reactor [108]. This study examined nickel and platinum-based catalysts achieving hydrogen yields of 88% and 58%, respectively. Overall, their group found that nickel-based catalysts performed better than platinum in both conversion and selectivity, but also resulted in higher carbon production. They recommend further investigation into bimetallic Ni-Pt catalysts. The primary catalyst studied in this dissertation is a proprietary design that is made from Pt-group metals, provided by Precision Combustion Incorporated (PCI).

## 5.2 PCI Microlith® Technology

The reformer used in the experiments reported in in this chapter was provided by Precision Combustion Inc. (PCI), and is based on their patented Microlith® technology [119]. The Microlith substrate consists of a series of catalytically coated metal meshes with very small channel diameters, allowing for ultra-short-channel-length. As compared to other SCT substrates such as ceramic monoliths and foams, the Microlith reactor provides a higher rate of reaction, lower thermal mass, and significantly higher heat and mass transfer coefficients [120]. The Microlith substrate performs favorably because of its high GSA per unit volume of the reactor, and high specific surface area of the catalyst support/washcoat [117]. Additionally, the low thermal mass of the Microlith elements allows for rapid start-up and transition to steady operating temperatures. Using a lumped sum capacitance model, a 30-fold increase in thermal response time was determined when comparing a Microlith reactor to a ceramic monolith substrate [121]. Furthermore, near theoretical equilibrium reactions for partial oxidation

experiments have been observed using these reactor designs, which results in high selectivity of the desired product as well as high reformer efficiencies [117].

Fuel reforming research using Microlith based catalysts has focused on fuels including gasoline [116], methane [122], methanol [123], JP-8, and diesel [124], but little research on propane reforming with a Microlith catalyst can be found in literature. The aim of this chapter is to discuss the reforming performance of a 31.75 mm diameter Inconel single tube reactor for propane cPOx, and to examine various operating points. Previous collaborative work with PCI has yielded impressive results using their Microlith catalysts that were developed for syngas production [120]. The operating envelope for this reformer is described in terms of temperature range, and the diatomic oxygen (from air)-to-carbon ratio ($O_2$/C). The catalytic performance is evaluated in terms of $H_2$ and CO yield, conversion efficiency, and solid carbon formation. Additionally, the optimal operating point that maximizes fuel conversion efficiency, and minimizes carbon formation is described. Thermodynamic modeling of propane cPOx was conducted using the Gibbs free energy minimization method with AspenOne® Engineering software, to complement the experimental data. All experimental testing was performed at an existing fuel cell and bio-fuel research facility at RIT's Golisano Institute for Sustainability (GIS).

## 5.3 Thermodynamic Modeling

In order to simulate the propane cPOx reaction, aspenOne® Engineering modeling software was employed. AspenOne Engineering is a comprehensive chemical process modeling software and is widely used in the petrochemical industry for refining simulation and optimization [125]. The propane cPOx model simulation was developed using Aspen HYSYS V8.4 of the aspenOne Engineering package, and primarily utilized the Gibbs reactor unit operation block. The Soave-

Redlich-Kwong (SRK) Eq. of state was the global property model used. In order to simulate the effects of temperature and input $O_2$/C ratio on propane cPOx, a case study was developed that varied the reformer temperature and $O_2$/C ratio with a propane fuel flow of 1 kmol/s. Previous investigations of propane reforming generally operate catalysts between 400 and 800$^o$C [108], [118], [126]. For the simulated case study, the reformer temperature was varied from 400 – 1000$^o$C with a step size of 10$^o$C.

The underlying science used in the Aspen software is based on the Gibbs free energy minimization method, subject to a mass balance. The Gibbs free energy minimization method has been widely used to simulate hydrocarbon catalytic reformation because this approach allows equilibrium products to be determined without knowing the catalyst performance, specific reactions involved, or the reaction kinetics [113], [127], [128], [129]. This greatly reduces the complexity of modeling propane cPOx as there are dozens of elementary reactions involved [113]. The total Gibbs free energy can be expressed as:

$$G = \sum_{i=1}^{N} n_i (G_i^o + RTln\phi_i y_i P) \qquad \textit{(Eq. 22)}$$

where $n_i$ is the number of moles of species $i$, $G_i^o$ is the Gibbs free energy of species $i$ at standard temperature and pressure, $R$ is the universal gas constant, $T$ is the temperature of reaction, $\phi_i$ is the fugacity coefficient of species $i$, $y_i$ is the mole fraction of species $i$, and $P$ is the total pressure of the system. When using the Gibbs free energy minimization method, the reaction is also subjected to a molar balance constraint:

$$\sum_{i=1}^{M} n_i a_{ik} = A_k \qquad \textit{(Eq. 23)}$$

where $a_{ik}$ is the number of gram atoms of element $k$ in species $i$, $A_k$ is the total number of gram atoms of element $k$ present in the reaction effluent. For the propane cPOx simulation, the following assumptions were made:

1) Uniform temperature distribution within the reformer.
2) The reformate gas mixture behaves as an ideal gas and pressure gradients were ignored within the reactor.
3) Inlet propane and air were well mixed and the reaction reaches thermodynamic equilibrium. The considered reformate species in this analysis were $H_2$, CO, $O_2$, $H_2O$, $CH_4$, $C_2H_4$, $C_2H_6$, $CO_2$, $C_3H_8$, C (solid graphite), and $N_2$.
4) The Gibbs reactor unit operates adiabatically.
5) The major modeling independent parameters were reformer temperature and $O_2$/C ratio. The effect of GHSV was not considered for this model.

The stoichiometric equilibrium for propane cPOx occurs at an $O_2$/C ratio of 0.5 as can be seen below.

$$C_3H_8 + 1.5O_2 \rightarrow 4H_2 + 3CO,\ \Delta H_{298°C} = -229\ \text{kJ/mol}\ \ [35] \qquad \textit{(Eq. 24 )}$$

Thus the simulated reaction was designed to vary the $O_2$/C ratio from 0.3 to 1.2 by changing the oxygen inlet flow from 1 to 3.5 kmole/s with a step size of 0.1. Results are plotted herein from this analysis using Matlab®, including the effluent composition and reformer efficiency as a function of temperature and $O_2$/C ratio.

The reformer efficiency was calculated based on the following Equation:

$$\eta_{ref} = \frac{\dot{x}_{H_2} * LHV_{H_2} + \dot{x}_{CO} * LHV_{CO}}{\dot{x}_{C_3H_8} * LHV_{C_3H_8}} \qquad \textit{(Eq. 25)}$$

where $\dot{x}$ represents the flow rate of the various gases in g/s, and $LHV$ represents the lower heating values that are 120.1 kJ/g, 10.1 kJ/g, and 46.4 kJ/g for hydrogen, carbon monoxide, and propane respectively [35]. From the results of this simulation, the optimal operating conditions

that maximize efficiency and minimize carbon formation are proposed and compared to experimental results.

## 5.4 Propane cPOx Experimental Methods and Materials

Figure 10 illustrates a schematic and the actual setup for the propane cPOx experiments. All tests were performed on a 31.75 mm diameter Inconel reactor tube containing PCI's Microlith based catalyst. The reformer was constructed and delivered to RIT by PCI with a single thermocouple installed directly on to the catalyst. The catalyst itself takes up only a small portion in the center of the reactor tube, and is 8.9 mm in length. The reformer was entirely encased within an electric tube furnace and was heated to obtain the desired catalyst temperatures for light-off. Once the light-off temperature was reached, upstream propane and air were sent through the reactor. Influent gas flows were controlled using Alicat mass flow controllers specifically calibrated to control propane and air flows within $\pm$ 1%. The propane used for these tests was industrial grade supplied by Airgas with a sulfur content of < 15 $ppm_v$. The effluent gas species were measured using a mass spectrometer (Applied Instrument Technologies, CA, USA), gas chromatograph (Model 490 Micro GC, Agilent Technologies, Santa Clara, CA) that were calibrated to quantify the species $H_2$, CO, $O_2$, $H_2O$, $CH_4$, $C_2H_4$, $C_2H_6$, $CO_2$, C, and $N_2$. Additionally, an AVL micro-soot meter (Model No. 483, AVL List GmbH, Graz, Austria) was used to measure the solid carbon formation of the reformate stream. This instrument utilizes the photo-acoustic effect to obtain accurate carbon concentration measurements as low as 5 $\mu g/m^3$.

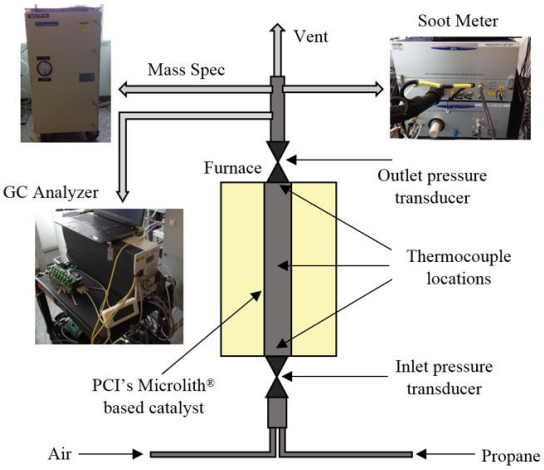


Figure 10: Left fuel reformer facility with associated instrumentation, right: propane cPOx test cell schematic containing Inconel single tube reactor based on Microlith (catalytically coated meshes) catalyst technology (31.75 mm diameter, 8.9 mm length).

The input and effluent compositions were all recorded using a reforming analysis program written in LabView. Each test point was run for a minimum of 20 minutes where the average values over this time period recorded.

The test apparatus employed the reformer in a vertical orientation with the propane and air introduced from the bottom. The inlet streams were not pre-heated and they were mixed with a custom manufactured tee manifold. The manifold was insulated up to the furnace and thermocouples measured the temperature of the inlet stream. Thermocouples were also installed upstream, internal to, and downstream of the catalyst. The catalyst thermocouple was installed by PCI, and was placed within the catalyst bed. Inlet and reformer differential pressure transducers were integrated into the stand design.

A multi-parameter experimental matrix including $O_2$/C, catalyst temperature, and gas hourly space velocity was developed for the propane cPOx reformation experiments. The propane flow rate used for all the experiments (0.02 g/s) was based on the estimated flow required to produce 500 W of power after reformer and fuel cell efficiency losses. Except for the light-off

temperature determination tests, the general method for reforming experiments was to preheat the catalyst up to a minimum of 10°C above the known light off temperature, whereupon propane was then allowed to flow. Air was then sent through the reformer and adjusted until the desired $O_2$/C was obtained. It can be noted that once propane and air were sent through the catalyst, the catalyst temperature would spike to the 700-800°C range in a matter of seconds. Based on the stoichiometric equilibrium, *Eq. 24*, an $O_2$/C ratio of greater than 0.5 was used for all experiments. The space velocity was determined using the void volume of the catalyst and the flow of the reactants at standard temperature and pressure. The gas hourly space velocity (GHSV) was controlled through a range of 1242 $hr^{-1}$ to 921 $hr^{-1}$.

The initial tests explored the temperature boundaries of the reformer including the light-off temperature and the auto-ignition temperature. The remainder of test points were conducted at operating conditions that would not cause irreversible catalyst degradation by maintaining the catalyst temperatures below 1000$^o$C. The majority of test points were taken by first sending the proper amount of air flow as determined by the $O_2$/C ratio, then the tube furnace set point temperature was adjusted until the desired catalyst temperature was reached. For each $O_2$/C ratio, the catalyst temperature was increased from 800°C to 1000$^o$C with a step size of 20$^o$C. Data was collected at each test point for a minimum of 20 minutes. For reporting, the average value over the 20 minute period was used. The reformer efficiency was calculated based on *Eq. 25*.

## 5.5 Propane cPOx Thermodynamic Simulation Results

From *Eq. 24*, it can be seen that complete propane conversion cannot occur below an $O_2$/C ratio of 0.5. However, increasing the $O_2$/C ratio beyond 0.5 may lead to increased amounts of undesired by-products such as $CO_2$ and $H_2O$ in the effluent gas. To develop an operating test matrix, a Gibbs free energy analysis was conducted using aspenOne Engineering software by

estimating the effluent gas composition that results from propane cPOx under equilibrium conditions. Figure 11 displays the effluent compositions from this analysis for $H_2$, CO, $CH_4$, $CO_2$, C, and the efficiency of the reaction. We assumed a uniform equilibrium temperature along the reactor for the analysis which may not be likely in reality. However, because experimental catalyst temperature data were measured from a thermocouple placed directly on the Microlith catalyst, we expect the equilibrium temperature used in the Gibbs analysis to correspond well to experimental methods. The $H_2$ yield, CO yield, and efficiency plots all follow similar trends where the maximum production points occur at $O_2/C = 0.53$, and a temperature of $1000^oC$. Conversely, the unwanted products such as $CH_4$ and $CO_2$ have high production rates at high $O_2/C$ ratios and temperatures around $700^oC$. For $O_2/C$ ratios below 0.53, hydrogen production decreases rapidly regardless of temperature however at ratios above 0.53, the $H_2$ production does not drop off as quickly. The CO and efficiency plots follow similar trends. The carbon free region occurs at temperatures above $650^oC$ with $O_2/C$ ratios of less than 0.6.

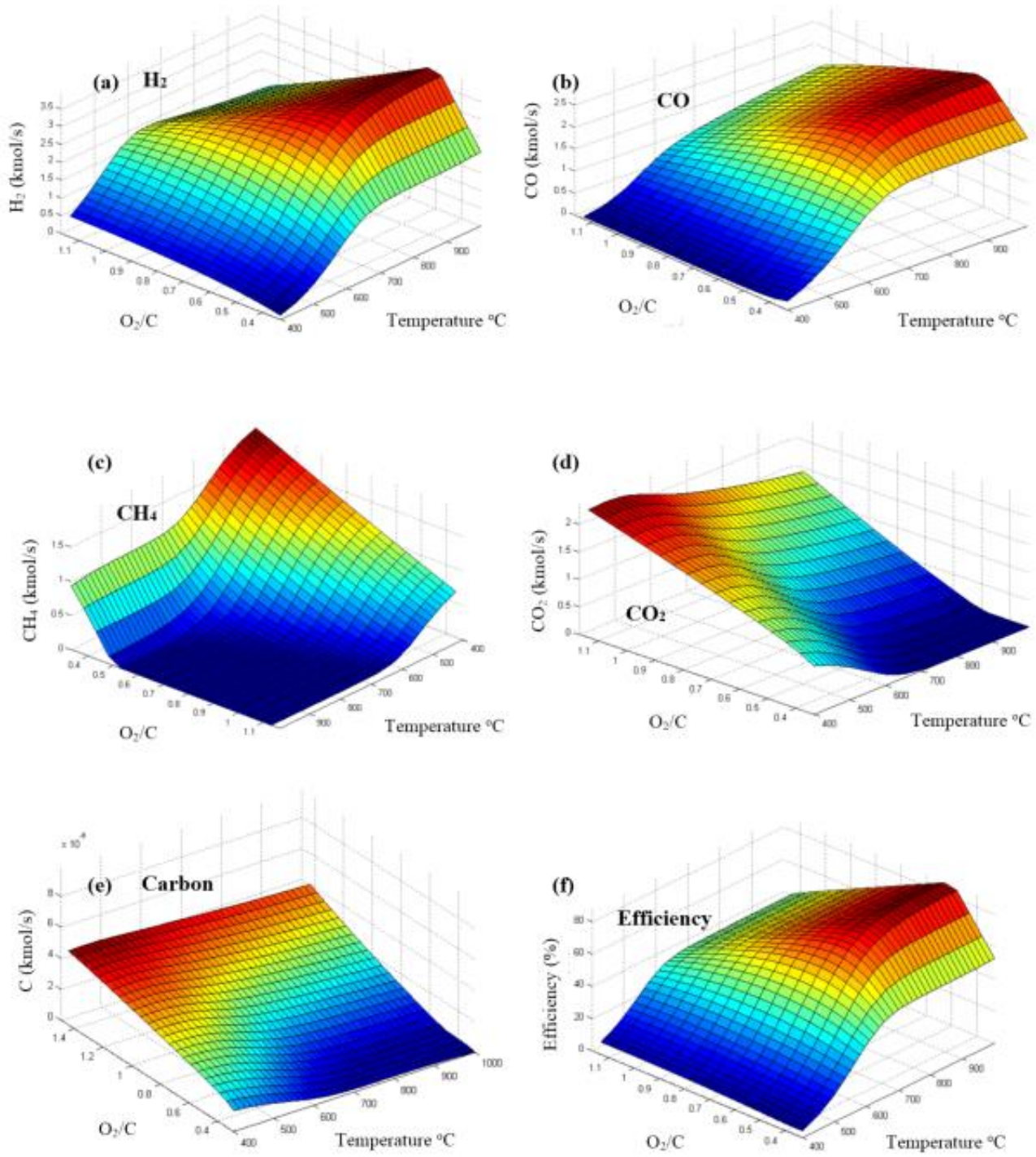


Figure 11: Equilibrium analysis of propane cPOx effluent composition yield and reformer efficiency as a function of $O_2/C$ and catalyst temperature. (Note: scale orientations were reversed in Figure 11c to enable adequate observation of surface plots).

Figure 12 shows the expected specific compositions of effluent gases at an $O_2$/C ratio of 0.53 as a function of temperature. Once the reaction reaches a temperature of approximately 800°C, increasing the temperature further does not have much of an impact on the reaction efficiency and effluent gas composition. Additionally, at above 850°C, essentially no $CH_4$, $C_2H_4$, $C_2H_6$, and $CO_2$ are produced in this reaction and the effluent gas is composed almost entirely of $H_2$, CO, and inert $N_2$.

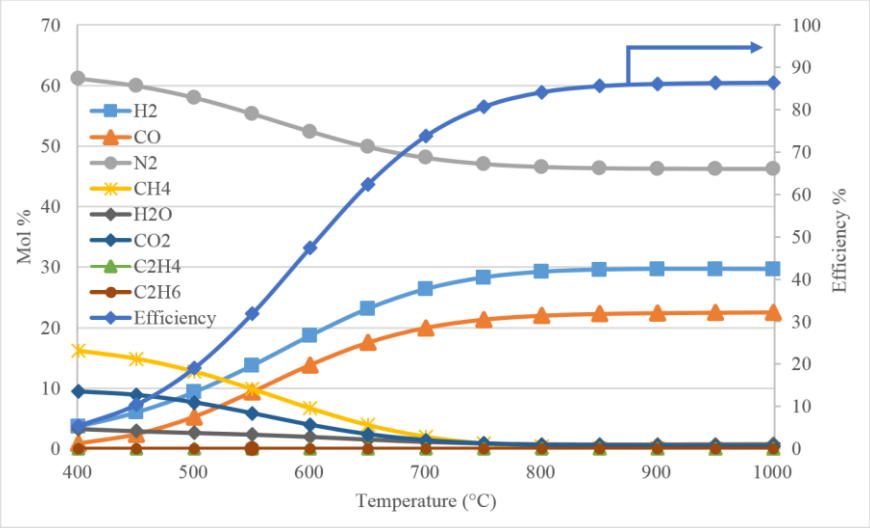


Figure 12: Anticipated effluent gas composition as a function of temperature at $O_2$/C = 0.53

Similarly when considering solid carbon formation shown in Figure 11e, while operating the reaction under equilibrium conditions and at temperatures above 750°C, there is little to no coke formation expected. Solid carbon formation is most likely caused by the Boudouard reaction [130], which is the disproportionation of CO into $CO_2$ and solid carbon as seen in the Eq. below.

$$2CO \rightleftharpoons CO_2 + C \qquad \textit{(Eq. 26)}$$

At high temperatures, the reverse Boudouard reaction is favored, converting $CO_2$ and C into CO while at low temperatures, CO is disproportioned into $CO_2$ and C. The effects of this on the

reformate constituents can be seen in both the carbon dioxide and solid carbon figures (Figure 11d and Figure 11e). As the temperature of the reaction increases, both carbon dioxide and solid carbon formation decrease. Thus to mitigate coke formation, the reaction must be run at a sufficiently high temperature. From Figure 11e, it appears that operating temperatures above 750$^{o}$C are sufficient to limit solid carbon formation.

Based on the thermodynamic simulation, it is anticipated that the optimal operating point for the reformer should lie between 800 and 1000$^{o}$C with an $O_2/C \approx 0.53$. The theoretical maximum efficiency of the reformer under equilibrium conditions can be calculated using *Eq. 25* and is approximately 89% as the effluent gases are composed almost entirely of $H_2$ and CO with the inert $N_2$. Under these conditions, it is anticipated that little to no coke formation will occur. Several experiments within this temperature range and approximate $O_2/C$ ratio were conducted to validate these results, and are discussed in the following sections.

## 5.6 Experimental Results

The results reported in this section describe the optimal operating conditions that maximize propane cPOx efficiency. These results are used to not only select the operating parameters for an integrated reformer fuel cell device, but also to develop proper startup/shutdown procedures for the fuel reformer.

### 5.5.1 Propane Auto-ignition Temperature

The Gibbs free energy analysis reveals that the optimal operating point for propane cPOx should lie within the temperature range of 800 – 1000$^{o}$C, with an $O_2/C$ of $\approx 0.53$. Experimental testing was conducted to corroborate the Gibbs energy analysis. Table 5 lists some of the primary test matrix points to assess the PCI reactor for propane cPOx reforming.

Table 5: Experimental Test Points

| Test Point | $O_2$ /C | Propane Flow (g/s) | Air Flow (g/s) | Temperature Range ($^oC$) | Temperature Step Size ($^oC$) |
|---|---|---|---|---|---|
| TP1 | 0.53 | 0.02 | 0.100 | 800 – 1000 | 20 |
| TP2 | 0.55 | 0.02 | 0.103 | 800 – 1000 | 20 |
| TP3 | 0.57 | 0.02 | 0.106 | 800 – 1000 | 20 |

There are two components of the reformer that require temperature control: the inlet fuel mixture and the reformer catalyst. The temperature of the fuel and air inlet mixture must be regulated because if the mixture becomes too hot, it will ignite before it reaches the catalyst bed. Thus, it is important to determine the auto-ignition temperature because premature ignition could have harmful impacts on the system and its users. One study described propane auto-ignition temperatures at around $577^oC$ [131]. A test run to determine the auto-ignition temperature of propane in the reformer was conducted by metering a small amount of propane while steadily increasing the furnace temperature, thus increasing temperature of the inlet gas to the reformer. The results in Figure 13 show the inlet temperature of the reformer, measuring the temperature of the fuel mixture right before it enters the catalyst. At approximately $557^oC$, the trumpet temperature began to increase rapidly, revealing the propane auto-ignition temperature had been reached.

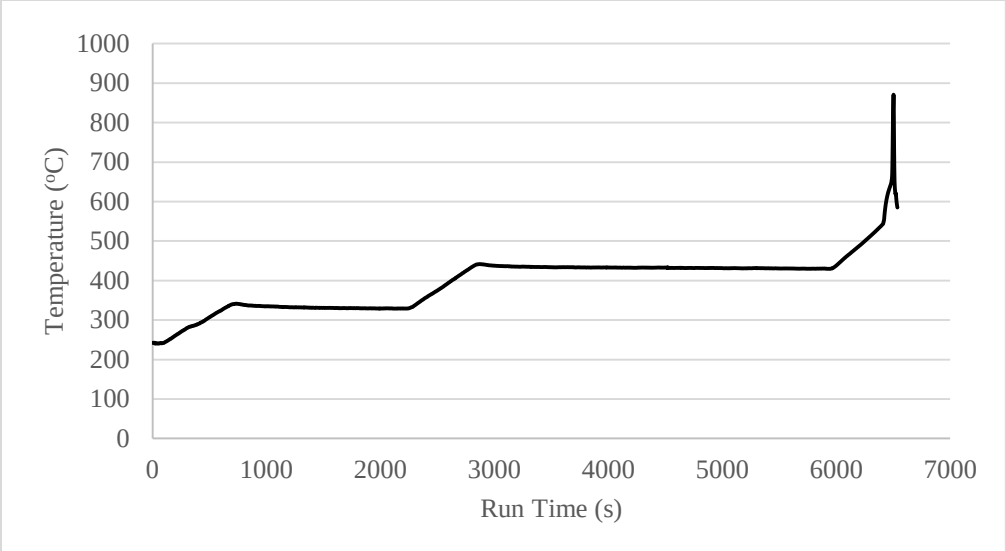


Figure 13: Inlet temperature of the reformer consisting of the Microlith based catalyst

### 5.5.2 Light-off Temperature

The light-off temperature for catalytic reactions is defined as the temperature at which cPOx first begins. This is additionally an important temperature to ascertain as it will define the minimum temperature that the reformer needs to be heated up to for propane cPOx to occur. This will allow for the required start-up time and protocol to be defined. Previous studies investigating propane reforming have found light-off temperatures ranging between 200 – 370$^{o}$C depending on the catalyst type [108], [132], [133]. The light-off temperature determination tests for this study were conducted by pre-heating the catalyst to around 300$^{o}$C, then metering the fuel-air mixture through the reformer. The furnace set point was then increased slowly to increase the catalyst temperature. Due to the exothermic nature of the cPOx reaction, the temperature of the catalyst increases rapidly once propane conversion begins indicating the light-off temperature. Using this procedure, the light-off temperature was determined to be approximately 360$^{o}$C.

### 5.5.3 Temperature Operating Limits and Coke Formation

The maximum operating temperature is limited by the propensity for metal sintering. In this research, the reformer temperature was kept below 1050°C in order to maintain the longevity of the catalyst. Tests where the catalyst was at a temperature below 1050°C were presumably safe, however, if the temperature drops too low, there is a risk of solid carbon formation and subsequent build-up inside the catalyst and/or downstream fuel cell, causing long-term degradation. Thus, the low operating temperature point is dictated by the point where significant carbon formation begins to occur, most likely due to the Boudouard reaction. From Figure 11e, the carbon free zone occurs at $O_2$/C ratios below 0.6 and temperatures above 750°C. At an $O_2$/C = 0.53 and using the AVL micro-soot meter, the amount of solid carbon was measured after taking samples of the effluent gas shown in Figure 14. From this experimental data, solid carbon formation shows an inverse relationship between carbon concentration in the effluent stream and catalyst.

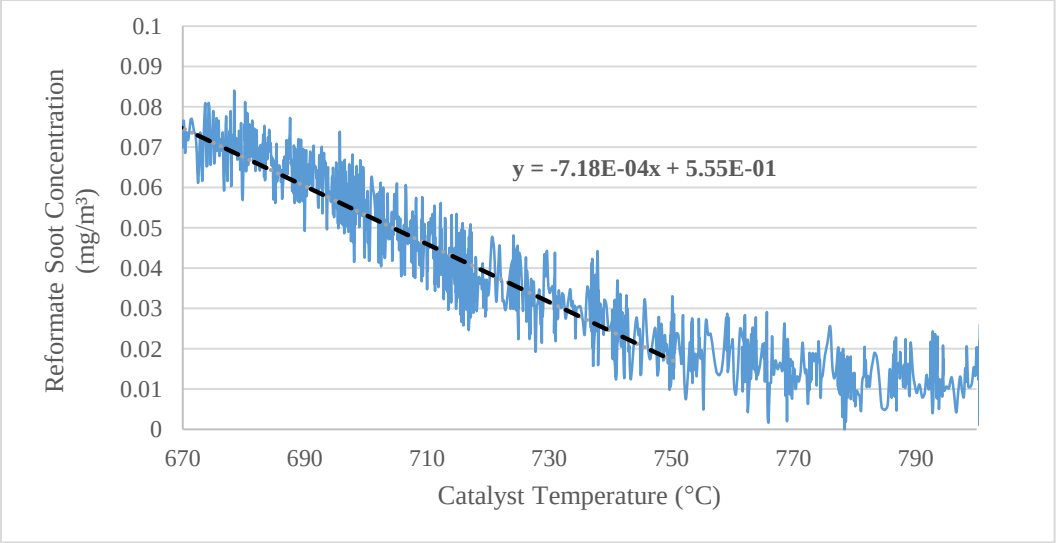


Figure 14: Experimental soot (solid carbon) formation from propane cPOx as a function of catalyst temperature operating with $O_2$/C = 0.53

According to the experimental data, coke formation is strongly correlated to catalyst temperature. Significant carbon formation began at approximately 750$^{o}$C, and steadily increased as the catalyst temperature was decreased. Above 800$^{o}$C, very little, if any, solid carbon was formed. To operate the reformer conservatively and to avoid known degradation modes, nearly all of the remaining tests were conducted with the catalyst operating within the temperature range of 800 – 1000$^{o}$C.

These results indicate that carbon substantial carbon formation is likely to only occur during the startup/shutdown of the reformer, when temperatures drop below 750$^{o}$C. Limiting the time that the reformer is held at these temperatures is the best mitigation strategy. One method might be to increase the air flow within the fuel reformer beyond an $O_2$/C ratio of 0.53, in order to heat up the reformer rapidly. Once a temperature greater than 750$^{o}$C is attained, the air flow could be reduced to an $O_2$/C ratio of 0.53. Additionally, it has been shown in literature that solid carbon oxidation can be used to regenerate the catalyst [134], [135]. This regeneration protocol can be run during shutdown by simply flowing air through the reformer without fuel for a short period of time.

### 5.5.4 Effects of Temperature an $O_2$/C Ratio

From the thermodynamic simulation, the most efficient operating point for propane cPOx exists within the temperature range of 800 – 1000$^{o}$C, and an $O_2$/C ratio from 0.5 – 0.6. The main method for running the experiments was to set the $O_2$/C ratio and step through the temperature range by increasing the furnace set point and thus increasing the effective catalyst temperature. Due to safety concerns, test points for catalyst temperatures around 1000$^{o}$C could not be obtained because the trumpet temperature of the test stand approached the propane auto-ignition

temperature of 560°C. However, based on the Gibbs free energy analysis, we anticipate little increase in efficiency with catalyst temperatures above 950°C.

The GHSV was held within the range of 1242 $hr^{-1}$ to 921 $hr^{-1}$. Overall, minor deviations in the GHSV had little impact on reactor performance. Figure 15 and Figure 16 show the results of two tests performed at $O_2$/C ratios of 0.53 and 0.57. Identifying the effect of a wide range of GHSV on the catalyst performance was beyond the scope of this effort.

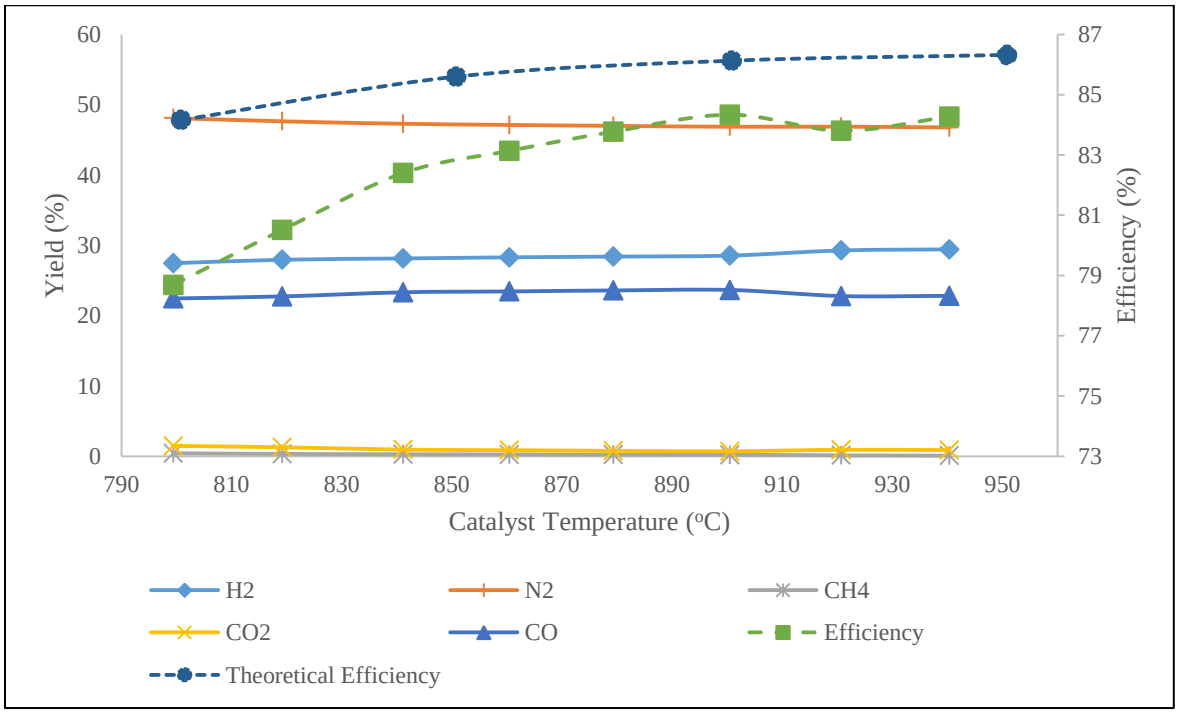


Figure 15: Propane cPOx yield and reformer efficiency at $O_2$/C = 0.53.

The results shown in Figure 15 display the most promising outcomes from our tests, indicating that a reformer efficiency, based on *Eq. 25*, of 84% was achieved while operating the catalyst at a temperature of 940°C with $O_2$/C of 0.53. The efficiency at this point is 94% of the theoretical limit results obtained from our thermodynamic analysis. While the maximum

efficiency is obtained at temperatures approaching 1000°C, temperatures down to 800°C had little negative impact on hydrogen yield.

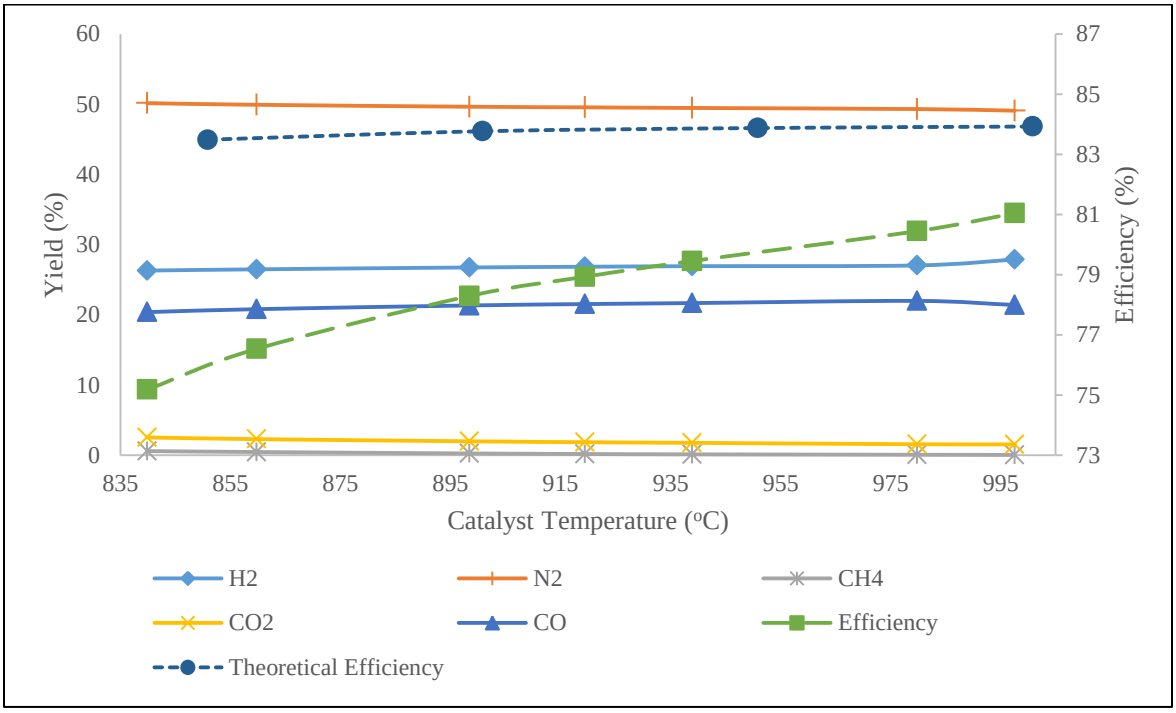


Figure 16: Propane cPOx yield and reformer efficiency at $O_2/C = 0.57$.

Figure 16 shows the results of testing at an $O_2/C$ of 0.57 where an efficiency of 81% was achieved, revealing some flexibility in the air to fuel ratio. The tabulated data for both of these tests can be found in Table 5. It is worth noting that the maximum performance was observed during the latter part of the 130 hours of recorded test time. Additionally, we cycled the reactor at least 80 times during these tests, which to some degree can be viewed as simulated start/stop cycles. Startup times for the reformer have not yet been explicitly tested and optimized; however, it is anticipated that once the reformer reaches its light-off temperature, the catalyst can reach the optimal operating temperature in less than 30 seconds as this occurred several times during testing.

Table 6: Experimental propane cPOx data.

| $O_2$/C | Catalyst Temperature ($^o$C) | Reformer Input (g/s) | | Reformer Yield (mol %) | | | | | | | |
|---|---|---|---|---|---|---|---|---|---|---|---|
| | | Air | Propane | H2 | CO | N2 | CH4 | CO2 | C2H4 + C2H6 | C3H8 | Net Syngas ($H_2$ + CO) |
| 0.53 | 841 | 0.100 | 0.020 | 28.10 | 23.32 | 47.30 | 0.28 | 0.94 | 0.041 | 0.00 | 51.42 |
| 0.53 | 879 | 0.100 | 0.020 | 28.40 | 23.58 | 47.00 | 0.07 | 0.76 | 0.029 | 0.00 | 51.98 |
| **0.53** | **940** | **0.100** | **0.020** | **29.43** | **22.82** | **46.78** | **0.07** | **0.87** | **0.030** | **0.00** | **52.25** |
| 0.57 | 840 | 0.106 | 0.020 | 26.30 | 20.39 | 50.14 | 0.59 | 2.54 | 0.032 | 0.004 | 46.69 |
| 0.57 | 920 | 0.106 | 0.020 | 26.85 | 21.54 | 49.55 | 0.18 | 1.86 | 0.027 | 0.00 | 48.38 |
| 0.57 | 998 | 0.106 | 0.020 | 27.89 | 21.40 | 49.08 | 0.05 | 1.55 | 0.032 | 0.00 | 49.29 |

In a real-world application, control of the temperature of the catalyst may not be as simple as in these experiments. As more air is added to the reactor, the generated heat from the reaction increases, thus driving up the catalyst temperature. However, additional air into the reactor further reduces the amount of $H_2$ generated from the reaction, and therefore the $O_2$/C ratio must be kept at the optimal point (0.53) for maximum performance. Careful flow regulation is necessary therefore to optimize performance. To determine the relationship between $O_2$/C and the catalyst temperature at the optimal $O_2$/C ratio of 0.53, several tests were conducted to measure the catalyst temperature without aid of the furnace. This was completed by simply opening the furnace door and removing the insulation surrounding the reformer once partial oxidation began. After the furnace had cooled to below 100$^o$C, the catalyst temperature would settle around 820$^o$C. This result revealed that for optimal operation of a real system, additional insulation or additional heat from some source (possibly external combustion of propane) for the reactor is desired. However, even at an operating temperature of 820$^o$C, the hydrogen molar yield was approximately 28.0% as compared to 29.4% at a temperature of 940$^o$C, indicating some temperature flexibility in the operating protocol.

## 5.6 Implications for System Integration

Based on the reforming experiments performed and reported here, propane is an attractive primary fuel for small scale fuel cell systems due to ease of reforming, transportability, familiarity, and high energy density. Of the various fuel reforming reactions, partial oxidation is advantageous for a small scale system because the only reactants are fuel and air, thus greatly simplifying the system design. In summary, the propane cPOx simulated results suggested that the most efficient operating point for maximizing hydrogen yield and reformer efficiency exists at catalyst temperatures between 800 – 1000$^{o}$C and an $O_2$/C ratio from 0.5 to 0.6. Within this range, it is anticipated that little to no coke formation will occur. Experimental tests revealed a maximum 84% reforming energy efficiency at a temperature of 940$^{o}$C and $O_2$/C = 0.53. Little to no solid carbon formation occurred at this operating point however, significant carbon formation was observed at catalyst temperatures below 750$^{o}$C. The light-off temperature for this reformer was found to be approximately 360$^{o}$C.

Integrating the reformer with a fuel cell is not a trivial task and there are several challenges such as thermal management, system startup, and minimization of parasitic losses. Probably the greatest challenge with this reformer system is maintaining the air flow at a precise flow rate as both an increase and decrease in air flow can have harmful effects. If the air flow were to decrease, the temperature of the reformer would drop and the chance for coking would increase. If the air flow were to increase, the temperature of the fuel reformer may spike to dangerous levels, and the concentration of hydrogen leaving the reformer would decrease. Lower concentrations of $H_2$ in the anode of the fuel cell would reduce its power output. It is important to note that there is flexibility in the air/fuel ratio ($\pm$ 0.02) and temperature operation ($\pm$ 50$^{o}$C) beyond the optimal operating conditions. Within these operational windows, effluent gas

concentrations of only ± 3% off of the optimal concentrations were observed, indicating stability over a range of operating conditions. This is an important finding when designing a practical device, as perturbations during operation that affect the air/fuel ratio and operating temperature will likely occur.

Although not specifically evaluated, the startup protocol for the fuel reformer in a final device could begin with electrically heating the catalyst up to its light-off temperature (360$^{o}$C) either by heating the entire reformer housing, or by sending current directly through the catalyst itself, assuming the catalyst support material is made of a conductive material. Then, the cPOx reaction could be initiated by sending propane and air through the fuel reformer. The $O_2$/C ratio could be slightly higher than 0.53, say 0.57, to heat the reactor up quickly. As the catalyst temperature approaches ~800$^{o}$C, then the $O_2$/C ratio could be lowered back down 0.53. This would minimize coke formation during startup because of the shorter operating times at temperatures within the solid carbon formation region. Additionally, because of the additional oxygen at high $O_2$/C ratios, any solid carbon formed has a greater chance to be oxidized. Shutdown of the reforming could simply occur by turning off the propane flow but continue to flow air through the reformer. The reformer itself will quickly cool as fresh air is brought into it. Sending air through the reformer during shut down will additionally serve as a regenerative cycle for any coke that was deposited on the reformer itself.

Using the results from these propane cPOx experiments, single cell HT-PEM tests were conducted to assess the performance of a HT-PEM fuel cell under various conditions, while operating with the anode feed gas composition highlighted in Table 6, and are discussed in the next section.

# 6 HT-PEMFC Experimentation

This Chapter reports the results from operating a HT-PEM fuel cell under varying operational protocols. In Section 6, the operational conditions studied included the inlet anode gas composition, anode/cathode or cell operating pressure, cell temperature, and the anode/cathode stoichiometric ratios. Each operating condition has unique implications at the system design level, where the various performance impacts from changes in each operating variable need to be understood so that a balance between proper operational protocols and BoP equipment can be developed.

There are many novel types of membranes used for HT-PEMFCs, such as those described in [136], [137], [138], and [139]; however, only a few have seen some commercial success. One of the commercially available membranes is based on a pyridine containing poly(ether sulfone) [140], [141], [42], also known as TPS®, and currently produced by Advent Technologies Inc. [47]. A large focus of researchers using TPS-based membrane electrode assembly (MEAs) has been on developing direct methanol fuel cells (DMFC) such as in [42] and [142]. While commercially available, there is, however, limited MEA performance data based on Advent's TPS technology in public literature.

The most widely studied HT-PEMFC membrane is the Celtec-P series developed by BASF based on acid-doped polybenzimidazole (PBI) [32], and it has seen some commercial success [46]. Other commercially available PBI-based MEAs can be purchased from Danish Power System [48], and was investigated in [143]. However, the performance of their MEAs is not quite as good when comparing their baseline polarization curves found on their website to those generated in published studies of Celtec series MEAs. Thus the Celtec MEAs were chosen for

use in our research as they represent the state-of-the-art in commercially available HT-PEM MEAs.

Numerous performance studies have been conducted using the Celtec series MEAs, investigating parameters such as temperature [144], [145], CO concentration [32], [51], [70], relative humidity [59], [146], and durability [147], [148], [149]. Most performance studies for PBI-based HT-PEMFCs have focused largely on cell performance when operating on pure $H_2$, or $H_2$ mixed with various amounts of CO, and at atmospheric pressure. However, if hydrogen is generated from an on-board fuel processor using catalytic partial oxidation (cPOx), steam reforming (SR), or autothermal reforming (ATR) processes, other gases may be produced that will enter into the anode of the fuel cell stack, such as $N_2$, $CO_2$, $H_2O$, $CH_4$, $C_2H_4$, and $C_2H_6$. For example, under optimal reforming operating conditions, propane cPOx will produce effluent gas composed of 28% $H_2$, 23% CO, and 49% $N_2$ [114].

Presently, very little data for HT-PEM fuel cells can be found while operating on high concentrations of $N_2$ in the anode, as well as under high pressures up to 200 kPa. If future integrated reformer HT-PEMFC systems are to be developed, the impact of $N_2$ dilution and operating pressure on the performance of HT-PEMFCs should be investigated. It is important to note that the effect of anode dilution is the focus of this Chapter rather than $CO_2$, another common fuel reforming effluent gas; this is for two reasons. The first is because some fuel reforming processes generate significant amounts of $N_2$ in the effluent, and very little if any $CO_2$, as described in the previous paragraph. The second is that several other publications that investigated the effect of $CO_2$ concentrations in the anode up to 25% versus $N_2$ concentrations at the same level, show that $N_2$ and $CO_2$ result in the same performance loss when operating at the temperatures investigated in this work [41]. Studies that described the performance loss from

$CO_2$ versus $N_2$ when operating at lower cell temperatures, such as 60$^oC$, did show that $CO_2$ has a greater negative impact than $N_2$ [150].

## 6.1 Effect of Temperature, Pressure, and Anode Dilution

In this section, the performance impact when varying the temperatures and cell operating pressures from 160 to 200$^oC$ and 101.3 to 200 kPa, respectively, for two commercially available MEAs, the Celtec P1100W and Advent's TPS MEAs, were studied and compared. Additionally, the effect of hydrogen dilution with nitrogen in the anode feed was examined with nitrogen concentrations up to 70%. Overall, the PBI MEA provided greater performance than the TPS for all tested conditions. Our results show that the performance loss due to high dilution levels can be wholly mitigated by an increase in operating temperature, pressure, or a combination of the two. For example, even at a dilution level containing 70% nitrogen, operating the cell at 200$^oC$ and at 200 kPa provides the same power output as running the cell at 160$^oC$ and atmospheric pressure. Each operating condition has unique implications at the system design level, where the various performance impacts from changes in each operating variable need to be understood so that a balance between proper operational protocols and BoP equipment can be developed. This data can be used to model the performance effect of high diluent concentrations in the anode gas feed when developing an integrated reformer-fuel cell system.

### 6.1.1 Experimental

All experiments were performed using a modified Hydrogenics fuel cell test stand. Several TPS and PBI-based MEAs were purchased from Advent Technologies with active cell areas of 45.2 $cm^2$ [47]. BASF has stopped manufacturing the Celtec series MEAs, but has licensed their technology to Advent Technologies, who manufactured the MEAs used in our experiments. The MEAs purchased were the Celtec P1100W and Advent's TPS series MEA, with a total precious

metal loading of 1.7 mg/cm$^2$ for the Celtec one, and 3 mg/cm$^2$ total precious metal loading for the TPS. The manufacturer did not provide the specific amount of precious metal loading on the anode/cathode, nor the catalyst composition. The MEAs were placed in a test cell supplied by Fuel Cell Technologies, shown in Figure 17, comprised of two graphite plates with flow channels cut in a quad serpentine pattern. The end plates contained heating rods in order to control the cell temperature through a computer-controlled relay.

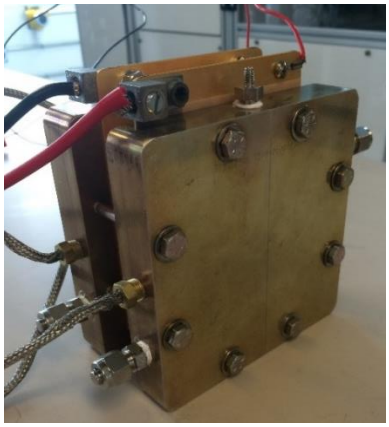

Figure 17: Picture of the actual test cell supplied by Fuel Cell Technologies

According to the manufacturer's specifications, a break-in period of 24 hours operating on pure hydrogen was completed for each cell, where power was drawn at a current density of 0.2 A/cm$^2$ at a temperature of 160$^o$C for the PBI, and 180$^o$C for the TPS. Figure 18 is a schematic representation of the test cell system. Gases $N_2$, $H_2$, and air were metered using Brooks mass flow controllers calibrated to control the desired gases. Cell back pressure was controlled using diaphragm regulators. The temperatures at the inlet and exit ports of the cell were maintained above 120$^o$C so water would not condense within the test cell, as liquid water formation is a well-known degradation phenomena [94]. Water generated in the cell was condensed and removed downstream of the exhaust, as shown in Figure 18.

A LabVIEW® control and data acquisition system was developed to automatically measure polarization curves and control gas flows. After the break-in, polarization curves were run from 0 – 1.5 A/cm$^2$ for the PBI MEAs, and 0 - 0.9 A/cm$^2$ for the TPS. All tests were run with a stoichiometric ratio of 1.5 at the anode, using either pure hydrogen or a specified mixture of $H_2$ and $N_2$, and a stoichiometric ratio of 2.0 at the cathode using air. Polarization curves were obtained by current step potentiometry and were measured beginning with the open circuit voltage. Because of the maximum flow rate capabilities of the hydrogen flow controller used, polarization curves with anode feeds containing 30% $H_2$ and 70% $N_2$ could only be measured up to 0.9 A/cm$^2$ while still maintaining a stoichiometric ratio of 1.5 at the anode.

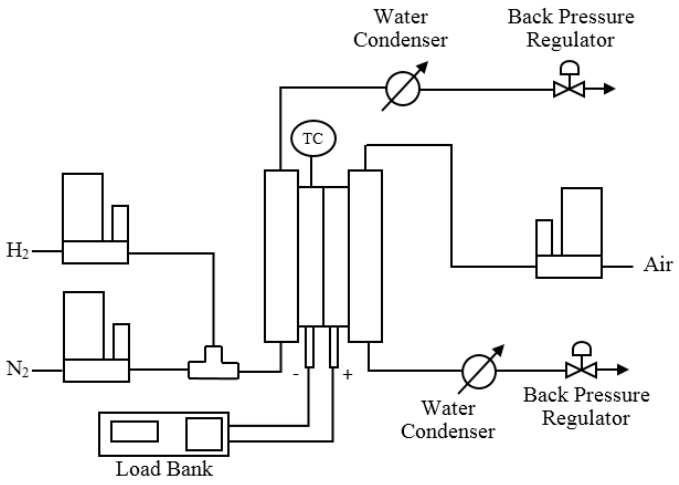


Figure 18: Schematic of the HT-PEMFC single cell test setup

All tests were performed on two MEAs for each cell type. For each different anode concentration, polarization curves were taken at three different temperatures, and three different pressures. The sequence for setting the test parameters was to first select the anode feed concentration, then the cell temperature, and finally cycle through the experimental pressures. The first polarization curve taken was run at an $H_2/N_2$ concentration of 100/0, a temperature of 160$^o$C, and at atmospheric pressure of 101.3 kPa. The last polarization curve was taken at an

$H_2/N_2$ concentration of 30/70, a temperature of 200°C, and at a pressure of 200 kPa. Including the 24 hour break-in procedure, the test protocol run on each cell required approximately 65 hours to complete.

### 6.1.2 Results and Discussion

Figure 19 compares several baseline polarization curves from our experiments with data generated by the manufacturers of the MEAs tested under similar operating conditions. The data obtained from our tests compares well with data from the manufacturers, indicating our experimental setup functions properly.

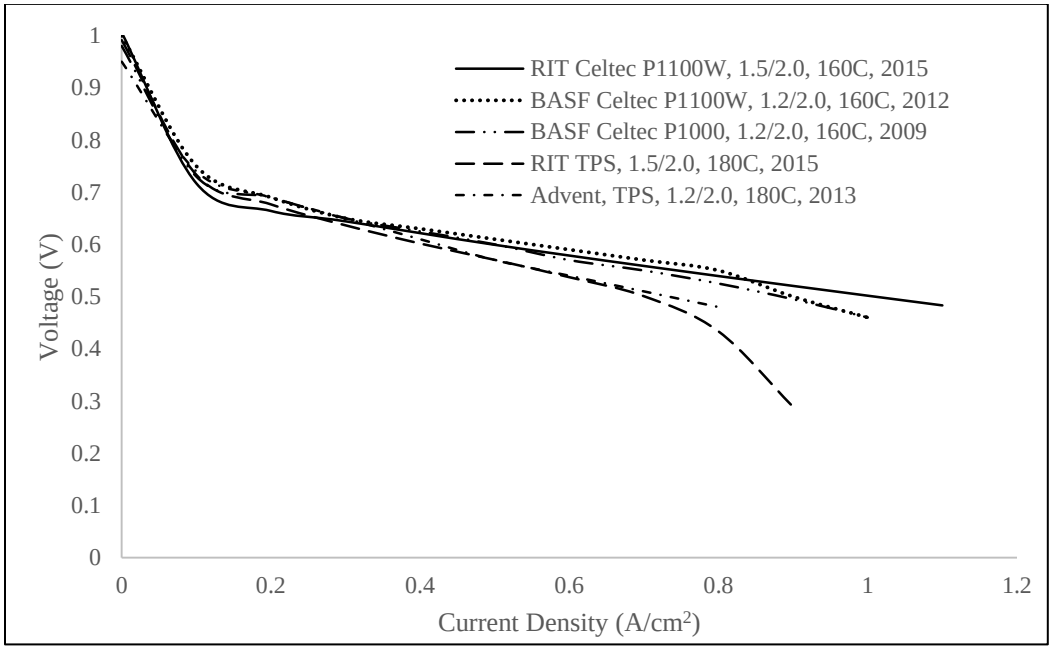


Figure 19: Performance of baseline RIT polarization curves of the tested MEAs as compared to data provided by the manufacturer. Each curve is labeled with the research organization and MEA type, the anode and cathode stoichiometric ratios, the operating temperature, and the publication year for the data source. The sources for each curve are as follows: this work, [45], [46], this work, [151].

Figure 20 displays the effects of temperature, pressure, and anode dilution for all tests run on the PBI type membrane. Increasing the temperature of the cell as well as operating pressure

resulted in improved voltage performance. The maximum power density of the lowest performing curve was 252 mW/cm$^2$ and was observed with 30/70 $H_2/N_2$ anode concentration mix, 160$^o$C, and 101.3 kPa. Conversely, the maximum power density of the highest performing curve of 754 mW/cm$^2$ was achieved with100/0 $H_2/N_2$ anode concentration mix, 200$^o$C, and 200 kPa. The maximum power densities of the lowest and highest performance curves are simultaneously the high and low boundary conditions for all experimental variables.

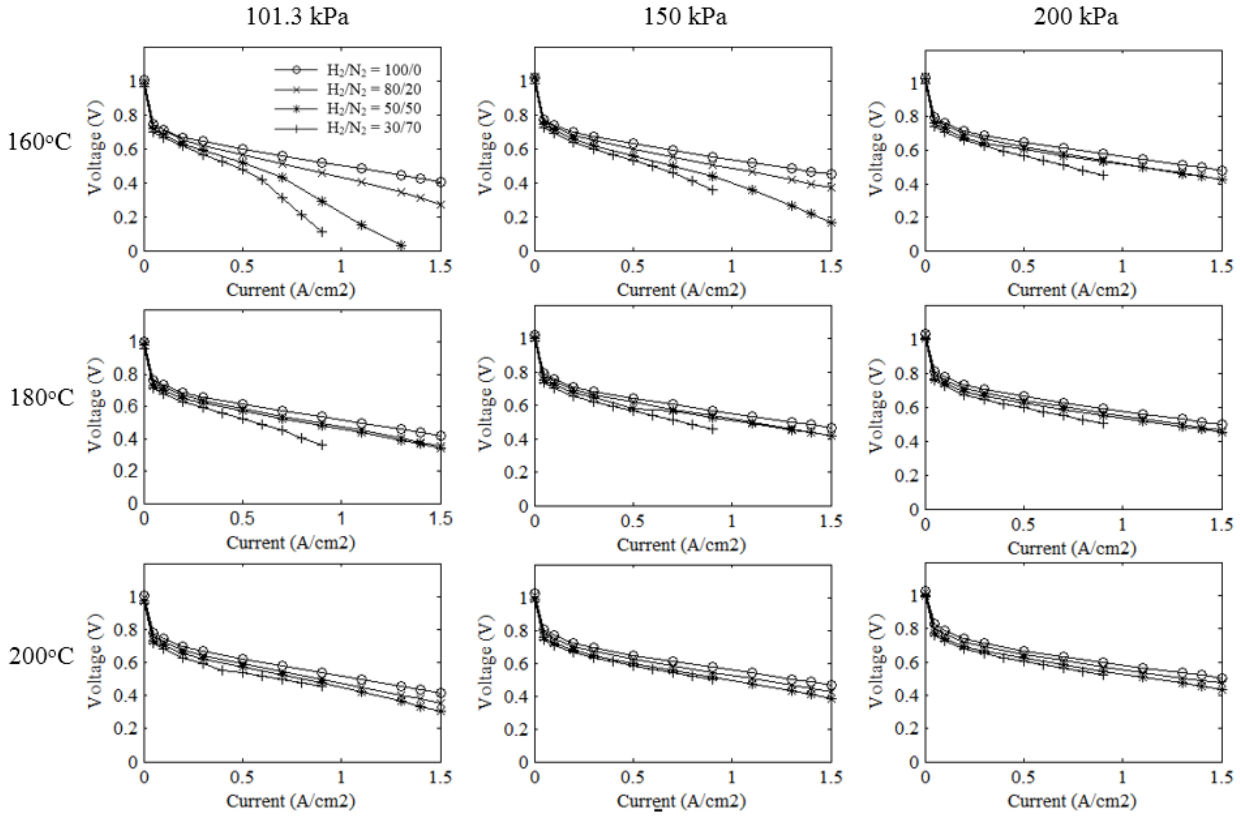


Figure 20: PBI MEA performance curves as a function of anode dilution, temperature, and pressure.

As can be seen in each sub figure of Figure 20, anode dilution has a significant impact on performance for the given test conditions, particularly at lower temperatures and pressures. This

can be interpreted when looking at the typical relationships used to model fuel cell polarization curves, which can be written as:

$$V_{cell} = E^0 + \frac{RT}{2F} ln\left(\frac{P_{H_2} P_{O_2}^{1/2}}{P_{H_2O}}\right) - \frac{RT}{2\alpha F} ln\left(\frac{i}{i_o}\right) - ir - m \exp(ni) \qquad \textit{(Eq. 27)}$$

The first two terms represents the Nernst voltage, where $E^0$ is the cell voltage at standard operating temperature and pressure, $R$ is the universal gas constant, $F$ is Faraday's number, and $P$ is the partial pressure of the different gas species. The third term is the Tafel Eq. used to determine the activation overpotential where $\alpha$ is the charge transfer coefficient, $i$ is the current density, and $i_o$ is the exchange current density. The fourth term defines the ohmic losses that are linearly related to the current density, where $r$ is the ohmic resistance. The final term is an empirical relationship used to represent the mass transport losses, and is one of the more common models because it provides an excellent fit [34]. While the mass transport term is useful for modeling polarization data, it is not very helpful in determining how increases in operational parameters such as cell temperature will affect these losses.

From a thermodynamic perspective, high dilution levels or low overall system pressures result in a decrease of the reactant partial pressures. This reduction in pressure affects multiple terms in the Eq. used to model the fuel cell voltage, including the Nernst voltage term resulting in a reduced open circuit voltage. Additionally, it was presumed that operating at lower reactant pressures resulted in lower catalyst site occupancy, thereby reducing the value of the exchange current density, $i_o$, and increasing the activation polarization losses [18]. The mass transport losses are also affected by pressure changes and increase from reduced partial pressures of the reactants as they are consumed. The mass transport effect is typically seen on the polarization curve at high current densities, but with a reduction in overall system pressure, the mass

transport loss will be observed on the polarization curve at lower current density. Conversely, an increase in the overall system pressure, which in turn increases the partial pressure of the reactants, pushes the mass transport effect further out on the polarization curve. This is evident in Figure 20 as the pressure increases from left to right.

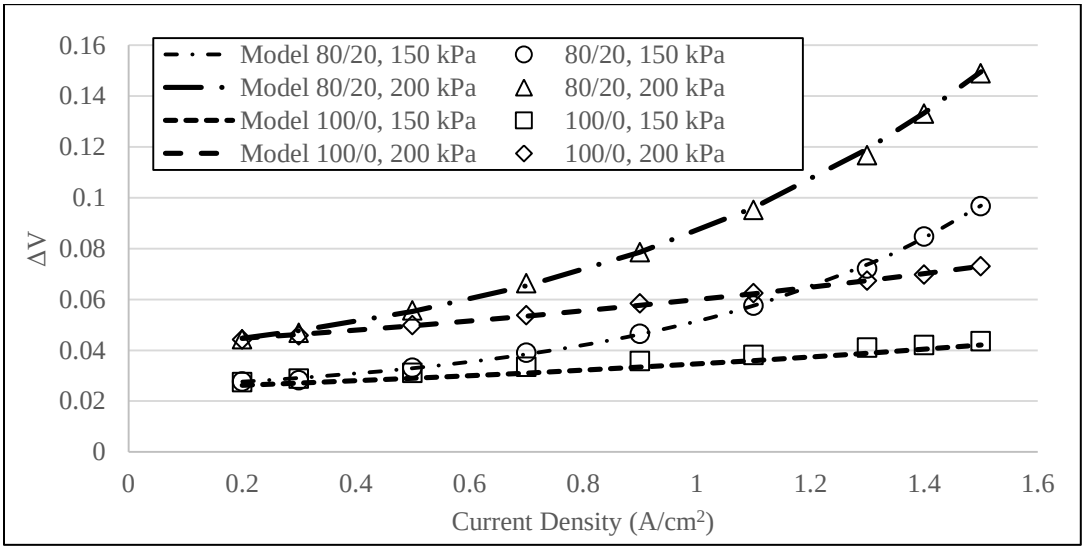


Figure 21: Differential voltage data and fitted models for the PBI MEA due to higher pressures relative to operation at atmospheric pressure for dilution levels of 0% and 20% at cell temperatures of 160°C.

Figure 21 shows the differential voltage for the PBI MEA due to higher pressures relative to operation at atmospheric pressure for dilution levels of 0% and 20%, and at cell temperatures of 160°C. Modeling the increase in voltage due to an increase in pressure for the open circuit voltage is relatively straightforward using the Nernst term in *Eq. 27*. If the system pressure changes from $P_1$ to $P_2$, the resulting change in OCV will be equal to:

$$\Delta V = \frac{RT}{4F} ln\left(\frac{P_2}{P_1}\right) \qquad \textit{(Eq. 28)}$$

Additionally, the change in voltage as a result of diluting the anode can be largely attributed to a reduction in $H_2$ partial pressure. Isolating the effect $H_2$ partial pressure has on the voltage model found in *Eq. 27* yields:

$$\Delta V = \frac{RT}{2F} ln\left(\frac{P_{2,H_2}}{P_{1,H_2}}\right) \qquad \textit{(Eq. 29)}$$

When increasing the pressure from 101.3 to 150 kPa and then from 101.3 to 200 kPa at 160$^o$C, the resulting increase in voltage due to the Nernst potential is 3.7 and 6.3 mV, respectively. The rest of the voltage increase due to pressure increase can be attributed to a reduction in the activation overpotential and the mass transport losses. However, there is no explicit relationship defining the effect pressure has on the exchange current density or the mass transport loss coefficients. Nevertheless, an empirical model can be developed that fits the data well by combining *Eq. 28* with the activation and mass transport overpotential terms found in *Eq. 27*. The effect pressure has on the voltage of the cell can be modeled as:

$$\Delta V = V_2 - V_1 = \frac{RT}{4F} ln\left(\frac{P_2}{P_1}\right) + A\ ln(B) + C\ exp(Di) \qquad \textit{(Eq. 30)}$$

where $A$, $B$, $C$, and $D$ are empirically determined coefficients. The coefficient $A$ represents the effect pressure has on the charge transfer coefficient $\alpha$ where $\alpha$ must be between 0 and 1 and is typically between 0.1 and 0.5. From the Tafel Eq., $A = \frac{RT}{2\alpha F}$, and since $\alpha$ is between 0.1 and 1, then $A$ must be between 0.0187 and 0.187. The coefficient $B$ incorporates the effect the change in pressure has on the exchange current density and is equal to the ratio of exchange current densities at different pressures, ($B = \frac{i_{o,2}}{i_{o,1}}$). As it is not expected that pressure will have a positive impact on the exchange current density, $B > 1$. $C$ and $D$ describe the impact the change in pressure has on the coefficients $m$ and $n$ used in *Eq. 27*. This model provides an excellent fit to

the data (within +/- 5 mV) and is plotted in Figure 21. Table 7 provides the parametric coefficients used for the empirical models shown in Figure 21. Note that in the model, $i$ is in units of mA/cm$^2$.

Table 7: Parametric coefficients used for models in Figure 21.

| Model ($H_2$/$N_2$%, kPa) | A | B | C | D |
|---|---|---|---|---|
| 80/20, 150 | 0.0771 | 1.24 | 5.15E-3 | 1.80E-3 |
| 80/20, 200 | 0.0801 | 1.29 | 1.56E-2 | 1.39E-3 |
| 100/0, 150 | 0.0622 | 1.12 | 1.39E-2 | 5.41E-4 |
| 100/0, 200 | 0.0814 | 1.14 | 2.74E-2 | 5.08E-4 |

Increasing the operating temperature of the cell also increased the performance of the cell. Particularly noticeable in Figure 19 is the effect temperature has on performance at anode dilution levels of 70% $N_2$. Increasing the cell operating temperature from 160 to 200$^o$C, while keeping the system pressure at 101.3 kPa, results in an increased voltage level of 342 mV at a current density of 0.9 A/cm$^2$. This equates to a power density increase of 308 mW/cm$^2$. At higher operating pressures, though, this effect is not as pronounced. When operating under 70% anode dilution at 200 kPa, increasing the cell temperature from 160 to 200$^o$C provides a voltage increase of 74 mV at 0.9 A/cm$^2$, and a power density increase of 67 mW/cm$^2$.

Although not apparent from *Eq. 27*, the increase in temperature affects each term, including the ohmic resistance and mass transport overpotentials. As seen in *Eq. 27*, the temperature of the cell is directly proportional to the Nernst voltage and activation polarization; however, its relationships with the exchange current density, ohmic resistance, and mass transport losses are not as well understood.

Several authors have investigated the effect of temperature on the exchange current density, developing complex models to account for many different parameters including temperature, pressure, electrochemical rate reactions, etc. [152]. Others, such as Korsgaard et al. [145], have

developed simple models that are a function of temperature only, where the authors suggest the exchange current density has an exponential relationship with temperature. Whatever the relationship is, it is clear that a higher operating temperature of the fuel cell leads to a larger exchange current density, which in turn reduces the activation losses.

It has also been suggested that an increase in temperature has a positive correlation with the ohmic losses. In [59] and [153], the authors suggest that the membrane temperature dependency of conductivity obeys an Arrhenius relation. In [145], the authors empirically determined a linear relationship between temperature and the ohmic loss parameter for a PBI MEA. The positive effect of temperature on the ohmic loss was also observed in this work.

The mass transport losses are also reduced by increasing the cell operating temperature, particularly at high dilution levels as is evidenced when comparing the 30/70 $H_2/N_2$ polarization curve at 160$^o$C, 101.3 kPa to the 30/70 $H_2/N_2$ curve at 200$^o$C, 101.3 kPa. Mass transport losses are a result of reactant depletion at catalyst sites and begin to appear when the reactant concentration at the surface of the catalyst approaches 0, or when the catalyst reaction cannot occur quickly enough for the desired current demand. Because increases in operating temperatures do not affect the reactant surface concentration, the positive effect an increase in fuel cell temperature has on the mass transport losses likely results from an increase in the reaction rate of the electrode catalysts.

While the negative performance effects of anode dilution are most strongly seen at low temperatures and pressures, even at anode concentrations of 30/70 $H_2/N_2$, increasing the temperature and/or pressure can drastically improve the performance of the MEA. For example, Figure 22 shows performance curves of diluted anode feeds that produce similar power levels

(within a voltage range of +/- 20 mV at 0.9 A/cm$^2$) for a PBI MEA operated on pure $H_2$ at 160$^o$C. Figure 26 shows similar results but for the TPS MEA.

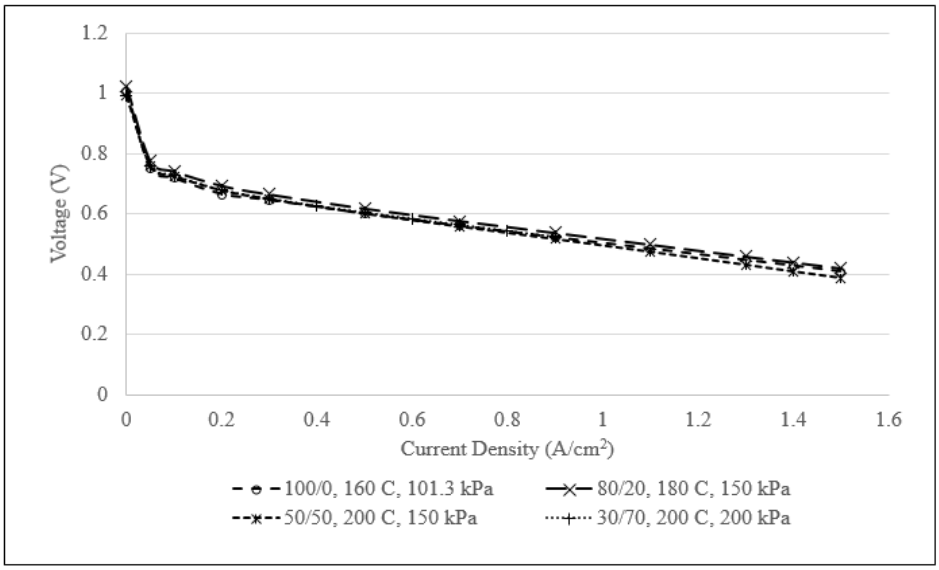


Figure 22: Performance curves of a PBI MEA under various operating conditions of anode dilution, temperature, and pressure, but with similar power outputs.

Even at high dilution levels of 70% $N_2$, similar performance can be obtained to that achieved by operating on pure $H_2$ at 101.3 kPa, by varying the cell temperature and pressure. This is a very interesting finding, particularly when designing a system capable of running on a reformed fuel feed. For some reforming processes, hydrogen concentrations in the effluent stream can be as low as 30%. To increase the hydrogen content to higher levels and boost performance, additional reactors are needed, further complicating the system design. A relatively simple approach might be to increase the temperature, operating pressure, or some combination of the two, to realize greater performance. Ultimately, an energy, durability, and economic tradeoff analysis is needed to determine the optimal design strategy, including the durability implications of operation at higher temperatures and pressure.

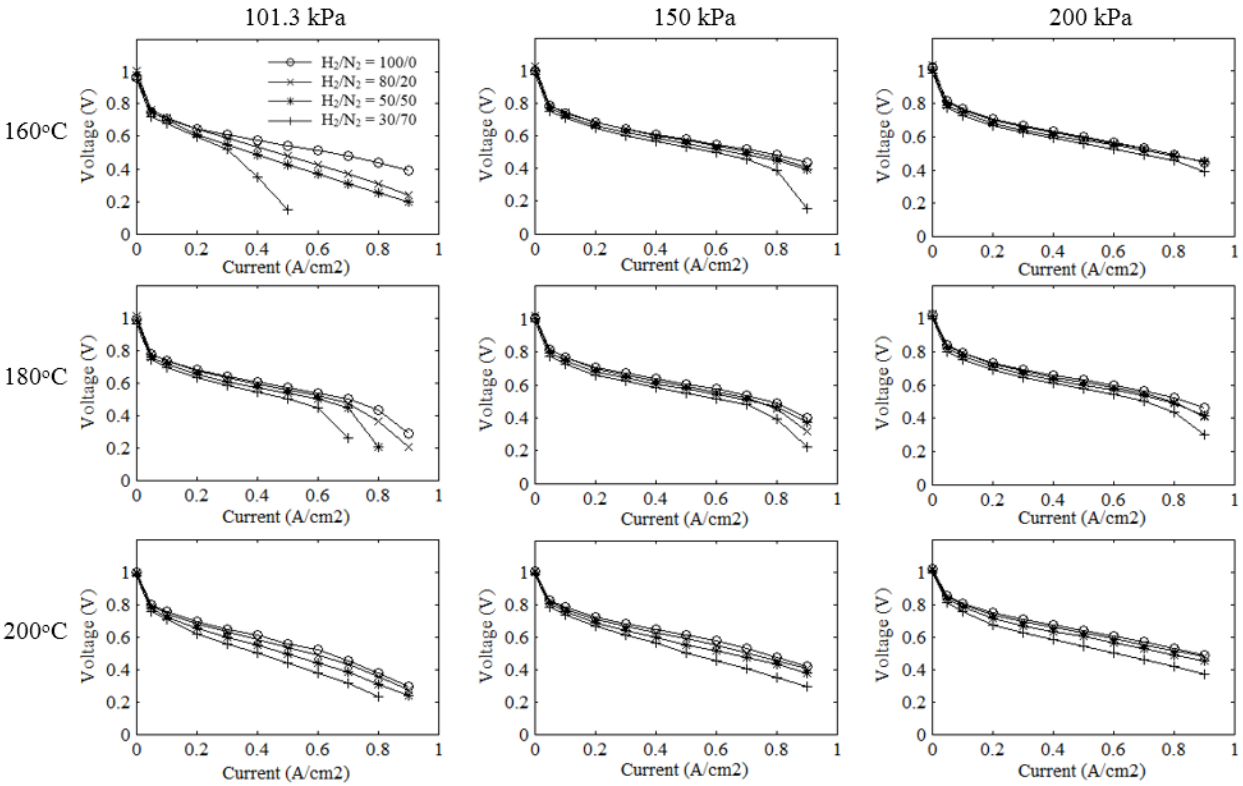


Figure 23: TPS MEA Performance curves as a function of anode dilution, temperature, and pressure

Figure 23 presents the performance curves measured for the TPS MEA under the same conditions used for the PBI MEA. Many of the general trends of the TPS MEA were similar to the PBI, but with some notable differences. Overall, the TPS did not perform as well as the PBI-based MEA. Additionally, the TPS MEA would not generate stable voltages beyond 0.9 A/cm$^2$ for most polarization curves, due to significant mass transport losses. As a result, the maximum power point for most curves occurred between 0.6 and 0.8 A/cm$^2$. The reasons for this are unclear and outside the scope of this work; further investigation is necessary. The maximum TPS power point of the lowest performing curve of 157 mW/cm$^2$ was measured at the same conditions as the PBI MEA (30/70 $H_2/N_2$ anode concentration mix, 160$^o$C, and 101.3 kPa). The maximum power density for the highest performing TPS curve was 418 mW/cm$^2$ and was observed at 100/0 $H_2/N_2$ anode concentration mix, 180$^o$C, and 200 kPa. This maximum power

density was 336 mW/cm$^2$ lower than the maximum power density achieved by the PBI, approximately 45% lower performance.

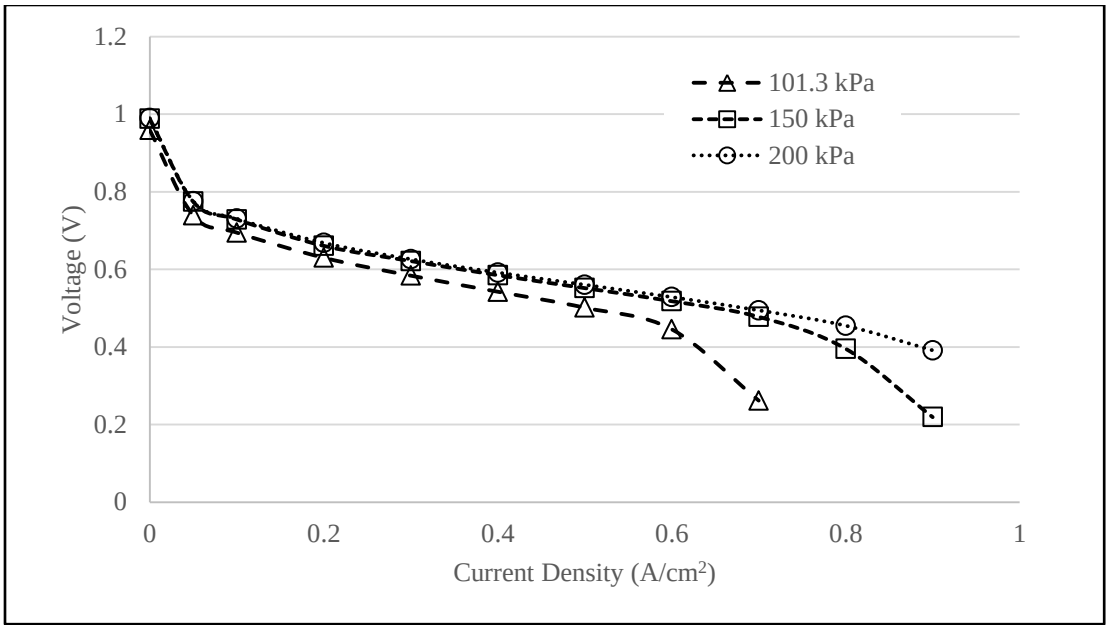


Figure 24: Performance of TPS MEA for various pressures at 180$^o$C and a 30/70 $H_2/N_2$ dilution level.

Similar to the PBI cell behavior, increasing the operating pressure of the TPS also resulted in a boost in performance, and was most significant at high dilution levels and at a temperature of 180$^o$C, as shown in Figure 24. At a current density of 0.7 A/cm$^2$, increasing the system pressure from 101.3 to 200 kPa resulted in a voltage increase of 242 mV, or a power density increase of 170 mW/cm$^2$. The change in voltage due to pressure can similarly be modeled using *Eq. 30*.

The effect temperature has on the cell performance for the TPS was not as pronounced as with the PBI. In some cases, performance of the TPS MEA at 200$^o$C was almost the same if not slightly lower than the performance at a temperature of 180$^o$C. As an example, Figure 25 displays the performance curves for the TPS MEA operating on pure $H_2$ at 150 kPa for various temperatures. For many of the tests conducted, increasing the operating temperature appeared to

increase the performance of the cell at lower current densities, but decrease performance at high current densities.

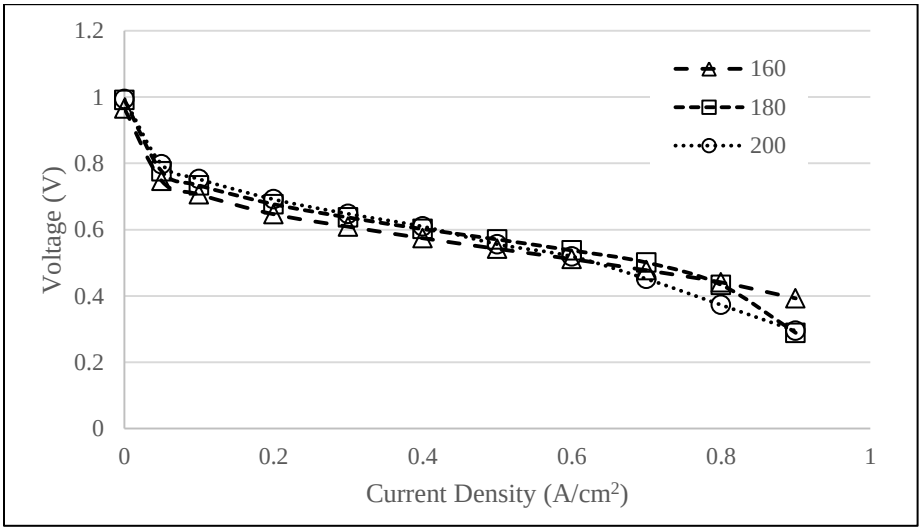


Figure 25: Performance of TPS MEA for various temperatures at 101.3 kPa operating on pure $H_2$ at the anode.

This trend was seen at various dilution levels and pressures, and appeared to result from a reduction in the activation losses coupled with an increase in the mass transport losses. The underlying reason for this trend is unclear as an increase in temperature is expected to reduce both the activation and mass transport losses through an increase in catalytic activity as a result of higher temperatures. Further investigation is necessary to better comprehend the effects of operating conditions on performance of TPS-based MEAs.

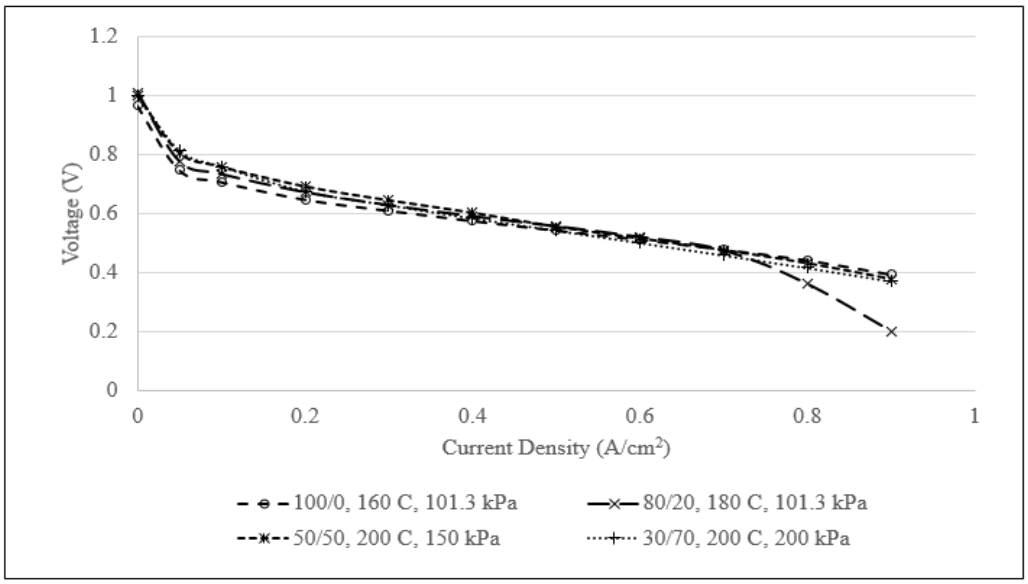


Figure 26: Performance curves of a TPS MEA under various operating conditions of anode dilution, temperature, and pressure, but with similar power outputs

Figure 26 displays several polarization curves that produced similar performance results (within a voltage range of +/- 20 mV at 0.6 A/cm$^2$) for the TPS MEA, but under different anode dilution levels, temperatures, and pressures. Similar to the performance curves presented in Figure 22 for the PBI MEA, varying the operating temperature and/or pressure within reasonable limits was an effective way to increase the performance, even when operating on highly diluted anode gas concentrations.

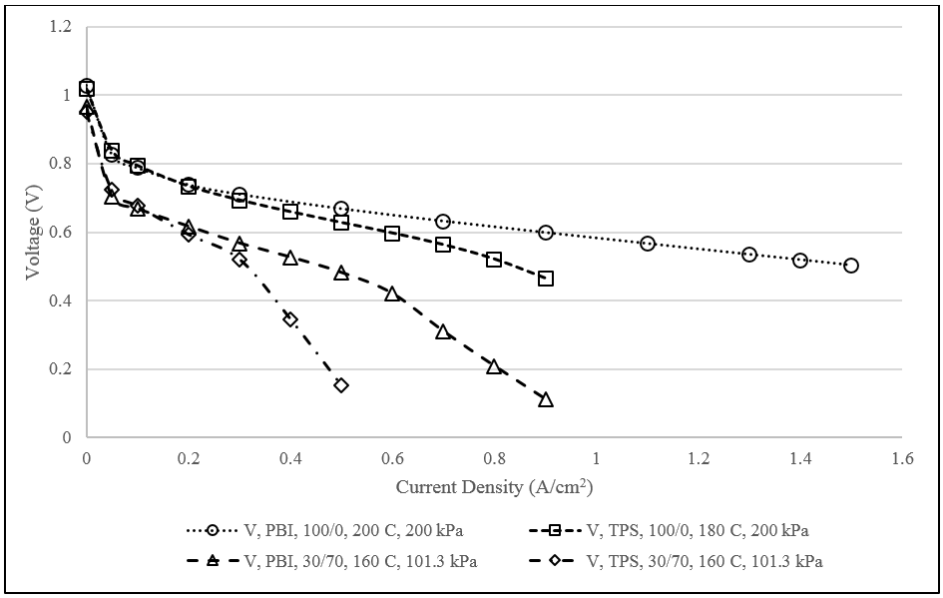


Figure 27: Comparison of the lowest and highest performing polarization curves for the PBI and TPS MEAs

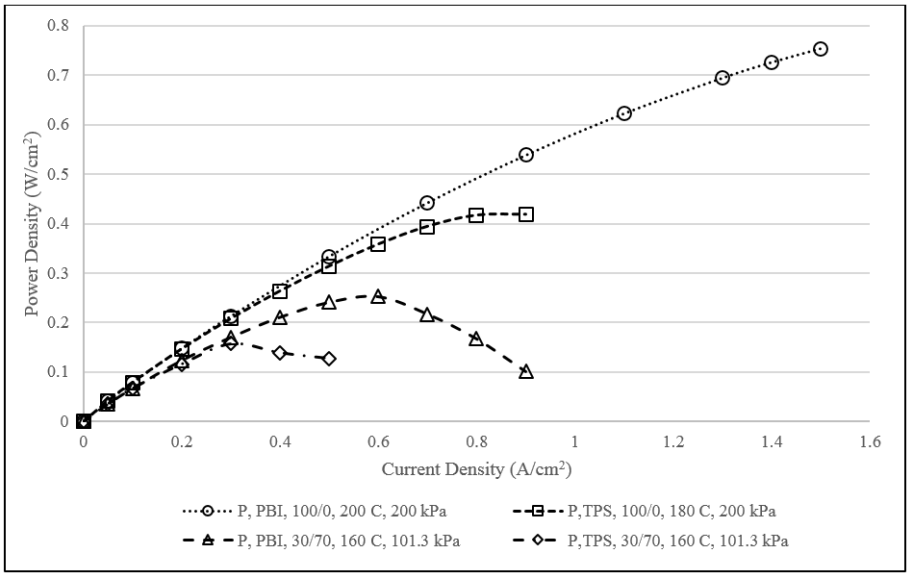


Figure 28: Power density curves of the lowest and highest performing polarization curves for the PBI and TPS MEAs

Figure 27 and Figure 28 compare the highest and lowest performance polarization and power density curves, respectively, of the tested conditions for both the PBI and TPS MEAs. The PBI MEA outperformed the TPS MEA significantly at both the “best” and “worst” test conditions. Additionally, higher operational current densities were achievable when using the PBI material,

as the mass transport losses became too large for stable voltage performance of the TPS MEA. These results indicate that the PBI MEA will likely substantially outperform the TPS when operating on cPOx reformate. The data presented in this Chapter do not address the MEA tolerance of other contaminants or durability under long-term operation. Durability issues, such as CO tolerance and long-term performance, are important considerations when designing an overall system, and will be considered in future research exploring integrated reformer/HT-PEM fuel cell systems.

Several authors have investigated the long-term durability of PBI MEAs, such as [139], [147], [149], and [94], but have only investigated the impact of a few variables. In [139], the authors tested a novel $TiO_2$ composite PBI membrane for over 1100 hours. While operating at 150$^{o}$C, their results revealed that acid loss was reduced by 2% when 2 wt.% of $TiO_2$ was added to the membrane. In [147], it was shown that the phosphoric acid evaporation rate of PBI MEAs increased exponentially as the temperature increased. At 200$^{o}$C, the phosphoric acid evaporation rate was found to be roughly six times the evaporation rate observed at 160$^{o}$C. The same study reported voltage loss of 40 mV after more than 6000 continuous hours (a loss of 6.67 µV/hr) while operating at 160$^{o}$C and current density of 0.2 A/cm$^2$. Assuming the voltage loss over time was largely due to phosphoric acid evaporation, operation at 200$^{o}$C might still allow for over 1000 hours of continuous operation with a voltage drop of 40 mV. However, further investigation of this theory is necessary. To the author's best knowledge, there are no long-term studies on TPS performance in the open literature. The cells tested in this work were only operated for 65 hours, exhibiting essentially no performance loss over the tested lifetime. This was surprising given the high temperature operation, however, the evaporation rate of phosphoric acid was likely reduced due to the high pressure operation at 200$^{o}$C. Further investigation into

longer lifetimes and the effects of operating pressure on evaporation rate is a topic of future research, and may have substantial system-level design implications.

Perhaps the most important result from the current study is that even while operating on highly diluted anode feed concentrations, modifications to the operating parameters, such as temperature and system pressure, can improve performance to the levels achieved under typical operating conditions (i.e. 160$^{o}$C, 101.3 kPa for the PBI). When designing a functional system using a HT-PEMFC to run on a hydrocarbon fuel, it may be less costly, both energetically and economically, to increase either the operating temperature or pressure of the fuel cell rather than incorporating a complex fuel reforming system to improve the quality of the anode feed gas stream. These trade-offs for practical HT-PEM systems are explored further in Chapter 7.

### 6.1.3 Conclusions and Implications

This section presented performance data for two commercial HT-PEM MEA materials, BASF's Celtec P1100W and Advent's TPS© based MEA, under a wide array of testing conditions. The effects of temperature and pressure for various levels of anode dilution were investigated over the ranges 160 to 200$^{o}$C, and 101.3 to 200 kPa, respectively. The hydrogen concentration examined was varied from 30-100%. Increases in pressure and temperature greatly enhanced fuel cell performance for both the PBI and TPS MEAs, with the PBI outperforming the TPS under all tested conditions. While there was a significant performance impact resulting from anode feed dilution, voltage losses could be overcome through increasing the operating temperature and/or pressure of the fuel cell within reasonable limits, even at high anode dilution levels of 70%. However, the energy cost, financial cost, durability, and system level complexity must all be considered when making a final design decision. The data generated from this work will be useful in assessing tradeoffs for full system designs.

## 6.2 Performance of a Celtec MEA on Simulated Propane ATR Reformate

As described in Section 4, there are generally three kinds of reforming processes that are briefly mentioned again here. The most widely known is steam reforming (SR) which is endothermic, and involves sending fuel and steam into a catalytic reactor. Depending on operating conditions, SR will primarily contain reformate species $H_2$, CO, $CO_2$, and $H_2O$. Catalytic partial oxidation (cPOx) is an exothermic reforming process that mixes fuel with oxygen from the air in a catalytic reactor. This reaction will most likely contain reformate species $H_2$, CO, and $N_2$ [114]. The final process is called autothermal reforming (ATR), where both steam and air are mixed with the fuel in a catalytic reactor. Because ATR effectively combines endothermic SR and exothermic cPOx, this reaction has the potential to be balanced such that heat will neither have to be added nor removed in order to sustain the reaction. ATR reformate is comprised of varying amounts of gas species $H_2$, CO, $CO_2$, $N_2$, and $H_2O$ depending on the reaction operating conditions. Although our initial fuel reforming investigations were focused on propane cPOx, it is useful to evaluate the performance of PBI MEAs while operating on common ATR reformate effluents in order to determine the most effective practical reformer fuel cell system design.

To date, there are only a few studies that have operated a PBI based HT-PEMFC on simulated or actual reformate containing species other than $H_2$ and CO. One study by Pan et al. successfully integrated a two-cell HT-PEMFC stack with a methanol reformer using a SR process [38]. Although they did not measure the reformer effluent concentration, they assumed the reformate CO concentration was $\leq$ 1% and the rest of the reformate was comprised of $H_2O$ and $CO_2$. The authors also measured the performance of the stack while operating on 75% $H_2$ and 25% $CO_2$ for comparison. In this scenario, $CO_2$ had little impact. Korsgaard et al. studied

PBI performance when operating on $H_2$ mixed with CO up to 5%, and $H_2$ mixed with $CO_2$ up to 25% [32]. They found that allowable CO concentration increases as the operating temperature increases. The authors also showed that $CO_2$ concentrations up to 25% had minimal effect on the cell performance. Andreasen et al. measured the impedance of a PBI fuel cell with different concentrations of $H_2$ mixed with CO and $CO_2$ in the anode [51]. Wang et al. experimented with anode compositions containing various amounts of $H_2$, CO, $CO_2$, and $N_2$, but their focus was on developing a model that predicts CO tolerance, and little performance data was provided [50]. Generally, all of the studies that analyzed the impact of $CO_2$ on cell performance determined that it has minimal impact other than acting as a diluent. Other studies considered the impact of RH on PBI conductivity, showing increased cell performance as RH increases [59], [146]. In this section, the performance of a Celtec P1100W MEA was evaluated while operating on simulated reformate containing varying concentrations of $H_2$, CO, $CO_2$, $N_2$, and $H_2O$, at levels that would be produced from propane ATR reforming reactions.

### 6.2.1 Propane ATR Simulation Methods

The composition of the simulated reformate was determined through modeling an integrated reformer fuel cell system using AspenOne® Engineering software. This simulation was built upon the previous work considering propane cPOx discussed in Chapter 5, also modeled in Aspen [114]. The propane ATR simulation was developed using Aspen HYSYS V8.4 of the AspenOne Engineering package, and primarily utilized the Gibbs reactor unit operation block. The Soave-Redlich-Kwong (SRK) Eq. of state was the global property model used. The variable parameters for propane ATR were the steam-to-carbon ratio ($H_2O$/C), the oxygen-to-carbon ratio ($O_2$/C), and the reactor operating temperature. In this simulation, the propane fuel flow was left fixed at 1 kmol/s, and the $H_2O$/C and $O_2$/C ratios were varied from 0 - 3 and 0 – 2 respectively.

The reforming reactor temperature was varied from 200 – 1000$^{o}$C. It is important to note that when the $H_2O$/C was 0, propane cPOx was being simulated and conversely, when the $O_2$/C was 0, the model was simulating propane SR. For the propane ATR simulations, the following assumptions were made:

1) Uniform temperature distribution within the reformer.
2) The reformate gas mixture behaves as an ideal gas and pressure gradients were ignored within the reactor.
3) Inlet propane and water were well mixed, and the reaction reaches thermodynamic equilibrium.
4) The considered reformate species for the simulation were $H_2$, CO, $O_2$, $H_2O$, $CH_4$, $C_2H_4$, $C_2H_6$, $CO_2$, $C_3H_8$, and $N_2$.
5) The Gibbs reactor unit operates adiabatically.
6) The major independent parameters were the water flow rate, air flow rate, and reformer temperature. The effect of gas hourly space velocity was not considered for this model.

Figure 29 shows a schematic of the simulated system. The results of the simulations describe the volumetric and mass based flow rates for the reformate species at various operating conditions. These results were imported into a format that could be read using Matlab©, so the data could be sorted based on parameters such as CO concentration and system efficiency.

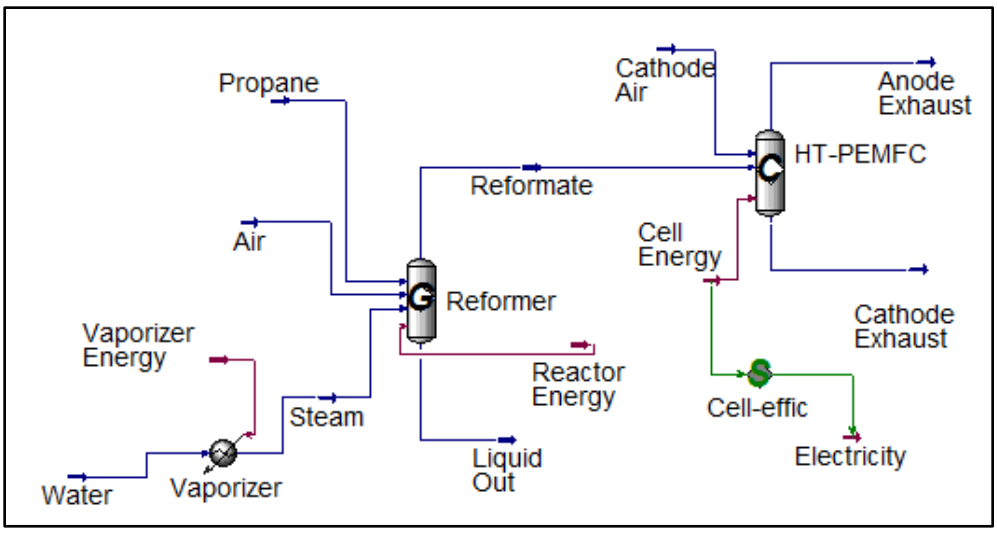


Figure 29: Propane ATR simulation schematic

### 6.2.2 Propane ATR Simulation Results

Using a multi-criteria algorithm, the results from the propane ATR simulation were sorted using a script written in Matlab. The goal of sorting the simulated results was to determine the effluent concentrations at the operating point that maximize system efficiency while limiting the CO concentration to a set amount. While a HT-PEMFC has a higher tolerance to CO than conventional PEMFCs, CO still has a substantial negative impact at high anode concentrations. When defining a significant negative impact as a voltage loss of 10 mV, many experimental studies suggest that CO concentrations up to 3% while operating at a temperature above 180$^{o}$C result in an insignificant loss in cell performance [32], [41], [49], [50], [154]. For this Chapter, the propane ATR data were sorted using an algorithm that maximized system efficiency with the CO concentrations limited to 1%, 3%, 5%, and 10%.

To facilitate propane ATR, additional heat energy will be required to vaporize water, and for the reformation reaction itself in some instances. This additional energy will negatively impact the overall efficiency of an integrated reformer fuel cell system, but can be offset by recycling

waste heat generated by the fuel cell. The efficiency of the reformer was determined using the following Equation:

$$\eta_{ref} = \frac{\dot{x}_{H_2} * LHV_{H_2}}{\dot{x}_{C_3H_8} * LHV_{C_3H_8} + \dot{q}_{vap} + \dot{q}_{ref} - HRR * \dot{q}_{fc}} \quad \textit{(Eq. 31)}$$

where $\dot{x}_{H_2}$ represents the flow rate of $H_2$ in g/s, $LHV$ represents the lower heating values that are 120.1 kJ/g for hydrogen and 46.4 kJ/g for propane [35], $\dot{q}_{vap}$ is the heat required to vaporize the steam entering the reactor, $\dot{q}_{ref}$ is the heat required to sustain the propane ATR reaction, HRR is the fuel cell heat recovery rate, and $\dot{q}_{fc}$ is the heat produced from the fuel cell reaction. Based on polarization curves in [41], [32], [154], [155], and those shown in Section 6, HT-PEMFCs are capable of achieving efficiencies greater than 40% at low current densities. The rest of the energy not converted to electricity may be lost to unconverted hydrogen, but is mainly lost in the form of heat. To be conservative, the HRR used in the efficiency calculation was 25%. After calculating the efficiency for each simulation point, the data were sorted by finding the operating conditions that maximized efficiency while limiting CO concentrations in the effluent to 1%, 3%, 5%, and 10%. An additional data point for testing was added to the table to determine the performance while operating on simulate reformate when generated from propane cPOx as discussed in the previous sections.

Table 8: Simulated propane ATR effluent concentration in volume % under different operating conditions

| **Test Point** | **$H_2$** | **$N_2$** | **$CO_2$** | **CO** | **$H_2O$** | **Reformer Temp ($^oC$)** | **$H_2O$/C** | **$O_2$/C** |
|---|---|---|---|---|---|---|---|---|
| 1 | 21 | 27 | 11 | 1 | 40 | 480 | 3 | 0.32 |
| 2 | 32 | 20 | 11 | 3 | 34 | 560 | 3 | 0.29 |
| 3 | 40 | 13 | 11 | 5 | 31 | 600 | 3 | 0.15 |
| 4 | 52 | 0 | 9 | 10 | 29 | 700 | 3 | 0 |
| 5 | 29 | 49 | 0 | 23 | 0 | 940 | 0 | 0.53 |

The first 3 rows of values in Table 8 describe the effluent gas compositions that would be produced given the provided operating conditions in a fuel reformer device operating under propane ATR. Each test point occurs at the high $H_2O/C$ ratio limit of 3 run in this simulation. Interestingly, for Test Point 4 where the CO concentration is limited to 10%, the most efficient system operating point occurs under SR conditions. There also seems to be a trade-off between high $H_2$ production and low CO production where increasing the operating temperature and the $H_2O/O_2$ ratio simultaneously produces greater amounts of CO and $H_2$. The final gas composition (Test Point 5) is that produced from propane cPOx as discussed earlier in Chapter 5.

### 6.2.3 Experimental Methods

Experiments were conducted to determine the performance of HT-PEM fuel cells when operating on the effluent gas compositions provided in Table 8. Anode feed gas compositions equal to the gas concentrations given in Table 8 were mixed at the volumetric flow rates required to maintain an anode $H_2$ stoichiometry of 1.5 for all tested current densities. The anode of the HT-PEM test cell was then fed with this gas mixtures to obtain the polarization data. All experiments were performed using a modified Hydrogenics test stand. Several Celtec P1100W MEAs, also investigated in [147], [156], were purchased from Advent Technologies with an active cell area of 45.2 $cm^2$ [47]. The MEAs were placed in a test cell comprised of two graphite plates with flow channels cut in a quad serpentine pattern. Before running the cell on reformate, a break-in period of 24 hours was completed for each cell, where power was drawn at a current density of 0.2 $A/cm^2$ at a temperature of 160$^oC$.

After the break-in, polarization curves were run from 0 – 1.5 A $cm^{-2}$, where each current density was held for a minimum of 3 minutes. All tests were run with a stoichiometric ratio of 1.5 at the anode using either pure hydrogen or reformate, and 2.0 at the cathode using air. Gases

$N_2$, CO, and $CO_2$ were metered using Alicat mass flow controllers calibrated to control the desired gases. The $N_2$ controller had a range from 0 – 5 slpm, and the CO and $CO_2$ controllers had ranges from 0 – 1 slpm. Two Brooks flow controllers were used to control the flow of $H_2$, one for flows below 0.2 slpm and the other for flows from 0.2 - 2 slpm. Air on the cathode side was controlled using a single Brooks flow controller with a range from 0 – 3 slpm.

The bubbler saturators in the stand were used to simulate the amount of $H_2O$ sent to the anode by setting the temperature of the bubblers to the saturation temperature corresponding with the desired water percentage. These set point temperatures were determined using the Antoine Eq. with parametric constants for water [157]. When running under dry conditions, the saturators were bypassed. All tests were conducted at 180$^o$C and atmospheric pressure. The temperature of 180$^o$C was chosen because it is a condition that balances durability and performance considerations. While the poisoning effect of high CO concentrations is lessened at higher temperatures, conversely, an increase in temperature greatly increases the evaporation rate of phosphoric acid (PA) within the MEA, limiting its overall lifetime. Polarization curves were obtained by current step potentiometry, and were measured beginning with the open circuit voltage. Each step lasted 3 minutes.

### 6.2.4 Performance Results

Figure 30 shows the results of the tests performed operating the PBI MEA at 180$^o$C on pure $H_2$ and several simulated reformates with concentrations described in Table 8. The anode/cathode stoichiometric ratios were held constant at 1.5/2.0, and the cell was operated at atmospheric pressure.

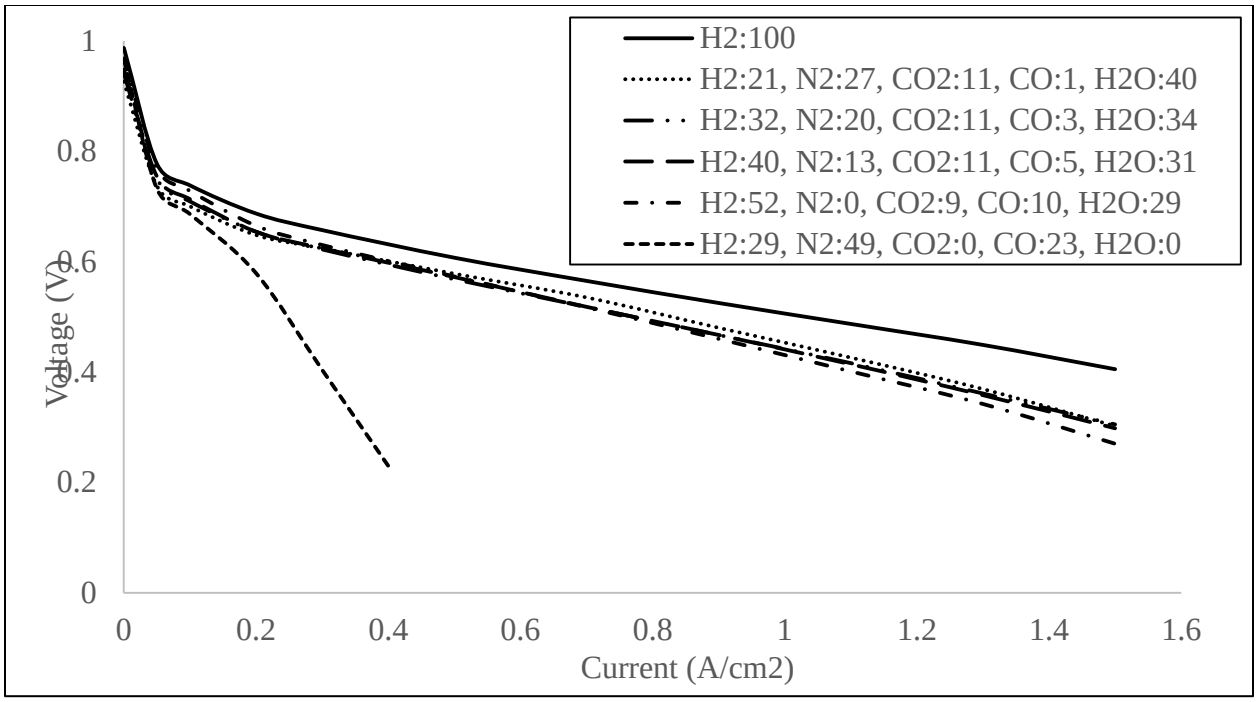


Figure 30: Performance of a PBI MEA while operating on simulated reformate.

Substantial voltage loss when operating on simulated reformate, defined as a 10 mV or more drop when compared to operating on pure $H_2$, occurs at current densities greater than 0.2 A/cm$^2$ for all of the tested conditions. The maximum power densities for test points 1-4 all occur at current densities of 1.3 A/cm$^2$, where the greatest maximum power point occurred for test point 1 and is 480 mW/cm$^2$. When operating the HT-PEM on pure $H_2$, the maximum power density occurs at 1.5 A/cm$^2$ at a voltage of 0.356 mV, a power density of 534 mW/cm$^2$. For comparison, typical power outputs for a PEM fuel cell running on pure $H_2$ at similar current densities are around 700 mW/cm$^2$, significantly higher than the results reported here. However, low temperature PEM fuel cells fueled with pure $H_2$ require significantly more BoP equipment such as high pressure air blowers and humidification equipment, than what is necessary for the HT-PEM fuel cell system under study here.

For Test Point 1, which has a CO concentration of 1%, significant performance loss occurs for most of the polarization curve. This performance loss is much greater than results from other studies that operated under similar test conditions. For example, Li et al. reported a current density loss of 1.3% at 0.5 V when testing a PBI MEA at a temperature of 175$^{o}$C with 1% CO in the anode feed [41]. The greater performance loss observed in these experiments is likely caused by the reduction of $H_2$ partial pressure as a result of the large concentrations of diluents $N_2$, $CO_2$, and $H_2O$ in the anode feed. The other test points with higher CO concentrations experience similar losses.

For Test Points 1-4, even though the CO content varies from 1-10%, the difference in performance is not very large. This phenomena may be explained when considering the different anode feed compositions tested. For the first four test points, anode feed gas compositions that contain higher CO concentrations correspond to relatively higher $H_2$ concentrations. Thus the poisoning effect resulting from a greater CO concentration is somewhat offset by the greater $H_2$ concentrations present in the anode. These results can be checked against the CO poisoning model discussed in *Eq. 18,* and the effect of $H_2$ partial pressure change discussed in *Eq. 29*. Using these models, the voltage losses, as compared to operating on pure $H_2$, for CO poisoning, and a drop in $H_2$ partial pressure, are compared to the measured voltage loss for the data presented in Figure 30.

Table 9: Modeled overpotentials at a current density of 1.1 A/cm$^2$ compared to experimental values

| Test Points from Table 8 | [CO/H2] | CO Poisoning Overpotential (mV) *(Eq. 18* | Pressure Loss Overpotential (mV) *(Eq. 28* | Modeled Total Overpotential (mV) | Experimental Overpotential (mV) |
|---|---|---|---|---|---|
| 1 | 0.05 | 53.3 | 15.2 | 68.5 | 61 |
| 2 | 0.09 | 66.6 | 11.1 | 77.7 | 71 |
| 3 | 0.13 | 72.3 | 8.9 | 81.2 | 73 |
| 4 | 0.19 | 80.7 | 6.4 | 87.1 | 86 |
| 5 | 0.79 | 108.6 | 12.1 | 120.7 | 487 |

Except for the last row of Table 9, the modeled overpotentials due to the CO poisoning and partial pressure of $H_2$ in the anode compare well with the experimental data, but with a slightly higher predicted voltage loss than observed. One reason for the small discrepancies in the first four test points might be that the water content within the anode lessens the poisoning effect of the CO in the anode, by serving to increase the rate of CO oxidation as described in *Eq. 21*. Another explanation is that some of the CO and $H_2O$ in the anode feed is converted to $H_2$ and $CO_2$ through a water gas shift reaction shown below at equilibrium.

$$CO + H_2O \rightarrow CO_2 + H_2 \qquad \textit{(Eq. 32)}$$

Low temperature WGS reactions occur at temperatures from 150 – 250$^o$C, and Pt based catalysts have been widely studied [158], [159], [160]. As the fuel cell in these tests were kept at a temperature of 180$^o$C, which is within the LT-WGS range, some of the CO may be converted into useable $H_2$. The extent of this conversion is outside the scope of this work, but is certainly an important topic for further investigation.

The final test point considered in Table 9, with polarization data shown in Figure 30, shows how the fuel cell might perform at 180$^o$C and at 101.3 kPa while operating on reformate generated from propane cPOx. Not only did the fuel cell perform unfavorably compared to the

other tested conditions, but current densities beyond 0.4 A/cm$^2$ could not be reached without the cell potential dropping to values below 0.2 V. The maximum power density of 121 mW/cm$^2$ occurs at 0.3 A/cm$^2$, a fairly low power density, albeit similar to levels of other widely studied fuel cell types such as direct methanol fuel cells. For comparison, recently developed direct methanol fuel cells can achieve power densities of around 100 mW/cm$^2$ at current densities of 0.3 A/cm$^2$, with maximum power densities peaking at 120 mW/cm$^2$ [14].

When operating on simulated propane cPOx, the experimental performance losses, shown in Table 9, do not compare well to the modeled overpotentials associated with CO poisoning and a reduction in $H_2$ partial pressure. This indicates that the CO poisoning model is not effective for high CO concentrations. Additionally, these results imply that operating the fuel cell at 180$^o$C may not be the best operating temperature at these high levels of CO concentration. The polarization data in Figure 30 also shows a mass transport loss at approximately 0.2 A/cm$^2$. As discussed in Section 2.3.2, increasing the catalyst surface area, operating temperature, or the cell pressure, can all serve to move the mass transport losses further down the polarization curve. Increasing the catalyst surface area while reducing the total amount of Pt has been the focus of many researchers for all types of fuel cells. Today, much of the novel research is now focused on developing core-shell catalysts that coat the Pt catalyst over a relatively cheaper core material [161]. Rather than pursue this approach, experiments that test how the fuel cell performs when increasing the operating temperature and pressure of the cell were conducted, and are described in Section 6.3. In this section, the performance of HT-PEM MEAs were examined when fueled with actual reformate gas feeds.

### 6.2.5 Conclusions and Implications

In this section, the performance of single PBI single cells were evaluated while operating on simulated reformate compositions containing various amounts of $H_2$, CO, $CO_2$, $N_2$, and $H_2O$ that would be generated from propane ATR fuel reformer. The highest PBI performance on reformate conditions produced power levels of 480 $mW/cm^2$ when operating on a fuel reformate composed of 21% $H_2$, 27% $N_2$, 11% $CO_2$, and 1% CO. This power output is approximately 30% lower than the power produced at the same current density when operating on pure $H_2$ instead of reformate. Therefore, if operating on reformate, the HT-PEMFC stack will need to be oversized to make up for the power loss. When designing a mobile fuel cell device, the additional stack cost and weight required from oversizing may be small in comparison to the additional BoP equipment required for the system to run on pure $H_2$ either stored on board, or generated via a more complex fuel reforming system.

Because a practical mobile device requires a low-weight, simple design, all fuel reformer designs should similarly be low-weight and relatively simple to control. In light of this, the additional water necessary to operate an ATR or SR reaction greatly complicates the overall fuel cell system, and adds extra weight. On-board water requirements necessitate BoP equipment such as storage tanks, vaporizers, and mass flow controllers. Additionally, because deionized water was used in these tests, it is unclear the effect typical contaminates found in water supplies might have on both the fuel reformer and fuel cells performance or durability. For a practical device, the requirement of adding deionized water to this system provides significant challenges in the field, since deionized water is typically unavailable unless generated on-site. Perhaps a closed-loop design could be developed where water generated in the fuel cell would be fed back into the reformer; however, this design suffers from drawbacks such as the additional weight and

complexity necessary for such a recycling system. Other operational changes such as increasing the operating pressure and temperature will also have drawbacks such as reduced durability when operating at higher temperatures, and more complex BoP when operating at higher pressures. However, the boost in performance from these changes may be enough to warrant their added complexities and additional weight in the final system.

## 6.3 Performance of PBI and TPS MEAs on Actual Propane cPOx Reformate

Section 6.2 revealed that operating a HT-PEM fuel cell on simulated reformate gas compositions most likely generated from a single stage cPOx, ATR, or SR reactor allows for useful power outputs to be generated. Although the performance of the fuel cell proved to be best when operated on reformate generated from propane SR and ATR reactions versus propane cPOx, the added complexities of managing an ATR or SR reformer on a mobile system is a difficult challenge at the system level that many researchers have abandoned. Although the fuel cell did not perform as well when operating on propane reformate generated from cPOx, controlling a propane cPOx reformer is relatively simpler as only the operating temperature, air flow, and the fuel flow need to be controlled for an effective system. Additionally, it is expected that increasing the operating temperature might boost the power output to higher levels. In this section, results from PBI MEAs tested with high concentrations of CO up to 20%, as well as their performance when using actual reformate, are discussed.

### 6.3.1 Experimental Methods

Experiments were conducted to determine the performance of HT-PEM fuel cells when operating on the effluent gas compositions generated from propane cPOx. All experiments were performed using a modified Hydrogenics test stand. Several Celtec P1100W MEAs purchased from Advent Technologies with an active cell area of 45.2 $cm^2$ were used for experimentation.

The MEAs were placed in a test cell comprised of two graphite plates with flow channels cut in a quad serpentine pattern. The cell followed the same break-in procedure as other tests, which consisted of heating the cell up to 160$^{o}$C and flowing pure $H_2$ and air with stoichiometric ratios of 1.5 and 2.0 at the anode and cathode respectively, at a current density of 0.2 A/cm$^2$. The test cell was kept at atmospheric pressure and run under these conditions for 24 hours.

After the break-in period, the anode of the HT-PEM test cell was fed with either simulated or and actual reformate gas mixture. Polarization curves were run from 0 – 1.5 A/cm$^2$, where each current density was held for a minimum of 3 minutes. All polarization curves were obtained by current step potentiometry, and were measured beginning with the open circuit voltage. Simulated anode feed gas compositions were mixed at volumetric flow rates to maintain a constant anode $H_2$ stoichiometric ratio of 1.5 for all tested current densities. The reformate gases tested were either a simulated gas feed composed of 28% $H_2$, 49% $N_2$, and 23% CO, or reformate generated directly from a fuel reformer operated under propane cPOx conditions. Simulated gases were metered using Alicat mass flow controllers calibrated to control the specific gas. The $N_2$ controller had a range from 0 – 5 slpm, and the CO and $H_2$ controllers both had a range from 0 – 1 slpm. Air on the cathode side was controlled using a single Brooks flow controller with a range from 0 – 3 slpm. The experiments using simulated reformate were operated under anhydrous conditions, where temperatures were varied from 160 to 200$^{o}$C, and pressures were varied from 101.3 to 200 kPa.

When testing a HT-PEM MEA on actual reformate, a baseline polarization curve using pure hydrogen at the anode was taken before operating the cell on reformate. While this polarization curve was being taken, the reformer startup procedure determined in Section 5.4 was followed, briefly described again here. The first step of this procedure was to heat up the reformer catalyst

to above 360°C, which is the light-off temperature of the reactor. Once the light-off temperature was reached, propane was allowed to flow at its full rate and air flow was slowly increased until the desired $O_2$/C ratio was reached. The temperature of the furnace was then increased until the desired catalyst temperature was reached. The optimal operating conditions for this reformer shown in Table 6 were $O_2$/C ratio of 0.53, and operating temperature of 940°C. Once the optimal reformer operating conditions are reached, the reformer effluent is composed of approximately 28% $H_2$, 49% $N_2$, and 23% CO. This effluent gas composition was verified using both a mass spectrometer (Applied Instrument Technologies, CA, USA) and a gas chromatograph (Model 490 Micro GC, Agilent Technologies, Santa Clara, CA). The actual setup of the reformer test stand and a schematic of its operation is shown in Figure 10 of Section 5.4.

Once the reformer reached the optimal operating conditions, the reformate was then piped over to the modified Hydrogenics single cell test stand using a manual three-way valve that flowed from the reformer to the exhaust or to the anode metering setup, schematically shown in Figure 31.

.

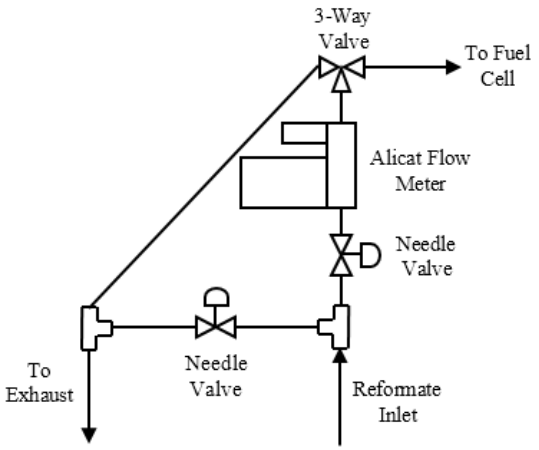


Figure 31: Reformer effluent metering setup schematic

In this setup, the amount of reformate sent to the fuel cell was controlled using two needle valves and an Alicat flow meter calibrated to measure gas flow comprised of 28% $H_2$, 49% $N_2$, and 23% CO. The complete setup connecting the reformer to the fuel cell is shown in Figure 32.

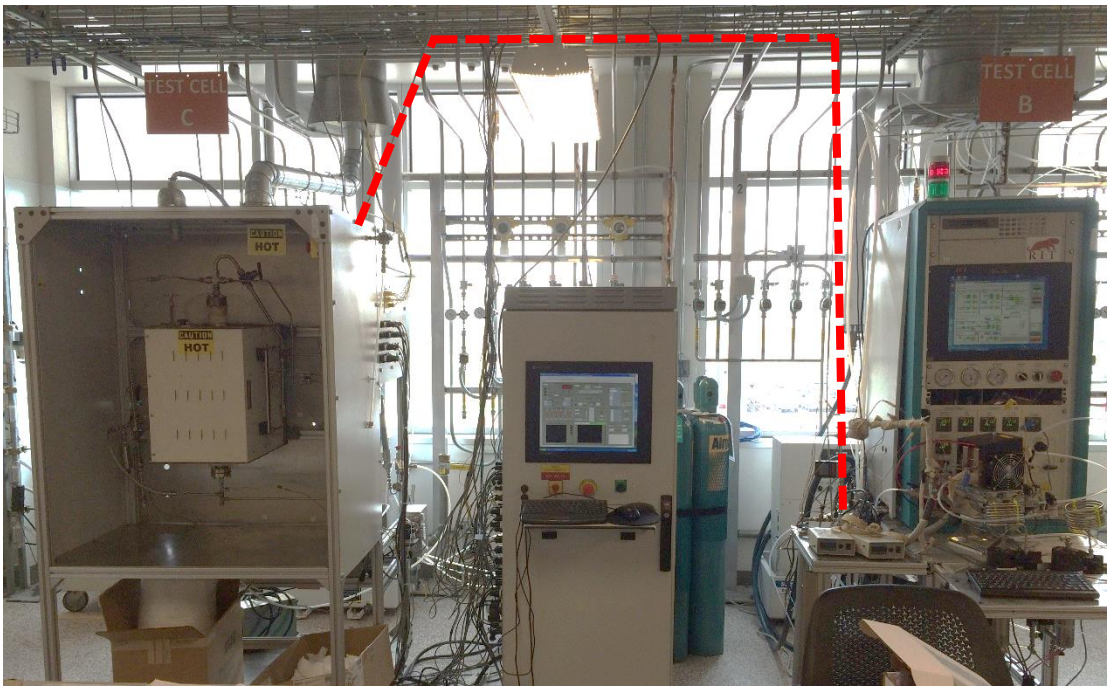


Figure 32: Experimental setup of the reformer test stand (left) connected to the single HT-PEMFC MEA test stand (right) with the reformer effluent pipe highlighted in red

The anode flow rate was controlled so that the $H_2$ amount in the anode inlet stream would provide a stoichiometric ratio of 1.5, while the cathode air flow was kept at a stoichiometric ratio of 2.0. The TPS test cell was maintained at a temperature of 180$^o$C while the PBI was tested at 160$^o$C, 180$^o$C, and 200$^o$C. Because it was expected that sulfur in the propane would negatively impact fuel cell performance, a desulfurizer was purchased from SulfaTrap [84], and placed between the propane flow controller and the inlet to the propane fuel reformer. The propane used for experiments has a sulfur level of 15 ppm or less. The SulfaTrap desulfurizer was capable of

reducing this amount of sulfur to levels less than 3 ppb, which would not negatively affect fuel cell performance.

### 6.3.2 Performance Results

Figure 33 shows the polarization data of a PBI MEA when operating at different concentrations of $H_2$ diluted with CO concentrations up to 20% at 200$^{o}$C and 101.3 kPa. CO concentrations at these levels are significantly higher than tested concentrations reported in the open literature. The closest level of CO of 16% was studied by Li et al. in 2003 [41]. In this research, the authors operated a PBI MEA at 200$^{o}$C and 101.3 kPa, using pure $O_2$ and a higher hydrogen stoichiometric ratio than used in this work. Even though the PBI MEA tested in this work was operated under less favorable conditions, it still exhibited greater performance, indicating significant progress has been made in the development of commercial HT-PEM MEAs since 2003 as reported in [41].

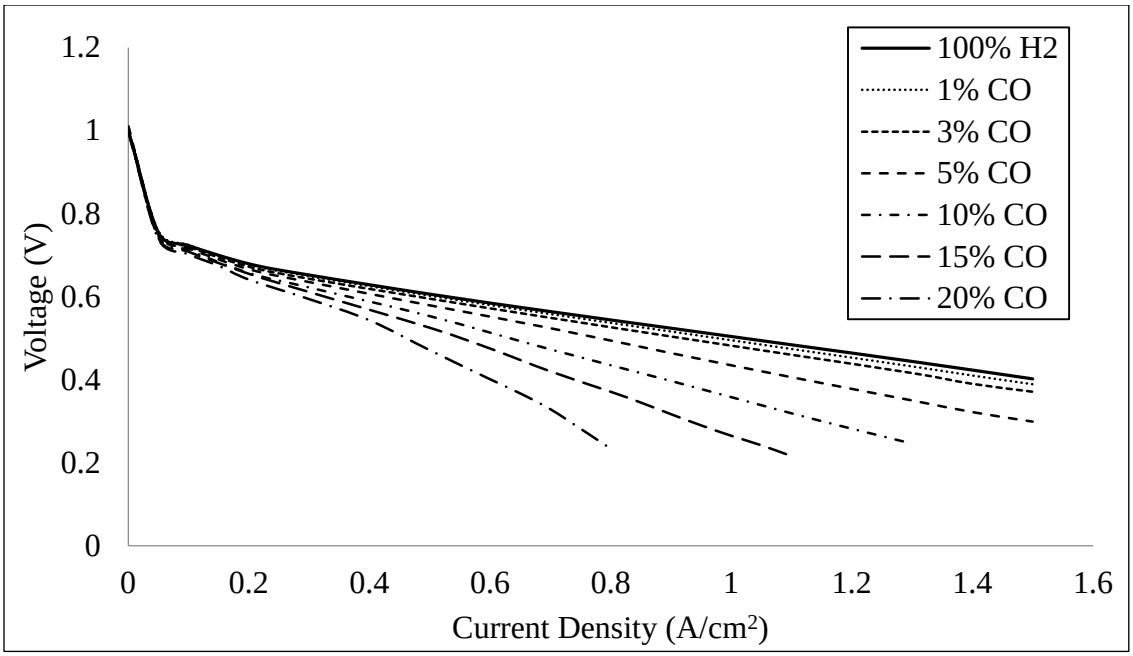


Figure 33: Polarization data of a Celtec P1100 W operated at 200°C, 101.3 kPa, and with different [$CO/H_2$] mixtures in the anode up to 20% CO. Anode and cathode stoichiometries were kept at 1.5 and 2.0 respectively.

Minimal voltage losses occurred at CO concentrations below 3%. However, when the CO concentration was increased above 5%, significant voltage losses appeared, particularly at higher current densities. At 0.6 A/cm$^2$, a 5% CO concentration resulted in a voltage loss of approximately 3.5%. At 10% CO, a voltage loss of 12% was seen, whereas at 20% CO, a voltage loss of 57% was observed. Another way to visualize the voltage drop resulting from CO poisoning, i.e. the voltage of CO-free hydrogen minus the voltage of CO-containing hydrogen, is to plot the cell voltage loss as a function of $\frac{[CO]}{[H_2]}$, as shown in Figure 34. From this data, the CO poisoning voltage losses can be empirically modeled using an Eq. with a similar form to *(Eq. 18,* first described in [71], which estimates the poisoning effect as a function of temperature, current density, and the $\frac{[CO]}{[H_2]}$ ratio.

$$\Delta V_{pois} = -2.5\ x\ 10^{7} \exp(-0.04603\ T)\ i + 7.48\ x\ 10^{6} \exp(-0.03274\ T)\ i\ \frac{[CO]}{[H_2]}$$

*(Eq. 33)*

The constants of the model shown in *(Eq.* 33 were determined by fitting the curve to the data shown graphically in Figure 34 using a least squares regression algorithm. Unlike the original model developed in [71], the model described in *(Eq.* 33 accurately predicts CO poisoning performance loss at current densities up to 1.5 A/cm$^2$. However, this model has only been fitted to data from tests at 200$^o$C, thus further verification at lower temperatures is needed.

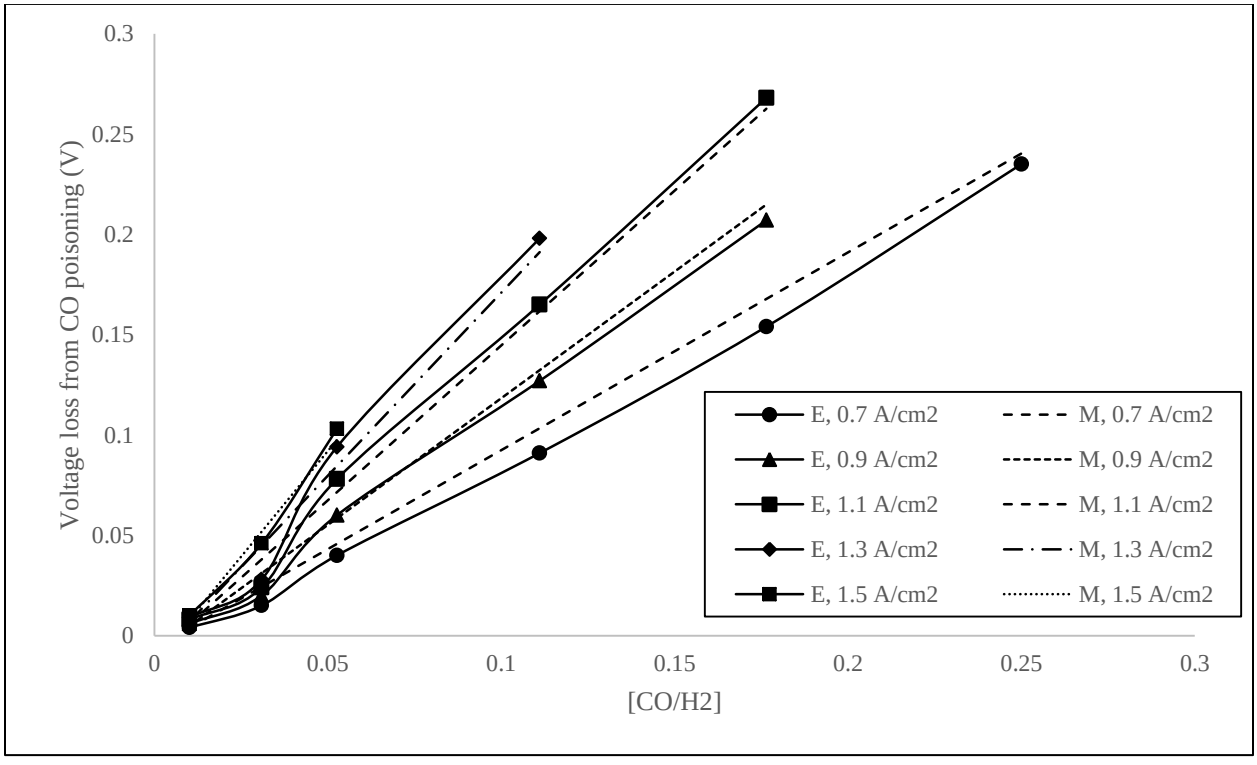


Figure 34: Experimental and modeled voltage loss due to CO poisoning in a Celtec P1100W MEA while operated at 200$^o$C and at 101.3 kPa.

After collecting data on the effect of simulated reformate with high CO concentrations, a PBI MEA was tested with actual propane reformate. Polarization curves of a Celtec P1100W MEA while operating on actual propane cPOx reformate generated on-site, are shown in Figure 35. The polarization data was taken at various temperatures and at atmospheric pressure. Data taken at 160$^{o}$C is not shown in the figure because the voltage of the cell dropped to below 200 mV at current densities below 0.2 A/cm$^{2}$.

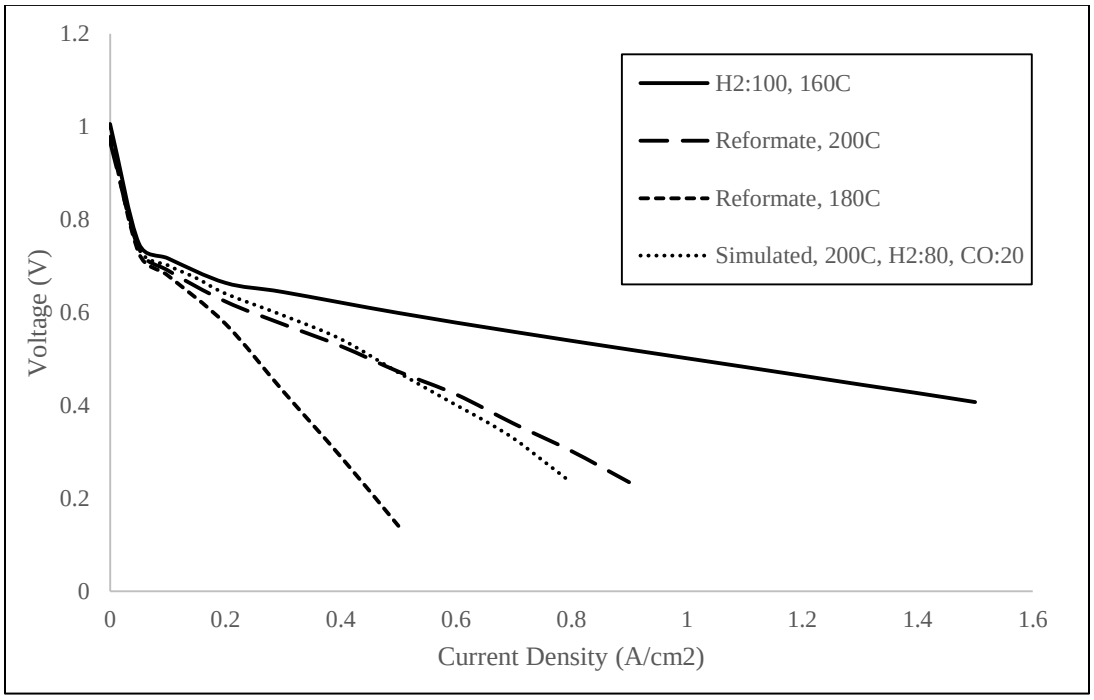


Figure 35: Polarization curves of a Celtec P1100W tested on actual reformate produced from propane cPOx at various temperatures and at atmospheric pressure and compared to simulated reformate at 200$^{o}$C.

When operating on actual reformate, the PBI performed best at 200$^{o}$C. Even though the concentrations of CO in the reformate was approximately 23%, a maximum power density of 257 mW/cm$^{2}$ was achieved at 0.6 A/cm$^{2}$. The performance when operating on actual reformate compares well to the performance when operating on $H_2$ mixed with 20% CO. This comparison

indicates that the CO concentration results in the majority of performance degradation rather than the hydrogen dilution. When operating on actual reformate, the fuel cell is approximately 22.5% efficient when dividing the electrical power output by the LHV of the hydrogen in the anode. The overall system efficiency, computed by dividing the electrical power by the LHV of the propane consumed, is 11.3%. When operating at 180$^{o}$C, the maximum power density was 156 mW/cm$^{2}$ at a current density of 0.4 A/cm$^{2}$. This only corresponds to a 14% conversion efficiency when dividing the electrical power output by the LHV of the hydrogen in the anode. For the polarization data in Figure 35 taken at 200$^{o}$C, the voltage decay shows a linear relationship with current density beginning at 0.05 A/cm$^{2}$. From 0.05 - 0.9 A/cm$^{2}$, the voltage level drops from 737 mV to 235 mV, almost 500 mV total. At 180$^{o}$C, the voltage drop is much more severe, and is not quite as linear over the same current density range. This indicates that a lower operating temperatures causes mass transport losses to appear at lower current densities, a trend also seen in the dilution data discussed in Section 6.

Although the performance loss of the PBI MEA when operating on actual cPOx reformate was significant, durability is also a great concern as operating at temperatures as high as 200$^{o}$C can cause substantial phosphoric acid loss. To determine the lifetime of the fuel cell when operating at high temperatures and on cPOx reformate, a durability test protocol was developed with the goal of operating the test cell for at least 200 hours. The ultimate end of life for the test cell was when the voltage level reached 200 mV at the chosen operating current density. For this test, the current density of the maximum power point of 0.6 A/cm$^{2}$, determined when operating on actual reformate, was used as the test current density. The cell was operated at 200$^{o}$C and 101.3 kPa. The voltage degradation over the tested time period is shown in Figure 36.

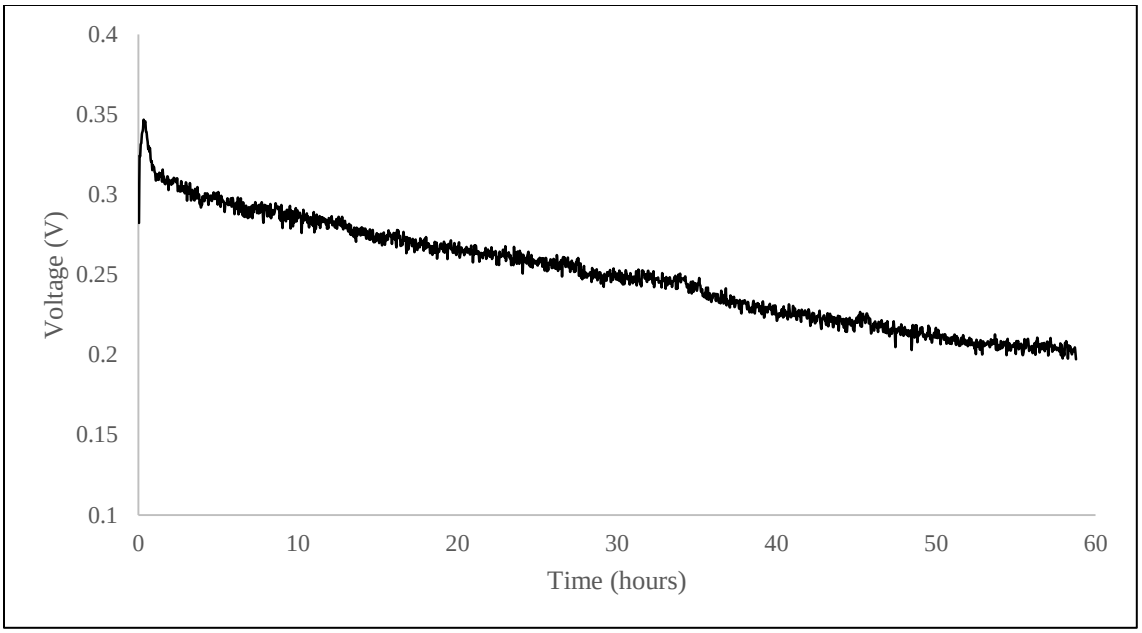


Figure 36: Long term durability test operating a Celtec P1100W at 200$^{o}$C, 101 kPa, at 0.6 A/cm$^{2}$, and with an anode gas composition of $H_2$:28%, $N_2$:49%, and CO:23%.

After following the same 24 hour break-in procedure as discussed previously, the test cell was run for a total of 59 hours before the voltage level dropped below 0.2 V. The start time of this experiment began the moment the anode gas feed was switch from pure $H_2$ to simulated cPOx reformate. At the beginning of the durability test, the voltage of the cell dropped from 0.509 V to 0.282 V. After 15 minutes, the voltage increased to 0.346 V. This was followed by a quick decline in voltage to 0.317 V after 1 hour of total test time. At approximately 59 hours, the cell voltage reached 0.197 V and the test was stopped. The sharp drop in voltage at the onset of $N_2$ and CO was expected due to the onset of CO, and the recovery up to a higher voltage followed shortly after is similar to trends seen in other work [41] and [162]. This recovery typically occurs more quickly at higher temperatures and is thought to be due to a reorganization of PA within the MEA [163].

The initial drop in voltage occurs very quickly, and is followed by a steady voltage decay after 1 hour. This decay rate is linear and is approximately 1845 µV/hour. At this decay rate, a voltage loss of 10% from the peak voltage occurs after 9.24 hours where a 20% voltage loss is seen after 26.4 hours. Other researchers in [90] and [94] have investigated voltage degradation rates for PBI MEAs while operating with pure $H_2$ at 160$^o$C, 101 kPa, and at a current density of 0.4 A/cm$^2$. Under these conditions, a voltage decay rates of 5.7-10 µV/hour is viewed. When increasing the temperature to 180$^o$C, a voltage decay rate of 19 µV/hour was witnessed in [94]. In [162], researchers operated PBI MEAs at various temperatures on pure $H_2$ and air, holding the cell at aconstant current density of 0.2 A/cm$^2$. When operating at 150$^o$C, fuel cell operation of over 17,000 hours was witnessed with less than 10% voltage decay. However, when operating at 190$^o$C, the cell voltage dropped to 10% of its initial value just after 1220 hours.

The primary culprit for such a high voltage decay rate of 1845 µV/hour is likely PA evaporation that happens much more rapidly while operating at high temperatures of 200$^o$C. Nevertheless, there may be other mechanisms contributing to the voltage loss. Most durability studies in reported literature are operated at 0.2 A/cm2 or 0.4 A/cm2. Operating at a relatively high current density has been shown to increase the degradation rate in [94] which may be contributing to such a high rate in this study. Additionally, operating on reformate has also been shown to exacerbate the voltage decay rate as seen in [163]. In that work, authors Zhou et al. tested a PBI MEA while operating on reformate generated from methanol SR at a cell temperature of 160$^o$C. They experienced a voltage decay rate of 600 µV/hour when operating continuously. The authors also tested a start/stop cycle when operating on reformate where they surprisingly witnessed a lower degradation rate under start/stop cycling than during continuous testing. It is unclear from the study what mechanism was causing this phenomenon. Finally,

Oono et al. [162] determined that voltage decay is primarily a result of platinum agglomeration in addition to PA evaporation. Their work also showed that the evaporation of PA from the membrane also leads to increased pin-hole formation, causing fuel crossover and voltage loss.

As it was hypothesized that much of the voltage decay was due to PA evaporation, another test was completed that considered how an increase in operating pressure might impact the overall degradation rate. Increasing the operating pressure will ultimately lower the partial pressure of the PA within the test cell. It was therefore expected that lower PA partial pressures would result in a lower evaporation rate. For this test, a PBI MEA fueled with simulated cPOx reformate at the anode was operated at 200$^{o}$C and 200 kPa. The MEA was held at a constant current density of 0.4 A/cm2 instead of 0.6 for this test. As the test would shut off once the cell voltage reached 0.2 V, a lower current density was chosen in the hope that the cell voltage would remain above 0.2 V for at least 200 hours. The results from this test are shown in Figure 37.

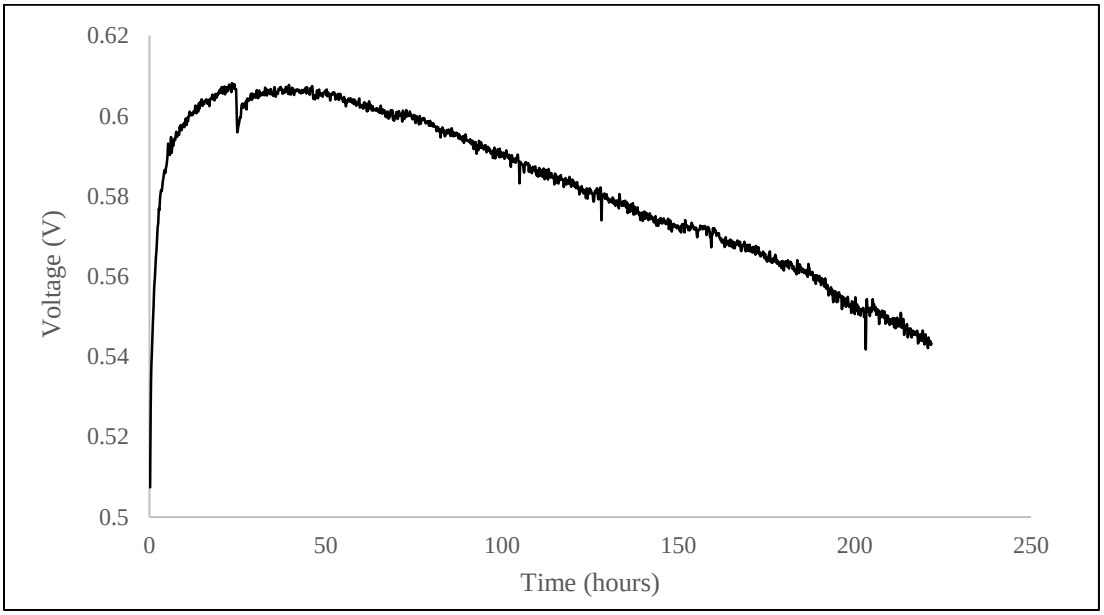


Figure 37: Long term durability test operating a Celtec P1100W at 200$^{o}$C, 200 kPa, at 0.4 A/cm$^{2}$, and with an anode gas composition of $H_2$:28%, $N_2$:49%, and CO:23%.

The total test time for this durability test was 221.75 hours. Similar to the last durability test, at the onset of CO and $N_2$, the voltage initially dropped to 0.507 V, and then increased to 0.607 V after 25 hours. This recovery back to a higher voltage level after the initial drop took much longer than in the previous test. After 25 hours, there was an accidental test stand shutdown. When restarted, the voltage increased back 0.607 V and stayed at this voltage level till the 50 hour mark, where it began to steadily decline for the remainder of the test. Interestingly, the pattern of a drop in voltage, a relatively quick recovery, a period of flat voltage level, and then a steady decline has been witnessed in other durability studies [162].

When operating at 200$^{o}$C and 200 kPa, it took approximately 204 hours for the voltage to decay 10% from its peak voltage level, and assuming the constant decay rate witnessed from the data after 50 hours, it would take approximately 374 hours to reach a 20% voltage loss. The voltage decline rate from 50 hours on is 355.9 μV/hour, approximately 1/5 of the decay rate observed in the previous durability test.

One other possible mechanism for the loss in voltage might be due to PA deposits on the flow field plates of the test cell, thereby increasing the contact resistance between the flow field plates and the MEA, although this was never specifically investigated here. In [66], Hartnig et al. tested the effect of voltage degradation when using different material types for flow field plates. They tested four different types of materials; two different phenolic resin based graphite composites for high temperature fuel cell applications, a set of pyrolytically surface treated and sealed graphite, and a set of gold coated stainless steel plates. Their results showed that the type of bipolar plate material significantly affected the voltage decay rate of the test cell, as well as the PA evaporation rate. The explanation for this is that some types of flow field plate materials act like a PA sponge, effectively furthering an increase in the PA loss rate from the MEA. In

[66], after 1600 h tests when operating the cell at 180$^{o}$C, the PA content in the MEA for the two graphite composite plates dropped to below 65%, where the PA content in the MEA fell to 92% and 98% for the sealed graphite and gold plated plates respectively. As the flow field plates absorbed more PA, the ohmic resistance within them increased leading to even larger voltage decay rates. Overall, while surface treated graphite plates compared favorably to untreated graphitic plates, ultimately gold-plated materials were the best option for long term tests.

Although never specifically investigated in this research program, start/stop cycles can play a significant role in durability considerations and should be studied in future research. If protocols are followed, such as the ones described in Section 7.2.4, that minimize carbon corrosion and liquid water formation, it is expected that the negative impact from startup/shutdown will be minimal compared to the impact of operating at high temperatures over the proposed lifetime of 200 hours.

### 6.3.3 Conclusions and Implications

Remarkably, even with CO concentrations as high as 23% the PBI MEA generates significant amounts of power when operating on reformate generated from propane cPOx. Although the fuel cell performance when operating on reformate is significantly lower than when operating on pure $H_2$, the maximum power density of the PBI MEA of 257 mW/cm$^2$ is still greater than state-of-the-art DMFCs at around 150 mW/cm$^2$ [28], which are touted as the ideal fuel cell type for small mobile applications [15]. These power production rates while operating on “real” reformate are significant because most researchers of HT-PEM fuel cells seem to assume operating PBI MEAs with CO concentrations beyond 5% renders the fuel cell useless, which is likely why it is underreported in published literature. However, when compared to other fuel cell system designs, these power levels are quite useful. If a fuel cell stack were to be

designed using the 45.2 $cm^2$ MEAs tested in this section, a 30 cell would produce almost 350 W of power at around 12.9 V when operating at 0.6 $A/cm^2$.

The results from this section revealed that a PBI based HT-PEM fuel cell was capable of generating useful amounts of power while operating on reformate generated directly from propane cPOx. The simplicity of propane cPOx allows it to be easily integrated with a PBI based HT-PEM fuel cell system. Additionally, the advantage of potentially having a quicker startup time as compared to an SOFC based system allow for a HT-PEM based mobile fuel cell system to be very attractive. In spite of these advantages, durability is still a concern. Long-term tests revealed that PA acid evaporation caused by high temperature operation can be mitigated when operating at higher pressures. Specifically, when operating at 200 kPa, a 200 hour lifetime with only 10% voltage decay can be realized even with cell temperatures of 200$^oC$. This result indicates that the fuel cell can be operated at temperatures beyond the manufacturer's recommendation with useful lifetimes, but only if the operating pressure is increased. While increasing the operating pressure greatly reduced the overall voltage decay rate, the added costs for the BoP equipment required to increase the operating pressure must be weighed against the durability constraints.

One possible operational strategy that can be used to maintain a constant voltage and balance the voltage decay might be to increase the fuel flow rate proportional to the amount of voltage loss. This would lower the overall efficiency of the system but it would allow for the power output to maintain at a constant level for a longer period of time. Also, this strategy will last for only so long as increasing the amount of fuel in the anode will eventually not generate significantly higher voltage levels. In Chapter 7, the performance data from this section was used

to inform the design of a mobile fuel cell system that integrated a propane cPOx reformer with a PBI based HT-PEM fuel cell stack.

# 7 Reformer Fuel Cell System Integration

There exists a vast literature addressing fuel cell system design. Most fuel cell system designs involve several primary sub-systems including the fuel cell stack, fuel processor, power conditioners, air compressor, and controlling hardware. The large majority of published literature is focused in-depth on one specific component, without necessarily considering how they will work together at the system level. Particularly with HT-PEM system development, there are very few focused system design publications, and most of the useful system-level design literature comes from publications focused on other fuel cell types such as LT-PEM, SOFC, or DMFC. Fortunately, most of the primary sub-systems for HT-PEM fuel cells are similar to the sub-systems found in other fuel cell based systems, thus much of the work focused on those fuel types can be adopted when integrating a HT-PEM fuel cell system.

The previous chapters describe the optimal conditions for a propane fuel reformer when operating under cPOx conditions, as well the performance of a HT-PEMFC when fueled with propane cPOx reformate. Using this performance data, a practical fuel cell stack and mobile fuel cell system can be designed. This chapter contributes to the existing fuel cell literature by presenting a practical design concept that pairs a HT-PEM fuel cell with a propane cPOx fuel reformer. In this chapter, a discussion of the existing literature regarding the primary system-level components is presented, and an integrated reformer HT-PEM fuel cell system design is proposed.

## 7.1 System Design Targets: a Case Study of Military UAVs

To design a practical fuel cell system, a specific application was chosen to set target power, energy, weight, and size requirements. The chosen application where a fuel cell device would provide several unique advantages is a mid-sized UAV (total weight < 55 lbs (25 kg), 6-10 ft (1.8-3 m) wingspan); these are mainly used in surveillance applications that require long endurance, but do not necessarily require high power densities for maneuverability. To further refine the target system requirements, the practical power, energy, and weight limitations for existing mid-sized UAVs were researched in literature and through discussions with experts in the industry to determine the practical design constraints for the fuel cell system focused on here.

Presently, UAVs are either powered using batteries or internal combustion engines (ICEs), which offer unique advantages but come with different drawbacks. ICEs are used to power most UAVs with long-term surveillance missions because of the extended durability afforded when fueled with a hydrocarbon fuel. Some of these UAVs can fly for over 24 hours between refueling operations. However, UAVs powered with ICE engines are often extremely noisy and therefore have to fly at high altitudes to ensure that those being surveilled cannot hear it approaching. These high altitude flights require expensive and complex optical equipment to properly view their targets from such far distances, and it is highly desirable to reduce the noise output of the propulsion system so that the flight altitude can be reduced and more cost-effective optics can be used. Additionally, most ICE engines require significant maintenance after each flight, typically with a major overhaul at 250 hours and a complete engine rebuild or replacement after 500 hours. ICEs additionally suffer from premature shut downs that may occur mid-flight, which are catastrophic.

Batteries are the other primary propulsion technology for UAVs. As batteries are much quieter than ICE engines, they allow for lower altitude flights and cheaper, less complicated optics. However, due to their low specific energy, they suffer from very short flight times that are typically no longer than 1.5 hours, such as with the RQ-11B Raven developed by AeroVironment [164]. As a result, UAVs powered with batteries can only be used for very short range reconnaissance missions. To watch a target for extended periods of time using a battery powered UAV, multiple UAVs are used for a single mission. At least three UAVs are in constant use for a long endurance mission, where one UAV is over the target, one is returning, and the other has just been launched towards the target. This greatly complicates and adds to the expense of each mission as several operators are required for each UAV used.

A fuel cell system has the potential to provide the advantages both batteries and ICEs offer, but with very few drawbacks. Because fuel cells generate power without any moving parts and can be fueled with energy-dense hydrocarbon fuels, they offer quiet operation, long flight times, and less maintenance than current battery and ICE technology. A fuel cell propulsion system that reliably meets the target energy, power, weight, and durability requirements would provide substantial advantages for military UAV missions. To date, however, few systems have been developed that meet the target requirements that would enable widespread adoption of fuel cells as the primary propulsion system for UAVs.

To determine the target requirements, discussions with engineers and program managers within the U.S. military that have first-hand experience designing and operating UAVs were conducted to determine the energy and power densities for existing mid-sized UAV power plants. While the particular sources cannot be listed for confidentiality reasons, those engaged have all developed UAVs for the U.S. Armed Forces. These discussions were intended to

determine the primary power, energy, and weight requirements for existing UAVs, as well as what is desirable for future designs. It was quickly realized that the primary problems facing small military UAVs used for surveillance is that those powered with ICEs are too noisy and require significant maintenance, and those powered with batteries have unacceptably short flight times. There is significant interest in technologies that can resolve both of these issues and fuel cells are a very viable candidate.

Many types of fuel cell systems have been proposed and demonstrated for use in UAVs where a particularly in-depth discussion for fuel cell UAV developments through 2010 can be found in [165]. A few of those systems are highlighted here. AeroVironment has demonstrated several fuel cell powered UAV systems intended to be used by the military, such as the Hornet [166] and Puma [167]. These systems utilize LT-PEM fuel cells that are capable of flights up to seven hours for the Puma, and are fueled with hydrogen stored in a sodium borohydride ($NaBH_4$) pellets that, when mixed with water, generate on-board hydrogen gas. Similarly, Kim et al. also demonstrated a UAV powered with a PEM fuel cell that utilized sodium borohydride for on-board hydrogen fuel storage [168]. Demonstrated flight times in their research have not quite reached two hours, substantially less than the Puma; however, the work done by Kim et al. is in the public domain, which provides significant insight into the fuel cell systems development. The Stalker XE UAV [169], constructed by Lockheed Martin, is powered with a SOFC developed by Ultra Electronics AMI [170]. The Stalker XE is fueled with propane and is capable of 8+ hours of flight time. Hydrogen Energy Systems (HES) develops commercial fuel cells for integration into UAVs [171]. They have developed methanol, $NaBH_4$, and pure hydrogen on-board fuel storage systems for their fuel cells, depending on the UAV application requirements.

With the exception of the SOFC-based power plant developed by Lockheed Martin, the fuel cell systems developed for UAVs all suffer from the main drawback in that they do not operate on a commonly available fuel that is used by the U.S. military. Fueling power plants with a commonly available fuel is an essential requirement for the U.S. military, as using uncommon fuels creates significant logistics problems when trying to bring different types of fuels to the military theatre. For equipment that requires refueling, the U.S. military has a single fuel policy, and strongly desires for all machines to run on the logistics fuel called JP-8, which is similar to diesel. Use of propane is one of the few exceptions allowed, particularly for special operations that involve UAVs. Because propane can be purchased almost anywhere in the world, it is often favored over JP-8 for some missions, as it can be purchased locally without raising suspicion. From discussions with military personnel, it is highly desirable to have a UAV propulsion plant that is fueled with JP-8 or propane, has a long run time, and is extremely quiet.

Beyond the existing problems with mid-sized UAVs currently faced by the U.S. military, the general technical requirements for UAV power plants were also determined. From the discussions, military UAV operators desire a minimum of ten hour runtimes for extended flight missions, and they require at least twenty missions before the power plant fails or needs to be replaced, equating to a total lifetime of 200 hours. It was also learned that a UAV will often experience a catastrophic crash during flight or while landing before its expected twenty mission lifetime, making longer power plant lifetime requirements somewhat irrelevant. Nevertheless, premature crashes are not always the case, and while military operators require a minimum of 200 hours, they ultimately desire lifetimes of 1000 hours.

Regarding the power, energy, and weight requirements, it was also learned that existing power plants for mid-sized UAVs, including the BoP equipment, typically take up no more than

a third of the total take-off weight, while another third of the weight is taken up by the fuel and fuel tank, and the rest includes the airframe, motor, and payload. Additionally, power plants are generally designed to produce at least 35 W/kg (power per mass of the entire aircraft) for fixed wing aircraft, and 140 W/kg for helicopters and multirotor aircraft. Current power plants used for mid-sized UAVs generate approximately 250 to 3500 W. Some of the military personnel also provided specific power output, weight, and volumetric data for the power plants currently used. For example, a 50 kg fixed wing aircraft presently uses a 3000 W engine with a volume of approximately 30 L. Although the engine in this example produces 3000 W, a 50 kg fixed wing plane could fly with only 1750 W of power assuming the described requirement of only 35 W/kg. Thus, the minimal power density of the engine and BoP equipment can be calculated as 58.3 W/liter. However, it was described that volumetric constraints are not as important as weight constraints, providing some flexibility in power density metrics.

For selecting a target fuel cell system size, many of the discussions with UAV operators indicated there is present need for power plants that provide approximately 250 W of net power for propulsion. In setting the target weight and volume requirements, it was assumed that the BoP equipment (electronic controller, air compressor, cooling fan, flow controllers, valves, and electronic control unit) consume approximately 20% of the total power output. Additionally, to be conservative, it was assumed that a full-sized fuel cell stack will generate a power density that is about 10% less than at the single cell level. Therefore, the gross power of the fuel cell stack should be designed assuming 30% will be lost, indicating that 360 W is needed to produce 250 W for the primary propulsion. With 250 W put towards the primary propulsion power plant, the UAV should weigh no more than 7.2 kg, and the fuel cell system including BoP equipment should weigh no more than 2.4 kg. Assuming a power density requirement of 58.3 W/liter, the

total volume of the fuel cell stack and BoP equipment should be no more than 4.3 L. The fuel cell system discussed in the remainder of this Chapter was designed to produce 360 W of power weighing no more than 2.4 kg within a 4.3 L volume.

## 7.2 Subsystem Design

The primary components in this system include the fuel cell stack, the fuel reformer, and the electronic control hardware. Each subsystem requires its own BoP equipment, startup/shutdown protocols, and operational protocols to operate effectively. Additionally, they must all allow for efficient integration that meets all of the target power, energy, and weight requirements. In the following sections, a description of commercially available parts and design considerations for the different components required in the proposed integrated reformer fuel cell system is presented.

### 7.2.1 High-Level Fuel Cell Stack Design

Fuel cell stacks involve complex designs of bipolar plates, gaskets, and MEAs. The most common design is to stack a number of nth unit cells, shown in Figure 2 and copied below, in order to achieve the desired voltage and power output level. Each component must be optimized so that when assembled, the final completed stack will meet the target weight, durability, and volume constraints. At a high level, the fuel cell stack must generate approximately 360 W, and the total system should weigh no more than 2.4 kg (5.3 lb). To operate the HT-PEM fuel cell on reformate produced from propane cPOx with high power densities, operating temperatures of 200$^{o}$C are desired. At this temperature, operating pressures of 200 kPa have been shown to be effective for meeting the required minimum 200-hour durability metric.

Practical fuel cell systems are designed with a target stack voltage that is a few volts higher than the operating voltage of commonly available electronic equipment which tend to operate on voltages that are multiples of 12, i.e. 12V, 24V, 36V, etc. In this design, the primary application to power is a UAV electric motor that commonly operates on 12V. Thus, a target stack voltage of 14-16 volts is desirable. When operating on propane cPOx reformate, single HT-PEM fuel cell tests achieved a power density of approximately 240 mW/cm$^2$ at 200$^o$C, 200 kPa, and at a current density of 0.4 A/cm$^2$ at 0.6 V. Under these operating conditions, a 25 cell stack of with an active area of 60 cm$^2$ per cell operating at 0.4 A/cm$^2$ and 0.6 volts would produce 360 W of power at 15 V and 24 A.

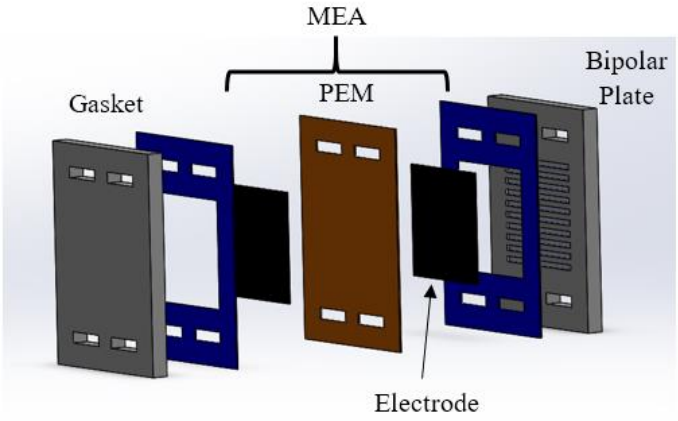


Figure 2: Exploded view of a single fuel cell

A 25 cell stack with a 60 cm$^2$ active area for each cell has approximately 1500 cm$^2$ of surface for both the anode and cathode. Therefore, to operate at a current density of 0.4 cm$^2$ with a stoichiometric ratio of 1.5 at the anode and 2.0 at the cathode, $H_2$ and air flow rates of 6.3 and 20.04 SLPM, respectively, are required. The $H_2$ flow to the stack will be generated from the fuel reformer, however the air required must be delivered at a pressure of at least 200 kPa in order to maintain the desired stack durability. Therefore, some sort of air compressor is required. The

majority of existing commercial air compressors used for mobile applications are designed to be used in ICEs, which require much larger amounts of air than are required for our small system. However, quite recently, a company named Celeroton, after being commissioned by the U.S. Department of Energy (DOE), developed small, electronically actuated air compressors specifically designed for mobile fuel cell systems [172]. One compressor listed with their available products, the CT-15-150, is capable of providing around 50 SLPM of gas flow at a pressure ratio of 1.5, for around 80 W of power, where the compressor only weighs 110 g. Generally, the isentropic efficiencies of these compressors are around 70%. Although pressure ratios around 2.0 are desired for the proposed fuel cell system here, the capabilities of the commercially available compressors from Celeroton are very appealing. It is mentioned on their site that customizable options can be designed by Celeroton where it seems likely that lower flow rates and high pressure ratios can be achieved.

For a fixed flow rate, one of the most lightweight options is to use a constant flow regulator such as those produced by The Lee Company [173]. These flow regulators provide a constant gas flow over a wide range of varying inlet pressures. A 20 SLPM flow regulator needed for air can be found on The Lee Company's product guide, and weighs only 28 g.

Although the air flow rate to the cathode can be held constant using a flow regulator, the flow regulator does not control the pressure. To ensure the cathode side of the stack is not over pressured, a pressure regulator must be added to the system to ensure proper flow control. Double stage pressure regulators are designed to reduce pressure progressively in two stages rather than one. Unlike a single stage pressure regulator, double stage regulators do not need constant adjustment if the inlet pressure falls, guaranteeing a consistent pressure at the outlet as long as gas is being supplied at a higher pressure on the inlet. Although a few companies exist

that make small two stage pressure regulators, Beswick Engineering produces a two stage pressure regulator (PRD 3) that reduces inlet pressure up to 500 psi (3447 kPa) down to pressures around 20 psi (138 kPa) [174]. It is approximately the same size as 10 quarters stacked together, and weighs only 23 grams when made of aluminum. When combined with a 28 g flow regulator and 110 g air compressor, the entire air flow regulating system weighs 161 g. The mass of the reformer will be considered in section 7.2.3. For completeness, it is also assumed that 2 cm of tubing will be necessary between each component for a total of four connections, as well as one thermocouple for measuring the cell temperature. Assuming the connection piping is made of stainless steel, is the same diameter, and has the same wall thickness as the fuel reformer housing (31.75 mm diameter, 2 mm thick), then the mass of the connection piping is approximately 27.1 g. If a 10 cm 14 gauge K-type thermocouple is used at the reformer, its mass will be 1.7 g. Overall, the mass of the compressor, air regulating equipment, and the interconnection piping is 189.8 g.

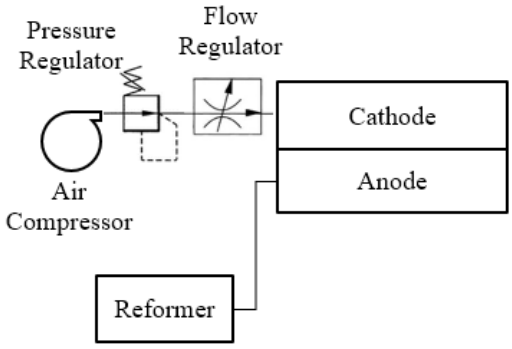


Figure 38: Simplified fuel cell stack and fuel/air flow control design schematic

### 7.2.2 Bipolar Plates and Fuel Cell Design

Conventional fuel cell stack designs incorporate multiple cells connected in series with bipolar plates placed on either side of each MEA. These bipolar plates provide the primary

structural support to the fuel cell stack, serve as current conductors between adjacent MEAs, facilitate heat management, and are also typically designed to serve as internal manifolds for the reactant gases and cooling fluids. To serve all of these functions, the bipolar plate must be an excellent current conductor, have high thermal conductivity, resistance to corrosion, be mechanically and chemically stable, and have very low gas permeability. Also, specific for UAV applications and most mobile applications, bipolar plate materials must also be low-weight. Due to the multifunctional nature of bipolar plate materials with extremely demanding requirements, many substrate materials and coating combinations have been recommended, and excellent reviews can be found in [175], [176], [177], [178]. As the focus of this research is not on improving or advancing a specific bipolar plate design, this section provides general recommendations regarding materials and design patterns that are most suitable for HT-PEM fuel cells.

The two most common types of bipolar plate materials for fuel cells are graphite and stainless steel alloys. Graphite has been the bipolar plate material of choice for decades due to its excellent chemical and electrical durability properties in the harsh fuel cell environment; however, its use was and remains limited to stationary and laboratory applications. Because of its brittleness, bipolar plates made from graphite need to be much thicker than metallic bipolar plates to be robust enough for long-term mobile operation, and thus they weigh significantly more than metallic bipolar plate designs. Additionally, graphite-based plates are difficult and expensive to produce in large quantities since milling and molding manufacturing techniques take much longer than quick stamping procedures used for metallic bipolar plates [179]. Because metallic bipolar plates can be manufactured more easily, are cheaper, and offer weight reductions

of around 60% when compared to graphite-based bipolar plates [180], they are the primary choice for mobile fuel cell operations.

Of the materials and material coatings examined, very few researchers have focused specifically on the best bipolar plate material for PBI-based HT-PEM fuel cells; however, much of the research in LT-PEM bipolar plate materials can be borrowed as they share similar requirements. In addition to similar durability, conductivity, and corrosion resistance requirements to LT-PEM bipolar plate materials, HT-PEM bipolar plates must also exhibit corrosion resistance to high concentrations of phosphoric acid (PA). If the bipolar plate material is not resistant to PA corrosion, pitting in the plate will occur, increasing its porosity. An increase in plate porosity will lead to PA migration from the membrane to the void volume of the bipolar plates, which will ultimately result in MEA degradation from PA loss and increased ohmic resistances within the fuel cell [66]. This effect was witnessed in the early development of PAFCs when investigating bipolar plate materials for their use. This ultimately led to the acid-filled porous graphite plate design, which is effective, but unsuitable for mobile applications as it is based on graphite [93]. Beyond stainless steels, other metals have been proposed for bipolar plate materials, including aluminum and titanium, which have lower densities than stainless steels and may provide lower system level weights. However, they tend to have much higher corrosion rates when compared to graphite and stainless steel based plates [181].

While the majority of metallic bipolar plate material studies are focused on designs for use in LT-PEM fuel cells, there are a few that consider metallic bipolar plates specifically suitable for HT-PEM fuel cells. Wang et al. examine the corrosion behavior of austenitic stainless steel without any kind of coating in a PA environment [182]. They observed severe surface changes of the stainless steel after being exposed to PA at 170$^{o}$C, indicating a corrosion-resistant coating is

needed if stainless steels are to be used as bipolar plate materials. In [183], the authors examined the corrosion rates, measured in $A/cm^2$, of several stainless steel and nickel-based materials in the presence of PA at temperatures up to $130^oC$. For the stainless steel materials, their results surprisingly revealed that the cheapest material, stainless steel 304 (18% Cr, 10% Ni, 72% Fe), exhibited the lowest corrosion rates. More expensive stainless steels that have Ti, Mn, and Mo, exhibit significantly higher corrosion rates, where a strong correlation was particularly witnessed with the addition of Mo. Of the nickel-based alloys, the alloy comprised of 80% Cr and 20% Ni exhibited the highest corrosion resistance. Similar to the stainless steels tested, as more Ti, Cu, Mo, and Nb were added to the nickel alloys, the corrosion rates increased. The desired corrosion rate for LT-PEM fuel cells set by the DOE is $< 1\ \mu A/cm^2$, which was never achieved for the tested materials. The best performing nickel alloy had a minimum corrosion current density of $16.1\ \mu A/cm^2$, where the best performing stainless steel showed a corrosion current density of $37.5\ \mu A/cm^2$. Ultimately, these results indicate that cheap stainless steel materials may be suitable for HT-PEM bipolar plates if some sort of surface treatment is applied that can reduce the corrosion rates to acceptable levels.

Similar to the studies on bipolar plate materials, extensive research into coatings of different bipolar plate materials has also been conducted. One extensive review conducted by Karimi et al. [178] describes that the greatest level of anti-corrosion resistance are seen when researchers used noble metal coatings such as gold and platinum. In [184], the authors examined the corrosion resistance of gold plating with thicknesses of 10 nm on stainless steel bipolar plates (stainless steel 316L). At 10 nm gold plated coating, corrosion current densities $< 1\ \mu A/cm^2$ were witnessed, meeting the DOE targets set earlier. Specific for HT-PEM fuel cells, Hartnig et al. compared four different types of bipolar plate materials/coatings in a HT-PEM environment to

study the phosphoric acid uptake and lifetime voltage degradation for the different bipolar plate materials [66]. Specifically, they examined two different high temperature graphite composites, surface treated graphite, and gold plated stainless steel. Both the surface treated graphite and gold plated stainless steel exhibited negligible phosphoric acid uptake in the bipolar plate, while the two graphite composite plates exhibited significant amount of acid uptake.

Coating bipolar plates with gold may sound prohibitively expensive; however, because the coating thickness required is so small, the material cost is actually quite low. For example, the fuel cell stack proposed in this chapter consists of 25 cells with an active area of 60 $cm^2$ each. Because each cell requires a bipolar plate on either side of the MEA, 50 bipolar plates with a total surface area of 3000 $cm^2$ must be coated in gold for the entire stack. If the gold coating is 10 nm thick, then the total volume of gold in the fuel cell stack is approximately 0.003 $cm^3$, equivalent to 0.058 g. Gold prices are currently around $34/g [185], thus the material cost of the gold in the entire fuel cell stack is only $1.97. Even if the amount of gold needed were to be doubled either for thicker plating or to cover more surface area, the material price of the gold in the entire stack is still less than $4. Overall, the material cost of gold does not seem to be a major cost barrier, although processing cost would need to be considered in developing a comprehensive cost estimate of a finished bipolar plate suitable for use in a HT-PEM stack.

Beyond the material requirements for bipolar plates, the physical design is also of the utmost importance. Much of the focus in literature on bipolar plate design is centered on the optimal flow field pattern used that most effectively facilitates reactant and coolant fluid flows. For mobile LT-PEM fuel cells, there are generally three types of channel designs commonly used by the major fuel cell manufacturers described as straight, serpentine, or zig zag pattern types. A recent review of the various patterns used in bipolar plates can be found in [186], where the

authors discuss a novel bipolar plate design using straight pattern flow field channels. Straight pattern bipolar plates, shown in Figure 39, result in the lowest pressure drop across the channels, minimizing the amount of energy required to pressurize inlet gas feeds. However, they often suffer from non-uniform reactant gases and coolant fluid flows because the gas flow distance from the fuel inlet manifold to the fuel outlet manifold is not uniform across the cell, leading to local fuel starvation in some part of the cell.

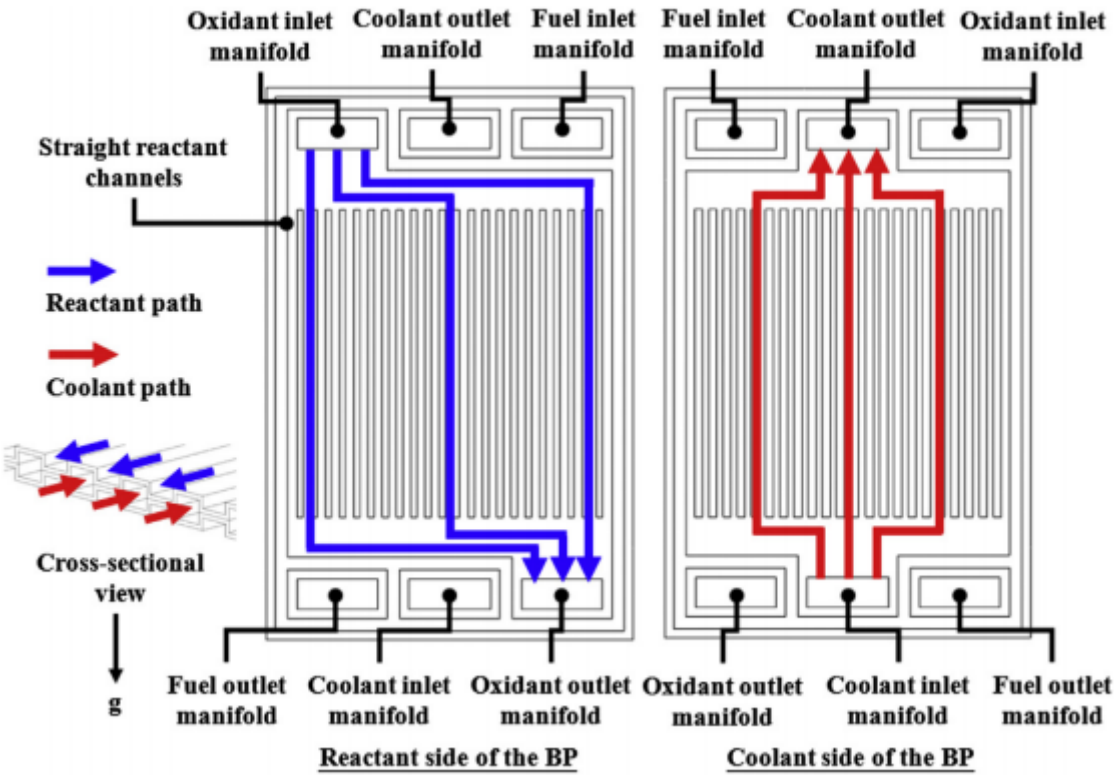


Figure 39: Design diagram of a stamped bipolar plate with straight reactant channels reprinted from [186] with permission.

Serpentine pattern bipolar plate designs, shown in Figure 40, address this issue by making each flow channel uniform; however, they tend to suffer from high pressure drops. In [187], the authors examined the impact of serpentine and straight flow channel designs for a HT-PEM fuel

cell. Their results show that serpentine patterns result in significantly better performance, albeit with higher pressure drop because of the more uniform flow channel lengths.

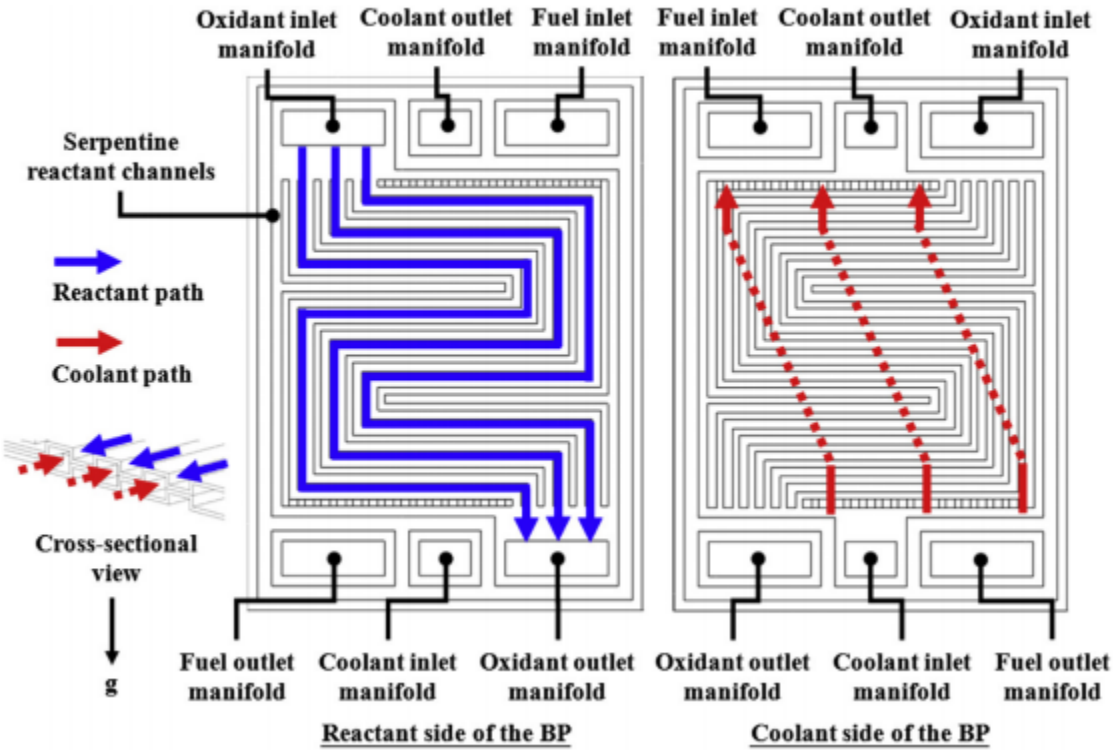


Figure 40: Design diagram of a stamped bipolar plate with serpentine reactant channels reprinted from [186] with permission.

Zig zag patterns, shown in Figure 41, provide marginally higher pressure drops than straight channels, but also allow for more uniform reactant and coolant coverage of each individual cell, providing a balance between the advantages of drawbacks of the straight and serpentine flow channel designs. Stacks utilizing a zig zag pattern tend to show the highest power densities. The zig zag pattern is most commonly adopted by automakers such as Honda for their fuel cell stacks [186], [188].

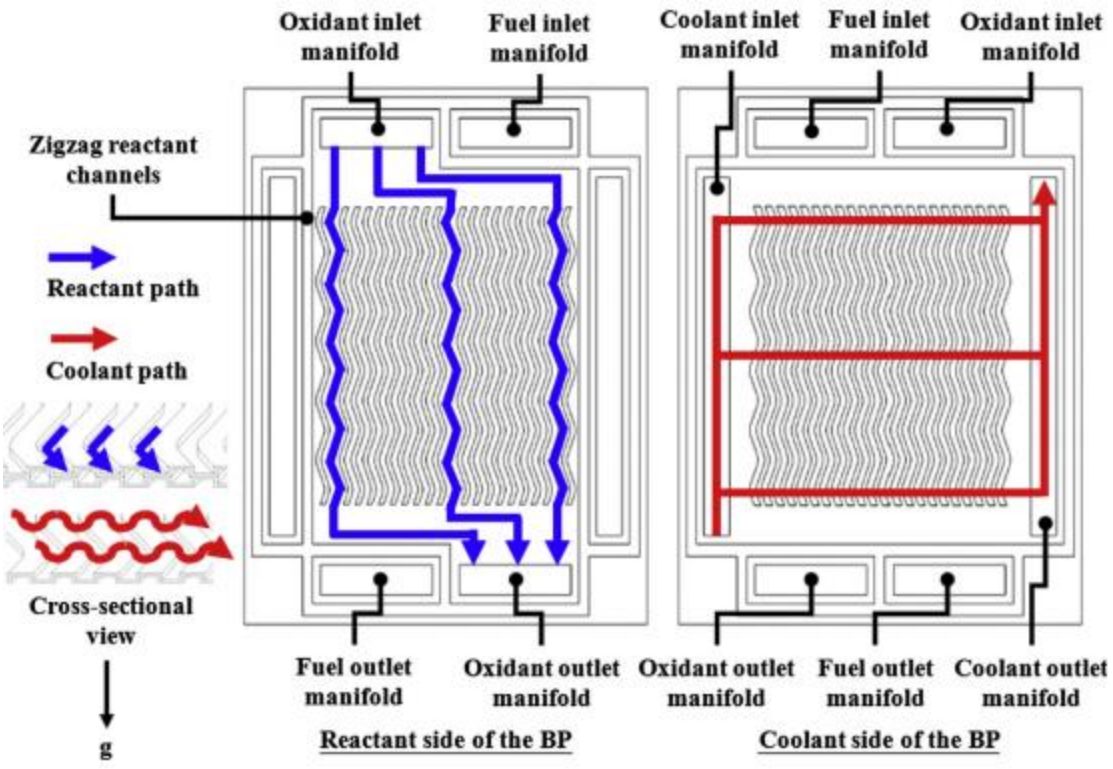


Figure 41: Design diagram of a stamped bipolar plate with zig zag reactant channels reprinted from [186] with permission.

As most of the literature on metallic bipolar plates is focused on development of LT-PEM fuel cells, liquid water management issues greatly influence the choice in flow channel design with an emphasis on low pressure drop flow field patterns [189]. Because liquid water removal is unnecessary in HT-PEM fuel cells, it is expected then that the pressure drop across the cell for HT-PEM bipolar plates will not be as high as comparable LT-PEM bipolar plates, regardless of the flow field pattern. Because pressure drop in a HT-PEM is not as great as a LT-PEM, a serpentine pattern would likely be the best suited because it offers the most uniform surface coverage. Nevertheless, a zig-zag pattern may also suffice providing adequate surface coverage of the reactant, and minimal pressure drop. A useful future analysis might focus on comparing these two flow channel designs in a PA doped PBI based HT-PEM fuel cell.

Beyond the gas flow channel design pattern, proper sealing of the bipolar plates that eliminates gas venting can be difficult. One common design is to have a channel along the perimeter of each bipolar plate where a gasket is placed, as shown in Figures 39-41. Effectiveness of these designs is typically only determined through trial and error.

In summary, the most suitable bipolar plates for mobile HT-PEM fuel cells would be constructed from a stainless steel alloy (304 or 316L for example) and coated with a thin layer of gold to provide corrosion resistance. Additionally, a flow field design based on a serpentine pattern would provide the best possible performance, as low pressure drop and water management issues are not as great of a concern for HT-PEM fuel cells.

To estimate the weight of a fuel cell stack design, the number of bipolar plates and their size must be estimated. In most PEM fuel cell designs, two bipolar plate materials are bonded together to form cooling channels in between, as shown on the left side of Figure 39. For the entire fuel cell stack, there are bipolar plates (formed by joining unipolar anode and cathode plates) in between each pair of MEAs, and one unipolar plate at either end of the fuel cell stack. For a 25 cell stack, this amounts to a total of 24 bipolar plates and 2 unipolar plates. When considering bipolar plate designs found in patent literature such as [190], the surface area of the bipolar plate that is in contact with the active area of the MEA is approximately 88% of the total bipolar plate surface area. Assuming this same relationship holds true for other bipolar plate designs, a 60 $cm^2$ MEA will require bipolar plates with total surface areas of 68.2 $cm^2$. If 0.25 mm thick sheet stock is used for the bipolar plate construction as suggested in [180], then the total volume of each plate is 1.705 $cm^3$. Because stainless steel has a density of 8000 $kg/m^3$, the total mass of 24 bipolar plates and 2 unipolar plates is approximately 0.682 kg. If it assumed that the bipolar plates account for approximately 80% of the total weight of the stack as suggested in

literature [191], then the total weight of a fuel cell stack that produces 360 W of power is approximately 853 g. If we add this to the air control hardware, including the air compressor, then the total weight of the system is now at 1,041.8 g.

### 7.2.3 Fuel Reformer

The proposed fuel reformer in this design utilizes a propane cPOx reaction. The primary advantage of using a cPOx fuel reformer is that it can be made to be very lightweight as only air flow, fuel flow, and operating temperature need to be controlled. A 25 cell stack with individual cell surface area of 60 $cm^2$ has a total stack surface area of 1500 $cm^2$ on either side of the MEA. Operating at a stoichiometric ratio of 1.5 at the anode, this requires 6.3 SLPM of $H_2$ flow at the anode. With the conversion rates of propane cPOx discussed in Chapter 5, the cPOx propane reformer requires an inlet flow of 1.57 SLPM (0.052 g/s) of propane to generate the necessary 6.3 SLPM of $H_2$. To maintain an $O_2$/C ratio of 0.53, air flow of 12.06 SLPM (0.26 g/s) is required.

In the fuel reformer, proper fuel and air flow control is of the utmost importance because if excess air is added to the reaction, then the reformer temperature may spike, and overheat the fuel reformer. Conversely, if too little air is added, then incomplete conversion will occur, and the temperature may drop too low, causing coke formation. Coke may plug up the reactor and/or be sent downstream into the fuel cell covering up catalyst activation sites. From a practical perspective, equilibrium data presented in Figure 11 (Chapter 5) shows that there is some margin of safety in the $O_2$/C ratio, where the hydrogen production will not vary too significantly if the $O_2$/C ratio drifts up or down. Interestingly, the amount of hydrogen produced reduces much more rapidly when the $O_2$/C ratio decreases than when the $O_2$/C ratio increases indicating that the chance of operating in a detrimental mode is greater for a reduction in the $O_2$/C ratio than an

increase. If the $H_2$ concentration reduction is limited at $\pm$ 2% net, then the safe range lies between an $O_2$/C of 0.52 and 0.57. Assuming the propane flow is held constant at 1.57 SLPM, then this limits the air flow between 11.77 and 12.91 SLPM.

The fuel reformer tested in Chapter 5 was built by PCI and uses the Microlith design, which is essentially a stack of several wire meshes that have been impregnated with the catalyst used. The reactor itself was only 31.75 mm in diameter, and 8.9 mm long, which is quite small. Although the weight of the reactor was unknown, other PCI reactors that are similar in diameter but four times greater in length are about 46 g [117]. For the cPOx experiments conducted, the reactor was placed in an oversized Inconel tube so it could fit into the testing furnace; however, the reactor housing could easily be much shorter if used in a mobile application. A 5 cm long Inconel tube (density of 8193 kg/m$^3$) that would fit a 31.75 mm reactor with 2 mm thick walls weighs approximately 11.6 g, leading conservatively to a total fuel reformer mass of 57.6 g.

There are several ways to control air and propane flow where the same pressure regulator (23 g) and flow regulator system used to control the air flow to the cathode (28 g) described in Section 7.2.1 can also be used for the air flow to fuel reformer. Flow regulators produced by The Lee Company [173], provide a constant gas flow over a wide range of varying inlet pressures. According to the company's product guide [173], a 12 SLPM flow regulator needed for air weighs only 28 g. Similarly, a 1.6 SLPM flow regulator needed for the propane flow weighs only 6.4 g. When combined with the 23 g pressure regulator for both air and propane, the air and propane flows to the fuel reformer can be controlled for a total 80.4 g.

The air provided to the fuel reformer must be supplied at a pressure greater than 200 kPa to ensure fuel pressures of 200 kPa at the anode of the fuel cell stack, requiring the use of an air compressor. The compressor used to supply air at the cathode supplies approximately 30 SLPM

more air than the 20 SLPM needed at the cathode. Thus, the air compressor should be capable of supplying air to the fuel reformer as well, for a total of 32 SLPM of air needed for the entire system.

The proposed reformer subsystem is illustrated schematically in Figure 42. Given the mass of the fuel reformer, flow and pressure regulators, the entire proposed fuel reformer subsystem would have a mass of 138 g. For completeness, the weight for the additional piping used between components, and a thermocouple place on the fuel reformer, should also be included. If there is approximately 2 cm of stainless steel tubing (8000 kg/m$^3$) connecting each component shown in Figure 42 (6 connections), and assuming the same pipe dimensions of the fuel reformer, then the rest of the piping is approximately 11.6 g. If a 10 cm 14 gauge K-type thermocouple is used at the reformer, its mass will be 1.7 g. This brings the total fuel reformer fuel cell system mass up to 1,193.1 g.

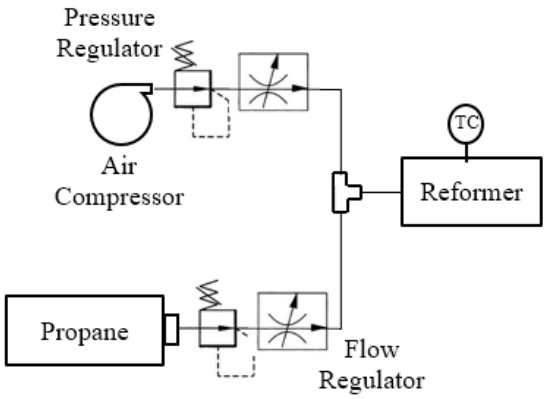


Figure 42: Simple fuel reformer and flow control design schematic

### 7.2.4 Startup and Shutdown Considerations

To ensure long-term durability of the fuel cell system, proper startup and shutdown protocols should be developed that mitigate voltage degradation that is commonly experienced during each

startup and shutdown sequence. Several protocols were discussed in Section 3.7, where the sequence labeled *Protocol C,* was suggested for minimal BoP equipment required in a mobile system.

The advantage of this startup/shutdown protocol is that a reducing gas is not required to fill the anode and cathode of the fuel cell for long term storage as indicated in *Protocol A*. Additionally, an inert gas such as pure $N_2$ is not required for startup. Eliminating the need for a reducing gas or inert gas flow during start/shutdown is very advantageous for a mobile fuel cell system design for use in the military, as those gases are difficult to obtain in the field. However, the primary concern with this procedure is that CO is sealed in both the cathode and anode during storage, which will likely occur at low temperatures where it adsorbs strongly onto Pt. Nevertheless, it is expected that once the fuel cell stack is heated up to its operating temperature with air flow at the cathode, then the CO that is formed will oxidize from the oxygen available in the air at the cathode, as well as the oxygen in the water in the anode that will be generated from the $H_2$-$O_2$ reaction, or from the reformate delivered to the anode.

To properly execute this protocol, a monitoring and control system is required to actuate gas flows to the fuel reformer and fuel cell. The design schematic (Figure 43) shows the necessary equipment, in addition to the equipment described earlier in Figure 38 and Figure *42*. In addition to the equipment discussed in the fuel cell stack and fuel reformer subsystem design sections, an additional seven solenoid valves (all set to normally closed), one check valve, and three filters are required for the full system design. The filters after the air compressor and propane tank ensure no particulates make their way downstream to the fuel reformer or fuel cell stack. A filter after the reformer protects the fuel cell stack in case of coke formation. The check valve

following the air flow regulator to the reformer ensures that propane does not flow back into the air line.

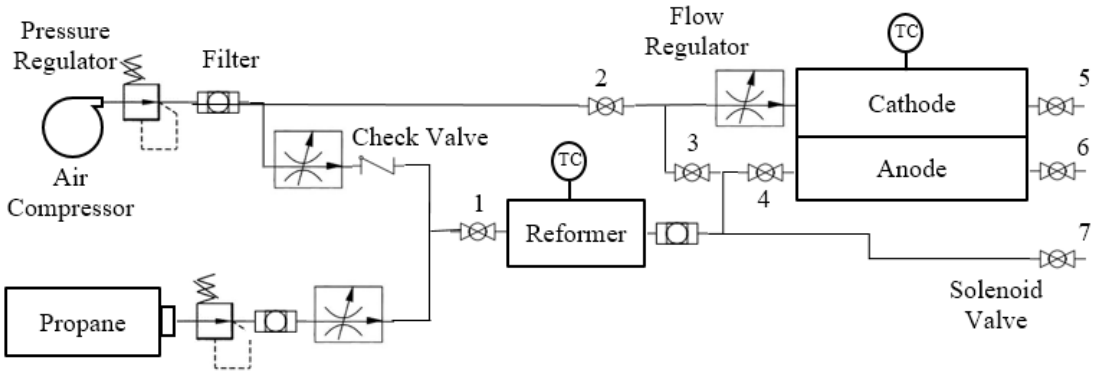


Figure 43: Full integrated reformer fuel cell system design schematic

For the startup and shutdown protocol, the individual solenoids that should be activated for each step of *Protocol C* are as follows (note the protocol has been slightly modified from the previous version to incorporate the reformer startup procedure):

1) For startup, heat the fuel cell up to operating temperature and once reached, heat the fuel reformer up to the light-off temperature.
2) Once the light-off temperature is reached, open solenoid valves 1 and 7, and turn the air compressor on.
3) After the reformer reaches its operating temperature, open solenoid valves 4 and 6 to allow fuel to flow in the anode, and close solenoid valve 7. Let reformate flow in the anode for ~10 seconds before moving on to the next step.
4) Open solenoid valves 2 and 5 to allow air to flow into the cathode while maintaining a dummy load that keeps the cell potential below 0.8 V.
5) Once the fuel cell reaches a steady voltage level (~30 seconds), set the load to the desired current density and run the fuel cell for the desired time frame.

6) To begin shutdown, turn off the primary load and switch over to a small dummy load that maintains the cell potential below 0.8 V.
7) Turn off air flow to the cathode by closing solenoid valve 2, and maintain a dummy load until the cell voltage drops to below 0.2 V.
8) Open solenoid valve 3, which allows the anode gas feed to fill both the anode and cathode, ensuring that the voltage of the cell remains below 0.2 V using a dummy load, and purge the cell for a period of time that allows for adequate removal of $H_2O$ and $O_2$ from the fuel cell (~2 min).
9) Open solenoid valve 7, then close solenoid valves 3, 4, 5, and 6, sealing both the inlet and exhaust ports of the anode and cathode for the cell to remain in storage.
10) Turn off the air compressor and close solenoid valve 1. The fuel cell is now ready for long-term storage.

It should be noted that there are several heating options for the fuel cell stack and fuel reformer. One option might be to use a combustor and burn some of the propane for stack startup. This may not be the best option as the combustion system adds additional weight to the overall device. A simpler setup might be to pre-heat the reformer and fuel cell stack using electrical resistive heating with some kind of wrap around heat tape or blanket. These systems can be used on the ground, then taken off for flight eliminating, the weight and complexity of an on-board heating system. For this analysis, it is assumed that an external electrical based heating system would be utilized and thus allows for the startup protocol, but adds no weight to the in-flight device.

Sourcing lightweight, commercially available solenoid valves that can also handle the flow rates required in this system was quite difficult, indicating that this may be a source of future

development. Perhaps a different system such as pneumatically operated valves might prove to be more light weight if designed properly; however, pneumatic valves that are lighter than solenoid valves could not be found. One of the primary issues with solenoid valves is that they constantly consume power, providing a continuous parasitic load. One solution to this might be to use latching valves, which lock open or closed after a quick burst of power. However, none could be found that satisfied the weight and flow requirements. In the end, careful attention was paid to finding low power consuming solenoid valves.

In the U.S., the mostly widely used valve sizing method is to calculate the required Cv or flow capacity index, which is defined as the number of U.S. gallons of water per minute that will flow through a valve with a pressure drop of 1 psi. While the definition is based on liquid flows, the Cv required for gas flows can still be determined where each manufacturer often has their own method for calculating the Cv. According to ASCO [192], for gases they use the Equation.:

$$Cv = \frac{Q}{960\sqrt{dP(P1+P2)/(S.G.*T)}} \qquad \textit{(Eq. 34)}$$

where $Q$ is the flow rate in SCFH, $P1$ and $P2$ are the inlet and outlet pressures, $dP$ is equal to $P1 - P2$, S.G. is the specific gravity of the gas at 60$^{o}$F and 14.7 psia, and T is the temperature of the gas in Rankine. To calculate the Cv, the highest flow rate that the solenoid valves will see is the 20 SLPM of air that is required for the cathode. Additionally, it is assumed that the inlet pressure to the valve is approximately 202 kPa, the outlet pressure is 200 kPa, S.G. of air is equal to 1, and the temperature is room temperature 72$^{o}$F or 532 Rankine. Converting these to the proper units, the Cv value calculated using *Eq. 34* is 0.24. Aside from the ASCO model, several other manufacturers models were used to validate ASCO's calculation. All of the models used resulted in a Cv of 0.24.

The ideal solenoid valve would be a latching valve that is lightweight and has a Cv value of at least 0.24 to ensure minimal pressure drop. There exists numerous solenoid valve manufacturers such as ASCO, Parker, SMC, Gems, and Pneumadyne, all of whom produce possible valve options. However, none of the commercially available valves seem to meet the desired specifications. The only commercial product to be found that almost meets all of the target requirements is the Parker's Series MX, Miniature Solenoid Actuated Poppet Valves [193]. These solenoid valves have a mass of 8.5 g, consume only 0.25 W of continuous power, but are only capable of flow rates around 17.5 SLPM, which is not quite the maximum required air flow amount of 20 SLPM. However, it is expected that a custom valve similar in construction may be capable of slightly larger flow rates, and therefore the valve described above will be used for modeling purposes here. Using this valve type, the seven solenoid valves have a mass of 59.5 g total. According to the operating protocol, the maximum number of valves running at any given time is five, consuming 1.25 W of power.

### 7.2.5 Controlling Hardware and Other BoP

Beyond the solenoid valves, there is other BoP equipment necessary for durable operations, such as filters and check valves. In-line 60 micron cartridge filters used to filter out particulates, such as the ones made by Swagelok [194], and the check valves, also made by Swagelok, have masses of 10 and 9.2 g respectively. These components therefore have a total mass of 39.2 g. If it is assumed that there are 22 total piping connections within the whole system, each about 2 cm long with the same cross-sectional dimensions as the fuel reformer, then the total mass from piping connections in the entire fuel cell system is 99.5 g.

To maintain an operating temperature of 200$^{o}$C, the fuel cell stack will likely need additional cooling. The amount of heat energy generated by the fuel cell stack can be determined by

comparing the operating individual cell voltage to the theoretical Nernst potential. When operating at 0.4 A/cm$^2$, the operating voltage is approximately 0.6 V. The theoretical voltage of the cell at 200$^o$C and 200 kPa, with a hydrogen concentration of 28%, can be calculated using *Eq. 5*, and is approximately 1.12 V. Thus the voltage produced is 54% of the theoretical voltage, indicating that 46% of the energy generated is lost to heat. For 360 W of electrical power generated by the fuel cell stack, an additional 306 W of heat will be generated.

A critical review article discussing the different methods used for heat removal in fuel cell stacks was published by Zhang and Kandlikar [195]. Because heat generation within a fuel cell stack is very non-uniform, proper thermal management can be quite difficult. The primary methods involve both active and passive cooling techniques. Passive technologies incorporate materials into the stack such as heat spreaders, also referred to as edge coolers [13], which serve to move heat from the central parts of the stack towards the edges. While this method may be very beneficial in terms of weight and material reduction, proper design to maintain a specific stack temperature, particularly with variable power outputs, can be quite complex. Active cooling techniques, which include some sort of liquid or air cooling technique, may require a number of additional components, but they are somewhat easier to model and control. Several papers discuss different air-cooled stack designs that use a simple axial fan to blow air through cooling channels formed between the bipolar plates of each individual cell [196] and [197].. From both of these analyses, the power required for cooling was around 2% of the total power produced. As the cooling technique is somewhat simpler and does not consume much power, an active air-cooled design was chosen for the current HT-PEM system design.

To determine the proper fan size for this system, a simple model that estimates the air flow required can be written as:

$$\dot{q} = \rho \, C_p \, \dot{m} \, dT \qquad \textit{(Eq. 35)}$$

where $\dot{q}$ is the amount of heat transfer in W, $\rho$ is the density of air (1.2 kg/m$^3$), $C_p$ is the specific heat of air in J/(kg-K), $\dot{m}$ is the amount of air flow required for cooling in m$^3$/s, and $dT$ is the temperature differential between the surface and the bulk fluid. For the proposed fuel cell stack design, 306 W of heat needs to be removed. Assuming that the cooling air used will be delivered at room temperature (20$^o$C), and the stack will be held constant at 200$^o$C, then the temperature difference is 180$^o$C. The specific heat capacity of air is 1005 J/(kg-K). With these assumptions, the air flow required is 5.07 m$^3$/hr (84.6 SLPM). A small 50 mm x 15 mm DC blower that can be readily purchased [198], and is capable of 7.15 m$^3$/hr air flow, consuming only 1.68 W with a weight of 27 g. To ensure proper temperature control, a simple control algorithm that turns the fans on or off when the temperature deviates from its set point could be used for this design.

To operate the valves and fans used during startup, operation, and shutdown, an electronic control unit (ECU) is necessary. The Arduino Uno [199] is an ECU that is low weight, low cost, and easily programmable for the requirements needed in this design. Since the Arduino is not capable of reading K-type thermocouple measurements on its own, an additional thermocouple multiplexer board is required to effectively read the thermocouple signals. An Arduino K-type thermocouple multiplexer shield can be purchased [200] which allows for the capacity of up to eight thermocouples to be read. Both of these boards weigh 25 g each for a total of 50 g.

In addition to controlling all of the actuated valves, the power output of the fuel cell must also be managed. Most often, DC-DC converters are used to regulate the power generated from the fuel cell before it is sent to the various loads. Many authors have studied different DC-DC converter designs and control mechanisms suitable for fuel cell use ([201], [202], and [203]),

where conversion efficiencies might range from 88% to as high as 97%. When selecting a suitable DC-DC converter to integrate into an overall system, it is prudent to select an output voltage that the electronic components will run on. For this design, almost all of the electrical equipment can run on DC current supplied at 12 V. The Arduino is powered using either 5 V or 9 V and will require an additional smaller ECU. DC-DC converters that step 12 V down are readily available [204], and weigh only 8.5 g. Very little information could be found on commercial DC-DC converters specifically built for fuel cell use. However, it is expected that the design of DC-DC converters used in other applications will change very little when applied to a fuel cell. To estimate the realistic weight for a DC-DC converter, a commercially available converter manufactured by DROK that is capable of regulating 600 W of power was used as a model [205]. This converter maintains a constant voltage output and weighs approximately 221 g.

In addition to the fuel cell system, a practical UAV propulsion power plant design will likely be hybridized with a battery for load balancing and short bursts of power needed for climbing, maneuverability, and stabilization in the event of high winds, for example. Additionally, in the event of a catastrophic failure in the fuel cell mid-flight, the battery can be used to control the aircraft for a certain period of time. If it is assumed that in a worst case scenario the battery will need to fully power the UAV for 15 minutes, then the total capacity of the battery required is 90 Wh. Assuming present state-of-the art Li-ion batteries with energy densities of 150 Wh/kg are used [206], then the mass of a 90 Wh battery is approximately 600 g.

When adding up the estimated weight from all of the different components, the total mass of the proposed integrated reformer fuel cell system is 2.23 kg, which meets the 2.4 kg weight limit

target described above. The breakdown of the different components and their weights are presented in Table 10, and the percentage of each component is shown graphically in Figure 44.

Table 10: Component list and weights of the proposed integrated reformer fuel cell system

| Component | Quantity | Weight (g) | Total Weight (g) |
|---|---|---|---|
| Air Compressor | 1 | 110 | 110 |
| Flow Regulator - Air | 2 | 28 | 56 |
| Flow Regulator - Propane | 1 | 6.4 | 6.4 |
| Pressure Regulator | 2 | 23 | 46 |
| Filter | 3 | 10 | 30 |
| Check Valve | 1 | 9.2 | 9.2 |
| Reformer | 1 | 57.6 | 57.6 |
| Solenoid Valve | 7 | 8.5 | 59.5 |
| Fuel Cell Stack | 1 | 682 | 853 |
| K-Type Thermocouple | 2 | 1.7 | 3.4 |
| Cooling Fans | 1 | 27 | 27 |
| ECU | 1 | 58.5 | 58.5 |
| DC-DC Converter | 1 | 221 | 221 |
| Piping | 1 | 99.5 | 99.5 |
| Battery | 1 | 600 | 600 |
| | | **System Total** | **2237.1** |

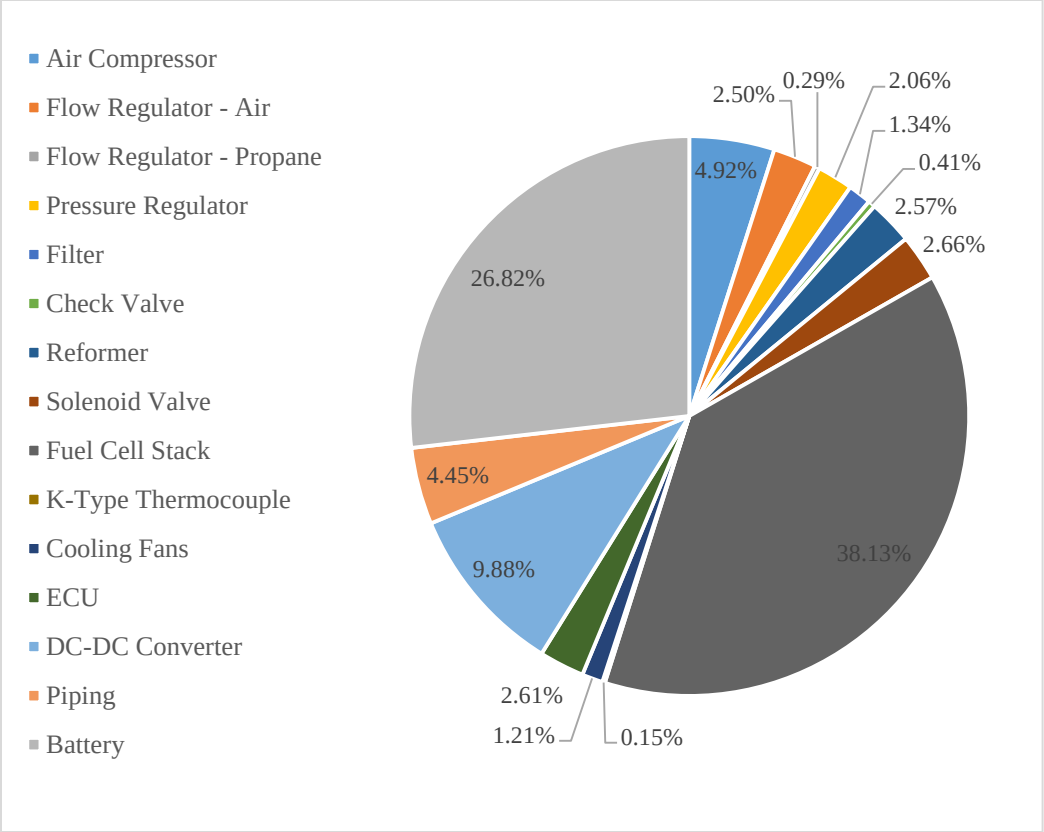


Figure 44: Component weight percentage breakdown of the proposed integrated reformer fuel cell system

For the proposed system, the fuel cell stack accounts for the highest weight percentage at 38.13% followed by the battery at 26.82%. The next largest component is the DC-DC converter, and then the weight from piping and the air compressor are roughly the same. Although the total weight of the proposed system is less than the target maximum, further weight reductions could be expected with increased refinement. For example, the weight of the battery could be greatly reduced if a battery chemistry with a higher specific energy were used. While mainstream batteries presently have specific energy values of around 150 Wh/kg, it is expected that 200 Wh/kg and higher battery chemistries are expected to become more common place in the near future [206]. If a 200 Wh/kg battery were used, then a 150 g reduction (6.7%) would be realized. Similarly, weight reductions in the stack could be realized through greater fuel cell performance,

which would in turn require a smaller fuel cell stack for the same power output. There is also an opportunity to use thinner stainless steel sheet stock to form the bipolar plates. A reduction of 60% from the assumed 0.25 mm thickness is achievable, based on current practice for automotive LT-PEM fuel cell stacks which use unipolar plates that are $\leq$ 0.1 mm thick [207]. Some studies have shown the viability of 0.051 mm thick which would achieve a weight reduction of 80% in the bipolar plate materials used [208]. Additionally, since many of the BoP components proposed are off-the-shelf components, such as the air compressor, solenoid valves, ECU, and DC-DC converter, weight reductions will likely occur if these components were designed specifically for the proposed system. Weight reduction in the fuel reformer and BoP subsystem can be made through advanced manufacturing techniques such as 3D printing. For example, a single part could be made that provides the housing for the pressure regulators, flow regulators, fuel reformer, air compressor, and some of the solenoid valves. This could result in significant weight savings as the individual components can share part of their housing material with another component, thus eliminating many of the piping connections required between parts.

# 8 Environmental Impact

In this section, the environmental impact of the proposed integrated reformer fuel cell system is examined and compared to other existing energy conversion technologies that produce similar levels of power in the 250 W to 5000 W range. Applications that require power levels of these levels use power plants that the Environmental Protection Agency (EPA) refers to as nonroad engines that are conventionally powered with two or four-stroke ICEs that produce significant amounts of emissions. Due to the large number of applications and engine types, regulations are difficult to design and implement because each sector is so small. Thus, nonroad engines

typically emit disproportionally large amounts of emissions compared to other engine types, and the aggregate amount of emissions is quite substantial. These emissions include high levels of carbon monoxide (CO), nitrous oxides (NOx), and various hydrocarbons (HC) that are very hazardous to human health even at low concentrations. Additionally, as many of these engines are typically run in close proximity to their operators, the risk of exceeding regulatory exposure limits is very high.

As the EPA and other organizations continue to pass legislation limiting emission levels, some of their targets may be met through a technology switch rather than advancing current internal combustion engine technology. Some of these technology options include fueling ICEs with ethanol or electrifying devices with fuel cells or batteries. In passenger vehicles, this change has already occurred, first with biofuels and now with both all-electric battery and fuel cell powered passenger vehicles. As renewable propulsion technologies begin to mature, it is likely that the advances found in the transportation sector will filter down to applications traditionally powered with nonroad ICEs.

Nonroad engines cover a broad scope of applications, including lawn and garden equipment, recreational devices, generators/compressors, marine engines, construction equipment, aircraft, and locomotives. There are several excellent studies investigating the energy and emissions for the full fuel cycle for some nonroad engine types including aircraft [209], marine vessels [210], and forklifts [211]; however, there remains a gap in analyses investigating the full fuel cycle energy use and emissions for nonroad applications powered by small spark ignition (SI) engines. These applications include lawn and garden equipment, recreational devices, generators/compressors, marine engines, and some construction equipment.

Several renewable technologies are appropriate for replacing present SI engine technology, such as utilizing biofuels, certain fuel cell types, and batteries. Converting ICEs to run on biofuels may be the simplest change, as retrofitting existing technology may be easier than implementing a completely new technology such as fuel cells. Electrifying devices using batteries has already been done with certain applications (i.e. lawn mowers), but batteries are impractical for powering applications that require significant run times with short refueling times. Fuel cells generate electrical power like batteries, but are capable of achieving significantly longer run times. As fuel cells can be fueled with hydrocarbons such as propane, run times similar to or longer than traditional ICEs allow for a user experience to which most are accustomed. However, adoption and design of fuel cell systems for small-scale power generation is still in its infancy, and well-vetted cost effective systems are uncommon.

The analysis in this chapter compares an ICE fueled with ethanol, a PEM fuel cell fueled with $H_2$, a high temperature PEM fuel cell fueled with propane, a SOFC fueled with propane, and a Li-ion battery which have been suggested as possible replacement technologies for small spark ignition engines used in nonroad applications requiring < 25 hp (19 kW). Argonne National Laboratory's Greenhouse gases, Regulated Emissions, and Energy use in Transportation (GREET) tool is used for estimating most of the well-to-pump fuel cycle emissions, while the use phase data is taken from published literature. This chapter is separated into several sections, one for each technology starting with conventional SI engines, and ends with a final comparative assessment and discussion of the full fuel cycle emissions for each technology.

## 8.1 Conventional two and four-stroke engines that operate on gasoline

Small SI nonroad engines that produce less than 25 hp or 19 kW are commonly used in applications such as lawn and garden equipment, small utility vehicles, generators, outboard and inboard marine engines, and various construction, farm, and industrial equipment. These engines and vehicles are a significant source of pollution, accounting for 26% of mobile source volatile organic carbons (i.e. various hydrocarbons such as gasoline) and 23% of mobile CO emissions [212]. These small engines are disproportionally inefficient compared to their larger counterparts due to low demand, as well as less strict regulations and oversight. Most nonroad engines are fueled by diesel, gasoline, compressed natural gas (CNG), or liquefied petroleum gas (LPG); however, small SI engines under 25 hp (19 kW) are primarily fueled with standard unleaded gasoline that is also used in motor vehicles.

Conventional small SI engines are either two-stroke or four-stroke where the "two" and "four" represent how many strokes the piston makes to complete an entire cycle that generates mechanical power. The steps in this cycle include intake, compression, power, and exhaust. Two-stroke engines have several advantages over four-stroke engines, including high power-to-weight ratios, simplicity, ease of starting, and lower manufacturing costs. As such, they are often favored for low-cost, lightweight applications where fuel efficiency is not that big of an issue. Two-stroke engines are commonly used in lawn mowers, chainsaws, snowmobiles, and recreational marine engines. However, these advantages typically come at the cost of higher emissions rates. For most current SI engines, the two primary variables that manufacturers can control to reduce emissions are the air-to-fuel ratio and the spark timing. This is often the most common method for controlling exhaust emissions. Due to the lack of emission standards and

validation of small-sized engines, air-to-fuel ratios and spark timing calibrations are typically optimized for engine performance and durability rather than for low emissions.

While there are many studies that provide emission values for small nonroad spark ignition engines, the total amount of data available is still not very large. A search of open literature reveals that there is a wide gap in per unit emissions because there are so many different manufacturers, types, sizes of engines, and unique calibrations. Alander et al. researched particle emissions from a small two-stroke engine with a focus on how lubricating oil and exhaust after treatment impact emissions [213]. This research group conducted all of their studies using a two-stroke chainsaw engine rated at 2.5 kW while operating on different lubricants and fuels. They provide several unit emission values while operating on traditional gasoline. Magnusson and Nilsson conducted a similar study using a 2-stroke chainsaw engine focusing on the impact of ethanol-based operation on emissions [214]. Similar to Alander, Magnusson and Nilsson provide reference emission values for operating the engine on gasoline. Christensen and Westerholm determined the emissions of four-stroke lawn mower engines with and without an oxidizing catalyst at the exhaust [215]. Their tests were completed using a 2.9 kW four-stroke lawn mower engine run on several fuels, including gasoline. Juttner et al. completed several experiments on three outboard engines, two of them rated at 7.5 kW and the other at 15 kW [216]. Gabele and Pyle investigated the emissions of a two-stroke and four-stroke 7.4 kW rated outboard engine, operating on typical reformulated gasoline [217]. They showed that some of the emission factors, such as hydrocarbons, are 10 to 20 times higher for two-stroke engines than four-stroke ones rated at the same power. Priest et al. compared the emissions from ten two-stroke engines and six four-stroke engines, which run on unleaded gasoline at a maximum load of 1.72 kW [218].

Most nonroad SI engine manufacturers have calibrated their fuel systems for rich operation (low air-to-fuel ratio) because this reduces the risk of a misfire and it allows for the possibility to get more power from the engine due to the availability of excess fuel. Because a fuel rich mixture lacks sufficient oxygen for full combustion, it results in incomplete combustion that requires greater fuel consumption and produces higher levels of HC and CO emissions. The studies mentioned in the previous paragraph show that four-stroke engines typically produce far fewer emissions than two-stroke ones even at similar power levels. While the discussed literature all report similar emissions data from small two- and four-stroke engines, the emissions data used in this study comes from the Priest et al. paper [218] due to the large sampling size of real world engines considered. Priest et al. investigated sixteen different engines built by manufacturers that produce some of the most widely used two- and four-stroke engines in the world, such as Briggs and Stratton and Yamaha.

## 8.2 Ethanol fueled engines

In the 1970s, the United States began its program to develop ethanol as a transportation fuel. The U.S. has grown from producing 175 million gallons in 1980 to 14.3 billion gallons in 2014 [219]. While the production and use of ethanol has often been criticized as environmentally, technically, and economically unfavorable [220], it is nevertheless a domestic fuel source that arguably alleviates oil supply insecurities and reduces overall GHG emissions [221]. In the U.S., over 95% of ethanol is produced from corn through a minimally-efficient seven step process [222]; still, ethanol production from corn appears to be one of the few methods that generates an energy return on investment [220], [221], [223]. It is anticipated, however, that much of the ethanol production in the U.S. will become cellulosic-derived ethanol that can be produced from a wide array of waste resources, such as paper and sewage sludge, corn stover, and municipal

residues. An excellent summary on the history of the evolution of ethanol in the U.S. can be found in [222].

Like gasoline, ethanol is stored in liquid form at room temperature and can, with relatively minor engine modifications, be used in two- and four-stroke engines much like gasoline is used today [224]. Ethanol has a lower energy density than gasoline, but it also has a higher octane rating than regular gasoline. A higher octane rating allows the engine to operate more efficiently and minimize performance loss that results from operating on a fuel with lower energy content. In the transition from operating engines on gasoline to running on pure ethanol, many advocate a blend of regular gasoline with ethanol to maximize the respective fuel type advantages while minimizing their drawbacks. The two most common blends are referred to as E10 and E85 that are 10% and 85% ethanol by volume. Using these level of ethanol blends, there are many studies that have investigated the emissions impact of ethanol in large four-stroke engines used in vehicles [225], [226], [227], [228], but few for small SI engines that produce less than 25 hp [214], [229], [230].

From existing studies, operating a SI engine with higher levels of ethanol reduces the amount of CO and HC in exhaust emissions. This reduction is caused by greater oxygen content within the ethanol that allows for more complete combustion of the fuel [230]. Yücesu et al. investigated the emissions performance of a 15 kW four-stroke engine powered with ethanol blends as high as E60 [229]. Their results show that substantial reductions of CO and HCs in the exhaust were obtained at E40 and E60 blend levels. Wu et al. realized similar conditions in their investigations showing that substantial reductions in CO and HC emissions are achieved with high levels of ethanol in fuel blends [231]. Magnusson et al. investigated the emissions and fuel use of a two-stroke 2.4 kW rated chainsaw engine operating on gasoline, pure ethanol, and

gasoline/ethanol blends [214]. They investigated the impacts of gasoline/ethanol blending level and the air/fuel ratio on exhaust emissions. For this study, emission and energy use values for engines operating on pure ethanol, E100, are taken from [214]. The specific energy and emissions data on ethanol production used in GREET comes largely from [232], a report conducted by Argonne National Labs that provides a thorough analysis of the energy and emissions associated with ethanol production and delivery to refueling stations for use as a transportation fuel. As corn is the primary feedstock for U.S. ethanol production, the emissions and energy use associated with ethanol production supplied to community refueling stations is used.

## 8.3 Battery powered nonroad systems requiring 19 kW or less

Battery powered mobile equipment is becoming increasingly popular due to low cost, ease of use, and quiet operation. Because they have low specific energy, batteries often provide relatively short run times compared to other technologies. However, for applications that do not require constant use for several hours with long periods of time between their primary uses, batteries may be a compelling option. For mobile applications, the primary battery technology used up until the late 1990s was Ni/Cd [233], with lead acid being used in applications such as golf carts, wheel chairs, and forklifts [211]. However, when Li-ion batteries came on the scene with much higher energy densities than other battery types could achieve, they quickly became the choice battery technology for portable electric powered applications. Today, they are used almost exclusively for rechargeable portable devices [234]. For this analysis, information calculating the emissions and energy use in batteries powering portable applications will be based on Li-ion technology.

Researchers of Li-ion batteries have essentially attained the highest achievable energy density with minor improvements in foreseeable future. Additionally, manufacturers have driven the costs to very low levels where minimal cost reductions are expected. Unless a major fundamental breakthrough in battery technology occurs, Li-ion will likely continue to be the main option for portable applications.

Batteries do not generate any emissions during their use phase, but rather all of the emissions result from electricity generation used for charging. The efficiency of both battery charging and discharging reported in literature is between 85% and 95% [103]. Combining both stages results in an overall efficiency range between 72% and 90%. For emissions and energy use calculations in this analysis, an average charging/discharging efficiency of 81% will be used, which is the average percentage of the 72-90% efficiency range.

## 8.4 Fuel Cell Technology

For mobile applications, there are generally three types of fuel cells considered for practical use: conventional PEM fuel cells, SOFC, and HT-PEMFC. Although fuel cell technology uses $H_2$ as its primary fuel, $H_2$ can be generated on-board using a hydrocarbon fuel reforming process. Single stage fuel reforming processes typically generate large amounts of $H_2$, CO, and $CO_2$. PEM fuel cells are extremely intolerant to fuel feed contaminants, and thus significant cleanup processes are required if they are to operate using an on-board fuel reformer. Due to the complex nature of these cleanup processes, it is often assumed that mobile applications that use PEM fuel cells will not run on hydrocarbon fuels and will instead require some sort of on-board $H_2$ storage device that can accommodate either liquid or gaseous $H_2$. Other fuel cells HT-PEMFC or SOFCs are much more tolerant of gas impurities, such as CO and $CO_2$, where the SOFC can actually

generate electricity from CO. While these fuel cells both have their design challenges, they are valid engine replacement alternatives.

Table 11: Advantages and disadvantages of fuel cell types

| Fuel Cell Type | Electrolyte | Advantages | Disadvantages |
|---|---|---|---|
| Proton exchange membrane (PEMFC) | Polymeric Membrane | High efficiency, low temperature operation, quick start-up | Requires high purity $H_2$, intolerant to fuel impurities |
| Solid Oxide Fuel Cell (SOFC) | Ceramic YSZ | High efficiency, can run on hydrocarbon fuels | Sensitive electrolyte, long start-up, high temperature operation |
| High temperature PEMFC (HT-PEMFC) | Polymeric Membrane | Can run on hydrocarbon fuels, quick start-up time, low temperature operation | Lower efficiency |

PEM fuel cells running on $H_2$ as its fuel can achieve efficiencies around 48% [103]. Although PEM fuel cells have much higher operating efficiencies than the other types, the overall system is complicated due to the requirement of pure $H_2$ for fuel, which is difficult to obtain and store on-board. Because PEM fuel cells convert $H_2$ and $O_2$ taken from the air into water, the only emission during the use phase is water vapor. Thus all emissions for a PEM fuel cell power plant result from the hydrogen generation and delivery process.

Mobile SOFCs operating on hydrocarbon fuels have the potential to obtain high efficiencies [235], [236]; however, demonstrated systems built for mobile applications show efficiencies around 20%, such as the one built for unmanned aerial vehicles by Applied Materials Incorporated, which runs on propane [170]. SOFCs operate at temperatures around 800$^{o}$C and use ceramic materials as electrolytes. The high temperature operation and ceramic electrolyte allow for lower catalyst material costs, but these cost reductions are somewhat offset due to the

requirement of exotic materials that can safely operate at such high temperatures necessary in the fuel cell system. SOFCs additionally suffer from long start-up times as rapidly heating the fuel cell to operating temperature may result in permanent damage to the electrolyte from thermal cracking.

In an SOFC system running on a hydrocarbon fuel, the fuel is first converted into a $H_2$ rich gas stream through some sort of fuel reforming process. For mobile applications, the simplest fuel reforming process is referred to as catalytic partial oxidation (cPOx), and involves flowing fuel and air over a catalyst at an elevated temperature [114]. The fuel reacts with the air and breaks apart into mainly $H_2$ and CO. Within the SOFC, the $H_2$ reacts with $O_2$ in the air to form $H_2O$, and the CO reacts with $O_2$ to form $CO_2$. Thus, the primary emission from SOFC systems is $CO_2$ and the production of other gases is very limited. While there is data in literature reporting the amount of emissions resulting from SOFC operation [237], a more accurate assessment results from a mass balance calculation where the variable inputs are fuel type and conversion efficiency. Based on existing commercial systems, in this analysis it is assumed that the fuel type used for a mobile SOFC is propane and that the LHV based conversion efficiency of propane to electricity in the fuel cell system is 20% [170]. Under these conditions, the use phase $CO_2$ emissions are 1163 g/kWh.

HT-PEMFC fuel cells are a relatively newer fuel cell type that offer many system-level advantages over traditional PEM and SOFC technologies [238]. HT-PEMFCs can achieve efficiencies around 40% if operating on pure $H_2$ as a fuel, but in lab tests they typically achieve efficiencies of 20-30% when operating on a hydrocarbon fuel. A HT-PEMFC operates similarly to an SOFC in that the hydrocarbon fuel must first be converted to a $H_2$ rich gas stream, before it is put into the fuel cell. Using a cPOx reaction like in an SOFC, a relatively simple onboard fuel

reforming system can be developed. While the efficiencies of a HT-PEMFC are much lower than a PEM or SOFC, the additional advantages at the system level, including the ability to operate on a hydrocarbon fuel, a lower operational temperature than an SOFC, and a quick start-up time while still achieving higher efficiencies than comparable combustion engines, provide a compelling solution for an engine replacement technology.

Lab test efficiencies of 17% have been achieved when converting propane into electricity using a HT-PEM fuel cell system. From an emissions perspective, the main disadvantage a HT-PEMFC has over other fuel cell types is that CO is not converted into $CO_2$ within the fuel cell itself, such as in an SOFC, or during the hydrogen generation process in the PEMFC pathway. One way to minimize CO production from a HT-PEMFC is to add on an exhaust catalytic converter much like the ones in passenger vehicles. These catalytic converters are capable of 100% CO conversion when mixed with high amounts of air [239]. For this analysis we will assume the CO generated from the propane fuel reforming process will be 100% converted to $CO_2$ in the exhaust of a HT-PEMFC system. Using a mass balance calculation, the HT-PEMFC generates $CO_2$ at an emissions rate of 1368 g/kWh.

## 8.5 Upstream Fuel Generation

The upstream emissions in this analysis were determined using the GREET model, and are added to the full fuel-cycle direct impacts. For the traditional SI engines, gasoline is used as the chosen fuel. In the GREET model, the pathway chosen for gasoline production is gasoline blendstock from crude oil recovery in U.S. refineries with data taken from [240]. The steps of this fuel production pathway involve crude oil recovery, refining, delivery to bulk terminal, and delivery to refueling stations. For the pure ethanol powered SI engines, over 95% of ethanol is produced from corn. In this pathway, the steps involved include corn production, dry and wet

mill ethanol production, and transportation to refueling stations. Within the GREET model, data is primarily taken from the publication [241] for the ethanol production and delivery emissions and energy use.

There are several ways to generate and store hydrogen gas ($H_2$) for use on mobile systems powered by fuel cells. Currently the most common way to generate $H_2$ is through steam methane reforming (SMR) which accounts for 95% of worldwide $H_2$ production [99]. Similar reforming processes could also be done using renewable biofuels, allowing the hydrogen generation process to be carbon neutral or even carbon negative. Water electrolysis is another hydrogen generation process where water is split into $H_2$ and $O_2$ molecules using electricity. If this electricity is generated from renewable sources such as wind or solar, then a completely renewable hydrogen generation process may be achievable. For this study, however, it is assumed that hydrogen is generated via SMR at a central plant, transported to refueling stations via pipeline, and then compressed to a higher pressure at the refueling station.

It is assumed that propane will be used to fuel both the SOFC and HT-PEMFC in this study as it is already used to power mobile SOFC systems, and is a suitable primary fuel for HT-PEMFCs as well. Production of propane, often referred to as liquefied petroleum gas (LPG), is typically produced during natural gas recovery. With minimal pressure, propane can be converted into a liquid fuel and sent to retailers for resale. Propane is often bought in 1 lb and 20 lb tanks for cooking, and it is also often bought by homeowners with large on-site storage tanks for heating. The emissions of this pathway within the GREET software are largely taken from the article [240].

## 8.6 Comparison of Technologies for Nonroad Engine Replacements

Figure 45: Upstream and operational phase CO emissions production from nonroad engines and their potential replacement technologies displays the amount of CO emissions resulting from nonroad engines and suitable renewable technology replacements in g/kWh. While only ICEs produce CO emissions at their point of use, all propulsion technologies compared in this analysis generate CO emissions upstream. However, these upstream emissions are less than 1 g/kWh for all pathways considered, and are minor when compared to the CO generated during the use phase for ICEs.

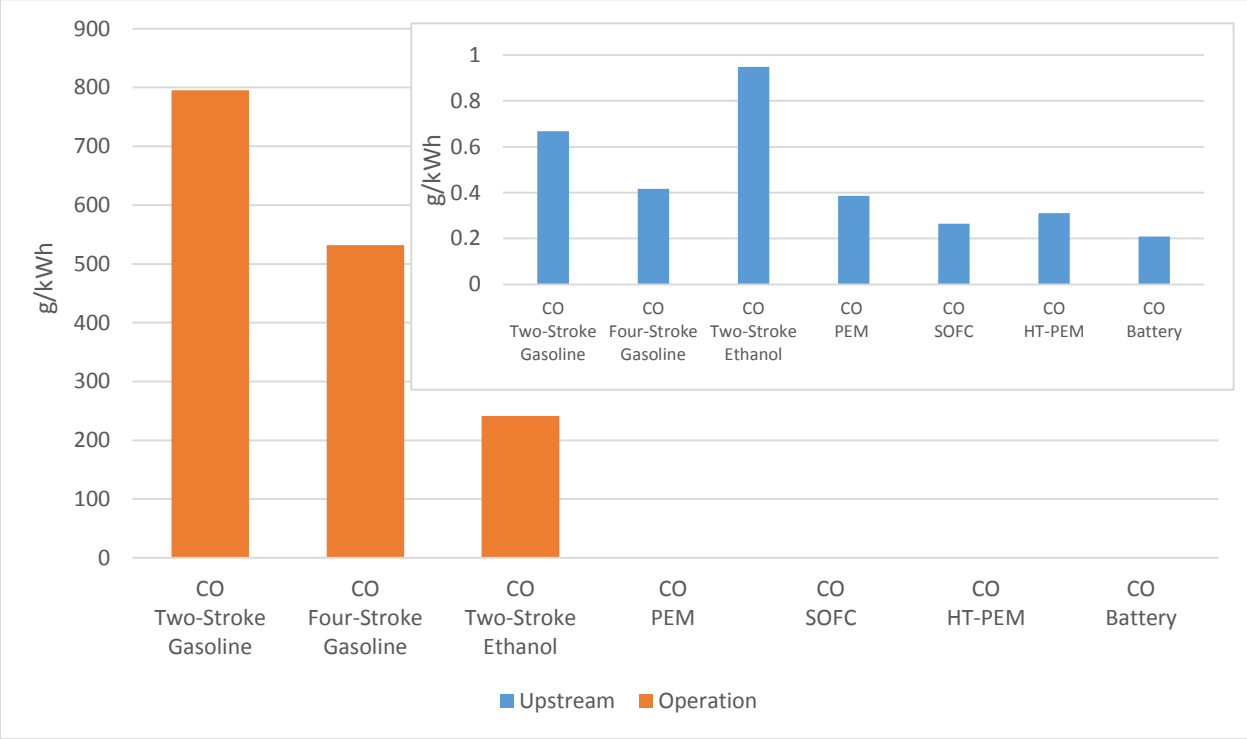


Figure 45: Upstream and operational phase CO emissions production from nonroad engines and their potential replacement technologies

Calculated efficiencies for the ICE technologies are 8.5%, 13.6% and 17% for the two-stroke running on gasoline, the four-stroke running on gasoline, and the two-stroke running on ethanol respectively. A four-stroke engine operating on gasoline generates approximately two-thirds the

amount of CO emissions as a two-stroke engine. This likely results from manufacturers designing their two-stroke engines to run under very fuel-rich conditions so they are more durable. Under fuel-rich conditions, complete combustion does not occur resulting in greater CO production in the exhaust. An engine with the same power output but based on a four-stroke design can operate a bit more efficiently, where many of the carbon atoms from the fuel are converted to $CO_2$ rather than CO.

A two-stroke engine running on ethanol generates less than half the amount of CO a four-stroke engine fueled by gasoline does. Although there was not enough data in the literature to accurately assess the performance of a four-stroke engine running on pure ethanol, it is likely these will produce even less CO than their two-stroke counterparts since they operate more efficiently.

While CO is not a GHG, it does have significant human health impacts. CO is a colorless, odorless, and nonirritant gas that is easily absorbed through the lungs [242]. The harmful effects of CO result from a combination of tissue hypoxia and direct damage generated at the cellular level. When inhaled at high concentrations, CO makes it so that cells are not able to respire regularly. CO binds onto hemoglobin in the blood stream, which results in a decrease of oxygen-carrying capacity and impaired oxygen release at the tissue level. Since the affinity of CO for binding on hemoglobin is 200 to 250 times greater than oxygen, small concentrations of CO can have significantly harmful impacts. The effects of CO range from subtle cardiovascular and negative neurological behavior to unconsciousness and death after prolonged levels of high exposure or acute exposures to very high concentrations of CO [243].

The limits and dangers of CO are typically described at different levels of concentration in ppm. The National Ambient Air Quality Standards (NAAQS) developed by the EPA state CO

levels of 9 ppm averaged over an 8 hour time period or 35 ppm averaged over a 1 hour time period should not be exceeded more than once per year [244]. Workers who consistently use two-stroke engines, such as the ones commonly found in lawn and garden equipment, should take care to always use them in very well ventilated spaces. For example, the two-stroke engine operating on gasoline used in this study produces about 0.92 kW of power. At a CO generation rate of 795 g/kWh, if this engine were operated in a typical two-car garage with minimal ventilation (24x24x10 ft), CO concentrations of 35 ppm would be reached in only 35 seconds! Although it is not likely anyone would be operating a two-stroke engine in an enclosed space, the potential for high concentrations of CO to be attained even outdoors might occur under common situations, such as when there are multiple pieces of equipment in a small area with low winds.

Figure 46 shows the g/kWh NOx emissions associated with the different power generating technologies throughout the full fuel cycle. Similar to CO generation, NOx is only generated in the use phase for ICEs and the NOx emissions associated with the other power generators are a result from fuel production and transportation. Unlike the CO emissions, however, the technology with the greatest NOx emissions is the four-stroke engine operating on gasoline. In many of the studies investigating emissions from small SI engines, CO and NOx production tend to have an inverse relationship, which explains these results. The full fuel cycle NOx production from an ethanol powered engine is lower than the engines fueled by gasoline, but only slightly less than the two-stroke gasoline fueled engine. This is because ethanol production and distribution generates much more NOx than any of the other primary fuels. The SOFC fuel cycle generates the least amount of NOx emissions. All non-ICE technologies emit less than 1 g/kWh for the full fuel cycle.

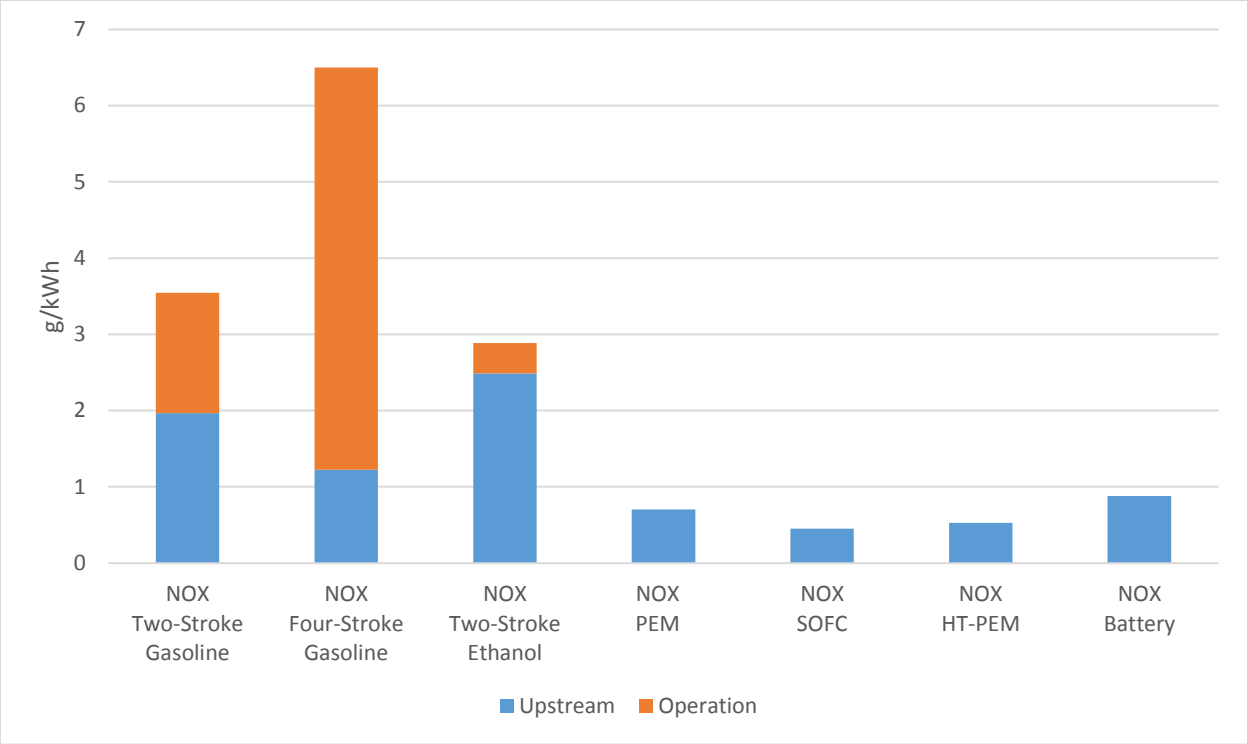


Figure 46: Upstream and operational phase NOx emissions production from nonroad engines and their potential replacement technologies

Nitrous oxides have significant direct human health impacts, particularly $NO_2$, as they may cause damage in lung cells through peroxidation of membrane lipids that may ultimately lead to injury and premature death [245]. While low levels of $NO_2$, less than 40 ppb, have been shown to have no effect in healthy infants or toddlers, the NAAQS says that exposure to $NO_2$ should not exceed 53 ppb averaged annually, while never exceeding 100 ppb averaged over 1 hour [244]. Using the same garage example as described above, operating a four-stroke engine producing 0.92 kW with $NO_2$ emissions of 5.27 g/kWh within an enclosed two-car garage would reach concentrations of 100 ppb of $NO_2$ in 15 seconds! Beyond human health impacts, NOx also contributes to smog and is considered a GHG with a global warming potential 298 times that of carbon dioxide [246]. Thus even small amounts can have a substantial indirect human health impact.

Figure 47 indicates the amount of hydrocarbon (HC) emissions produced for the different power generating technologies. It is important to note that the operational phase of HC emissions includes many different hydrocarbons such as methane, propane, propylene, benzene, toluene, xylene, and isobutene [218], [214], [247]. However, upstream HC emissions only include methane, which is the only hydrocarbon assessed in the GREET software. Much like CO and NOx emissions, only the ICEs emit substantial amounts of HC for the full fuel cycle. The different fuel cell types and batteries only have HC emission during the upstream fuel production and delivery phase. HC emissions are most often generated from incomplete fuel combustion that typically occurs when operating under fuel-rich conditions. This is typical in two-stroke engines, which explains why both of the two-stroke engines fueled with gasoline and ethanol produce substantially more HC emissions than the four-stroke engine fueled by gasoline does.

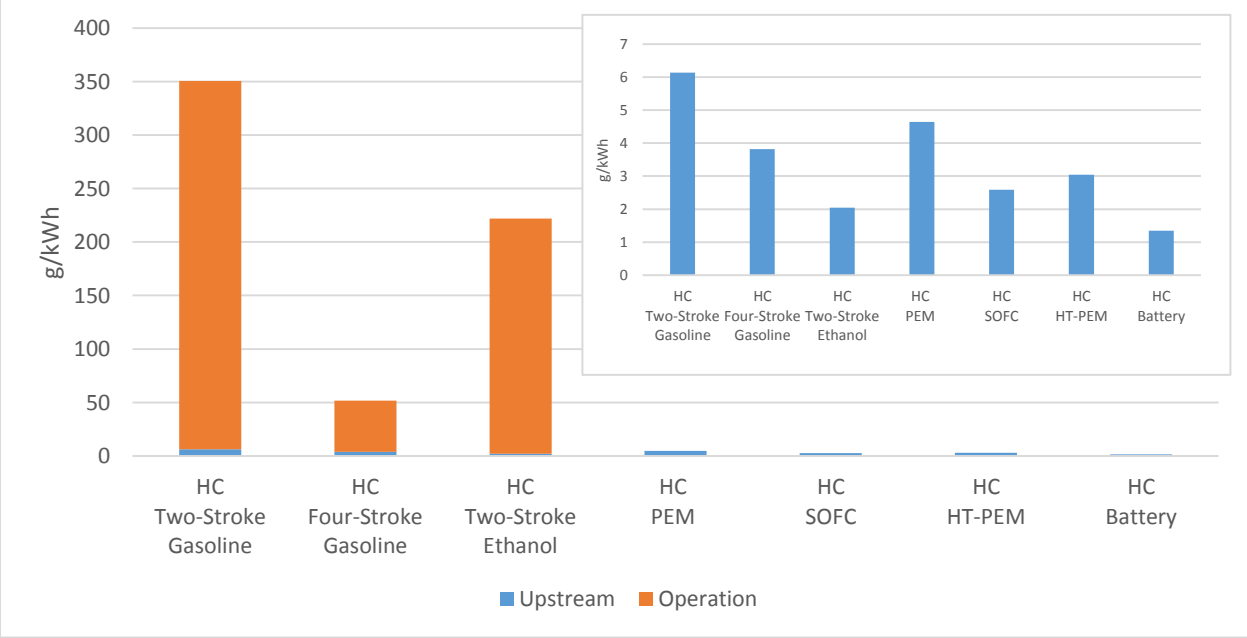


Figure 47: Upstream and operational phase HC emissions production from nonroad engines and their potential replacement technologies

The two-stroke engine fueled with gasoline produces the most amount of upstream HC emissions at 6.1 g/kWh. This is largely due to the inefficiency of the engine, and thus more fuel is required per kWh of energy generated. The production of hydrogen for use in the PEM fuel cell accounts for the second largest amount of upstream HC emissions at 4.6 g/kWh. The lowest amount of upstream HC emissions occurs during the generation of electricity for battery recharging at 1.4 g/kWh.

There is insufficient data differentiating between the various hydrocarbons as many of the measuring equipment used in studies found in literature measures methane and/or non-methane hydrocarbons [218]. Additionally, while many hydrocarbons have known toxicity levels (i.e. benzene), some are not well defined, such as ethane and propane. Nevertheless, acute effects from exposure to hydrocarbons include skin and eye irritation, nausea and vomiting, and inflammation [248]. As many of the hydrocarbons emitted are known carcinogens, long-term health effects include skin, lung, and bladder cancers, as well as cell damage to internal organs [247]. Certain hydrocarbons are also considered GHGs and contribute to global warming. Methane in particular has a $CO_2$ global warming equivalent potential of 28-36 [249].

Figure 48 shows the $CO_2$ fuel cycle emissions for the different power generating technologies. All technologies release a significant amount of $CO_2$ either during the operation, upstream, or during both phases of the fuel cycle. Only the PEM fuel cell and battery technologies do not emit $CO_2$ during the operation phase. The fuel cell technologies based on a SOFC or a HT-PEMFC emit the most amount of $CO_2$ during the use phase compared to the others, but they have the fewest amount of $CO_2$ emissions generated from the upstream emissions. The battery emits the least amount of $CO_2$ from a full fuel cycle perspective. Of the

ICE technologies, the four-stroke engine operating on gasoline has the fewest amount of upstream $CO_2$ emissions.

In addition to being considered a GHG, $CO_2$ does pose a direct risk to humans, but only at very high concentrations. OSHA has a 1% (10,000 ppm) averaged over 8 hours limit for $CO_2$ exposure, with a 3% (30,000 ppm) short-term (15 min) exposure limit [250]. While it is thought that the harmful effects should be attributed to $O_2$ displacement, other studies suggest that even in high $O_2$ environments, $CO_2$ concentrations above 5% may lead to unconsciousness [251]. When operating ICEs in poorly ventilated areas, the CO and NOx exposure limits will be reached far before the $CO_2$ exposure limits. However if the HT-PEM or SOFC technologies are being used, the amount of $CO_2$ generated can be of concern if operated in enclosed spaces.

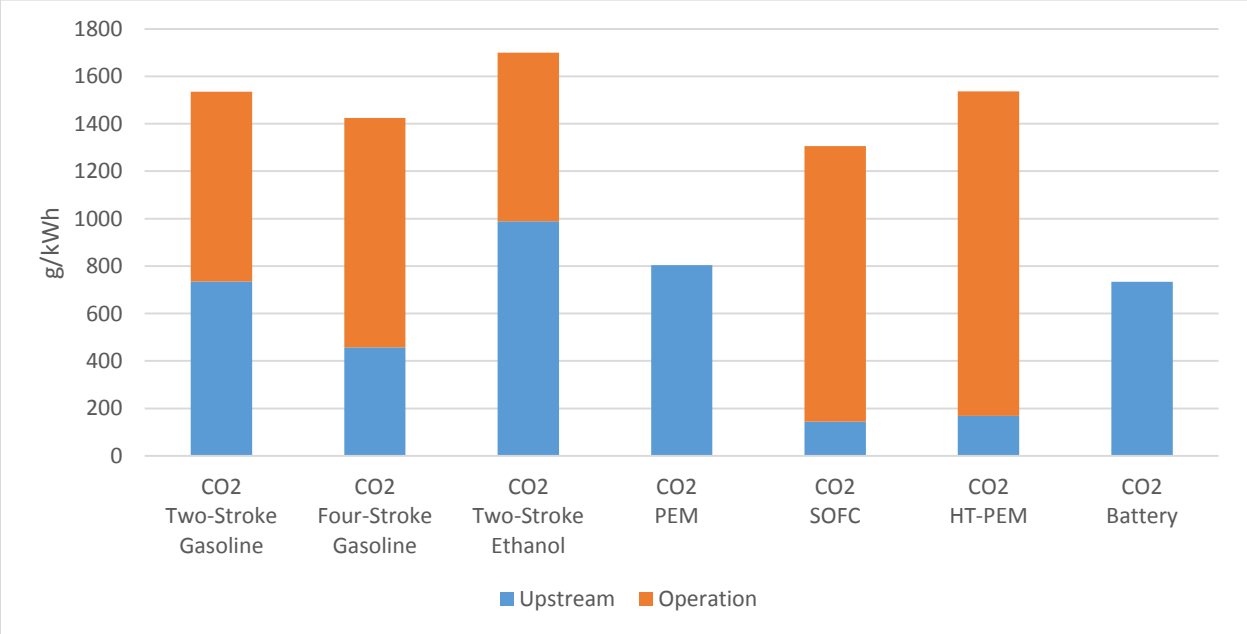


Figure 48: Upstream and operational phase $CO_2$ emissions production from nonroad engines and their potential replacement technologies

Except for NOx emissions, the battery emits the fewest amount of emissions in all categories for the full fuel cycle. The difference in the NOx emissions generated by the battery fuel cycle as

compared to other technologies is quite small. While all the ICE types emit the most amount of harmful emissions, there are relatively simple solutions to reduce them. For CO and HC emission reduction, manufacturers could use four-stroke engines rather than two-stroke ones. They could also modify them to operate under higher air/fuel ratios, which would increase the chance of complete combustion occurring. This would greatly reduce the amount of CO and HC emissions. CO, HC, and NOx emissions could be reduced through the addition of an exhaust catalytic converters such as those used in automobiles to convert exhaust emissions into $N_2$ and $CO_2$ [239]. These catalytic converters have been shown to reduce CO, HC and NOx levels very effectively, with close to 100% conversion under certain operating conditions.

If emissions generation is the main driver for switching to a new technology, powering equipment using batteries would be the most effective technological change. All of the harmful emissions produced for the full battery fuel cycle are generated in the upstream process. If renewable technologies are used to generate upstream electricity, however, the full fuel cycle may generate little to no emissions at all. The main drawbacks of batteries are their lower energy density and inability to recharge quickly. The only effective solution to remedy this is to pre-charge many different batteries and swap them out when necessary. For many applications though, this is not a viable solution. Switching the fuel source of ICEs from gasoline to pure ethanol may also result in fewer emissions for the full fuel cycle. This conversion may be the simplest from a manufacturing and consumer perspective as only the type of fuel is changed.

Of the fuel cell options, the PEM fuel cell fueled with pure $H_2$ generates the fewest fuel cycle emissions where all of the harmful emissions are generated upstream. Additionally, like the battery fuel cycle, the PEM fuel cell can potentially be a completely renewable pathway if renewable power generating technologies are used to generate $H_2$ instead of natural gas.

Nevertheless, the practical limitations of $H_2$ refueling and onboard fuel storage need to be overcome before widespread adoption of PEM fuel cell technology. The SOFC and HT-PEMFC offer a significant technical advantage over the PEM fuel cell in that they are both capable of operating on readily available hydrocarbon fuels such as propane. Additionally, the operational emissions generated by the HT-PEMFC and SOFC are almost all in the form of $CO_2$, which does not have a direct human health impact.

## 8.7 Future Environmental Outlook of Nonroad Engine Replacement Technologies

Traditional ICEs used to power nonroad applications under 25 hp (19 kW) produce substantial amounts of CO, HC, NOx, and $CO_2$ on a g/kWh basis. As many of these types of engines are operated in environments where workers can easily inhale exhaust fumes (i.e. lawn and garden workers), acute and long-term exposures to these gases can cause significant harm to human health. Operating engines on a renewable fuel such as ethanol, or converting the power plant to a fuel cell or battery technology, may offer substantial reductions in emissions both during the operational phase and the upstream fuel generation phase. The environmental impacts of fueling traditional ICEs with ethanol are typically much lower, while technical improvements could further reduce these impacts. Greater reductions in environmental impacts are found when using PEM fuel cell technology fueled with hydrogen or hydrocarbons such as propane. The greatest reduction in emissions from a full fuel cycle perspective though are seen when using Li-ion battery technology, but their greatest hindrance of low energy density make them impractical for many applications. Fuel cells powered from hydrocarbons have the potential to offer substantial reductions in emissions; however, the technology is still too immature for widespread adoption.

# 9 Conclusions and Future Outlook

The majority of fuel cell research to date has mainly been focused on developing systems to power passenger vehicles, commercial buildings, and small handheld devices. These applications typically require power outputs that are either greater than 100 kW or less than 20 W, and a gap remains in developing viable fuel cell systems for portable applications requiring power between 100 W and 100 kW. Key requirements for these portable applications include a light-weight power plant that has a quick startup time, and can be easily refueled. Most proposed fuel cell systems today meet some of these requirements, but not all. In this dissertation, an integrated reformer fuel cell system is proposed that utilizes a reformer operating under propane cPOx conditions coupled with a HT-PEM fuel cell. Using this structure, a system is proposed that is lightweight, can be quickly started, and is easily refueled.

The development of this system required investigation into two main subsystems, the fuel reformer and HT-PEM fuel cell. Using a Microlith fuel reformer built by PCI, the optimal operating conditions that maximize the efficiency of propane cPOx were determined. It is shown that the most efficient operation occurs at an $O_2$/C ratio of 0.53 and at an operating temperature around 950$^o$C. The performance of a HT-PEM fuel cell while operating directly on the propane reformate produced by the Microlith reformer was also assessed. It was shown that when operating at 200$^o$C and 200 kPa, the HT-PEM fuel cell can provide high power densities and durable operation.

In order to further investigate solutions for a viable system, the target weight, power, run time, and durability requirements for military UAVs were assessed, so that the feasibility of a practical system could be determined. Based off of this information, it was determined that a net 250 W fuel cell power plant should weigh no more than 2.4 kg, and have a minimum of a 200

hour lifetime. Using this information, an integrated fuel reformer system was proposed that is produces a net power output of 250 W, has a weight of 2.23 kg, and is capable of a 200 hour lifetime, satisfying all of the design requirements. This proposed design offers significant advantages over current UAV propulsion technologies in that it is both quiet and capable of long flight durations, unlike battery and internal combustion engine technology presently used that suffer from either low specific energy, or are too noisy. Also, the proposed system also has advantages over other fuel cell systems in that it is fueled with commonly available propane where other mobile fuel cells require high purity $H_2$ that is difficult to obtain.

In addition to assessing the technical feasibility of such a system, the potential environmental benefits relative to incumbent technology were investigated through a full fuel cycle analysis. While batteries proved to provide the greatest reductions for all of the emissions investigated, the proposed fuel cell system offers substantial NOx and HC emission reductions over traditional ICEs. When developing viable power plant systems, the technical targets, operational requirements, and environmental concerns for a given application must all be properly balanced in order to come up with the best design.

Future research that builds on this work could focus on constructing a prototype fuel cell system using the materials and components described in the Chapter 7. Additionally, the feasibility of adapting the proposed system to other applications could also be considered. Specific to the HT-PEM fuel cell, methods for extending the lifetime beyond 200 hours should be investigated. One of the simplest ways to extend its lifetime would be to lower the operating temperature from 200$^{o}$C to 160$^{o}$C, which would result in a lower PA evaporation within the PBI MEA. If CO concentrations generated through the fuel reformer reaction were reduced, then

lower fuel cell operating temperatures may be feasible while still maintaining the same power densities currently achieved.

In order for fuel cells to play a large part in a global sustainable energy infrastructure, fuel cell-based systems that meet the demands of a wide range of applications and power requirements must be designed. The work discussed in this dissertation contributes to the scientific community through investigating the feasibility of an integrated reformer HT-PEM fuel cell system for applications requiring medium levels of power. A novel fuel cell system that is fueled with propane effluent generated using a cPOx reactor is proposed that meets the target power, weight, durability, and run time conditions required for military UAVs. This research shows that for applications requiring medium levels of power, fuel cells are a viable solution. The technology powering applications such as unmanned aerial vehicles (UAVs), residential power generators, equipment pumps, camping and recreational devices, lawn and garden equipment, and auxiliary power units can be updated to use fuel cell systems and create a cleaner, more sustainable world.

# 10 Bibliography


[1] I. P. on C. Change, *Climate Change 2014: Mitigation of Climate Change*, vol. 3. Cambridge University Press, 2015.

[2] S. Solomon, G.-K. Plattner, R. Knutti, and P. Friedlingstein, "Irreversible climate change due to carbon dioxide emissions," *Proc. Natl. Acad. Sci. U. S. A.*, vol. 106, no. 6, pp. 1704–1709, Feb. 2009.

[3] J. R. Petit, J. Jouzel, D. Raynaud, N. I. Barkov, J.-M. Barnola, I. Basile, M. Bender, J. Chappellaz, M. Davis, G. Delaygue, M. Delmotte, V. M. Kotlyakov, M. Legrand, V. Y. Lipenkov, C. Lorius, L. PÉpin, C. Ritz, E. Saltzman, and M. Stievenard, "Climate and atmospheric history of the past 420,000 years from the Vostok ice core, Antarctica," *Nature*, vol. 399, no. 6735, pp. 429–436, Jun. 1999.

[4] OECD, "The OECD Environmental Outlook to 2050 Key Findings on Climate Change," 2012.

[5] "The Toyota Fuel Cell Vehicle." [Online]. Available: http://www.toyota.com/fuelcell/. [Accessed: 04-Aug-2014].

[6] "General Electric is building a fuel cell pilot development and manufacturing plant in Malta, New York," *Albany Business Review*. [Online]. Available: http://www.bizjournals.com/albany/news/2014/07/22/general-electric-is-building-a-fuel-cell-pilot.html. [Accessed: 04-Aug-2014].

[7] "Horizon Fuel Cell Technologies," *Horizon Fuel Cell Technologies*. [Online]. Available: http://www.horizonfuelcell.com/. [Accessed: 30-Dec-2013].

[8] E. Egeland, "2016 Mirai Product Information," Toyota, Specification Sheet, 2015.

[9] A. Chandan, M. Hattenberger, A. El-kharouf, S. Du, A. Dhir, V. Self, B. G. Pollet, A. Ingram, and W. Bujalski, "High temperature (HT) polymer electrolyte membrane fuel cells (PEMFC) – A review," *J. Power Sources*, vol. 231, pp. 264–278, Jun. 2013.

[10] J. M. Andújar and F. Segura, "Fuel cells: History and updating. A walk along two centuries," *Renew. Sustain. Energy Rev.*, vol. 13, no. 9, pp. 2309–2322, Dec. 2009.

[11] H. Davy, "An Account of Some Galvanic Combinations, Formed by the Arrangement of Single Metallic Plates and Fluids, Analogous to the New Galvanic Apparatus of Mr. Volta," *Philos. Trans. R. Soc. Lond.*, vol. 91, pp. 397–402, 1801.

[12] W. R. G. E. M.A, "XXIV. On voltaic series and the combination of gases by platinum," *Philos. Mag. Ser. 3*, vol. 14, no. 86, pp. 127–130, Feb. 1839.

[13] F. Barbir, *PEM fuel cells: Theory and prectice, ed.* RC Dorf, 2005.

[14] K. Kang, G. Lee, G. Gwak, Y. Choi, and H. Ju, "Development of an advanced MEA to use high-concentration methanol fuel in a direct methanol fuel cell system," *Int. J. Hydrog. Energy*, vol. 37, no. 7, pp. 6285–6291, Apr. 2012.

[15] S. K. Kamarudin, F. Achmad, and W. R. W. Daud, "Overview on the application of direct methanol fuel cell (DMFC) for portable electronic devices," *Int. J. Hydrog. Energy*, vol. 34, no. 16, pp. 6902–6916, Aug. 2009.

[16] G. F. McLean, T. Niet, S. Prince-Richard, and N. Djilali, "An assessment of alkaline fuel cell technology," *Int. J. Hydrog. Energy*, vol. 27, no. 5, pp. 507–526, May 2002.

[17] M. K. Debe, "Electrocatalyst approaches and challenges for automotive fuel cells," *Nature*, vol. 486, no. 7401, pp. 43–51, Jun. 2012.

[18] J. Larminie, A. Dicks, and M. S. McDonald, *Fuel cell systems explained*, vol. 2. Wiley New York, 2003.

[19] N. Sammes, R. Bove, and K. Stahl, “Phosphoric acid fuel cells: Fundamentals and applications,” *Curr. Opin. Solid State Mater. Sci.*, vol. 8, no. 5, pp. 372–378, Oct. 2004.
[20] S. C. Singhal and K. Kendall, *High-temperature Solid Oxide Fuel Cells: Fundamentals, Design and Applications: Fundamentals, Design and Applications*. Elsevier, 2003.
[21] J. M. Ralph, A. C. Schoeler, and M. Krumpelt, “Materials for lower temperature solid oxide fuel cells,” *J. Mater. Sci.*, vol. 36, no. 5, pp. 1161–1172, 2001.
[22] R. Payne, J. Love, and M. Kah, “Generating Electricity at 60% Electrical Efficiency from 1 - 2 kWe SOFC Products,” *ECS Trans.*, vol. 25, no. 2, pp. 231–239, Sep. 2009.
[23] S. R. Narayan and T. I. Valdez, “High-Energy Portable Fuel Cell power Sources,” *Electrochem. Soc. Interface*, pp. 40–45, Winter 2008.
[24] “Engine | WEN Products.” .
[25] Y. Ding, Y. Zhao, and G. Yu, “A Membrane-Free Ferrocene-Based High-Rate Semiliquid Battery,” *Nano Lett.*, vol. 15, no. 6, pp. 4108–4113, Jun. 2015.
[26] ICC Nexergy, “Battery Energy Density Comparison,” *ICCNexergy*. [Online]. Available: http://www.iccnexergy.com/battery-systems/battery-energy-density-comparison/. [Accessed: 21-Nov-2015].
[27] Cubewano, “Cubewano Commercial Engine Comparison,” Nov-2015. .
[28] K. Kang, G. Lee, G. Gwak, Y. Choi, and H. Ju, “Development of an advanced MEA to use high-concentration methanol fuel in a direct methanol fuel cell system,” *Int. J. Hydrog. Energy*, vol. 37, no. 7, pp. 6285–6291, Apr. 2012.
[29] J. Zhang, Z. Xie, J. Zhang, Y. Tang, C. Song, T. Navessin, Z. Shi, D. Song, H. Wang, D. P. Wilkinson, Z.-S. Liu, and S. Holdcroft, “High temperature PEM fuel cells,” *J. Power Sources*, vol. 160, no. 2, pp. 872–891, Oct. 2006.
[30] G. Hoogers, *Fuel Cell Technology Handbook*. 2003.
[31] D. Cheddie and N. Munroe, “Mathematical model of a PEMFC using a PBI membrane,” *Energy Convers. Manag.*, vol. 47, no. 11–12, pp. 1490–1504, Jul. 2006.
[32] A. R. Korsgaard, M. P. Nielsen, M. Bang, and S. K. Kær, “Modeling of CO Influence in PBI Electrolyte PEM Fuel Cells,” pp. 911–915, Jan. 2006.
[33] J. Hu, H. Zhang, and L. Gang, “Diffusion–convection/electrochemical model studies on polybenzimidazole (PBI) fuel cell based on AC impedance technique,” *Energy Convers. Manag.*, vol. 49, no. 5, pp. 1019–1027, May 2008.
[34] J. Kim, S.-M. Lee, S. Srinivasan, and C. E. Chamberlin, “Modeling of Proton Exchange Membrane Fuel Cell Performance with an Empirical Equation,” *J. Electrochem. Soc.*, vol. 142, no. 8, pp. 2670–2674, Aug. 1995.
[35] NIST, “Reference Fluid and Thermodynamic and Transport Properties Database (REFPROP): Version 9.1,” *NIST Standard Reference Database 23*, 2013. [Online]. Available: http://www.nist.gov/srd/nist23.cfm. [Accessed: 29-Jul-2013].
[36] Z. Qi, C. He, and A. Kaufman, “Effect of CO in the anode fuel on the performance of PEM fuel cell cathode,” *J. Power Sources*, vol. 111, no. 2, pp. 239–247, Sep. 2002.
[37] A. R. Korsgaard, M. P. Nielsen, and S. K. Kær, “Part one: A novel model of HTPEM-based micro-combined heat and power fuel cell system,” *Int. J. Hydrog. Energy*, vol. 33, no. 7, pp. 1909–1920, Apr. 2008.
[38] C. Pan, R. He, Q. Li, J. O. Jensen, N. J. Bjerrum, H. A. Hjulmand, and A. B. Jensen, “Integration of high temperature PEM fuel cells with a methanol reformer,” *J. Power Sources*, vol. 145, no. 2, pp. 392–398, Aug. 2005.
[39] C. B. Keith and M. R. Ivan, “Polybenzimidazoles,” US2895948 A, 21-Jul-1959.

[40] J. S. Wainright, J.-T. Wang, D. Weng, R. F. Savinell, and M. Litt, “Acid-Doped Polybenzimidazoles: A New Polymer Electrolyte,” *J. Electrochem. Soc.*, vol. 142, no. 7, pp. L121–L123, Jul. 1995.
[41] Q. Li, R. He, J.-A. Gao, J. O. Jensen, and N. J. Bjerrum, “The CO Poisoning Effect in PEMFCs Operational at Temperatures up to 200°C,” *J. Electrochem. Soc.*, vol. 150, no. 12, pp. A1599–A1605, Dec. 2003.
[42] G. Avgouropoulos, J. Papavasiliou, M. K. Daletou, J. K. Kallitsis, T. Ioannides, and S. Neophytides, “Reforming methanol to electricity in a high temperature PEM fuel cell,” *Appl. Catal. B Environ.*, vol. 90, no. 3–4, pp. 628–632, Aug. 2009.
[43] N. H. Jalani, M. Ramani, K. Ohlsson, S. Buelte, G. Pacifico, R. Pollard, R. Staudt, and R. Datta, “Performance analysis and impedance spectral signatures of high temperature PBI–phosphoric acid gel membrane fuel cells,” *J. Power Sources*, vol. 160, no. 2, pp. 1096–1103, Oct. 2006.
[44] T. J. Schmidt, “Durability and degradation in high-temperature polymer electrolyte fuel cells,” *ECS Trans.*, vol. 1, no. 8, pp. 19–31, 2006.
[45] BASF, “Celtec MEAs. Membrane Electrode Assemblies for High Temperature PEM Fuel Cells,” 2012.
[46] E. De Castro, “PBI-Phosphoric Acid Based Membrane Electrode Assemblies: Status Update,” PAFC Workship, 16-Nov-2009.
[47] “Advent Technologies Inc.,” 2014. [Online]. Available: http://www.advent-energy.com/. [Accessed: 22-Apr-2014].
[48] “Danish Power Systems | Danish Power Systems.” [Online]. Available: http://daposy.com/. [Accessed: 10-Nov-2015].
[49] M. Mamlouk and K. Scott, “The effect of electrode parameters on performance of a phosphoric acid-doped PBI membrane fuel cell,” *Int. J. Hydrog. Energy*, vol. 35, no. 2, pp. 784–793, Jan. 2010.
[50] C.-P. Wang, H.-S. Chu, Y.-Y. Yan, and K.-L. Hsueh, “Transient evolution of carbon monoxide poisoning effect of PBI membrane fuel cells,” *J. Power Sources*, vol. 170, no. 2, pp. 235–241, Jul. 2007.
[51] S. J. Andreasen, J. R. Vang, and S. K. Kær, “High temperature PEM fuel cell performance characterisation with CO and CO2 using electrochemical impedance spectroscopy,” *Int. J. Hydrog. Energy*, vol. 36, no. 16, pp. 9815–9830, Aug. 2011.
[52] J. Weiss-Ungethüm, I. Bürger, N. Schmidt, M. Linder, and J. Kallo, “Experimental investigation of a liquid cooled high temperature proton exchange membrane (HT-PEM) fuel cell coupled to a sodium alanate tank,” *Int. J. Hydrog. Energy*, vol. 39, no. 11, pp. 5931–5941, Apr. 2014.
[53] “Serenergy - The Power of Simplicity,” 2014. [Online]. Available: http://serenergy.com/. [Accessed: 22-Apr-2014].
[54] H.-S. Lee, A. Roy, O. Lane, and J. E. McGrath, “Synthesis and characterization of poly(arylene ether sulfone)-b-polybenzimidazole copolymers for high temperature low humidity proton exchange membrane fuel cells,” *Polymer*, vol. 49, no. 25, pp. 5387–5396, Nov. 2008.
[55] Q. Li, R. He, R. W. Berg, H. A. Hjuler, and N. J. Bjerrum, “Water uptake and acid doping of polybenzimidazoles as electrolyte membranes for fuel cells,” *Solid State Ion.*, vol. 168, no. 1–2, pp. 177–185, Mar. 2004.

[56] S. Galbiati, A. Baricci, A. Casalegno, and R. Marchesi, “Experimental study of water transport in a polybenzimidazole-based high temperature PEMFC,” *Int. J. Hydrog. Energy*, vol. 37, no. 3, pp. 2462–2469, Feb. 2012.
[57] D. Hoel and E. Grunwald, “High protonic conduction of polybenzimidazole films,” *J. Phys. Chem.*, vol. 81, no. 22, pp. 2135–2136, Nov. 1977.
[58] D. Aili, Q. Li, E. Christensen, J. O. Jensen, and N. J. Bjerrum, “Crosslinking of polybenzimidazole membranes by divinylsulfone post-treatment for high-temperature proton exchange membrane fuel cell applications,” *Polym. Int.*, vol. 60, no. 8, pp. 1201–1207, Aug. 2011.
[59] Y.-L. Ma, J. S. Wainright, M. H. Litt, and R. F. Savinell, “Conductivity of PBI Membranes for High-Temperature Polymer Electrolyte Fuel Cells,” *J. Electrochem. Soc.*, vol. 151, no. 1, pp. A8–A16, Jan. 2004.
[60] C. Hasiotis, L. Qingfeng, V. Deimede, J. K. Kallitsis, C. G. Kontoyannis, and N. J. Bjerrum, “Development and Characterization of Acid-Doped Polybenzimidazole/Sulfonated Polysulfone Blend Polymer Electrolytes for Fuel Cells,” *J. Electrochem. Soc.*, vol. 148, no. 5, pp. A513–A519, May 2001.
[61] S.-K. Kim, S.-W. Choi, W. S. Jeon, J. O. Park, T. Ko, H. Chang, and J.-C. Lee, “Cross-Linked Benzoxazine–Benzimidazole Copolymer Electrolyte Membranes for Fuel Cells at Elevated Temperature,” *Macromolecules*, vol. 45, no. 3, pp. 1438–1446, Feb. 2012.
[62] A. Verma and K. Scott, “Development of high-temperature PEMFC based on heteropolyacids and polybenzimidazole,” *J. Solid State Electrochem.*, vol. 14, no. 2, pp. 213–219, Sep. 2008.
[63] J. A. Mader and B. C. Benicewicz, “Sulfonated Polybenzimidazoles for High Temperature PEM Fuel Cells,” *Macromolecules*, vol. 43, no. 16, pp. 6706–6715, Aug. 2010.
[64] D. W. Green and others, *Perry’s chemical engineers’ handbook*, vol. 796. McGraw-hill New York, 2008.
[65] A. Guenbour, H. Iken, N. Kebkab, A. Bellaouchou, R. Boulif, and A. B. Bachir, “Corrosion of graphite in industrial phosphoric acid,” *Appl. Surf. Sci.*, vol. 252, no. 24, pp. 8710–8715, Oct. 2006.
[66] C. Hartnig and T. J. Schmidt, “On a new degradation mode for high-temperature polymer electrolyte fuel cells: How bipolar plate degradation affects cell performance,” *Electrochimica Acta*, vol. 56, no. 11, pp. 4237–4242, Apr. 2011.
[67] J. J. Linares, C. Sanches, V. A. Paganin, and E. R. Gonzalez, “Performance of a poly(2,5-benzimidazole)-based polymer electrolyte membrane fuel cell,” *Int. J. Hydrog. Energy*, vol. 37, no. 8, pp. 7212–7220, Apr. 2012.
[68] W. Vogel, L. Lundquist, P. Ross, and P. Stonehart, “Reaction pathways and poisons—II: The rate controlling step for electrochemical oxidation of hydrogen on Pt in acid and poisoning of the reaction by CO,” *Electrochimica Acta*, vol. 20, no. 1, pp. 79–93, Jan. 1975.
[69] H. Igarashi, T. Fujino, and M. Watanabe, “Hydrogen electro-oxidation on platinum catalysts in the presence of trace carbon monoxide,” *J. Electroanal. Chem.*, vol. 391, no. 1–2, pp. 119–123, Jul. 1995.
[70] S. K. Das, A. Reis, and K. J. Berry, “Experimental evaluation of CO poisoning on the performance of a high temperature proton exchange membrane fuel cell,” *J. Power Sources*, vol. 193, no. 2, pp. 691–698, Sep. 2009.

[71] H. P. Dhar, L. G. Christner, and A. K. Kush, “Nature of CO Adsorption during H 2 Oxidation in Relation to Modeling for CO Poisoning of a Fuel Cell Anode,” *J. Electrochem. Soc.*, vol. 134, no. 12, pp. 3021–3026, Dec. 1987.
[72] T. E. Springer, T. Rockward, T. A. Zawodzinski, and S. Gottesfeld, “Model for Polymer Electrolyte Fuel Cell Operation on Reformate Feed: Effects of CO, H;2 Dilution, and High Fuel Utilization,” *J. Electrochem. Soc.*, vol. 148, no. 1, pp. A11–A23, Jan. 2001.
[73] K. Oh, G. Jeong, E. Cho, W. Kim, and H. Ju, “A CO poisoning model for high-temperature proton exchange membrane fuel cells comprising phosphoric acid-doped polybenzimidazole membranes,” *Int. J. Hydrog. Energy*, vol. 39, no. 36, pp. 21915–21926, 2014.
[74] L. W. Niedrach, D. W. McKee, J. Paynter, and I. F. Danzig, “Electrocatalysts for hydrogen/carbon monoxide fuel cell anodes. i. platinum-ruthenium system,” *Electrochem. Technol.*, vol. 5, no. 7–8, p. 318, 1967.
[75] S. Ball, A. Hodgkinson, G. Hoogers, S. Maniguet, D. Thompsett, and B. Wong, “The proton exchange membrane fuel cell performance of a carbon supported PtMo catalyst operating on reformate,” *Electrochem. Solid-State Lett.*, vol. 5, no. 2, pp. A31–A34, 2002.
[76] M. K. Jeon, H. Daimon, K. R. Lee, A. Nakahara, and S. I. Woo, “CO tolerant Pt/WC methanol electro-oxidation catalyst,” *Electrochem. Commun.*, vol. 9, no. 11, pp. 2692–2695, 2007.
[77] Y. Liang, H. Zhang, Z. Tian, X. Zhu, X. Wang, and B. Yi, “Synthesis and structure-activity relationship exploration of carbon-supported PtRuNi nanocomposite as a CO-tolerant electrocatalyst for proton exchange membrane fuel cells,” *J. Phys. Chem. B*, vol. 110, no. 15, pp. 7828–7834, 2006.
[78] K. Scott, S. Pilditch, and M. Mamlouk, “Modelling and experimental validation of a high temperature polymer electrolyte fuel cell,” *J. Appl. Electrochem.*, vol. 37, no. 11, pp. 1245–1259, Sep. 2007.
[79] A. R. Korsgaard, R. Refshauge, M. P. Nielsen, M. Bang, and S. K. Kær, “Experimental characterization and modeling of commercial polybenzimidazole-based MEA performance,” *J. Power Sources*, vol. 162, no. 1, pp. 239–245, Nov. 2006.
[80] F. Garzon, “Effect of Fuel and Air Impurities on PEM Fuel Cell Performance,” presented at the 2006 Annual Merit Review Proceedings Fuel Cells, LANL, 16-May-2006.
[81] F. A. Uribe, S. Gottesfeld, and T. A. Zawodzinski, “Effect of Ammonia as Potential Fuel Impurity on Proton Exchange Membrane Fuel Cell Performance,” *J. Electrochem. Soc.*, vol. 149, no. 3, pp. A293–A296, Mar. 2002.
[82] F. Garzon, F. A. Uribe, T. Rockward, I. G. Urdampilleta, and E. L. Brosha, “The Impact of Hydrogen Fuel Contaminates on Long-Term PMFC Performance,” *ECS Trans.*, vol. 3, no. 1, pp. 695–703, Oct. 2006.
[83] D. Yang, J. Ma, L. Xu, M. Wu, and H. Wang, “The effect of nitrogen oxides in air on the performance of proton exchange membrane fuel cell,” *Electrochimica Acta*, vol. 51, no. 19, pp. 4039–4044, May 2006.
[84] “Desulfurization – SulfaTrap – Global Leader in Sulfur Removal Sorbents.” [Online]. Available: http://sulfatrap.com/. [Accessed: 03-Nov-2015].
[85] C. A. Reiser, L. Bregoli, T. W. Patterson, J. S. Yi, J. D. Yang, M. L. Perry, and T. D. Jarvi, “A Reverse-Current Decay Mechanism for Fuel Cells,” *Electrochem. Solid-State Lett.*, vol. 8, no. 6, pp. A273–A276, Jun. 2005.

[86] M. F. Mathias, R. Makharia, H. A. Gasteiger, J. J. Conley, T. J. Fuller, C. J. Gittleman, S. S. Kocha, D. P. Miller, C. K. Mittelsteadt, T. Xie, and others, "Two fuel cell cars in every garage," *Electrochem Soc Interface*, vol. 14, no. 3, pp. 24–35, 2005.
[87] Q. Shen, M. Hou, D. Liang, Z. Zhou, X. Li, Z. Shao, and B. Yi, "Study on the processes of start-up and shutdown in proton exchange membrane fuel cells," *J. Power Sources*, vol. 189, no. 2, pp. 1114–1119, Apr. 2009.
[88] B. Avasarala, R. Moore, and P. Haldar, "Surface oxidation of carbon supports due to potential cycling under PEM fuel cell conditions," *Electrochimica Acta*, vol. 55, no. 16, pp. 4765–4771, Jun. 2010.
[89] Z. Siroma, K. Ishii, K. Yasuda, Y. Miyazaki, M. Inaba, and A. Tasaka, "Imaging of highly oriented pyrolytic graphite corrosion accelerated by Pt particles," *Electrochem. Commun.*, vol. 7, no. 11, pp. 1153–1156, Nov. 2005.
[90] T. J. Schmidt, "High-Temperature Polymer Electrolyte Fuel Cells: Durability Insights," in *Polymer Electrolyte Fuel Cell Durability*, F. N. Büchi, M. Inaba, and T. J. Schmidt, Eds. Springer New York, 2009, pp. 199–221.
[91] R. Borup, J. Meyers, B. Pivovar, Y. S. Kim, R. Mukundan, N. Garland, D. Myers, M. Wilson, F. Garzon, D. Wood, and others, "Scientific aspects of polymer electrolyte fuel cell durability and degradation," *Chem. Rev.*, vol. 107, no. 10, pp. 3904–3951, 2007.
[92] A. Honji, T. Mori, K. Tamura, and Y. Hishinuma, "Agglomeration of Platinum Particles Supported on Carbon in Phosphoric Acid," *J. Electrochem. Soc.*, vol. 135, no. 2, pp. 355–359, Feb. 1988.
[93] R. D. Breault, "Stack materials and stack design," in *Handbook of Fuel Cells*, John Wiley & Sons, Ltd, 2010.
[94] S. Galbiati, A. Baricci, A. Casalegno, and R. Marchesi, "Degradation in phosphoric acid doped polymer fuel cells: A 6000 h parametric investigation," *Int. J. Hydrog. Energy*, vol. 38, no. 15, pp. 6469–6480, May 2013.
[95] L. Xiao, H. Zhang, E. Scanlon, L. S. Ramanathan, E.-W. Choe, D. Rogers, T. Apple, and B. C. Benicewicz, "High-Temperature Polybenzimidazole Fuel Cell Membranes via a Sol−Gel Process," *Chem. Mater.*, vol. 17, no. 21, pp. 5328–5333, Oct. 2005.
[96] D. A. Condit and R. D. Breault, "Shut-down procedure for hydrogen-air fuel cell system," US6635370 B2, 21-Oct-2003.
[97] A. Kannan, A. Kabza, and J. Scholta, "Long term testing of start–stop cycles on high temperature PEM fuel cell stack," *J. Power Sources*, vol. 277, pp. 312–316, Mar. 2015.
[98] S. Yu, L. Xiao, and B. C. Benicewicz, "Durability Studies of PBI-based High Temperature PEMFCs," *Fuel Cells*, vol. 8, no. 3–4, pp. 165–174, Jul. 2008.
[99] U. S. DOE, "Hydrogen Production: Natural Gas Reforming," *U.S. Department of Energy:: Energy Efiiciency and Renwable Energy*, 20-Nov-2012. [Online]. Available: https://www1.eere.energy.gov/hydrogenandfuelcells/production/natural_gas.html. [Accessed: 13-Apr-2013].
[100] G. Thomas and J. Keller, "Hydrogen Storage - Overview," presented at the H2 Delivery and Infrstructure Workship, Sandia National Laboratories, 07-May-2003.
[101] P. Sabatier and J. B. Senderens, "Compt. rend. 134, 514 (1902) und J. Soc," *Chem Ind*, vol. 21, p. 504, 1902.
[102] N. Hajjaji, M.-N. Pons, A. Houas, and V. Renaudin, "Exergy analysis: An efficient tool for understanding and improving hydrogen production via the steam methane reforming process," *Energy Policy*, vol. 42, pp. 392–399, Mar. 2012.

[103] M. G. Waller, E. D. Williams, S. W. Matteson, and T. A. Trabold, “Current and theoretical maximum well-to-wheels exergy efficiency of options to power vehicles with natural gas,” *Appl. Energy*, vol. 127, pp. 55–63, Aug. 2014.
[104] S. Ayabe, H. Omoto, T. Utaka, R. Kikuchi, K. Sasaki, Y. Teraoka, and K. Eguchi, “Catalytic autothermal reforming of methane and propane over supported metal catalysts,” *Appl. Catal. Gen.*, vol. 241, no. 1–2, pp. 261–269, Feb. 2003.
[105] M. K. Nikoo and N. A. S. Amin, “Thermodynamic analysis of carbon dioxide reforming of methane in view of solid carbon formation,” *Fuel Process. Technol.*, vol. 92, no. 3, pp. 678–691, Mar. 2011.
[106] V. Recupero, L. Pino, R. Di Leonardo, M. Lagana’, and G. Maggio, “Hydrogen generator, via catalytic partial oxidation of methane for fuel cells,” *J. Power Sources*, vol. 71, no. 1–2, pp. 208–214, Mar. 1998.
[107] B. Christian Enger, R. Lødeng, and A. Holmen, “A review of catalytic partial oxidation of methane to synthesis gas with emphasis on reaction mechanisms over transition metal catalysts,” *Appl. Catal. Gen.*, vol. 346, no. 1–2, pp. 1–27, Aug. 2008.
[108] P. Corbo and F. Migliardini, “Hydrogen production by catalytic partial oxidation of methane and propane on Ni and Pt catalysts,” *Int. J. Hydrog. Energy*, vol. 32, no. 1, pp. 55–66, Jan. 2007.
[109] J. Rostrup-Nielsen and L. J. Christiansen, *Concepts in syngas manufacture*, vol. 10. World Scientific, 2011.
[110] B. T. Schädel, M. Duisberg, and O. Deutschmann, “Steam reforming of methane, ethane, propane, butane, and natural gas over a rhodium-based catalyst,” *Catal. Today*, vol. 142, no. 1–2, pp. 42–51, Apr. 2009.
[111] T. A. Trabold, J. S. Lylak, M. R. Walluk, J. F. Lin, and D. R. Troiani, “Measurement and analysis of carbon formation during diesel reforming for solid oxide fuel cells,” *Int. J. Hydrog. Energy*, vol. 37, no. 6, pp. 5190–5201, Mar. 2012.
[112] H. Pennemann, V. Hessel, G. Kolb, H. Löwe, and R. Zapf, “Partial oxidation of propane using micro structured reactors,” *Chem. Eng. J.*, vol. 135, Supplement 1, pp. S66–S73, Jan. 2008.
[113] G. Zeng, Y. Tian, and Y. Li, “Thermodynamic analysis of hydrogen production for fuel cell via oxidative steam reforming of propane,” *Int. J. Hydrog. Energy*, vol. 35, no. 13, pp. 6726–6737, Jul. 2010.
[114] M. G. Waller, M. R. Walluk, and T. A. Trabold, “Operating envelope of a short contact time fuel reformer for propane catalytic partial oxidation,” *J. Power Sources*, vol. 274, pp. 149–155, Jan. 2015.
[115] J. J. Krummenacher, K. N. West, and L. D. Schmidt, “Catalytic partial oxidation of higher hydrocarbons at millisecond contact times: decane, hexadecane, and diesel fuel,” *J. Catal.*, vol. 215, no. 2, pp. 332–343, Apr. 2003.
[116] M. Castaldi, M. Lyubovsky, R. LaPierre, W. C. Pfefferle, and S. Roychoudhury, “Performance of Microlith Based Catalytic Reactors for an Isooctane Reforming System,” *SAE Int.*, 2003.
[117] S. Roychoudhury, M. Castaldi, M. Lyubovsky, R. LaPierre, and S. Ahmed, “Microlith catalytic reactors for reforming iso-octane-based fuels into hydrogen,” *J. Power Sources*, vol. 152, pp. 75–86, Dec. 2005.

[118] V. Modafferi, G. Panzera, V. Baglio, F. Frusteri, and P. L. Antonucci, "Propane reforming on Ni–Ru/GDC catalyst: H2 production for IT-SOFCs under SR and ATR conditions," *Appl. Catal. Gen.*, vol. 334, no. 1–2, pp. 1–9, Jan. 2008.
[119] W. C. Pfefferle, "Microlith catalytic reaction system," US5051241 A, 24-Sep-1991.
[120] C. Junaedi, S. A. Vilekar, D. Walsh, R. Mastanduno, C. Morgan, and S. Roychoudhury, "Development of integrated reformer systems for syngas production," *Int. J. Hydrog. Energy*, vol. 37, no. 13, pp. 10435–10443, Jul. 2012.
[121] R. N. Carter, S. Roychoudhury, G. Muench, H. Karim, and W. Pfefferle, "Rapid Thermal Response Catalyst for Treatment of Automotive Exhaust," *MRS Online Proc. Libr.*, vol. 454, p. null–null, 1996.
[122] M. Lyubovsky, S. Roychoudhury, and R. LaPierre, "Catalytic partial 'oxidation of methane to syngas' at elevated pressures," *Catal. Lett.*, vol. 99, no. 3–4, pp. 113–117, Feb. 2005.
[123] M. Lyubovsky and S. Roychoudhury, "Novel catalytic reactor for oxidative reforming of methanol," *Appl. Catal. B Environ.*, vol. 54, no. 4, pp. 203–215, Dec. 2004.
[124] S. Roychoudhury, M. Lyubovsky, D. Walsh, D. Chu, and E. Kallio, "Design and development of a diesel and JP-8 logistic fuel processor," *J. Power Sources*, vol. 160, no. 1, pp. 510–513, Sep. 2006.
[125] "AspenTech: Optimizing Process Manufacturing," *Optimize Design and Operations with aspenONE Engineering*, 2014. [Online]. Available: http://www.aspentech.com/products/aspenone-engineering/. [Accessed: 18-Feb-2014].
[126] C. Resini, M. C. Herrera Delgado, L. Arrighi, L. J. Alemany, R. Marazza, and G. Busca, "Propene versus propane steam reforming for hydrogen production over Pd-based and Ni-based catalysts," *Catal. Commun.*, vol. 6, no. 7, pp. 441–445, Jul. 2005.
[127] X. Wang, N. Wang, J. Zhao, and L. Wang, "Thermodynamic analysis of propane dry and steam reforming for synthesis gas or hydrogen production," *Int. J. Hydrog. Energy*, vol. 35, no. 23, pp. 12800–12807, Dec. 2010.
[128] K. Vasudeva, N. Mitra, P. Umasankar, and S. C. Dhingra, "Steam reforming of ethanol for hydrogen production: Thermodynamic analysis," *Int. J. Hydrog. Energy*, vol. 21, no. 1, pp. 13–18, Jan. 1996.
[129] S. H. Chan and H. M. Wang, "Thermodynamic analysis of natural-gas fuel processing for fuel cell applications," *Int. J. Hydrog. Energy*, vol. 25, no. 5, pp. 441–449, May 2000.
[130] J.-W. Snoeck, G. F. Froment, and M. Fowles, "Steam/CO2 Reforming of Methane. Carbon Filament Formation by the Boudouard Reaction and Gasification by CO2, by H2, and by Steam: Kinetic Study," *Ind. Eng. Chem. Res.*, vol. 41, no. 17, pp. 4252–4265, Jul. 2002.
[131] P. Cadman, G. O. Thomas, and P. Butler, "The auto-ignition of propane at intermediate temperatures and high pressures," *Phys. Chem. Chem. Phys.*, vol. 2, no. 23, pp. 5411–5419, Jan. 2000.
[132] B. S. Çağlayan, A. K. Avcı, Z. İ. Önsan, and A. E. Aksoylu, "Production of hydrogen over bimetallic Pt–Ni/δ-Al2O3: I. Indirect partial oxidation of propane," *Appl. Catal. Gen.*, vol. 280, no. 2, pp. 181–188, Mar. 2005.
[133] A. K. Avcı, D. L. Trimm, A. E. Aksoylu, and Z. İ. Önsan, "Ignition Characteristics of Pt, Ni and Pt-Ni Catalysts Used for Autothermal Fuel Processing," *Catal. Lett.*, vol. 88, no. 1–2, pp. 17–22, May 2003.

[134] B. R. Stanmore, J. F. Brilhac, and P. Gilot, “The oxidation of soot: a review of experiments, mechanisms and models,” *Carbon*, vol. 39, no. 15, pp. 2247–2268, Dec. 2001.
[135] T. Zhang and M. D. Amiridis, “Hydrogen production via the direct cracking of methane over silica-supported nickel catalysts,” *Appl. Catal. Gen.*, vol. 167, no. 2, pp. 161–172, Feb. 1998.
[136] S. J. Park, D. H. Lee, and Y. S. Kang, “High temperature proton exchange membranes based on triazoles attached onto SBA-15 type mesoporous silica,” *J. Membr. Sci.*, vol. 357, no. 1–2, pp. 1–5, Jul. 2010.
[137] M. Li and K. Scott, “A polymer electrolyte membrane for high temperature fuel cells to fit vehicle applications,” *Electrochimica Acta*, vol. 55, no. 6, pp. 2123–2128, Feb. 2010.
[138] J. Lobato, P. Cañizares, M. A. Rodrigo, D. Úbeda, and F. J. Pinar, “Enhancement of the fuel cell performance of a high temperature proton exchange membrane fuel cell running with titanium composite polybenzimidazole-based membranes,” *J. Power Sources*, vol. 196, no. 20, pp. 8265–8271, Oct. 2011.
[139] F. J. Pinar, P. Cañizares, M. A. Rodrigo, D. Úbeda, and J. Lobato, “Long-term testing of a high-temperature proton exchange membrane fuel cell short stack operated with improved polybenzimidazole-based composite membranes,” *J. Power Sources*, vol. 274, pp. 177–185, Jan. 2015.
[140] E. K. Pefkianakis, V. Deimede, M. K. Daletou, N. Gourdoupi, and J. K. Kallitsis, “Novel Polymer Electrolyte Membrane, Based on Pyridine Containing Poly(ether sulfone), for Application in High-Temperature Fuel Cells,” *Macromol. Rapid Commun.*, vol. 26, no. 21, pp. 1724–1728, Nov. 2005.
[141] N. Gourdoupi, N. Triantafyllopoulos, V. Deimede, L. Pefkianakis, M. Daletou, S. Neophytides, and J. Kallitsis, “Aromatic polyether copolymers and polymer blends and fuel cells comprising same,” US20080063923 A1, 13-Mar-2008.
[142] G. Avgouropoulos, T. Ioannides, J. K. Kallitsis, and S. Neophytides, “Development of an internal reforming alcohol fuel cell: Concept, challenges and opportunities,” *Chem. Eng. J.*, vol. 176–177, pp. 95–101, Dec. 2011.
[143] J. Lobato, H. Zamora, P. Cañizares, J. Plaza, and M. A. Rodrigo, “Microporous layer based on SiC for high temperature proton exchange membrane fuel cells,” *J. Power Sources*, vol. 288, pp. 288–295, Aug. 2015.
[144] C.-Y. Chen and W.-H. Lai, “Effects of temperature and humidity on the cell performance and resistance of a phosphoric acid doped polybenzimidazole fuel cell,” *J. Power Sources*, vol. 195, no. 21, pp. 7152–7159, Nov. 2010.
[145] A. R. Korsgaard, R. Refshauge, M. P. Nielsen, M. Bang, and S. K. Kær, “Experimental characterization and modeling of commercial polybenzimidazole-based MEA performance,” *J. Power Sources*, vol. 162, no. 1, pp. 239–245, Nov. 2006.
[146] M. K. Daletou, J. K. Kallitsis, G. Voyiatzis, and S. G. Neophytides, “The interaction of water vapors with H3PO4 imbibed electrolyte based on PBI/polysulfone copolymer blends,” *J. Membr. Sci.*, vol. 326, no. 1, pp. 76–83, Jan. 2009.
[147] T. J. Schmidt and J. Baurmeister, “Properties of high-temperature PEFC Celtec®-P 1000 MEAs in start/stop operation mode,” *J. Power Sources*, vol. 176, no. 2, pp. 428–434, Feb. 2008.
[148] P. Moçotéguy, B. Ludwig, J. Scholta, R. Barrera, and S. Ginocchio, “Long Term Testing in Continuous Mode of HT-PEMFC Based H3PO4/PBI Celtec-P MEAs for µ-CHP Applications,” *Fuel Cells*, vol. 9, no. 4, pp. 325–348, 2009.

[149] P. Moçotéguy, B. Ludwig, J. Scholta, Y. Nedellec, D. J. Jones, and J. Rozière, "Long-Term Testing in Dynamic Mode of HT-PEMFC H3PO4/PBI Celtec-P Based Membrane Electrode Assemblies for Micro-CHP Applications," *Fuel Cells*, vol. 10, no. 2, pp. 299–311, Apr. 2010.

[150] L. Hedström, T. Tingelöf, P. Alvfors, and G. Lindbergh, "Experimental results from a 5 kW PEM fuel cell stack operated on simulated reformate from highly diluted hydrocarbon fuels: Efficiency, dilution, fuel utilisation, CO poisoning and design criteria," *Int. J. Hydrog. Energy*, vol. 34, no. 3, pp. 1508–1514, Feb. 2009.

[151] Advent Technologies, "Advent TPS HT MEAs Product Sheet." 2013.

[152] T. Hosoi, T. Yonekura, K. Sunada, and K. Sasaki, "Exchange Current Density of SOFC Electrodes: Theoretical Relations and Partial Pressure Dependencies Rate-Determined by Electrochemical Reactions," *J. Electrochem. Soc.*, vol. 162, no. 1, pp. F136–F152, Jan. 2015.

[153] R. Bouchet and E. Siebert, "Proton conduction in acid doped polybenzimidazole," *Solid State Ion.*, vol. 118, no. 3–4, pp. 287–299, Mar. 1999.

[154] P. Krishnan, J.-S. Park, and C.-S. Kim, "Performance of a poly(2,5-benzimidazole) membrane based high temperature PEM fuel cell in the presence of carbon monoxide," *J. Power Sources*, vol. 159, no. 2, pp. 817–823, Sep. 2006.

[155] Q. Li, J. O. Jensen, R. F. Savinell, and N. J. Bjerrum, "High temperature proton exchange membranes based on polybenzimidazoles for fuel cells," *Prog. Polym. Sci.*, vol. 34, no. 5, pp. 449–477, May 2009.

[156] J. Song, E. S. De Castro, and S. Yu, "BASF Stack Handbook. How to build, test, and diagnose high temperature PEM fuel cell stacks with Celtec® P1100W." BASF Fuel Cell Inc., 2013.

[157] G. W. Thomson, "The Antoine Equation for Vapor-pressure Data.," *Chem. Rev.*, vol. 38, no. 1, pp. 1–39, 1946.

[158] A. Luengnaruemitchai, S. Osuwan, and E. Gulari, "Comparative studies of low-temperature water–gas shift reaction over Pt/CeO2, Au/CeO2, and Au/Fe2O3 catalysts," *Catal. Commun.*, vol. 4, no. 5, pp. 215–221, May 2003.

[159] G. Jacobs, U. M. Graham, E. Chenu, P. M. Patterson, A. Dozier, and B. H. Davis, "Low-temperature water–gas shift: impact of Pt promoter loading on the partial reduction of ceria and consequences for catalyst design," *J. Catal.*, vol. 229, no. 2, pp. 499–512, Jan. 2005.

[160] S. Ricote, G. Jacobs, M. Milling, Y. Ji, P. M. Patterson, and B. H. Davis, "Low temperature water–gas shift: Characterization and testing of binary mixed oxides of ceria and zirconia promoted with Pt," *Appl. Catal. Gen.*, vol. 303, no. 1, pp. 35–47, Apr. 2006.

[161] D. Wang, H. L. Xin, R. Hovden, H. Wang, Y. Yu, D. A. Muller, F. J. DiSalvo, and H. D. Abruña, "Structurally ordered intermetallic platinum–cobalt core–shell nanoparticles with enhanced activity and stability as oxygen reduction electrocatalysts," *Nat. Mater.*, vol. 12, no. 1, pp. 81–87, Jan. 2013.

[162] Y. Oono, T. Fukuda, A. Sounai, and M. Hori, "Influence of operating temperature on cell performance and endurance of high temperature proton exchange membrane fuel cells," *J. Power Sources*, vol. 195, no. 4, pp. 1007–1014, Feb. 2010.

[163] F. Zhou, S. Simon Araya, I. Florentina Grigoras, S. Juhl Andreasen, and S. Knudsen Kær, "Performance Degradation Tests of Phosphoric Acid Doped Polybenzimidazole Membrane Based High Temperature Polymer Electrolyte Membrane Fuel Cells," *J. Fuel Cell Sci. Technol.*, vol. 12, no. 2, pp. 021002–021002, Apr. 2015.

[164] "RQ-11B Raven Unmanned Air Vehicle (UAV)," *Airforce Technology*. [Online]. Available: http://www.airforce-technology.com/projects/rq11braven/. [Accessed: 08-Dec-2015].
[165] B. A. Moffitt, "A methodology for the validated design space exploration of fuel cell powered unmanned aerial vehicles," 2010.
[166] "Hornet (UAV) : UAS Advanced Development Center - AeroVironment, Inc." [Online]. Available: https://www.avinc.com/uas/adc/hornet/. [Accessed: 10-Dec-2015].
[167] "Fuel Cell Puma (UAV) : UAS Advanced Development Center - AeroVironment, Inc." [Online]. Available: https://www.avinc.com/uas/adc/fuel_cell_puma/. [Accessed: 10-Dec-2015].
[168] K. Kim, T. Kim, K. Lee, and S. Kwon, "Fuel cell system with sodium borohydride as hydrogen source for unmanned aerial vehicles," *J. Power Sources*, vol. 196, no. 21, pp. 9069–9075, Nov. 2011.
[169] "Stalker UAS · Lockheed Martin." [Online]. Available: http://www.lockheedmartin.com/us/products/stalker-uas.html. [Accessed: 10-Dec-2015].
[170] "ROAMIO Defender Series | Ultra Electronics AMI | Fuel Cell Manufacturer." [Online]. Available: http://www.ultra-ami.com/portable-power-fuel-cell-products/roamio-defender-series/. [Accessed: 04-Sep-2015].
[171] "HES Energy Systems," *HORIZON ENERGY SYSTEMS: In the air*. [Online]. Available: http://www.hes.sg/. [Accessed: 10-Dec-2015].
[172] Celeroton, "Compressors ~ Celeroton AG - Ultra-high-speed electrical drive systems." [Online]. Available: http://www.celeroton.com/en/products/compressors.html. [Accessed: 20-Dec-2015].
[173] The Lee Company, "Flow Control from the Lee Company." [Online]. Available: http://www.theleeco.com/flow-control/flow-control.cfm. [Accessed: 20-Dec-2015].
[174] M. Donati, "Miniature Two-stage Diaphragm Pressure Regulator," *Beswick Engineering*. [Online]. Available: http://www.beswick.com/article/miniature-two-stage-diaphragm-pressure-regulator-10-32-threaded-prd3. [Accessed: 20-Dec-2015].
[175] A. Hermann, T. Chaudhuri, and P. Spagnol, "Bipolar plates for PEM fuel cells: A review," *Int. J. Hydrog. Energy*, vol. 30, no. 12, pp. 1297–1302, Sep. 2005.
[176] X. Li and I. Sabir, "Review of bipolar plates in PEM fuel cells: Flow-field designs," *Int. J. Hydrog. Energy*, vol. 30, no. 4, pp. 359–371, Mar. 2005.
[177] H. Tawfik, Y. Hung, and D. Mahajan, "Metal bipolar plates for PEM fuel cell—A review," *J. Power Sources*, vol. 163, no. 2, pp. 755–767, Jan. 2007.
[178] S. Karimi, N. Fraser, B. Roberts, and F. R. Foulkes, "A Review of Metallic Bipolar Plates for Proton Exchange Membrane Fuel Cells: Materials and Fabrication Methods," *Adv. Mater. Sci. Eng.*, vol. 2012, p. e828070, Aug. 2012.
[179] H.-C. Kuan, C.-C. M. Ma, K. H. Chen, and S.-M. Chen, "Preparation, electrical, mechanical and thermal properties of composite bipolar plate for a fuel cell," *J. Power Sources*, vol. 134, no. 1, pp. 7–17, Jul. 2004.
[180] A. S. Woodman, K. D. Jayne, E. B. Anderson, and M. C. Kimble, "Development of corrosion-resistant coatings for fuel cell bipolar plates," in *AESF SUR FIN-PROCEEDINGS-*, 1999, pp. 717–726.
[181] Y.-C. Park, S.-H. Lee, S.-K. Kim, S. Lim, D.-H. Jung, D.-Y. Lee, S.-Y. Choi, H. ji, and D.-H. Peck, "Performance and long-term stability of Ti metal and stainless steels as a metal

bipolar plate for a direct methanol fuel cell," *Int. J. Hydrog. Energy*, vol. 35, no. 9, pp. 4320–4328, May 2010.
[182] H. Wang and J. A. Turner, "Austenitic stainless steels in high temperature phosphoric acid," *J. Power Sources*, vol. 180, no. 2, pp. 803–807, Jun. 2008.
[183] V. Weissbecker, K. Wippermann, and W. Lehnert, "Electrochemical Corrosion Study of Metallic Materials in Phosphoric Acid as Bipolar Plates for HT-PEFCs," *J. Electrochem. Soc.*, vol. 161, no. 14, pp. F1437–F1447, Jan. 2014.
[184] A. Kumar, M. Ricketts, and S. Hirano, "Ex situ evaluation of nanometer range gold coating on stainless steel substrate for automotive polymer electrolyte membrane fuel cell bipolar plate," *J. Power Sources*, vol. 195, no. 5, pp. 1401–1407, Mar. 2010.
[185] "Gold Prices Per Gram Today - Gold Price OZ." [Online]. Available: http://www.goldpriceoz.com/gold-price-per-gram/. [Accessed: 19-Dec-2015].
[186] S.-P. Jung, C.-I. Lee, C.-C. Chen, W.-S. Chang, and C.-C. Yang, "Development of novel proton exchange membrane fuel cells using stamped metallic bipolar plates," *J. Power Sources*, vol. 283, pp. 429–442, Jun. 2015.
[187] R. Taccani and N. Zuliani, "Effect of flow field design on performances of high temperature PEM fuel cells: Experimental analysis," *Int. J. Hydrog. Energy*, vol. 36, no. 16, pp. 10282–10287, Aug. 2011.
[188] N. Sugita, M. Oda, M. Sakano, N. Kawagoe, and T. Kosaka, "Fuel cell," US7695845 B2, 13-Apr-2010.
[189] H. Li, Y. Tang, Z. Wang, Z. Shi, S. Wu, D. Song, J. Zhang, K. Fatih, J. Zhang, H. Wang, Z. Liu, R. Abouatallah, and A. Mazza, "A review of water flooding issues in the proton exchange membrane fuel cell," *J. Power Sources*, vol. 178, no. 1, pp. 103–117, Mar. 2008.
[190] J. A. Rock, H. Schlag, and K. R. Griffith, *Stamped fuel cell bipolar plate*. Google Patents, 2010.
[191] A. Kumar and R. G. Reddy, "Materials and design development for bipolar/end plates in fuel cells," *J. Power Sources*, vol. 129, no. 1, pp. 62–67, Apr. 2004.
[192] ASCO, "ASCO Cv Calculation Formula." [Online]. Available: https://www.ascovalvenet.com/Ascovalvenet/Applications/ValveSizingglobal/valve_sizing_help.htm. [Accessed: 21-Dec-2015].
[193] Parker, "Series MX - Miniature Solenoid Actuated Poppet Valve | ParkerExportStore." [Online]. Available: http://ph.parker.com/us/12051/en/series-mx-miniature-solenoid-actuated-poppet-valve/961-721112-000. [Accessed: 20-Dec-2015].
[194] Swagelok, "SS-4F-T7-60 | Swagelok." [Online]. Available: http://www.swagelok.com/en/catalog/Product/Detail?part=SS-4F-T7-60&item=. [Accessed: 20-Dec-2015].
[195] G. Zhang and S. G. Kandlikar, "A critical review of cooling techniques in proton exchange membrane fuel cell stacks," *Int. J. Hydrog. Energy*, vol. 37, no. 3, pp. 2412–2429, Feb. 2012.
[196] H. Schmidt, P. Buchner, A. Datz, K. Dennerlein, S. Lang, and M. Waidhas, "Low-cost air-cooled PEFC stacks," *J. Power Sources*, vol. 105, no. 2, pp. 243–249, Mar. 2002.
[197] Y.-J. Sohn, G.-G. Park, T.-H. Yang, Y.-G. Yoon, W.-Y. Lee, S.-D. Yim, and C.-S. Kim, "Operating characteristics of an air-cooling PEMFC for portable applications," *J. Power Sources*, vol. 145, no. 2, pp. 604–609, Aug. 2005.
[198] Gino, "Black Brushless DC Cooling Blower Fan 5015S 12V 0.14A 50mm x 15mm," *Amazon*, 21-Dec-2015. [Online]. Available: http://www.amazon.com/Black-Brushless-

Cooling-Blower-5015S/dp/B008P72QYS/ref=pd_sim_147_2?ie=UTF8&dpID=31RljfOHa3L&dpSrc=sims&preST=_AC_UL160_SR160%2C160_&refRID=08XVAPZ6KFFMQED4KDWZ.

[199] Arduino, "Arduino - ArduinoBoardUno." [Online]. Available: https://www.arduino.cc/en/Main/ArduinoBoardUno. [Accessed: 20-Dec-2015].

[200] Electronics123.com, "Arduino Thermocouple Multiplexer Shield (K - MAX31855K) | Electronics123." [Online]. Available: http://www.electronics123.com/shop/product/arduino-thermocouple-multiplexer-shield-k-max31855k-4830?page=2. [Accessed: 20-Dec-2015].

[201] F. Zenith, F. Seland, O. E. Kongstein, B. Børresen, R. Tunold, and S. Skogestad, "Control-oriented modelling and experimental study of the transient response of a high-temperature polymer fuel cell," *J. Power Sources*, vol. 162, no. 1, pp. 215–227, Nov. 2006.

[202] M. Harfman Todorovic, L. Palma, and P. N. Enjeti, "Design of a Wide Input Range DC #x2013;DC Converter With a Robust Power Control Scheme Suitable for Fuel Cell Power Conversion," *IEEE Trans. Ind. Electron.*, vol. 55, no. 3, pp. 1247–1255, Mar. 2008.

[203] M. S. Ali, S. K. Kamarudin, M. S. Masdar, A. Mohamed, M. S. Ali, S. K. Kamarudin, M. S. Masdar, and A. Mohamed, "An Overview of Power Electronics Applications in Fuel Cell Systems: DC and AC Converters, An Overview of Power Electronics Applications in Fuel Cell Systems: DC and AC Converters," *Sci. World J. Sci. World J.*, vol. 2014, 2014, p. e103709, Nov. 2014.

[204] Nextrox, "KEEDOX® DC/DC Converter 12V Step Down to 5V 3A Power Supply Module," *Amazon*, 21-Dec-2015. [Online]. Available: http://www.amazon.com/KEEDOX%C2%AE-Converter-Power-Supply-Module/dp/B00A71CMDU/ref=sr_1_4?s=electronics&ie=UTF8&qid=1450696033&sr=1-4&keywords=5+V+DC+to+DC+converter.

[205] DROK, "DROK® 600W 12A DC Boost Voltage Converter 12-60V to 12-80V Step-up Power Supply Transformer Module Regulator Controller Constant Volt/Amp Car Regulated Laptop Battery Charger LED Driver Generator," *Amazon*, 21-Dec-2015. [Online]. Available: http://www.amazon.com/DROK-Converter-Transformer-Regulator-Controller/dp/B00E8D7XYG/ref=pd_sim_sbs_23_1?ie=UTF8&dpID=51bkqmJ38SL&dpSrc=sims&preST=_AC_UL160_SR160%2C160_&refRID=19127SV0D79RP14PBCHW.

[206] M. M. Thackeray, C. Wolverton, and E. D. Isaacs, "Electrical energy storage for transportation—approaching the limits of, and going beyond, lithium-ion batteries," *Energy Environ. Sci.*, vol. 5, no. 7, p. 7854, 2012.

[207] USDRIVE, "Fuel Cell Technical Team Roadmap," U.S. Drive, Jun. 2013.

[208] S. Mahabunphachai, Ö. N. Cora, and M. Koç, "Effect of manufacturing processes on formability and surface topography of proton exchange membrane fuel cell metallic bipolar plates," *J. Power Sources*, vol. 195, no. 16, pp. 5269–5277, Aug. 2010.

[209] A. Elgowainy, J. Han, M. Wang, N. Carter, R. Stratton, J. Hileman, A. Malwitz, and S. (Energy S. Balasubramanian, "Life-Cycle Analysis of Alternative Aviation Fuels in Greet," Argonne National Laboratory (ANL), ANL/ESD/12-8, Jul. 2012.

[210] J. J. Corbett and J. J. Winebrake, "Emissions Tradeoffs among Alternative Marine Fuels: Total Fuel Cycle Analysis of Residual Oil, Marine Gas Oil, and Marine Diesel Oil," *J. Air Waste Manag. Assoc.*, vol. 58, no. 4, pp. 538–542, Apr. 2008.

[211] A. Elgowainy, L. Gaines, and M. Wang, "Fuel-cycle analysis of early market applications of fuel cells: Forklift propulsion systems and distributed power generation," *Int. J. Hydrog. Energy*, vol. 34, no. 9, pp. 3557–3570, May 2009.
[212] U. EPA, "EPA Finalizes Emission Standards for New Nonroad Spark Ignition Engines, Equipment, and Vessels," EPA-420-F-08-013, Sep. 2008.
[213] T. Ålander, E. Antikainen, T. Raunemaa, E. Elonen, A. Rautiola, and K. Torkkell, "Particle Emissions from a Small Two-Stroke Engine: Effects of Fuel, Lubricating Oil, and Exhaust Aftertreatment on Particle Characteristics," *Aerosol Sci. Technol.*, vol. 39, no. 2, pp. 151–161, 2005.
[214] R. Magnusson, C. Nilsson, and B. Andersson, "Emissions of Aldehydes and Ketones from a Two-Stroke Engine Using Ethanol and Ethanol-Blended Gasoline as Fuel," *Environ. Sci. Technol.*, vol. 36, no. 8, pp. 1656–1664, Apr. 2002.
[215] A. Christensen, R. Westerholm, and J. Almén, "Measurement of Regulated and Unregulated Exhaust Emissions from a Lawn Mower with and without an Oxidizing Catalyst: A Comparison of Two Different Fuels," *Environ. Sci. Technol.*, vol. 35, no. 11, pp. 2166–2170, Jun. 2001.
[216] F. Jüttner, D. Backhaus, U. Matthias, U. Essers, R. Greiner, and B. Mahr, "Emissions of two- and four-stroke outboard engines—I. Quantification of gases and VOC," *Water Res.*, vol. 29, no. 8, pp. 1976–1982, Aug. 1995.
[217] P. A. Gabele and S. M. Pyle, "Emissions from Two Outboard Engines Operating on Reformulated Gasoline Containing MTBE," *Environ. Sci. Technol.*, vol. 34, no. 3, pp. 368–372, Feb. 2000.
[218] M. W. Priest, D. J. Williams, and H. A. Bridgman, "Emissions from in-use lawn-mowers in Australia," *Atmos. Environ.*, vol. 34, no. 4, pp. 657–664, Jan. 2000.
[219] "Historic U.S. Fuel Ethanol Production Statistics," *Renewable Fuels Association*, 2015. [Online]. Available: http://www.ethanolrfa.org/pages/statistics. [Accessed: 28-Aug-2015].
[220] D. Pimentel and T. W. Patzek, "Ethanol Production Using Corn, Switchgrass, and Wood; Biodiesel Production Using Soybean and Sunflower," *Nat. Resour. Res.*, vol. 14, no. 1, pp. 65–76, Mar. 2005.
[221] A. E. Farrell, R. J. Plevin, B. T. Turner, A. D. Jones, M. O'Hare, and D. M. Kammen, "Ethanol Can Contribute to Energy and Environmental Goals," *Science*, vol. 311, no. 5760, pp. 506–508, Jan. 2006.
[222] B. D. Solomon, J. R. Barnes, and K. E. Halvorsen, "Grain and cellulosic ethanol: History, economics, and energy policy," *Biomass Bioenergy*, vol. 31, no. 6, pp. 416–425, Jun. 2007.
[223] R. Hammerschlag, "Ethanol's Energy Return on Investment: A Survey of the Literature 1990−Present," *Environ. Sci. Technol.*, vol. 40, no. 6, pp. 1744–1750, Mar. 2006.
[224] G. P. Hammond, S. Kallu, and M. C. McManus, "Development of biofuels for the UK automotive market," *Appl. Energy*, vol. 85, no. 6, pp. 506–515, Jun. 2008.
[225] K. Nakata, S. Utsumi, A. Ota, K. Kawatake, T. Kawai, and T. Tsunooka, "The Effect of Ethanol Fuel on a Spark Ignition Engine," SAE International, Warrendale, PA, SAE Technical Paper 2006-01-3380, Oct. 2006.
[226] M. Al-Hasan, "Effect of ethanol–unleaded gasoline blends on engine performance and exhaust emission," *Energy Convers. Manag.*, vol. 44, no. 9, pp. 1547–1561, Jun. 2003.
[227] M. Wang, C. Saricks, and D. Santini, "EFFECTS OF FUEL ETHANOL USE ON FUEL-CYCLE ENERGY AND GREENHOUSE GAS EMISSIONS," Jan. 1999.

[228] S. G. Poulopoulos, D. P. Samaras, and C. J. Philippopoulos, “Regulated and unregulated emissions from an internal combustion engine operating on ethanol-containing fuels,” *Atmos. Environ.*, vol. 35, no. 26, pp. 4399–4406, Sep. 2001.
[229] H. S. Yücesu, T. Topgül, C. Çinar, and M. Okur, “Effect of ethanol–gasoline blends on engine performance and exhaust emissions in different compression ratios,” *Appl. Therm. Eng.*, vol. 26, no. 17–18, pp. 2272–2278, Dec. 2006.
[230] M. Koç, Y. Sekmen, T. Topgül, and H. S. Yücesu, “The effects of ethanol–unleaded gasoline blends on engine performance and exhaust emissions in a spark-ignition engine,” *Renew. Energy*, vol. 34, no. 10, pp. 2101–2106, Oct. 2009.
[231] C.-W. Wu, R.-H. Chen, J.-Y. Pu, and T.-H. Lin, “The influence of air–fuel ratio on engine performance and pollutant emission of an SI engine using ethanol–gasoline-blended fuels,” *Atmos. Environ.*, vol. 38, no. 40, pp. 7093–7100, Dec. 2004.
[232] M. Wu, M. Wang, and H. Huo, “Fuel-Cycle Assessment of Selected Bioethanol Production Pathways in the United States,” Argonne National Laboratory, Oak Ridge, TN, ANL/ESD/06-7, Nov. 2006.
[233] M. Broussely and G. Archdale, “Li-ion batteries and portable power source prospects for the next 5–10 years,” *J. Power Sources*, vol. 136, no. 2, pp. 386–394, Oct. 2004.
[234] “Global Battery Markets Information – Battery University.” [Online]. Available: http://batteryuniversity.com/learn/article/global_battery_markets. [Accessed: 01-Sep-2015].
[235] T. Tanim, D. J. Bayless, and J. P. Trembly, “Modeling a 5 kWe planar solid oxide fuel cell based system operating on JP-8 fuel and a comparison with tubular cell based system for auxiliary and mobile power applications,” *J. Power Sources*, vol. 245, pp. 986–997, Jan. 2014.
[236] M. Powell, K. Meinhardt, V. Sprenkle, L. Chick, and G. McVay, “Demonstration of a highly efficient solid oxide fuel cell power system using adiabatic steam reforming and anode gas recirculation,” *J. Power Sources*, vol. 205, pp. 377–384, May 2012.
[237] A. B. Stambouli and E. Traversa, “Solid oxide fuel cells (SOFCs): a review of an environmentally clean and efficient source of energy,” *Renew. Sustain. Energy Rev.*, vol. 6, no. 5, pp. 433–455, Oct. 2002.
[238] M. G. Waller, M. R. Walluk, and T. A. Trabold, “Performance of a high-temperature proton exchange membrane fuel cell (HT-PEMFC) operating on simulated reformate,” in *Proceedings of the ASME Power and Energy Conversion Conference*, San Diego, CA, 2015, vol. PowerEnergy2015–49562.
[239] R. M. Heck and R. J. Farrauto, “Automobile exhaust catalysts,” *Appl. Catal. Gen.*, vol. 221, no. 1–2, pp. 443–457, Nov. 2001.
[240] H. Cai, J. Han, G. Forman, V. Divita, A. Elgowainy, and M. Wang, “Analysis of Petroleum Refining Energy Efficiency of U.S. Refineries,” Systems Assessment Group, Energy Systems Division, Argonne National Laboratory, Oct. 2013.
[241] M. Wu, M. Wang, and H. Huo, “Fuel-cycle assessment of selected bioethanol production pathways in the United States,” *Argonne Ill Argonne Natl. Lab. ANLESD06-7*, vol. 120, 2006.
[242] A. Ernst and J. D. Zibrak, “Carbon Monoxide Poisoning,” *N. Engl. J. Med.*, vol. 339, no. 22, pp. 1603–1608, Nov. 1998.
[243] J. A. Raub, M. Mathieu-Nolf, N. B. Hampson, and S. R. Thom, “Carbon monoxide poisoning — a public health perspective,” *Toxicology*, vol. 145, no. 1, pp. 1–14, Apr. 2000.

[244] U. EPA, “National Ambient Air Quality Standards (NAAQS) | Air and Radiation,” *U.S. Environmental Protection Agency: Air and Radiation*, 16-Jul-2012. [Online]. Available: http://www.epa.gov/air/criteria.html. [Accessed: 03-Dec-2012].

[245] A. H. Wolfe and J. A. Patz, “Reactive Nitrogen and Human Health:Acute and Long-term Implications,” *AMBIO J. Hum. Environ.*, vol. 31, no. 2, pp. 120–125, Mar. 2002.

[246] C. C. D. US EPA, “Nitrous Oxide Emissions.” [Online]. Available: http://epa.gov/climatechange/ghgemissions/gases/n2o.html. [Accessed: 10-Sep-2015].

[247] L. M. McKenzie, R. Z. Witter, L. S. Newman, and J. L. Adgate, “Human health risk assessment of air emissions from development of unconventional natural gas resources,” *Sci. Total Environ.*, vol. 424, pp. 79–87, May 2012.

[248] K.-H. Kim, S. A. Jahan, E. Kabir, and R. J. C. Brown, “A review of airborne polycyclic aromatic hydrocarbons (PAHs) and their human health effects,” *Environ. Int.*, vol. 60, pp. 71–80, Oct. 2013.

[249] C. C. D. US EPA, “Methane Emissions.” [Online]. Available: http://epa.gov/climatechange/ghgemissions/gases/ch4.html. [Accessed: 10-Sep-2015].

[250] “CDC - NIOSH 1988 OSHA PEL Project Documentation: List by Chemical Name: CARBON DIOXIDE.” [Online]. Available: http://www.cdc.gov/niosh/pel88/124-38.html. [Accessed: 12-Sep-2015].

[251] S. A. Rice, “Human Health Risk Assessment of CO2: Survivors of Acute High-Level Exposure and Populations Sensitive to Prolonged Low-Level Exposure,” in *Third Annual Conference on Carbon Sequestration*, Alexandria, VA, 2004.

# 11 Author's Publications and Oral Presentation Contributions

**M. G. Waller**, M. R. Walluk, and T. A. Trabold, "Performance of High Temperature PEM Fuel Cell Materials. Part 1: Effects of Temperature, Pressure and Anode Dilution," International Journal of Hydrogen Energy, Accepted Dec 2015.

**M. G. Waller**, M. R. Walluk, and T. A. Trabold, "Performance of a high-temperature proton exchange membrane fuel cell (HT-PEMFC) operating on simulated reformate," in *Proceedings of the ASME Power and Energy Conversion Conference*, San Diego, CA, 2015, vol. PowerEnergy2015–49562. *Oral Presentation*

**M. G. Waller**, M. R. Walluk, and T. A. Trabold, "Operating envelope of a short contact time fuel reformer for propane catalytic partial oxidation," *J. Power Sources*, vol. 274, pp. 149–155, Jan. 2015.

**M. G. Waller**, M. R. Walluk, and T. A. Trabold, "Towards the development of a fuel cell system for low power residential applications with experimental results of propane reforming via catalytic partial oxidation," in *ASME 2014 8th International Conference on Energy Sustainability*, Boston, MA, 2014. *Oral Presentation*

M. R. Walluk, J. Lin, **M. G. Waller**, D. F. Smith, and T. A. Trabold, "Diesel auto-thermal reforming for solid oxide fuel cell systems: Anode off-gas recycle simulation," *Appl. Energy*, vol. 130, pp. 94–102, Oct. 2014.

**M. G. Waller**, E. D. Williams, S. W. Matteson, and T. A. Trabold, "Current and theoretical maximum well-to-wheels exergy efficiency of options to power vehicles with natural gas," *Appl. Energy*, vol. 127, pp. 55–63, Aug. 2014.

**M. G. Waller** and T. A. Trabold, "Review of microbial fuel cells for wastewater treatment: large-scale applications, future needs and current research gaps," *ASME 2013 7th Int. Conf. Energy Sustain.*, 2013. *Oral Presentaion*

# 12 Appendix A – Experimental PBI Performance Data

| | | | | Anode Gas % | | | | | | | |
|---|---|---|---|---|---|---|---|---|---|---|---|
| **Anode Stoic** | **Cathode Stoic** | **Temp ($^oC$)** | **Pressure (kPa)** | **$H_2$** | **$N_2$** | **$CO_2$** | **CO** | **$H_2O$** | **Current Density ($A/cm^2$)** | **Voltage (V)** | **Power ($W/cm^2$)** |
| 1.5 | 2 | 160 | 101.3 | 100 | 0 | 0 | 0 | 0 | 0 | 1.006 | 0.000 |
| 1.5 | 2 | 160 | 101.3 | 100 | 0 | 0 | 0 | 0 | 0.05 | 0.748 | 0.037 |
| 1.5 | 2 | 160 | 101.3 | 100 | 0 | 0 | 0 | 0 | 0.1 | 0.717 | 0.072 |
| 1.5 | 2 | 160 | 101.3 | 100 | 0 | 0 | 0 | 0 | 0.2 | 0.664 | 0.133 |
| 1.5 | 2 | 160 | 101.3 | 100 | 0 | 0 | 0 | 0 | 0.3 | 0.644 | 0.193 |
| 1.5 | 2 | 160 | 101.3 | 100 | 0 | 0 | 0 | 0 | 0.5 | 0.599 | 0.300 |
| 1.5 | 2 | 160 | 101.3 | 100 | 0 | 0 | 0 | 0 | 0.7 | 0.559 | 0.391 |
| 1.5 | 2 | 160 | 101.3 | 100 | 0 | 0 | 0 | 0 | 0.9 | 0.520 | 0.468 |
| 1.5 | 2 | 160 | 101.3 | 100 | 0 | 0 | 0 | 0 | 1.1 | 0.483 | 0.531 |
| 1.5 | 2 | 160 | 101.3 | 100 | 0 | 0 | 0 | 0 | 1.3 | 0.445 | 0.579 |
| 1.5 | 2 | 160 | 101.3 | 100 | 0 | 0 | 0 | 0 | 1.4 | 0.427 | 0.598 |
| 1.5 | 2 | 160 | 101.3 | 100 | 0 | 0 | 0 | 0 | 1.5 | 0.407 | 0.611 |
| | | | | | | | | | | | |
| 1.5 | 2 | 180 | 101.3 | 100 | 0 | 0 | 0 | 0 | 0 | 1.000 | 0.000 |
| 1.5 | 2 | 180 | 101.3 | 100 | 0 | 0 | 0 | 0 | 0.05 | 0.764 | 0.038 |
| 1.5 | 2 | 180 | 101.3 | 100 | 0 | 0 | 0 | 0 | 0.1 | 0.732 | 0.073 |
| 1.5 | 2 | 180 | 101.3 | 100 | 0 | 0 | 0 | 0 | 0.2 | 0.686 | 0.137 |
| 1.5 | 2 | 180 | 101.3 | 100 | 0 | 0 | 0 | 0 | 0.3 | 0.659 | 0.198 |
| 1.5 | 2 | 180 | 101.3 | 100 | 0 | 0 | 0 | 0 | 0.5 | 0.614 | 0.307 |
| 1.5 | 2 | 180 | 101.3 | 100 | 0 | 0 | 0 | 0 | 0.7 | 0.574 | 0.402 |
| 1.5 | 2 | 180 | 101.3 | 100 | 0 | 0 | 0 | 0 | 0.9 | 0.536 | 0.482 |
| 1.5 | 2 | 180 | 101.3 | 100 | 0 | 0 | 0 | 0 | 1.1 | 0.498 | 0.547 |
| 1.5 | 2 | 180 | 101.3 | 100 | 0 | 0 | 0 | 0 | 1.3 | 0.459 | 0.597 |
| 1.5 | 2 | 180 | 101.3 | 100 | 0 | 0 | 0 | 0 | 1.4 | 0.439 | 0.615 |
| 1.5 | 2 | 180 | 101.3 | 100 | 0 | 0 | 0 | 0 | 1.5 | 0.418 | 0.627 |

| | | | | Anode Gas % | | | | | | | |
|---|---|---|---|---|---|---|---|---|---|---|---|
| **Anode Stoic** | **Cathode Stoic** | **Temp ($^oC$)** | **Pressure (kPa)** | **$H_2$** | **$N_2$** | **$CO_2$** | **CO** | **$H_2O$** | **Current Density ($A/cm^2$)** | **Voltage (V)** | **Power ($W/cm^2$)** |
| 1.5 | 2 | 200 | 101.3 | 100 | 0 | 0 | 0 | 0 | 0.05 | 0.777 | 0.039 |
| 1.5 | 2 | 200 | 101.3 | 100 | 0 | 0 | 0 | 0 | 0.1 | 0.742 | 0.074 |
| 1.5 | 2 | 200 | 101.3 | 100 | 0 | 0 | 0 | 0 | 0.2 | 0.694 | 0.139 |
| 1.5 | 2 | 200 | 101.3 | 100 | 0 | 0 | 0 | 0 | 0.3 | 0.666 | 0.200 |
| 1.5 | 2 | 200 | 101.3 | 100 | 0 | 0 | 0 | 0 | 0.5 | 0.619 | 0.310 |
| 1.5 | 2 | 200 | 101.3 | 100 | 0 | 0 | 0 | 0 | 0.7 | 0.578 | 0.405 |
| 1.5 | 2 | 200 | 101.3 | 100 | 0 | 0 | 0 | 0 | 0.9 | 0.539 | 0.485 |
| 1.5 | 2 | 200 | 101.3 | 100 | 0 | 0 | 0 | 0 | 1.1 | 0.499 | 0.549 |
| 1.5 | 2 | 200 | 101.3 | 100 | 0 | 0 | 0 | 0 | 1.3 | 0.459 | 0.597 |
| 1.5 | 2 | 200 | 101.3 | 100 | 0 | 0 | 0 | 0 | 1.4 | 0.438 | 0.614 |
| 1.5 | 2 | 200 | 101.3 | 100 | 0 | 0 | 0 | 0 | 1.5 | 0.417 | 0.625 |
| | | | | | | | | | | | |
| 1.5 | 2 | 160 | 150 | 100 | 0 | 0 | 0 | 0 | 0 | 1.025 | 0.000 |
| 1.5 | 2 | 160 | 150 | 100 | 0 | 0 | 0 | 0 | 0.05 | 0.776 | 0.039 |
| 1.5 | 2 | 160 | 150 | 100 | 0 | 0 | 0 | 0 | 0.1 | 0.744 | 0.074 |
| 1.5 | 2 | 160 | 150 | 100 | 0 | 0 | 0 | 0 | 0.2 | 0.699 | 0.140 |
| 1.5 | 2 | 160 | 150 | 100 | 0 | 0 | 0 | 0 | 0.3 | 0.673 | 0.202 |
| 1.5 | 2 | 160 | 150 | 100 | 0 | 0 | 0 | 0 | 0.5 | 0.630 | 0.315 |
| 1.5 | 2 | 160 | 150 | 100 | 0 | 0 | 0 | 0 | 0.7 | 0.592 | 0.415 |
| 1.5 | 2 | 160 | 150 | 100 | 0 | 0 | 0 | 0 | 0.9 | 0.556 | 0.501 |
| 1.5 | 2 | 160 | 150 | 100 | 0 | 0 | 0 | 0 | 1.1 | 0.521 | 0.573 |
| 1.5 | 2 | 160 | 150 | 100 | 0 | 0 | 0 | 0 | 1.3 | 0.486 | 0.632 |
| 1.5 | 2 | 160 | 150 | 100 | 0 | 0 | 0 | 0 | 1.4 | 0.469 | 0.656 |
| 1.5 | 2 | 160 | 150 | 100 | 0 | 0 | 0 | 0 | 1.5 | 0.451 | 0.677 |
| | | | | | | | | | | | |
| | | | | | | | | | | | |
| | | | | | | | | | | | |

| | | | | Anode Gas % | | | | | | | |
|---|---|---|---|---|---|---|---|---|---|---|---|
| **Anode Stoic** | **Cathode Stoic** | **Temp ($^oC$)** | **Pressure (kPa)** | **$H_2$** | **$N_2$** | **$CO_2$** | **CO** | **$H_2O$** | **Current Density ($A/cm^2$)** | **Voltage (V)** | **Power ($W/cm^2$)** |
| 1.5 | 2 | 180 | 150 | 100 | 0 | 0 | 0 | 0 | 0.05 | 0.791 | 0.040 |
| 1.5 | 2 | 180 | 150 | 100 | 0 | 0 | 0 | 0 | 0.1 | 0.757 | 0.076 |
| 1.5 | 2 | 180 | 150 | 100 | 0 | 0 | 0 | 0 | 0.2 | 0.711 | 0.142 |
| 1.5 | 2 | 180 | 150 | 100 | 0 | 0 | 0 | 0 | 0.3 | 0.684 | 0.205 |
| 1.5 | 2 | 180 | 150 | 100 | 0 | 0 | 0 | 0 | 0.5 | 0.641 | 0.321 |
| 1.5 | 2 | 180 | 150 | 100 | 0 | 0 | 0 | 0 | 0.7 | 0.604 | 0.422 |
| 1.5 | 2 | 180 | 150 | 100 | 0 | 0 | 0 | 0 | 0.9 | 0.568 | 0.511 |
| 1.5 | 2 | 180 | 150 | 100 | 0 | 0 | 0 | 0 | 1.1 | 0.533 | 0.587 |
| 1.5 | 2 | 180 | 150 | 100 | 0 | 0 | 0 | 0 | 1.3 | 0.499 | 0.648 |
| 1.5 | 2 | 180 | 150 | 100 | 0 | 0 | 0 | 0 | 1.4 | 0.481 | 0.674 |
| 1.5 | 2 | 180 | 150 | 100 | 0 | 0 | 0 | 0 | 1.5 | 0.464 | 0.696 |
| | | | | | | | | | | | |
| 1.5 | 2 | 200 | 150 | 100 | 0 | 0 | 0 | 0 | 0 | 1.021 | 0.000 |
| 1.5 | 2 | 200 | 150 | 100 | 0 | 0 | 0 | 0 | 0.05 | 0.805 | 0.040 |
| 1.5 | 2 | 200 | 150 | 100 | 0 | 0 | 0 | 0 | 0.1 | 0.768 | 0.077 |
| 1.5 | 2 | 200 | 150 | 100 | 0 | 0 | 0 | 0 | 0.2 | 0.720 | 0.144 |
| 1.5 | 2 | 200 | 150 | 100 | 0 | 0 | 0 | 0 | 0.3 | 0.692 | 0.208 |
| 1.5 | 2 | 200 | 150 | 100 | 0 | 0 | 0 | 0 | 0.5 | 0.648 | 0.324 |
| 1.5 | 2 | 200 | 150 | 100 | 0 | 0 | 0 | 0 | 0.7 | 0.610 | 0.427 |
| 1.5 | 2 | 200 | 150 | 100 | 0 | 0 | 0 | 0 | 0.9 | 0.574 | 0.516 |
| 1.5 | 2 | 200 | 150 | 100 | 0 | 0 | 0 | 0 | 1.1 | 0.539 | 0.592 |
| 1.5 | 2 | 200 | 150 | 100 | 0 | 0 | 0 | 0 | 1.3 | 0.503 | 0.654 |
| 1.5 | 2 | 200 | 150 | 100 | 0 | 0 | 0 | 0 | 1.4 | 0.486 | 0.680 |
| 1.5 | 2 | 200 | 150 | 100 | 0 | 0 | 0 | 0 | 1.5 | 0.467 | 0.701 |
| | | | | | | | | | | | |
| | | | | | | | | | | | |
| | | | | | | | | | | | |

| | | | | Anode Gas % | | | | | | | |
|---|---|---|---|---|---|---|---|---|---|---|---|
| **Anode Stoic** | **Cathode Stoic** | **Temp ($^oC$)** | **Pressure (kPa)** | **$H_2$** | **$N_2$** | **$CO_2$** | **CO** | **$H_2O$** | **Current Density ($A/cm^2$)** | **Voltage (V)** | **Power ($W/cm^2$)** |
| 1.5 | 2 | 160 | 200 | 100 | 0 | 0 | 0 | 0 | 0.05 | 0.793 | 0.040 |
| 1.5 | 2 | 160 | 200 | 100 | 0 | 0 | 0 | 0 | 0.1 | 0.760 | 0.076 |
| 1.5 | 2 | 160 | 200 | 100 | 0 | 0 | 0 | 0 | 0.2 | 0.715 | 0.143 |
| 1.5 | 2 | 160 | 200 | 100 | 0 | 0 | 0 | 0 | 0.3 | 0.690 | 0.207 |
| 1.5 | 2 | 160 | 200 | 100 | 0 | 0 | 0 | 0 | 0.5 | 0.649 | 0.325 |
| 1.5 | 2 | 160 | 200 | 100 | 0 | 0 | 0 | 0 | 0.7 | 0.613 | 0.429 |
| 1.5 | 2 | 160 | 200 | 100 | 0 | 0 | 0 | 0 | 0.9 | 0.579 | 0.521 |
| 1.5 | 2 | 160 | 200 | 100 | 0 | 0 | 0 | 0 | 1.1 | 0.546 | 0.600 |
| 1.5 | 2 | 160 | 200 | 100 | 0 | 0 | 0 | 0 | 1.3 | 0.513 | 0.666 |
| 1.5 | 2 | 160 | 200 | 100 | 0 | 0 | 0 | 0 | 1.4 | 0.497 | 0.695 |
| 1.5 | 2 | 160 | 200 | 100 | 0 | 0 | 0 | 0 | 1.5 | 0.480 | 0.721 |
| | | | | | | | | | | | |
| 1.5 | 2 | 180 | 200 | 100 | 0 | 0 | 0 | 0 | 0 | 1.032 | 0.000 |
| 1.5 | 2 | 180 | 200 | 100 | 0 | 0 | 0 | 0 | 0.05 | 0.812 | 0.041 |
| 1.5 | 2 | 180 | 200 | 100 | 0 | 0 | 0 | 0 | 0.1 | 0.776 | 0.078 |
| 1.5 | 2 | 180 | 200 | 100 | 0 | 0 | 0 | 0 | 0.2 | 0.729 | 0.146 |
| 1.5 | 2 | 180 | 200 | 100 | 0 | 0 | 0 | 0 | 0.3 | 0.702 | 0.211 |
| 1.5 | 2 | 180 | 200 | 100 | 0 | 0 | 0 | 0 | 0.5 | 0.661 | 0.331 |
| 1.5 | 2 | 180 | 200 | 100 | 0 | 0 | 0 | 0 | 0.7 | 0.625 | 0.438 |
| 1.5 | 2 | 180 | 200 | 100 | 0 | 0 | 0 | 0 | 0.9 | 0.592 | 0.533 |
| 1.5 | 2 | 180 | 200 | 100 | 0 | 0 | 0 | 0 | 1.1 | 0.560 | 0.616 |
| 1.5 | 2 | 180 | 200 | 100 | 0 | 0 | 0 | 0 | 1.3 | 0.528 | 0.686 |
| 1.5 | 2 | 180 | 200 | 100 | 0 | 0 | 0 | 0 | 1.4 | 0.513 | 0.718 |
| 1.5 | 2 | 180 | 200 | 100 | 0 | 0 | 0 | 0 | 1.5 | 0.497 | 0.745 |
| | | | | | | | | | | | |
| | | | | | | | | | | | |
| | | | | | | | | | | | |

| | | | | Anode Gas % | | | | | | | |
|---|---|---|---|---|---|---|---|---|---|---|---|
| **Anode Stoic** | **Cathode Stoic** | **Temp ($^oC$)** | **Pressure (kPa)** | **$H_2$** | **$N_2$** | **$CO_2$** | **CO** | **$H_2O$** | **Current Density ($A/cm^2$)** | **Voltage (V)** | **Power ($W/cm^2$)** |
| 1.5 | 2 | 200 | 200 | 100 | 0 | 0 | 0 | 0 | 0.05 | 0.826 | 0.041 |
| 1.5 | 2 | 200 | 200 | 100 | 0 | 0 | 0 | 0 | 0.1 | 0.787 | 0.079 |
| 1.5 | 2 | 200 | 200 | 100 | 0 | 0 | 0 | 0 | 0.2 | 0.737 | 0.147 |
| 1.5 | 2 | 200 | 200 | 100 | 0 | 0 | 0 | 0 | 0.3 | 0.709 | 0.213 |
| 1.5 | 2 | 200 | 200 | 100 | 0 | 0 | 0 | 0 | 0.5 | 0.667 | 0.334 |
| 1.5 | 2 | 200 | 200 | 100 | 0 | 0 | 0 | 0 | 0.7 | 0.631 | 0.442 |
| 1.5 | 2 | 200 | 200 | 100 | 0 | 0 | 0 | 0 | 0.9 | 0.598 | 0.538 |
| 1.5 | 2 | 200 | 200 | 100 | 0 | 0 | 0 | 0 | 1.1 | 0.566 | 0.622 |
| 1.5 | 2 | 200 | 200 | 100 | 0 | 0 | 0 | 0 | 1.3 | 0.534 | 0.694 |
| 1.5 | 2 | 200 | 200 | 100 | 0 | 0 | 0 | 0 | 1.4 | 0.518 | 0.726 |
| 1.5 | 2 | 200 | 200 | 100 | 0 | 0 | 0 | 0 | 1.5 | 0.502 | 0.754 |
| | | | | | | | | | | | |
| 1.5 | 2 | 160 | 101.3 | 80 | 20 | 0 | 0 | 0 | 0 | 1.004 | 0.000 |
| 1.5 | 2 | 160 | 101.3 | 80 | 20 | 0 | 0 | 0 | 0.05 | 0.747 | 0.037 |
| 1.5 | 2 | 160 | 101.3 | 80 | 20 | 0 | 0 | 0 | 0.1 | 0.711 | 0.071 |
| 1.5 | 2 | 160 | 101.3 | 80 | 20 | 0 | 0 | 0 | 0.2 | 0.655 | 0.131 |
| 1.5 | 2 | 160 | 101.3 | 80 | 20 | 0 | 0 | 0 | 0.3 | 0.623 | 0.187 |
| 1.5 | 2 | 160 | 101.3 | 80 | 20 | 0 | 0 | 0 | 0.5 | 0.566 | 0.283 |
| 1.5 | 2 | 160 | 101.3 | 80 | 20 | 0 | 0 | 0 | 0.7 | 0.514 | 0.360 |
| 1.5 | 2 | 160 | 101.3 | 80 | 20 | 0 | 0 | 0 | 0.9 | 0.461 | 0.415 |
| 1.5 | 2 | 160 | 101.3 | 80 | 20 | 0 | 0 | 0 | 1.1 | 0.405 | 0.446 |
| 1.5 | 2 | 160 | 101.3 | 80 | 20 | 0 | 0 | 0 | 1.3 | 0.345 | 0.449 |
| 1.5 | 2 | 160 | 101.3 | 80 | 20 | 0 | 0 | 0 | 1.4 | 0.310 | 0.433 |
| 1.5 | 2 | 160 | 101.3 | 80 | 20 | 0 | 0 | 0 | 1.5 | 0.273 | 0.410 |
| | | | | | | | | | | | |
| | | | | | | | | | | | |
| | | | | | | | | | | | |

| | | | | Anode Gas % | | | | | | | |
|---|---|---|---|---|---|---|---|---|---|---|---|
| **Anode Stoic** | **Cathode Stoic** | **Temp ($^oC$)** | **Pressure (kPa)** | **$H_2$** | **$N_2$** | **$CO_2$** | **CO** | **$H_2O$** | **Current Density ($A/cm^2$)** | **Voltage (V)** | **Power ($W/cm^2$)** |
| 1.5 | 2 | 180 | 101.3 | 80 | 20 | 0 | 0 | 0 | 0.05 | 0.751 | 0.038 |
| 1.5 | 2 | 180 | 101.3 | 80 | 20 | 0 | 0 | 0 | 0.1 | 0.717 | 0.072 |
| 1.5 | 2 | 180 | 101.3 | 80 | 20 | 0 | 0 | 0 | 0.2 | 0.669 | 0.134 |
| 1.5 | 2 | 180 | 101.3 | 80 | 20 | 0 | 0 | 0 | 0.3 | 0.637 | 0.191 |
| 1.5 | 2 | 180 | 101.3 | 80 | 20 | 0 | 0 | 0 | 0.5 | 0.587 | 0.293 |
| 1.5 | 2 | 180 | 101.3 | 80 | 20 | 0 | 0 | 0 | 0.7 | 0.540 | 0.378 |
| 1.5 | 2 | 180 | 101.3 | 80 | 20 | 0 | 0 | 0 | 0.9 | 0.495 | 0.446 |
| 1.5 | 2 | 180 | 101.3 | 80 | 20 | 0 | 0 | 0 | 1.1 | 0.450 | 0.495 |
| 1.5 | 2 | 180 | 101.3 | 80 | 20 | 0 | 0 | 0 | 1.3 | 0.403 | 0.523 |
| 1.5 | 2 | 180 | 101.3 | 80 | 20 | 0 | 0 | 0 | 1.4 | 0.378 | 0.530 |
| 1.5 | 2 | 180 | 101.3 | 80 | 20 | 0 | 0 | 0 | 1.5 | 0.353 | 0.529 |
| | | | | | | | | | | | |
| 1.5 | 2 | 200 | 101.3 | 80 | 20 | 0 | 0 | 0 | 0 | 0.988 | 0.000 |
| 1.5 | 2 | 200 | 101.3 | 80 | 20 | 0 | 0 | 0 | 0.05 | 0.755 | 0.038 |
| 1.5 | 2 | 200 | 101.3 | 80 | 20 | 0 | 0 | 0 | 0.1 | 0.722 | 0.072 |
| 1.5 | 2 | 200 | 101.3 | 80 | 20 | 0 | 0 | 0 | 0.2 | 0.674 | 0.135 |
| 1.5 | 2 | 200 | 101.3 | 80 | 20 | 0 | 0 | 0 | 0.3 | 0.644 | 0.193 |
| 1.5 | 2 | 200 | 101.3 | 80 | 20 | 0 | 0 | 0 | 0.5 | 0.591 | 0.295 |
| 1.5 | 2 | 200 | 101.3 | 80 | 20 | 0 | 0 | 0 | 0.7 | 0.543 | 0.380 |
| 1.5 | 2 | 200 | 101.3 | 80 | 20 | 0 | 0 | 0 | 0.9 | 0.498 | 0.448 |
| 1.5 | 2 | 200 | 101.3 | 80 | 20 | 0 | 0 | 0 | 1.1 | 0.451 | 0.496 |
| 1.5 | 2 | 200 | 101.3 | 80 | 20 | 0 | 0 | 0 | 1.3 | 0.401 | 0.522 |
| 1.5 | 2 | 200 | 101.3 | 80 | 20 | 0 | 0 | 0 | 1.4 | 0.377 | 0.528 |
| 1.5 | 2 | 200 | 101.3 | 80 | 20 | 0 | 0 | 0 | 1.5 | 0.351 | 0.527 |
| | | | | | | | | | | | |
| | | | | | | | | | | | |
| | | | | | | | | | | | |

| | | | | Anode Gas % | | | | | | | |
|---|---|---|---|---|---|---|---|---|---|---|---|
| **Anode Stoic** | **Cathode Stoic** | **Temp ($^oC$)** | **Pressure (kPa)** | **$H_2$** | **$N_2$** | **$CO_2$** | **CO** | **$H_2O$** | **Current Density ($A/cm^2$)** | **Voltage (V)** | **Power ($W/cm^2$)** |
| 1.5 | 2 | 160 | 150 | 80 | 20 | 0 | 0 | 0 | 0.05 | 0.770 | 0.039 |
| 1.5 | 2 | 160 | 150 | 80 | 20 | 0 | 0 | 0 | 0.1 | 0.734 | 0.073 |
| 1.5 | 2 | 160 | 150 | 80 | 20 | 0 | 0 | 0 | 0.2 | 0.682 | 0.136 |
| 1.5 | 2 | 160 | 150 | 80 | 20 | 0 | 0 | 0 | 0.3 | 0.651 | 0.195 |
| 1.5 | 2 | 160 | 150 | 80 | 20 | 0 | 0 | 0 | 0.5 | 0.599 | 0.300 |
| 1.5 | 2 | 160 | 150 | 80 | 20 | 0 | 0 | 0 | 0.7 | 0.553 | 0.387 |
| 1.5 | 2 | 160 | 150 | 80 | 20 | 0 | 0 | 0 | 0.9 | 0.508 | 0.457 |
| 1.5 | 2 | 160 | 150 | 80 | 20 | 0 | 0 | 0 | 1.1 | 0.463 | 0.509 |
| 1.5 | 2 | 160 | 150 | 80 | 20 | 0 | 0 | 0 | 1.3 | 0.417 | 0.543 |
| 1.5 | 2 | 160 | 150 | 80 | 20 | 0 | 0 | 0 | 1.4 | 0.394 | 0.552 |
| 1.5 | 2 | 160 | 150 | 80 | 20 | 0 | 0 | 0 | 1.5 | 0.370 | 0.555 |
| | | | | | | | | | | | |
| 1.5 | 2 | 180 | 150 | 80 | 20 | 0 | 0 | 0 | 0 | 1.021 | 0.000 |
| 1.5 | 2 | 180 | 150 | 80 | 20 | 0 | 0 | 0 | 0.05 | 0.774 | 0.039 |
| 1.5 | 2 | 180 | 150 | 80 | 20 | 0 | 0 | 0 | 0.1 | 0.741 | 0.074 |
| 1.5 | 2 | 180 | 150 | 80 | 20 | 0 | 0 | 0 | 0.2 | 0.693 | 0.139 |
| 1.5 | 2 | 180 | 150 | 80 | 20 | 0 | 0 | 0 | 0.3 | 0.664 | 0.199 |
| 1.5 | 2 | 180 | 150 | 80 | 20 | 0 | 0 | 0 | 0.5 | 0.617 | 0.309 |
| 1.5 | 2 | 180 | 150 | 80 | 20 | 0 | 0 | 0 | 0.7 | 0.576 | 0.403 |
| 1.5 | 2 | 180 | 150 | 80 | 20 | 0 | 0 | 0 | 1.1 | 0.497 | 0.547 |
| 1.5 | 2 | 180 | 150 | 80 | 20 | 0 | 0 | 0 | 1.3 | 0.458 | 0.595 |
| 1.5 | 2 | 180 | 150 | 80 | 20 | 0 | 0 | 0 | 1.4 | 0.439 | 0.614 |
| 1.5 | 2 | 180 | 150 | 80 | 20 | 0 | 0 | 0 | 1.5 | 0.419 | 0.628 |
| | | | | | | | | | | | |
| | | | | | | | | | | | |
| | | | | | | | | | | | |
| | | | | | | | | | | | |

| | | | | Anode Gas % | | | | | | | |
|---|---|---|---|---|---|---|---|---|---|---|---|
| **Anode Stoic** | **Cathode Stoic** | **Temp ($^oC$)** | **Pressure (kPa)** | **$H_2$** | **$N_2$** | **$CO_2$** | **CO** | **$H_2O$** | **Current Density ($A/cm^2$)** | **Voltage (V)** | **Power ($W/cm^2$)** |
| 1.5 | 2 | 200 | 150 | 80 | 20 | 0 | 0 | 0 | 0 | 1.012 | 0.000 |
| 1.5 | 2 | 200 | 150 | 80 | 20 | 0 | 0 | 0 | 0.05 | 0.782 | 0.039 |
| 1.5 | 2 | 200 | 150 | 80 | 20 | 0 | 0 | 0 | 0.1 | 0.747 | 0.075 |
| 1.5 | 2 | 200 | 150 | 80 | 20 | 0 | 0 | 0 | 0.2 | 0.700 | 0.140 |
| 1.5 | 2 | 200 | 150 | 80 | 20 | 0 | 0 | 0 | 0.3 | 0.671 | 0.201 |
| 1.5 | 2 | 200 | 150 | 80 | 20 | 0 | 0 | 0 | 0.5 | 0.625 | 0.312 |
| 1.5 | 2 | 200 | 150 | 80 | 20 | 0 | 0 | 0 | 0.7 | 0.584 | 0.409 |
| 1.5 | 2 | 200 | 150 | 80 | 20 | 0 | 0 | 0 | 0.9 | 0.544 | 0.490 |
| 1.5 | 2 | 200 | 150 | 80 | 20 | 0 | 0 | 0 | 1.1 | 0.505 | 0.556 |
| 1.5 | 2 | 200 | 150 | 80 | 20 | 0 | 0 | 0 | 1.3 | 0.466 | 0.606 |
| 1.5 | 2 | 200 | 150 | 80 | 20 | 0 | 0 | 0 | 1.4 | 0.447 | 0.625 |
| 1.5 | 2 | 200 | 150 | 80 | 20 | 0 | 0 | 0 | 1.5 | 0.426 | 0.640 |
| | | | | | | | | | | | |
| 1.5 | 2 | 160 | 200 | 80 | 20 | 0 | 0 | 0 | 0 | 1.038 | 0.000 |
| 1.5 | 2 | 160 | 200 | 80 | 20 | 0 | 0 | 0 | 0.05 | 0.785 | 0.039 |
| 1.5 | 2 | 160 | 200 | 80 | 20 | 0 | 0 | 0 | 0.1 | 0.748 | 0.075 |
| 1.5 | 2 | 160 | 200 | 80 | 20 | 0 | 0 | 0 | 0.2 | 0.699 | 0.140 |
| 1.5 | 2 | 160 | 200 | 80 | 20 | 0 | 0 | 0 | 0.3 | 0.669 | 0.201 |
| 1.5 | 2 | 160 | 200 | 80 | 20 | 0 | 0 | 0 | 0.5 | 0.622 | 0.311 |
| 1.5 | 2 | 160 | 200 | 80 | 20 | 0 | 0 | 0 | 0.7 | 0.580 | 0.406 |
| 1.5 | 2 | 160 | 200 | 80 | 20 | 0 | 0 | 0 | 0.9 | 0.540 | 0.486 |
| 1.5 | 2 | 160 | 200 | 80 | 20 | 0 | 0 | 0 | 1.1 | 0.501 | 0.551 |
| 1.5 | 2 | 160 | 200 | 80 | 20 | 0 | 0 | 0 | 1.3 | 0.462 | 0.601 |
| 1.5 | 2 | 160 | 200 | 80 | 20 | 0 | 0 | 0 | 1.4 | 0.443 | 0.620 |
| 1.5 | 2 | 160 | 200 | 80 | 20 | 0 | 0 | 0 | 1.5 | 0.422 | 0.634 |
| | | | | | | | | | | | |
| | | | | | | | | | | | |

| | | | | Anode Gas % | | | | | | | |
|---|---|---|---|---|---|---|---|---|---|---|---|
| **Anode Stoic** | **Cathode Stoic** | **Temp ($^oC$)** | **Pressure (kPa)** | **$H_2$** | **$N_2$** | **$CO_2$** | **CO** | **$H_2O$** | **Current Density ($A/cm^2$)** | **Voltage (V)** | **Power ($W/cm^2$)** |
| 1.5 | 2 | 180 | 200 | 80 | 20 | 0 | 0 | 0 | 0.05 | 0.791 | 0.040 |
| 1.5 | 2 | 180 | 200 | 80 | 20 | 0 | 0 | 0 | 0.1 | 0.757 | 0.076 |
| 1.5 | 2 | 180 | 200 | 80 | 20 | 0 | 0 | 0 | 0.2 | 0.710 | 0.142 |
| 1.5 | 2 | 180 | 200 | 80 | 20 | 0 | 0 | 0 | 0.3 | 0.682 | 0.205 |
| 1.5 | 2 | 180 | 200 | 80 | 20 | 0 | 0 | 0 | 0.5 | 0.638 | 0.319 |
| 1.5 | 2 | 180 | 200 | 80 | 20 | 0 | 0 | 0 | 0.7 | 0.600 | 0.420 |
| 1.5 | 2 | 180 | 200 | 80 | 20 | 0 | 0 | 0 | 0.9 | 0.564 | 0.508 |
| 1.5 | 2 | 180 | 200 | 80 | 20 | 0 | 0 | 0 | 1.1 | 0.530 | 0.583 |
| 1.5 | 2 | 180 | 200 | 80 | 20 | 0 | 0 | 0 | 1.3 | 0.495 | 0.643 |
| 1.5 | 2 | 180 | 200 | 80 | 20 | 0 | 0 | 0 | 1.4 | 0.478 | 0.669 |
| 1.5 | 2 | 180 | 200 | 80 | 20 | 0 | 0 | 0 | 1.5 | 0.460 | 0.691 |
| | | | | | | | | | | | |
| 1.5 | 2 | 200 | 200 | 80 | 20 | 0 | 0 | 0 | 0 | 1.021 | 0.000 |
| 1.5 | 2 | 200 | 200 | 80 | 20 | 0 | 0 | 0 | 0.05 | 0.801 | 0.040 |
| 1.5 | 2 | 200 | 200 | 80 | 20 | 0 | 0 | 0 | 0.1 | 0.765 | 0.076 |
| 1.5 | 2 | 200 | 200 | 80 | 20 | 0 | 0 | 0 | 0.2 | 0.717 | 0.143 |
| 1.5 | 2 | 200 | 200 | 80 | 20 | 0 | 0 | 0 | 0.3 | 0.689 | 0.207 |
| 1.5 | 2 | 200 | 200 | 80 | 20 | 0 | 0 | 0 | 0.5 | 0.646 | 0.323 |
| 1.5 | 2 | 200 | 200 | 80 | 20 | 0 | 0 | 0 | 0.7 | 0.608 | 0.425 |
| 1.5 | 2 | 200 | 200 | 80 | 20 | 0 | 0 | 0 | 0.9 | 0.572 | 0.515 |
| 1.5 | 2 | 200 | 200 | 80 | 20 | 0 | 0 | 0 | 1.1 | 0.538 | 0.592 |
| 1.5 | 2 | 200 | 200 | 80 | 20 | 0 | 0 | 0 | 1.3 | 0.504 | 0.655 |
| 1.5 | 2 | 200 | 200 | 80 | 20 | 0 | 0 | 0 | 1.4 | 0.488 | 0.683 |
| 1.5 | 2 | 200 | 200 | 80 | 20 | 0 | 0 | 0 | 1.5 | 0.471 | 0.706 |
| | | | | | | | | | | | |
| | | | | | | | | | | | |
| | | | | | | | | | | | |

| | | | | Anode Gas % | | | | | | | |
|---|---|---|---|---|---|---|---|---|---|---|---|
| **Anode Stoic** | **Cathode Stoic** | **Temp ($^oC$)** | **Pressure (kPa)** | **$H_2$** | **$N_2$** | **$CO_2$** | **CO** | **$H_2O$** | **Current Density ($A/cm^2$)** | **Voltage (V)** | **Power ($W/cm^2$)** |
| 1.5 | 2 | 160 | 101.3 | 50 | 50 | 0 | 0 | 0 | 0.05 | 0.723 | 0.036 |
| 1.5 | 2 | 160 | 101.3 | 50 | 50 | 0 | 0 | 0 | 0.1 | 0.687 | 0.069 |
| 1.5 | 2 | 160 | 101.3 | 50 | 50 | 0 | 0 | 0 | 0.2 | 0.629 | 0.126 |
| 1.5 | 2 | 160 | 101.3 | 50 | 50 | 0 | 0 | 0 | 0.3 | 0.591 | 0.177 |
| 1.5 | 2 | 160 | 101.3 | 50 | 50 | 0 | 0 | 0 | 0.5 | 0.519 | 0.260 |
| 1.5 | 2 | 160 | 101.3 | 50 | 50 | 0 | 0 | 0 | 0.7 | 0.434 | 0.304 |
| 1.5 | 2 | 160 | 101.3 | 50 | 50 | 0 | 0 | 0 | 0.9 | 0.292 | 0.263 |
| 1.5 | 2 | 160 | 101.3 | 50 | 50 | 0 | 0 | 0 | 1.1 | 0.151 | 0.166 |
| 1.5 | 2 | 160 | 101.3 | 50 | 50 | 0 | 0 | 0 | 1.3 | 0.031 | 0.040 |
| 1.5 | 2 | 160 | 101.3 | 50 | 50 | 0 | 0 | 0 | 1.5 | 0.137 | 0.205 |
| | | | | | | | | | | | |
| 1.5 | 2 | 180 | 101.3 | 50 | 50 | 0 | 0 | 0 | 0 | 0.980 | 0.000 |
| 1.5 | 2 | 180 | 101.3 | 50 | 50 | 0 | 0 | 0 | 0.05 | 0.727 | 0.036 |
| 1.5 | 2 | 180 | 101.3 | 50 | 50 | 0 | 0 | 0 | 0.1 | 0.696 | 0.070 |
| 1.5 | 2 | 180 | 101.3 | 50 | 50 | 0 | 0 | 0 | 0.2 | 0.649 | 0.130 |
| 1.5 | 2 | 180 | 101.3 | 50 | 50 | 0 | 0 | 0 | 0.3 | 0.619 | 0.186 |
| 1.5 | 2 | 180 | 101.3 | 50 | 50 | 0 | 0 | 0 | 0.5 | 0.568 | 0.284 |
| 1.5 | 2 | 180 | 101.3 | 50 | 50 | 0 | 0 | 0 | 0.7 | 0.524 | 0.367 |
| 1.5 | 2 | 180 | 101.3 | 50 | 50 | 0 | 0 | 0 | 0.9 | 0.481 | 0.433 |
| 1.5 | 2 | 180 | 101.3 | 50 | 50 | 0 | 0 | 0 | 1.1 | 0.438 | 0.482 |
| 1.5 | 2 | 180 | 101.3 | 50 | 50 | 0 | 0 | 0 | 1.3 | 0.393 | 0.511 |
| 1.5 | 2 | 180 | 101.3 | 50 | 50 | 0 | 0 | 0 | 1.4 | 0.368 | 0.515 |
| 1.5 | 2 | 180 | 101.3 | 50 | 50 | 0 | 0 | 0 | 1.5 | 0.342 | 0.512 |
| | | | | | | | | | | | |
| | | | | | | | | | | | |
| | | | | | | | | | | | |
| | | | | | | | | | | | |

| | | | | Anode Gas % | | | | | | | |
|---|---|---|---|---|---|---|---|---|---|---|---|
| **Anode Stoic** | **Cathode Stoic** | **Temp ($^oC$)** | **Pressure (kPa)** | **$H_2$** | **$N_2$** | **$CO_2$** | **CO** | **$H_2O$** | **Current Density ($A/cm^2$)** | **Voltage (V)** | **Power ($W/cm^2$)** |
| 1.5 | 2 | 200 | 101.3 | 50 | 50 | 0 | 0 | 0 | 0.05 | 0.732 | 0.037 |
| 1.5 | 2 | 200 | 101.3 | 50 | 50 | 0 | 0 | 0 | 0.1 | 0.700 | 0.070 |
| 1.5 | 2 | 200 | 101.3 | 50 | 50 | 0 | 0 | 0 | 0.2 | 0.652 | 0.130 |
| 1.5 | 2 | 200 | 101.3 | 50 | 50 | 0 | 0 | 0 | 0.3 | 0.621 | 0.186 |
| 1.5 | 2 | 200 | 101.3 | 50 | 50 | 0 | 0 | 0 | 0.5 | 0.569 | 0.285 |
| 1.5 | 2 | 200 | 101.3 | 50 | 50 | 0 | 0 | 0 | 0.7 | 0.521 | 0.365 |
| 1.5 | 2 | 200 | 101.3 | 50 | 50 | 0 | 0 | 0 | 0.9 | 0.474 | 0.426 |
| 1.5 | 2 | 200 | 101.3 | 50 | 50 | 0 | 0 | 0 | 1.1 | 0.423 | 0.465 |
| 1.5 | 2 | 200 | 101.3 | 50 | 50 | 0 | 0 | 0 | 1.3 | 0.367 | 0.477 |
| 1.5 | 2 | 200 | 101.3 | 50 | 50 | 0 | 0 | 0 | 1.4 | 0.336 | 0.470 |
| 1.5 | 2 | 200 | 101.3 | 50 | 50 | 0 | 0 | 0 | 1.5 | 0.307 | 0.460 |
| | | | | | | | | | | | |
| 1.5 | 2 | 160 | 150 | 50 | 50 | 0 | 0 | 0 | 0 | 1.020 | 0.000 |
| 1.5 | 2 | 160 | 150 | 50 | 50 | 0 | 0 | 0 | 0.05 | 0.747 | 0.037 |
| 1.5 | 2 | 160 | 150 | 50 | 50 | 0 | 0 | 0 | 0.1 | 0.711 | 0.071 |
| 1.5 | 2 | 160 | 150 | 50 | 50 | 0 | 0 | 0 | 0.2 | 0.657 | 0.131 |
| 1.5 | 2 | 160 | 150 | 50 | 50 | 0 | 0 | 0 | 0.3 | 0.623 | 0.187 |
| 1.5 | 2 | 160 | 150 | 50 | 50 | 0 | 0 | 0 | 0.5 | 0.562 | 0.281 |
| 1.5 | 2 | 160 | 150 | 50 | 50 | 0 | 0 | 0 | 0.7 | 0.502 | 0.351 |
| 1.5 | 2 | 160 | 150 | 50 | 50 | 0 | 0 | 0 | 0.9 | 0.436 | 0.393 |
| 1.5 | 2 | 160 | 150 | 50 | 50 | 0 | 0 | 0 | 1.1 | 0.358 | 0.394 |
| 1.5 | 2 | 160 | 150 | 50 | 50 | 0 | 0 | 0 | 1.3 | 0.266 | 0.346 |
| 1.5 | 2 | 160 | 150 | 50 | 50 | 0 | 0 | 0 | 1.4 | 0.219 | 0.307 |
| 1.5 | 2 | 160 | 150 | 50 | 50 | 0 | 0 | 0 | 1.5 | 0.166 | 0.250 |
| | | | | | | | | | | | |
| | | | | | | | | | | | |
| | | | | | | | | | | | |

| | | | | Anode Gas % | | | | | | | |
|---|---|---|---|---|---|---|---|---|---|---|---|
| **Anode Stoic** | **Cathode Stoic** | **Temp ($^oC$)** | **Pressure (kPa)** | **$H_2$** | **$N_2$** | **$CO_2$** | **CO** | **$H_2O$** | **Current Density ($A/cm^2$)** | **Voltage (V)** | **Power ($W/cm^2$)** |
| 1.5 | 2 | 180 | 150 | 50 | 50 | 0 | 0 | 0 | 0.05 | 0.750 | 0.038 |
| 1.5 | 2 | 180 | 150 | 50 | 50 | 0 | 0 | 0 | 0.1 | 0.719 | 0.072 |
| 1.5 | 2 | 180 | 150 | 50 | 50 | 0 | 0 | 0 | 0.2 | 0.673 | 0.135 |
| 1.5 | 2 | 180 | 150 | 50 | 50 | 0 | 0 | 0 | 0.3 | 0.645 | 0.194 |
| 1.5 | 2 | 180 | 150 | 50 | 50 | 0 | 0 | 0 | 0.5 | 0.582 | 0.291 |
| 1.5 | 2 | 180 | 150 | 50 | 50 | 0 | 0 | 0 | 0.7 | 0.564 | 0.394 |
| 1.5 | 2 | 180 | 150 | 50 | 50 | 0 | 0 | 0 | 0.9 | 0.527 | 0.474 |
| 1.5 | 2 | 180 | 150 | 50 | 50 | 0 | 0 | 0 | 1.1 | 0.490 | 0.539 |
| 1.5 | 2 | 180 | 150 | 50 | 50 | 0 | 0 | 0 | 1.3 | 0.453 | 0.590 |
| 1.5 | 2 | 180 | 150 | 50 | 50 | 0 | 0 | 0 | 1.4 | 0.435 | 0.610 |
| 1.5 | 2 | 180 | 150 | 50 | 50 | 0 | 0 | 0 | 1.5 | 0.415 | 0.623 |
| | | | | | | | | | | | |
| 1.5 | 2 | 200 | 150 | 50 | 50 | 0 | 0 | 0 | 0 | 0.990 | 0.000 |
| 1.5 | 2 | 200 | 150 | 50 | 50 | 0 | 0 | 0 | 0.05 | 0.757 | 0.038 |
| 1.5 | 2 | 200 | 150 | 50 | 50 | 0 | 0 | 0 | 0.1 | 0.724 | 0.072 |
| 1.5 | 2 | 200 | 150 | 50 | 50 | 0 | 0 | 0 | 0.2 | 0.677 | 0.135 |
| 1.5 | 2 | 200 | 150 | 50 | 50 | 0 | 0 | 0 | 0.3 | 0.648 | 0.194 |
| 1.5 | 2 | 200 | 150 | 50 | 50 | 0 | 0 | 0 | 0.5 | 0.600 | 0.300 |
| 1.5 | 2 | 200 | 150 | 50 | 50 | 0 | 0 | 0 | 0.7 | 0.556 | 0.389 |
| 1.5 | 2 | 200 | 150 | 50 | 50 | 0 | 0 | 0 | 0.9 | 0.515 | 0.463 |
| 1.5 | 2 | 200 | 150 | 50 | 50 | 0 | 0 | 0 | 1.1 | 0.473 | 0.520 |
| 1.5 | 2 | 200 | 150 | 50 | 50 | 0 | 0 | 0 | 1.3 | 0.429 | 0.558 |
| 1.5 | 2 | 200 | 150 | 50 | 50 | 0 | 0 | 0 | 1.4 | 0.407 | 0.570 |
| 1.5 | 2 | 200 | 150 | 50 | 50 | 0 | 0 | 0 | 1.5 | 0.386 | 0.578 |
| | | | | | | | | | | | |
| | | | | | | | | | | | |
| | | | | | | | | | | | |

| | | | | Anode Gas % | | | | | | | |
|---|---|---|---|---|---|---|---|---|---|---|---|
| **Anode Stoic** | **Cathode Stoic** | **Temp ($^oC$)** | **Pressure (kPa)** | **$H_2$** | **$N_2$** | **$CO_2$** | **CO** | **$H_2O$** | **Current Density ($A/cm^2$)** | **Voltage (V)** | **Power ($W/cm^2$)** |
| 1.5 | 2 | 160 | 200 | 50 | 50 | 0 | 0 | 0 | 0.05 | 0.762 | 0.038 |
| 1.5 | 2 | 160 | 200 | 50 | 50 | 0 | 0 | 0 | 0.1 | 0.727 | 0.073 |
| 1.5 | 2 | 160 | 200 | 50 | 50 | 0 | 0 | 0 | 0.2 | 0.675 | 0.135 |
| 1.5 | 2 | 160 | 200 | 50 | 50 | 0 | 0 | 0 | 0.3 | 0.644 | 0.193 |
| 1.5 | 2 | 160 | 200 | 50 | 50 | 0 | 0 | 0 | 0.5 | 0.587 | 0.294 |
| 1.5 | 2 | 160 | 200 | 50 | 50 | 0 | 0 | 0 | 0.7 | 0.569 | 0.398 |
| 1.5 | 2 | 160 | 200 | 50 | 50 | 0 | 0 | 0 | 0.9 | 0.532 | 0.479 |
| 1.5 | 2 | 160 | 200 | 50 | 50 | 0 | 0 | 0 | 1.1 | 0.496 | 0.545 |
| 1.5 | 2 | 160 | 200 | 50 | 50 | 0 | 0 | 0 | 1.3 | 0.459 | 0.597 |
| 1.5 | 2 | 160 | 200 | 50 | 50 | 0 | 0 | 0 | 1.4 | 0.441 | 0.618 |
| 1.5 | 2 | 160 | 200 | 50 | 50 | 0 | 0 | 0 | 1.5 | 0.423 | 0.634 |
| | | | | | | | | | | | |
| 1.5 | 2 | 180 | 200 | 50 | 50 | 0 | 0 | 0 | 0 | 1.006 | 0.000 |
| 1.5 | 2 | 180 | 200 | 50 | 50 | 0 | 0 | 0 | 0.05 | 0.765 | 0.038 |
| 1.5 | 2 | 180 | 200 | 50 | 50 | 0 | 0 | 0 | 0.1 | 0.734 | 0.073 |
| 1.5 | 2 | 180 | 200 | 50 | 50 | 0 | 0 | 0 | 0.2 | 0.689 | 0.138 |
| 1.5 | 2 | 180 | 200 | 50 | 50 | 0 | 0 | 0 | 0.3 | 0.663 | 0.199 |
| 1.5 | 2 | 180 | 200 | 50 | 50 | 0 | 0 | 0 | 0.5 | 0.621 | 0.311 |
| 1.5 | 2 | 180 | 200 | 50 | 50 | 0 | 0 | 0 | 0.7 | 0.585 | 0.409 |
| 1.5 | 2 | 180 | 200 | 50 | 50 | 0 | 0 | 0 | 0.9 | 0.551 | 0.496 |
| 1.5 | 2 | 180 | 200 | 50 | 50 | 0 | 0 | 0 | 1.1 | 0.517 | 0.569 |
| 1.5 | 2 | 180 | 200 | 50 | 50 | 0 | 0 | 0 | 1.3 | 0.484 | 0.629 |
| 1.5 | 2 | 180 | 200 | 50 | 50 | 0 | 0 | 0 | 1.4 | 0.467 | 0.654 |
| 1.5 | 2 | 180 | 200 | 50 | 50 | 0 | 0 | 0 | 1.5 | 0.450 | 0.675 |
| | | | | | | | | | | | |
| | | | | | | | | | | | |
| | | | | | | | | | | | |

| | | | | Anode Gas % | | | | | | | |
|---|---|---|---|---|---|---|---|---|---|---|---|
| **Anode Stoic** | **Cathode Stoic** | **Temp ($^oC$)** | **Pressure (kPa)** | **$H_2$** | **$N_2$** | **$CO_2$** | **CO** | **$H_2O$** | **Current Density ($A/cm^2$)** | **Voltage (V)** | **Power ($W/cm^2$)** |
| 1.5 | 2 | 200 | 200 | 50 | 50 | 0 | 0 | 0 | 0.05 | 0.776 | 0.039 |
| 1.5 | 2 | 200 | 200 | 50 | 50 | 0 | 0 | 0 | 0.1 | 0.742 | 0.074 |
| 1.5 | 2 | 200 | 200 | 50 | 50 | 0 | 0 | 0 | 0.2 | 0.694 | 0.139 |
| 1.5 | 2 | 200 | 200 | 50 | 50 | 0 | 0 | 0 | 0.3 | 0.666 | 0.200 |
| 1.5 | 2 | 200 | 200 | 50 | 50 | 0 | 0 | 0 | 0.5 | 0.621 | 0.310 |
| 1.5 | 2 | 200 | 200 | 50 | 50 | 0 | 0 | 0 | 0.7 | 0.582 | 0.407 |
| 1.5 | 2 | 200 | 200 | 50 | 50 | 0 | 0 | 0 | 0.9 | 0.545 | 0.490 |
| 1.5 | 2 | 200 | 200 | 50 | 50 | 0 | 0 | 0 | 1.1 | 0.508 | 0.559 |
| 1.5 | 2 | 200 | 200 | 50 | 50 | 0 | 0 | 0 | 1.3 | 0.472 | 0.613 |
| 1.5 | 2 | 200 | 200 | 50 | 50 | 0 | 0 | 0 | 1.4 | 0.454 | 0.636 |
| 1.5 | 2 | 200 | 200 | 50 | 50 | 0 | 0 | 0 | 1.5 | 0.436 | 0.654 |
| | | | | | | | | | | | |
| 1.5 | 2 | 160 | 101.3 | 30 | 70 | 0 | 0 | 0 | 0 | 0.966 | 0.000 |
| 1.5 | 2 | 160 | 101.3 | 30 | 70 | 0 | 0 | 0 | 0.05 | 0.704 | 0.035 |
| 1.5 | 2 | 160 | 101.3 | 30 | 70 | 0 | 0 | 0 | 0.1 | 0.668 | 0.067 |
| 1.5 | 2 | 160 | 101.3 | 30 | 70 | 0 | 0 | 0 | 0.2 | 0.617 | 0.123 |
| 1.5 | 2 | 160 | 101.3 | 30 | 70 | 0 | 0 | 0 | 0.3 | 0.568 | 0.170 |
| 1.5 | 2 | 160 | 101.3 | 30 | 70 | 0 | 0 | 0 | 0.4 | 0.527 | 0.211 |
| 1.5 | 2 | 160 | 101.3 | 30 | 70 | 0 | 0 | 0 | 0.5 | 0.482 | 0.241 |
| 1.5 | 2 | 160 | 101.3 | 30 | 70 | 0 | 0 | 0 | 0.6 | 0.421 | 0.252 |
| 1.5 | 2 | 160 | 101.3 | 30 | 70 | 0 | 0 | 0 | 0.7 | 0.310 | 0.217 |
| 1.5 | 2 | 160 | 101.3 | 30 | 70 | 0 | 0 | 0 | 0.8 | 0.209 | 0.167 |
| 1.5 | 2 | 160 | 101.3 | 30 | 70 | 0 | 0 | 0 | 0.9 | 0.112 | 0.101 |
| | | | | | | | | | | | |
| | | | | | | | | | | | |
| | | | | | | | | | | | |
| | | | | | | | | | | | |

| | | | | Anode Gas % | | | | | | | |
|---|---|---|---|---|---|---|---|---|---|---|---|
| **Anode Stoic** | **Cathode Stoic** | **Temp ($^oC$)** | **Pressure (kPa)** | **$H_2$** | **$N_2$** | **$CO_2$** | **CO** | **$H_2O$** | **Current Density ($A/cm^2$)** | **Voltage (V)** | **Power ($W/cm^2$)** |
| 1.5 | 2 | 180 | 101.3 | 30 | 70 | 0 | 0 | 0 | 0.05 | 0.712 | 0.036 |
| 1.5 | 2 | 180 | 101.3 | 30 | 70 | 0 | 0 | 0 | 0.1 | 0.679 | 0.068 |
| 1.5 | 2 | 180 | 101.3 | 30 | 70 | 0 | 0 | 0 | 0.2 | 0.626 | 0.125 |
| 1.5 | 2 | 180 | 101.3 | 30 | 70 | 0 | 0 | 0 | 0.3 | 0.590 | 0.177 |
| 1.5 | 2 | 180 | 101.3 | 30 | 70 | 0 | 0 | 0 | 0.4 | 0.556 | 0.222 |
| 1.5 | 2 | 180 | 101.3 | 30 | 70 | 0 | 0 | 0 | 0.5 | 0.523 | 0.262 |
| 1.5 | 2 | 180 | 101.3 | 30 | 70 | 0 | 0 | 0 | 0.6 | 0.488 | 0.293 |
| 1.5 | 2 | 180 | 101.3 | 30 | 70 | 0 | 0 | 0 | 0.7 | 0.449 | 0.314 |
| 1.5 | 2 | 180 | 101.3 | 30 | 70 | 0 | 0 | 0 | 0.8 | 0.406 | 0.325 |
| 1.5 | 2 | 180 | 101.3 | 30 | 70 | 0 | 0 | 0 | 0.9 | 0.361 | 0.325 |
| | | | | | | | | | | | |
| 1.5 | 2 | 200 | 101.3 | 30 | 70 | 0 | 0 | 0 | 0 | 0.960 | 0.000 |
| 1.5 | 2 | 200 | 101.3 | 30 | 70 | 0 | 0 | 0 | 0.05 | 0.718 | 0.036 |
| 1.5 | 2 | 200 | 101.3 | 30 | 70 | 0 | 0 | 0 | 0.1 | 0.683 | 0.068 |
| 1.5 | 2 | 200 | 101.3 | 30 | 70 | 0 | 0 | 0 | 0.2 | 0.628 | 0.126 |
| 1.5 | 2 | 200 | 101.3 | 30 | 70 | 0 | 0 | 0 | 0.3 | 0.590 | 0.177 |
| 1.5 | 2 | 200 | 101.3 | 30 | 70 | 0 | 0 | 0 | 0.4 | 0.554 | 0.221 |
| 1.5 | 2 | 200 | 101.3 | 30 | 70 | 0 | 0 | 0 | 0.5 | 0.564 | 0.282 |
| 1.5 | 2 | 200 | 101.3 | 30 | 70 | 0 | 0 | 0 | 0.6 | 0.542 | 0.325 |
| 1.5 | 2 | 200 | 101.3 | 30 | 70 | 0 | 0 | 0 | 0.7 | 0.520 | 0.364 |
| 1.5 | 2 | 200 | 101.3 | 30 | 70 | 0 | 0 | 0 | 0.8 | 0.498 | 0.399 |
| 1.5 | 2 | 200 | 101.3 | 30 | 70 | 0 | 0 | 0 | 0.9 | 0.476 | 0.429 |
| | | | | | | | | | | | |
| | | | | | | | | | | | |
| | | | | | | | | | | | |
| | | | | | | | | | | | |
| | | | | | | | | | | | |

| | | | | Anode Gas % | | | | | | | |
|---|---|---|---|---|---|---|---|---|---|---|---|
| **Anode Stoic** | **Cathode Stoic** | **Temp ($^oC$)** | **Pressure (kPa)** | **$H_2$** | **$N_2$** | **$CO_2$** | **CO** | **$H_2O$** | **Current Density ($A/cm^2$)** | **Voltage (V)** | **Power ($W/cm^2$)** |
| 1.5 | 2 | 160 | 150 | 30 | 70 | 0 | 0 | 0 | 0.05 | 0.729 | 0.036 |
| 1.5 | 2 | 160 | 150 | 30 | 70 | 0 | 0 | 0 | 0.1 | 0.694 | 0.069 |
| 1.5 | 2 | 160 | 150 | 30 | 70 | 0 | 0 | 0 | 0.2 | 0.639 | 0.128 |
| 1.5 | 2 | 160 | 150 | 30 | 70 | 0 | 0 | 0 | 0.3 | 0.602 | 0.181 |
| 1.5 | 2 | 160 | 150 | 30 | 70 | 0 | 0 | 0 | 0.4 | 0.568 | 0.227 |
| 1.5 | 2 | 160 | 150 | 30 | 70 | 0 | 0 | 0 | 0.5 | 0.535 | 0.267 |
| 1.5 | 2 | 160 | 150 | 30 | 70 | 0 | 0 | 0 | 0.6 | 0.498 | 0.299 |
| 1.5 | 2 | 160 | 150 | 30 | 70 | 0 | 0 | 0 | 0.7 | 0.458 | 0.321 |
| 1.5 | 2 | 160 | 150 | 30 | 70 | 0 | 0 | 0 | 0.8 | 0.412 | 0.329 |
| 1.5 | 2 | 160 | 150 | 30 | 70 | 0 | 0 | 0 | 0.9 | 0.359 | 0.323 |
| | | | | | | | | | | | |
| 1.5 | 2 | 180 | 150 | 30 | 70 | 0 | 0 | 0 | 0 | 0.986 | 0.000 |
| 1.5 | 2 | 180 | 150 | 30 | 70 | 0 | 0 | 0 | 0.05 | 0.736 | 0.037 |
| 1.5 | 2 | 180 | 150 | 30 | 70 | 0 | 0 | 0 | 0.1 | 0.704 | 0.070 |
| 1.5 | 2 | 180 | 150 | 30 | 70 | 0 | 0 | 0 | 0.2 | 0.655 | 0.131 |
| 1.5 | 2 | 180 | 150 | 30 | 70 | 0 | 0 | 0 | 0.3 | 0.621 | 0.186 |
| 1.5 | 2 | 180 | 150 | 30 | 70 | 0 | 0 | 0 | 0.4 | 0.593 | 0.237 |
| 1.5 | 2 | 180 | 150 | 30 | 70 | 0 | 0 | 0 | 0.5 | 0.566 | 0.283 |
| 1.5 | 2 | 180 | 150 | 30 | 70 | 0 | 0 | 0 | 0.6 | 0.539 | 0.324 |
| 1.5 | 2 | 180 | 150 | 30 | 70 | 0 | 0 | 0 | 0.7 | 0.513 | 0.359 |
| 1.5 | 2 | 180 | 150 | 30 | 70 | 0 | 0 | 0 | 0.8 | 0.485 | 0.388 |
| 1.5 | 2 | 180 | 150 | 30 | 70 | 0 | 0 | 0 | 0.9 | 0.456 | 0.410 |
| | | | | | | | | | | | |
| | | | | | | | | | | | |
| | | | | | | | | | | | |
| | | | | | | | | | | | |
| | | | | | | | | | | | |

| | | | | Anode Gas % | | | | | | | |
|---|---|---|---|---|---|---|---|---|---|---|---|
| **Anode Stoic** | **Cathode Stoic** | **Temp ($^oC$)** | **Pressure (kPa)** | **$H_2$** | **$N_2$** | **$CO_2$** | **CO** | **$H_2O$** | **Current Density ($A/cm^2$)** | **Voltage (V)** | **Power ($W/cm^2$)** |
| 1.5 | 2 | 200 | 150 | 30 | 70 | 0 | 0 | 0 | 0.05 | 0.742 | 0.037 |
| 1.5 | 2 | 200 | 150 | 30 | 70 | 0 | 0 | 0 | 0.1 | 0.710 | 0.071 |
| 1.5 | 2 | 200 | 150 | 30 | 70 | 0 | 0 | 0 | 0.2 | 0.663 | 0.133 |
| 1.5 | 2 | 200 | 150 | 30 | 70 | 0 | 0 | 0 | 0.3 | 0.633 | 0.190 |
| 1.5 | 2 | 200 | 150 | 30 | 70 | 0 | 0 | 0 | 0.4 | 0.608 | 0.243 |
| 1.5 | 2 | 200 | 150 | 30 | 70 | 0 | 0 | 0 | 0.5 | 0.586 | 0.293 |
| 1.5 | 2 | 200 | 150 | 30 | 70 | 0 | 0 | 0 | 0.6 | 0.564 | 0.338 |
| 1.5 | 2 | 200 | 150 | 30 | 70 | 0 | 0 | 0 | 0.7 | 0.542 | 0.379 |
| 1.5 | 2 | 200 | 150 | 30 | 70 | 0 | 0 | 0 | 0.8 | 0.520 | 0.416 |
| 1.5 | 2 | 200 | 150 | 30 | 70 | 0 | 0 | 0 | 0.9 | 0.499 | 0.449 |
| | | | | | | | | | | | |
| 1.5 | 2 | 160 | 200 | 30 | 70 | 0 | 0 | 0 | 0 | 0.999 | 0.000 |
| 1.5 | 2 | 160 | 200 | 30 | 70 | 0 | 0 | 0 | 0.05 | 0.745 | 0.037 |
| 1.5 | 2 | 160 | 200 | 30 | 70 | 0 | 0 | 0 | 0.1 | 0.711 | 0.071 |
| 1.5 | 2 | 160 | 200 | 30 | 70 | 0 | 0 | 0 | 0.2 | 0.658 | 0.132 |
| 1.5 | 2 | 160 | 200 | 30 | 70 | 0 | 0 | 0 | 0.3 | 0.625 | 0.188 |
| 1.5 | 2 | 160 | 200 | 30 | 70 | 0 | 0 | 0 | 0.4 | 0.596 | 0.238 |
| 1.5 | 2 | 160 | 200 | 30 | 70 | 0 | 0 | 0 | 0.5 | 0.569 | 0.284 |
| 1.5 | 2 | 160 | 200 | 30 | 70 | 0 | 0 | 0 | 0.6 | 0.540 | 0.324 |
| 1.5 | 2 | 160 | 200 | 30 | 70 | 0 | 0 | 0 | 0.7 | 0.511 | 0.358 |
| 1.5 | 2 | 160 | 200 | 30 | 70 | 0 | 0 | 0 | 0.8 | 0.480 | 0.384 |
| 1.5 | 2 | 160 | 200 | 30 | 70 | 0 | 0 | 0 | 0.9 | 0.449 | 0.404 |
| | | | | | | | | | | | |
| | | | | | | | | | | | |
| | | | | | | | | | | | |
| | | | | | | | | | | | |
| | | | | | | | | | | | |

| | | | | Anode Gas % | | | | | | | |
|---|---|---|---|---|---|---|---|---|---|---|---|
| **Anode Stoic** | **Cathode Stoic** | **Temp ($^oC$)** | **Pressure (kPa)** | **$H_2$** | **$N_2$** | **$CO_2$** | **CO** | **$H_2O$** | **Current Density ($A/cm^2$)** | **Voltage (V)** | **Power ($W/cm^2$)** |
| 1.5 | 2 | 180 | 200 | 30 | 70 | 0 | 0 | 0 | 0.05 | 0.754 | 0.038 |
| 1.5 | 2 | 180 | 200 | 30 | 70 | 0 | 0 | 0 | 0.1 | 0.721 | 0.072 |
| 1.5 | 2 | 180 | 200 | 30 | 70 | 0 | 0 | 0 | 0.2 | 0.672 | 0.134 |
| 1.5 | 2 | 180 | 200 | 30 | 70 | 0 | 0 | 0 | 0.3 | 0.642 | 0.193 |
| 1.5 | 2 | 180 | 200 | 30 | 70 | 0 | 0 | 0 | 0.4 | 0.618 | 0.247 |
| 1.5 | 2 | 180 | 200 | 30 | 70 | 0 | 0 | 0 | 0.5 | 0.594 | 0.297 |
| 1.5 | 2 | 180 | 200 | 30 | 70 | 0 | 0 | 0 | 0.6 | 0.571 | 0.343 |
| 1.5 | 2 | 180 | 200 | 30 | 70 | 0 | 0 | 0 | 0.7 | 0.548 | 0.384 |
| 1.5 | 2 | 180 | 200 | 30 | 70 | 0 | 0 | 0 | 0.8 | 0.525 | 0.420 |
| 1.5 | 2 | 180 | 200 | 30 | 70 | 0 | 0 | 0 | 0.9 | 0.502 | 0.452 |
| | | | | | | | | | | | |
| 1.5 | 2 | 200 | 200 | 30 | 70 | 0 | 0 | 0 | 0 | 0.990 | 0.000 |
| 1.5 | 2 | 200 | 200 | 30 | 70 | 0 | 0 | 0 | 0.05 | 0.761 | 0.038 |
| 1.5 | 2 | 200 | 200 | 30 | 70 | 0 | 0 | 0 | 0.1 | 0.727 | 0.073 |
| 1.5 | 2 | 200 | 200 | 30 | 70 | 0 | 0 | 0 | 0.2 | 0.679 | 0.136 |
| 1.5 | 2 | 200 | 200 | 30 | 70 | 0 | 0 | 0 | 0.3 | 0.650 | 0.195 |
| 1.5 | 2 | 200 | 200 | 30 | 70 | 0 | 0 | 0 | 0.4 | 0.626 | 0.250 |
| 1.5 | 2 | 200 | 200 | 30 | 70 | 0 | 0 | 0 | 0.5 | 0.604 | 0.302 |
| 1.5 | 2 | 200 | 200 | 30 | 70 | 0 | 0 | 0 | 0.6 | 0.583 | 0.350 |
| 1.5 | 2 | 200 | 200 | 30 | 70 | 0 | 0 | 0 | 0.7 | 0.563 | 0.394 |
| 1.5 | 2 | 200 | 200 | 30 | 70 | 0 | 0 | 0 | 0.8 | 0.543 | 0.435 |
| 1.5 | 2 | 200 | 200 | 30 | 70 | 0 | 0 | 0 | 0.9 | 0.523 | 0.471 |

PBI Performance on Actual Reformate

| | | | | Anode Gas % | | | | | | | |
|---|---|---|---|---|---|---|---|---|---|---|---|
| **Anode Stoic** | **Cathode Stoic** | **Temp ($^oC$)** | **Pressure (kPa)** | **$H_2$** | **$N_2$** | **$CO_2$** | **CO** | **Anode Stoic** | **Current Density ($A/cm^2$)** | **Voltage (V)** | **Power ($W/cm^2$)** |
| 1.5 | 2 | 180 | 101.3 | 28 | 48 | 1 | 23 | 0 | 0 | 0.978 | 0.000 |
| 1.5 | 2 | 180 | 101.3 | 28 | 48 | 1 | 23 | 0 | 0.05 | 0.728 | 0.036 |
| 1.5 | 2 | 180 | 101.3 | 28 | 48 | 1 | 23 | 0 | 0.1 | 0.68 | 0.068 |
| 1.5 | 2 | 180 | 101.3 | 28 | 48 | 1 | 23 | 0 | 0.2 | 0.576 | 0.115 |
| 1.5 | 2 | 180 | 101.3 | 28 | 48 | 1 | 23 | 0 | 0.3 | 0.431 | 0.129 |
| 1.5 | 2 | 180 | 101.3 | 28 | 48 | 1 | 23 | 0 | 0.4 | 0.29 | 0.116 |
| 1.5 | 2 | 180 | 101.3 | 28 | 48 | 1 | 23 | 0 | 0.5 | 0.141 | 0.071 |
| | | | | | | | | | | | |
| 1.5 | 2 | 200 | 101.3 | 28 | 48 | 1 | 23 | 0 | 0 | 0.968 | 0.000 |
| 1.5 | 2 | 200 | 101.3 | 28 | 48 | 1 | 23 | 0 | 0.05 | 0.737 | 0.037 |
| 1.5 | 2 | 200 | 101.3 | 28 | 48 | 1 | 23 | 0 | 0.1 | 0.691 | 0.069 |
| 1.5 | 2 | 200 | 101.3 | 28 | 48 | 1 | 23 | 0 | 0.2 | 0.624 | 0.125 |
| 1.5 | 2 | 200 | 101.3 | 28 | 48 | 1 | 23 | 0 | 0.3 | 0.575 | 0.173 |
| 1.5 | 2 | 200 | 101.3 | 28 | 48 | 1 | 23 | 0 | 0.4 | 0.528 | 0.211 |
| 1.5 | 2 | 200 | 101.3 | 28 | 48 | 1 | 23 | 0 | 0.5 | 0.473 | 0.237 |
| 1.5 | 2 | 200 | 101.3 | 28 | 48 | 1 | 23 | 0 | 0.6 | 0.424 | 0.254 |
| 1.5 | 2 | 200 | 101.3 | 28 | 48 | 1 | 23 | 0 | 0.7 | 0.361 | 0.253 |
| 1.5 | 2 | 200 | 101.3 | 28 | 48 | 1 | 23 | 0 | 0.8 | 0.302 | 0.242 |
| 1.5 | 2 | 200 | 101.3 | 28 | 48 | 1 | 23 | 0 | 0.9 | 0.235 | 0.212 |

PBI performance of $H_2$ mixed with CO at various concentrations

| | | | | Anode Gas % | | | | | | | |
|---|---|---|---|---|---|---|---|---|---|---|---|
| **Anode Stoic** | **Cathode Stoic** | **Temp ($^oC$)** | **Pressure (kPa)** | **$H_2$** | **$N_2$** | **$CO_2$** | **CO** | **Anode Stoic** | **Current Density ($A/cm^2$)** | **Voltage (V)** | **Power ($W/cm^2$)** |
| 1.5 | 2 | 200 | 101.3 | 99 | 0 | 0 | 1 | 0 | 0 | 1.002 | 0 |
| 1.5 | 2 | 200 | 101.3 | 99 | 0 | 0 | 1 | 0 | 0.05 | 0.758 | 0.0379 |
| 1.5 | 2 | 200 | 101.3 | 99 | 0 | 0 | 1 | 0 | 0.1 | 0.724 | 0.0724 |
| 1.5 | 2 | 200 | 101.3 | 99 | 0 | 0 | 1 | 0 | 0.2 | 0.677 | 0.1354 |
| 1.5 | 2 | 200 | 101.3 | 99 | 0 | 0 | 1 | 0 | 0.3 | 0.649 | 0.1947 |
| 1.5 | 2 | 200 | 101.3 | 99 | 0 | 0 | 1 | 0 | 0.5 | 0.602 | 0.301 |
| 1.5 | 2 | 200 | 101.3 | 99 | 0 | 0 | 1 | 0 | 0.7 | 0.558 | 0.3906 |
| 1.5 | 2 | 200 | 101.3 | 99 | 0 | 0 | 1 | 0 | 0.9 | 0.516 | 0.4644 |
| 1.5 | 2 | 200 | 101.3 | 99 | 0 | 0 | 1 | 0 | 1.1 | 0.474 | 0.5214 |
| 1.5 | 2 | 200 | 101.3 | 99 | 0 | 0 | 1 | 0 | 1.3 | 0.432 | 0.5616 |
| 1.5 | 2 | 200 | 101.3 | 99 | 0 | 0 | 1 | 0 | 1.4 | 0.41 | 0.574 |
| 1.5 | 2 | 200 | 101.3 | 99 | 0 | 0 | 1 | 0 | 1.5 | 0.389 | 0.5835 |
| 1.5 | 2 | 200 | 101.3 | 99 | 0 | 0 | 1 | 0 | 1.6 | 0.366 | 0.5856 |
| 1.5 | 2 | 200 | 101.3 | 99 | 0 | 0 | 1 | 0 | 1.7 | 0.344 | 0.5848 |
| 1.5 | 2 | 200 | 101.3 | 99 | 0 | 0 | 1 | 0 | 1.8 | 0.303 | 0.5454 |

| | | | | Anode Gas % | | | | | | | |
|---|---|---|---|---|---|---|---|---|---|---|---|
| **Anode Stoic** | **Cathode Stoic** | **Temp (°C)** | **Pressure (kPa)** | **$H_2$** | **$N_2$** | **$CO_2$** | **CO** | **Anode Stoic** | **Current Density ($A/cm^2$)** | **Voltage (V)** | **Power ($W/cm^2$)** |
| 1.5 | 2 | 200 | 101.3 | 97 | 0 | 0 | 3 | 0 | 0.05 | 0.754 | 0.0377 |
| 1.5 | 2 | 200 | 101.3 | 97 | 0 | 0 | 3 | 0 | 0.1 | 0.72 | 0.072 |
| 1.5 | 2 | 200 | 101.3 | 97 | 0 | 0 | 3 | 0 | 0.2 | 0.672 | 0.1344 |
| 1.5 | 2 | 200 | 101.3 | 97 | 0 | 0 | 3 | 0 | 0.3 | 0.643 | 0.1929 |
| 1.5 | 2 | 200 | 101.3 | 97 | 0 | 0 | 3 | 0 | 0.5 | 0.595 | 0.2975 |
| 1.5 | 2 | 200 | 101.3 | 97 | 0 | 0 | 3 | 0 | 0.7 | 0.549 | 0.3843 |
| 1.5 | 2 | 200 | 101.3 | 97 | 0 | 0 | 3 | 0 | 0.9 | 0.504 | 0.4536 |
| 1.5 | 2 | 200 | 101.3 | 97 | 0 | 0 | 3 | 0 | 1.1 | 0.46 | 0.506 |
| 1.5 | 2 | 200 | 101.3 | 97 | 0 | 0 | 3 | 0 | 1.3 | 0.416 | 0.5408 |
| 1.5 | 2 | 200 | 101.3 | 97 | 0 | 0 | 3 | 0 | 1.4 | 0.39 | 0.546 |
| 1.5 | 2 | 200 | 101.3 | 97 | 0 | 0 | 3 | 0 | 1.5 | 0.371 | 0.5565 |
| 1.5 | 2 | 200 | 101.3 | 97 | 0 | 0 | 3 | 0 | 1.6 | 0.347 | 0.5552 |
| 1.5 | 2 | 200 | 101.3 | 97 | 0 | 0 | 3 | 0 | 1.7 | 0.322 | 0.5474 |
| 1.5 | 2 | 200 | 101.3 | 97 | 0 | 0 | 3 | 0 | 1.8 | 0.295 | 0.531 |
| 1.5 | 2 | 200 | 101.3 | 97 | 0 | 0 | 3 | 0 | 1.9 | 0.267 | 0.5073 |
| | | | | | | | | | | | |
| 1.5 | 2 | 200 | 101.3 | 95 | 5 | 0 | 0 | 0 | 0 | 1 | 0 |
| 1.5 | 2 | 200 | 101.3 | 95 | 5 | 0 | 0 | 0 | 0.05 | 0.752 | 0.0376 |
| 1.5 | 2 | 200 | 101.3 | 95 | 5 | 0 | 0 | 0 | 0.1 | 0.7205 | 0.07205 |
| 1.5 | 2 | 200 | 101.3 | 95 | 5 | 0 | 0 | 0 | 0.2 | 0.676 | 0.1352 |
| 1.5 | 2 | 200 | 101.3 | 95 | 5 | 0 | 0 | 0 | 0.3 | 0.648 | 0.1944 |
| 1.5 | 2 | 200 | 101.3 | 95 | 5 | 0 | 0 | 0 | 0.5 | 0.601 | 0.3005 |
| 1.5 | 2 | 200 | 101.3 | 95 | 5 | 0 | 0 | 0 | 0.7 | 0.557 | 0.3899 |
| 1.5 | 2 | 200 | 101.3 | 95 | 5 | 0 | 0 | 0 | 0.9 | 0.515 | 0.4635 |
| 1.5 | 2 | 200 | 101.3 | 95 | 5 | 0 | 0 | 0 | 1.1 | 0.4735 | 0.52085 |
| 1.5 | 2 | 200 | 101.3 | 95 | 5 | 0 | 0 | 0 | 1.3 | 0.4315 | 0.56095 |
| 1.5 | 2 | 200 | 101.3 | 95 | 5 | 0 | 0 | 0 | 1.4 | 0.41 | 0.574 |

| | | | | Anode Gas % | | | | | | | |
|---|---|---|---|---|---|---|---|---|---|---|---|
| **Anode Stoic** | **Cathode Stoic** | **Temp ($^oC$)** | **Pressure (kPa)** | **$H_2$** | **$N_2$** | **$CO_2$** | **CO** | **Anode Stoic** | **Cathode Stoic** | **Temp ($^oC$)** | **Pressure (kPa)** |
| 1.5 | 2 | 200 | 101.3 | 90 | 0 | 0 | 10 | 0 | 0 | 1.01 | 0 |
| 1.5 | 2 | 200 | 101.3 | 90 | 0 | 0 | 10 | 0 | 0.05 | 0.746 | 0.0373 |
| 1.5 | 2 | 200 | 101.3 | 90 | 0 | 0 | 10 | 0 | 0.1 | 0.712 | 0.0712 |
| 1.5 | 2 | 200 | 101.3 | 90 | 0 | 0 | 10 | 0 | 0.2 | 0.657 | 0.1314 |
| 1.5 | 2 | 200 | 101.3 | 90 | 0 | 0 | 10 | 0 | 0.3 | 0.622 | 0.1866 |
| 1.5 | 2 | 200 | 101.3 | 90 | 0 | 0 | 10 | 0 | 0.5 | 0.553 | 0.2765 |
| 1.5 | 2 | 200 | 101.3 | 90 | 0 | 0 | 10 | 0 | 0.7 | 0.473 | 0.3311 |
| 1.5 | 2 | 200 | 101.3 | 90 | 0 | 0 | 10 | 0 | 0.9 | 0.397 | 0.3573 |
| 1.5 | 2 | 200 | 101.3 | 90 | 0 | 0 | 10 | 0 | 1.1 | 0.319 | 0.3509 |
| 1.5 | 2 | 200 | 101.3 | 90 | 0 | 0 | 10 | 0 | 1.2 | 0.282 | 0.3384 |
| 1.5 | 2 | 200 | 101.3 | 90 | 0 | 0 | 10 | 0 | 1.3 | 0.246 | 0.3198 |
| | | | | | | | | | | | |
| 1.5 | 2 | 200 | 101.3 | 85 | 0 | 0 | 15 | 0 | 0 | 1.001 | 0 |
| 1.5 | 2 | 200 | 101.3 | 85 | 0 | 0 | 15 | 0 | 0.05 | 0.741 | 0.03705 |
| 1.5 | 2 | 200 | 101.3 | 85 | 0 | 0 | 15 | 0 | 0.1 | 0.708 | 0.0708 |
| 1.5 | 2 | 200 | 101.3 | 85 | 0 | 0 | 15 | 0 | 0.2 | 0.655 | 0.131 |
| 1.5 | 2 | 200 | 101.3 | 85 | 0 | 0 | 15 | 0 | 0.3 | 0.611 | 0.1833 |
| 1.5 | 2 | 200 | 101.3 | 85 | 0 | 0 | 15 | 0 | 0.5 | 0.525 | 0.2625 |
| 1.5 | 2 | 200 | 101.3 | 85 | 0 | 0 | 15 | 0 | 0.6 | 0.475 | 0.285 |
| 1.5 | 2 | 200 | 101.3 | 85 | 0 | 0 | 15 | 0 | 0.7 | 0.42 | 0.294 |
| 1.5 | 2 | 200 | 101.3 | 85 | 0 | 0 | 15 | 0 | 0.8 | 0.371 | 0.2968 |
| 1.5 | 2 | 200 | 101.3 | 85 | 0 | 0 | 15 | 0 | 0.85 | 0.345 | 0.29325 |
| 1.5 | 2 | 200 | 101.3 | 85 | 0 | 0 | 15 | 0 | 0.9 | 0.317 | 0.2853 |
| 1.5 | 2 | 200 | 101.3 | 85 | 0 | 0 | 15 | 0 | 0.95 | 0.29 | 0.2755 |
| 1.5 | 2 | 200 | 101.3 | 85 | 0 | 0 | 15 | 0 | 1 | 0.265 | 0.265 |
| 1.5 | 2 | 200 | 101.3 | 85 | 0 | 0 | 15 | 0 | 1.05 | 0.242 | 0.2541 |
| 1.5 | 2 | 200 | 101.3 | 85 | 0 | 0 | 15 | 0 | 1.1 | 0.216 | 0.2376 |
| | | | | | | | | | | | |

| | | | | Anode Gas % | | | | | | | |
|---|---|---|---|---|---|---|---|---|---|---|---|
| **Anode Stoic** | **Cathode Stoic** | **Temp ($^oC$)** | **Pressure (kPa)** | **$H_2$** | **$N_2$** | **$CO_2$** | **CO** | **Anode Stoic** | **Cathode Stoic** | **Temp ($^oC$)** | **Pressure (kPa)** |
| 1.5 | 2 | 200 | 101.3 | 80 | 0 | 0 | 20 | 0 | 0 | 0.998 | 0 |
| 1.5 | 2 | 200 | 101.3 | 80 | 0 | 0 | 20 | 0 | 0.05 | 0.738 | 0.0369 |
| 1.5 | 2 | 200 | 101.3 | 80 | 0 | 0 | 20 | 0 | 0.1 | 0.702 | 0.0702 |
| 1.5 | 2 | 200 | 101.3 | 80 | 0 | 0 | 20 | 0 | 0.15 | 0.674 | 0.1011 |
| 1.5 | 2 | 200 | 101.3 | 80 | 0 | 0 | 20 | 0 | 0.2 | 0.641 | 0.1282 |
| 1.5 | 2 | 200 | 101.3 | 80 | 0 | 0 | 20 | 0 | 0.3 | 0.594 | 0.1782 |
| 1.5 | 2 | 200 | 101.3 | 80 | 0 | 0 | 20 | 0 | 0.4 | 0.543 | 0.2172 |
| 1.5 | 2 | 200 | 101.3 | 80 | 0 | 0 | 20 | 0 | 0.5 | 0.471 | 0.2355 |
| 1.5 | 2 | 200 | 101.3 | 80 | 0 | 0 | 20 | 0 | 0.6 | 0.401 | 0.2406 |
| 1.5 | 2 | 200 | 101.3 | 80 | 0 | 0 | 20 | 0 | 0.65 | 0.367 | 0.23855 |
| 1.5 | 2 | 200 | 101.3 | 80 | 0 | 0 | 20 | 0 | 0.7 | 0.329 | 0.2303 |
| 1.5 | 2 | 200 | 101.3 | 80 | 0 | 0 | 20 | 0 | 0.75 | 0.282 | 0.2115 |